

Polimery w Medycynie

Polymers in Medicine

BIANNUAL ISSN: 0370-0747 e-ISSN: 2451-2699

polimery.umw.edu.pl

2024, Vol. 54, No. 1 (January–June)

Ministry of Science and Higher Education – 70 pts.
Index Copernicus (ICV) – 121.55 pts.



WROCLAW
MEDICAL UNIVERSITY

Polimery w Medycynie
Polymers in Medicine



Polimery w Medycynie

Polymers in Medicine

ISSN 0370-0747 (PRINT)

ISSN 2451-2699 (ONLINE)

polimery.umw.edu.pl

BIANNUAL
2024, Vol. 54, No. 1
(January–June)

“Polymers in Medicine” is an independent, multidisciplinary forum to exchange scientific and clinical information, which publishes original papers (technical, analytical, experimental, clinical), preliminary reports and reviews regarding the use of polymers (natural and synthetic) and biomaterials in different specialties of medicine (biochemistry, clinical medicine, pharmacology, dentistry, implantology), biotechnology and veterinary science.

Address of Editorial Office

Marcinkowskiego 2–6
50-368 Wrocław, Poland
Tel.: +48 71 784 11 33
E-mail: redakcja@umw.edu.pl

Editor-in-Chief

Prof. Witold Musiał

Deputy Editor

Dr. Konrad Szustakiewicz, DSc., Eng.

Statistical Editors

Wojciech Bombała, MSc
Łucja Janek, MSc
Anna Kopszak, MSc
Dr. Krzysztof Kujawa
Jakub Wronowicz, MSc

Publisher

Wrocław Medical University
Wybrzeże L. Pasteura 1
50-367 Wrocław, Poland

Scientific Committee

Prof. Mirosława El-Fray
Prof. Franciszek Główka
Prof. Jörg Kreßler
Dr. Anna Krupa
Prof. Maciej Małecki
Prof. Bożena B. Michniak-Kohn

Prof. Wojciech Milyk
Prof. Masami Okamoto
Prof. Elżbieta Pamała
Prof. Wiesław Sawicki
Prof. Szczepan Zapotoczny

Online edition is the original version of the journal

Section Editors

Dr. Tomasz Urbaniak
(synthesis, evaluation, medical use of polymers, sensitive to environmental factors, applied in controlled and targeted drug delivery)

Dr. Monika Gasztych
(preparation, assessment and application of polymers in pharmaceutical technology and medical devices)

Dr. BEng., Agnieszka Gadomska-Gajadur
(synthesis and characterization of polymers having biomedical potential, composites for regenerative medicine)

Manuscript editing

Marek Misiak, Jolanta Krzyżak

Editorial Policy

During the review process, the Editorial Board conforms to the "Uniform Requirements for Manuscripts Submitted to Biomedical Journals: Writing and Editing for Biomedical Publication" approved by the International Committee of Medical Journal Editors (<http://www.icmje.org/>). Experimental studies must include a statement that the experimental protocol and informed consent procedure were in compliance with the Helsinki Convention and were approved by the ethics committee.

For more information visit the following page: <https://polimery.umw.edu.pl>

Polimery w Medycynie – Polymers in Medicine has received financial support from the resources of Ministry of Science and Higher Education within the "Social Responsibility of Science – Support for Academic Publishing" project based on agreement No. RCN/SP/0504/2021.



Ministry of Education and Science
Republic of Poland

Czasopismo Polimery w Medycynie – Polymers in Medicine korzysta ze wsparcia finansowego ze środków Ministerstwa Edukacji i Nauki w ramach programu „Społeczna Odpowiedzialność Nauki – Rozwój Czasopism Naukowych” na podstawie umowy nr RCN/SP/0504/2021.



Ministerstwo
Edukacji i Nauki

Indexed in: OCLC, WorldCat, PBL, EBSCO, MEDLINE, Index Copernicus

Typographic design: Monika Kołęda, Piotr Gil

Cover: Monika Kołęda

DTP: Wrocław Medical University Press

Printing and binding: PRINT PROFIT Sp. z o.o., Koźmin 27, 59-900 Zgorzelec

Circulation: 11 copies

Contents

- 5 Preface
- 6 Wstęp

Original papers

- 7 Santiago Herrera-Guardiola, Carlos H. Valencia-Llano, Miguel Á. Casillas-Santana, Farid A. Dipp-Velázquez, Juan F. Aristizábal-Pérez
Evaluation of cellular viability in chitosan/L-arginine hydrogels
- 15 Tomasz Jeliński, Maciej Przybyłek, Rafał Różalski, Piotr Cysewski
Solubility of dapsone in deep eutectic solvents: Experimental analysis, molecular insights and machine learning predictions
- 27 Piotr Cysewski, Maciej Przybyłek, Tomasz Jeliński
Predicting sulfanilamide solubility in the binary mixtures using a reference solvent approach
- 35 Joanna Kotyńska, Marcin Zajac, Agnieszka Mikłosz, Adrian Chabowski, Monika Naumowicz
Alteration of zeta potential and cell viability in rat-derived L6 skeletal muscle cells and H9c2 cardiomyocytes: A study with submicron polystyrene particles
- 45 Andrzej Ślęzak, Sławomir M. Grzegorzczyn
L version of the transformed Kedem–Katchalsky equations for membrane transport of electrolyte solutions and internal energy conversion
- 59 Martyna Sokołowska, Moein Zarei, Mirosława El Fray
Enzymatic synthesis of furan-based copolymers: Material characterization and potential for biomedical applications

Reviews

- 71 Pravin Kondiba Pawar, Raju Dubaji Rathod, Satyajeet Ramesh Jagadale
A review on topical ophthalmic drug delivery system: Reference to viscosity enhancer

PREFACE

Dear Readers,



Modern medicine is built on the pillar of empirical basic research and as such requires continuous research efforts to maintain a high pace of development for the health of humanity. The content of this issue of our journal reflects a wide range of basic research useful for medicine in the area of small and large molecules, in particular macromolecules. The interactions of polymers with living tissue or living cells are an important way to determine the safety of pharmaceutical preparations based on synthetic or natural polymers.

This issue includes experimental work on the synthesis and safety of interesting chitin-arginine hydrogels developed by a team of researchers from Colombia and Mexico. A similar topic, using specialized enzymatic synthesis of furan copolymers, was proposed by a team from Szczecin. Polymers interact with living tissues not only as drugs, but also as unplanned xenobiotics – authors from Wrocław presented the interaction of polystyrene microparticles with animal myocytes and cardiomyocytes. The introduction of a drug into a polymer carrier requires the development of detailed characteristics of the solubility of this drug – two studies from the Bydgoszcz–Toruń center describe the solubility tests of dapsone and sulfanilamide, respectively. However, not only solubility determines the behavior of the drug in the polymer matrix. Valuable article on computational aspects of drug transport according to the modified Kedem–Katchalsky model was submitted by authors from Opole. The first issue of our semi-annual in 2024 is summarized by two review articles: one on the effectiveness of sulforaphane in skin applications, and the other on the importance of polymeric substances modifying viscosity in ophthalmological preparations.

Some of the articles presented here are the results of the conference “Physical Chemistry and Biophysics for Pharmacy”, organized at the Wrocław Medical University on December 8, 2023, with the participation of researchers from the USA, Czech Republic and Estonia, among other countries. Therefore, I would like to invite you to publish in our magazine on the occasion of the next edition of the abovementioned conference on September 27, 2024. Our Editorial Team wishes you a good read and a relaxing summer holiday.

Editor-in-Chief
Witold Musiał, Prof., PhD, DSc

WSTĘP

Drodzy czytelnicy,

współczesna medycyna zbudowana jest na filarze empirycznych badań podstawowych i jako taka wymaga nieustannych wysiłków badawczych, aby utrzymać wysokie tempo rozwoju na rzecz zdrowia ludzkości. Treść niniejszego numeru czasopisma odzwierciedla szeroki zakres badań podstawowych użytecznych dla medycyny w obszarze małych i dużych molekuł, w szczególności zaś makromolekuł. Oddziaływania polimerów z żywą tkanką lub żywymi komórkami stanowią ważną drogę ustalania bezpieczeństwa preparatów farmaceutycznych opartych o polimery syntetyczne lub naturalne.

W tym numerze znajdziemy prace eksperymentalne dotyczące syntezy i bezpieczeństwa ciekawych hydrożeli chitynowo-argininowych opracowanych przez zespół badaczy z Kolumbii i Meksyku. Podobną tematykę, wykorzystującą specjalistyczną syntezę enzymatyczną kopolimerów furanowych, zaproponował zespół ze Szczecina. Polimery oddziałują z żywymi tkankami nie tylko jako leki, ale także jako nieplanowane ksenobiotyki – autorzy z Wrocławia zaprezentowali oddziaływanie mikrocząstek polistyrenu z miocytami i kardiomiocytami zwierzęcymi. Wprowadzenie leku do nośnika polimerowego wymaga opracowania szczegółowej charakterystyki rozpuszczalności tego leku – w dwóch pracach z ośrodka bydgosko-toruńskiego omówiono badania rozpuszczalności odpowiednio dapsonu i sulfanilamidu. Nie tylko rozpuszczalność determinuje zachowanie się leku w matrycy polimerowej. Cenny artykuł nt. obliczeniowych aspektów transportu leku wg. zmodyfikowanego modelu Kedem–Katchalsky’ego nadesłali autorzy z Opola. Podsumowaniem pierwsze wydanie naszego półrocznika w 2024 roku są dwa artykuły przeglądowe: nt. efektywności sulforafanu w podaniach na skórę oraz nt. znaczenia polimerowych substancji modyfikujących lepkość w preparatach oftalmologicznych.

Część prezentowanych tutaj artykułów jest pokłosiem konferencji pt. „Chemia Fizyczna i Biofizyka dla farmacji”, zorganizowanej na Uniwersytecie Medycznym we Wrocławiu 8 grudnia 2023 r., w której brali udział naukowcy m.in. z USA, Czech i Estonii. Pragnę zatem zaprosić Państwa do publikowania w naszym czasopiśmie, między innymi przy okazji kolejnej edycji ww. konferencji – 27 września 2024 r. Wraz z zespołem Wydawnictwa życzymy dobrej lektury oraz wypoczynku wakacyjnego.



Witold Musiał

Evaluation of cellular viability in chitosan/L-arginine hydrogels

Santiago Herrera-Guardiola^{1,A–F}, Carlos H. Valencia-Llano^{2,A–F}, Miguel Á. Casillas-Santana^{3,A–F}, Farid A. Dipp-Velázquez^{4,A–F}, Juan F. Aristizábal-Pérez^{1,A–F}

¹ Department of Orthodontics, University of Valle, Cali, Colombia

² School of Dentistry, University of Valle, Cali, Colombia

³ Faculty of Stomatology, Meritorious Autonomous University of Puebla, México

⁴ Department of Orthodontics, Meritorious Autonomous University of Puebla, México

A – research concept and design; B – collection and/or assembly of data; C – data analysis and interpretation;

D – writing the article; E – critical revision of the article; F – final approval of the article

Polymers in Medicine, ISSN 0370-0747 (print), ISSN 2451-2699 (online)

Polim Med. 2024;54(1):7–14

Address for correspondence

Juan F. Aristizábal-Pérez

E-mail: juan.aristizabal@correounivalle.edu.co

Funding sources

None declared

Conflict of interest

None declared

Received on October 3, 2023

Reviewed on February 14, 2024

Accepted on February 19, 2024

Published online on March 28, 2024

Abstract

Background. There is a lack of studies evaluating the toxicity of nitric oxide (NO) precursors in chitosan/L-arginine hydrogels and their topical administration. However, clarifying the characteristics of these elements is essential for their possible use in non-surgical techniques of tooth movement acceleration. Such characteristics include interaction with different cell types, metabolism and drug safety.

Objectives. This in vitro study aimed to assess the cytotoxicity of chitosan hydrogels on human HeLa cells using different concentrations of L-arginine.

Materials and methods. The hydrogels were synthesized in a materials engineering laboratory, with a controlled environment, using 4 different L-arginine concentrations of 0%, 10%, 15%, and 20%. Once the hydrogels were prepared, their physical and chemical properties were characterized, and viability analysis was performed using 2 different methods, including a 48-h assay with *Artemia salina* nauplii and a 24-h cell culture with human HeLa cells followed by a 3-(4,5-dimethylthiazol-2-yl)-2,5-diphenyltetrazolium bromide (MTT) proliferation assay. Data analysis was performed using a Mann–Whitney U test to evaluate positive and negative controls in the cell culture, with a significance level of 0.01. A Wilcoxon paired test contrasted the 24-h compared to 48-h *Artemia salina* assays, with a Kruskal–Wallis and post hoc Dunn test used to compare groups using a significance level of 0.05.

Results. In the more viscous hydrogels, *Artemia salina* nauplii decreased drastically in 24 h, while the 15% and 20% hydrogels had no statistical differences from the negative control. The 10% and 20% hydrogels were statistically different from the negative control when comparing cell culture data.

Conclusions. Our findings suggest that chitosan/L-arginine hydrogels could be used in humans without toxic effects. However, more trials and tests are needed to evaluate tooth movement rate during orthodontic treatment.

Key words: hydrogels, in vitro techniques, cell culture techniques

Cite as

Herrera-Guardiola S, Valencia-Llano CH, Casillas-Santana MA, Dipp-Velázquez FA, Aristizábal-Pérez JF. Evaluation of cellular viability in chitosan/L-arginine hydrogels.

Polim Med. 2024;54(1):7–14. doi:10.17219/pim/184260

DOI

10.17219/pim/184260

Copyright

Copyright by Author(s)

This is an article distributed under the terms of the Creative Commons Attribution 3.0 Unported (CC BY 3.0) (<https://creativecommons.org/licenses/by/3.0/>)

Background

The current goal of orthodontic processes is to reduce treatment time and avoid the deleterious effects of controlled dental movement. As for the possibilities of movement acceleration, there are multiple approaches, including vibration stimulation,^{1–3} low-intensity laser^{4,5} and surgical techniques (piezosin, corticotomy or surgeries to generate regional acceleration (RAP)).^{6–8} However, these approaches may negatively affect dental roots.⁹ There is a non-surgical or radiation alternative involving drug stimulation with hydrogels containing nitric oxide (NO) precursors as mediators to eliminate possible adverse effects.

Given the physical and chemical characteristics of hydrogels, they can be modulated through structural modifications. Hydrogels composed of natural polymers are used in tissue engineering to control bioactive molecule delivery.^{10–13} Also, collagen scaffolds are used for drug delivery in tissue engineering.¹⁴

Chitosan is an alkaline deacetylated co-polymer of chitin of the amino-polysaccharide type, consisting of D-glucosamine and N-acetyl-D-glucosamine.¹⁰ Nitric oxide is an endogenously produced diatomic molecule that plays a crucial role in physiological processes such as angiogenesis, healing, neurotransmission, smooth muscle relaxation, inflammation, and bone metabolism.^{15,16} The role of NO in osteogenesis depends on its concentration, with models using NO disruption demonstrating inhibition of osteoblast differentiation and a decrease in their activity.^{17–19} Under normal physiological conditions, the effect of NO is biphasic, with the cytokines that promote osteoclastogenesis inhibited at high concentrations and their impact enhanced at low concentrations.^{10,20–23}

Since there are no studies reporting NO toxicity precursors in chitosan/L-arginine hydrogels and their topical administration, it is essential to clarify their characteristics for use in non-surgical dental movement acceleration techniques, their interaction with different cell types, metabolism, and drug safety. This study aimed to evaluate the cytotoxicity of multiple chitosan hydrogels using different L-arginine concentrations in human HeLa cell cultures.

Materials and methods

Chitosan hydrogels

This *in vitro* study used a hybrid chitosan gel, obtained following the formulation and protocols developed by the research group of Faculty of Stomatology (Meritorious Autonomous University of Puebla, Mexico),^{23,24} with a texture suitable for typical intraoral use. Once the gel was synthesized, the amino acid (L-arginine) was adhered, and the link was made chemically.²⁵

Hydrogels were obtained using L-arginine concentrations of 0%, 10%, 15%, and 20%, according to protocols standardized by the laboratory. A hydrogel with a percentage

lower than 10% was not selected because it was important to ensure an adequate arginine concentration.

The hydrogel was prepared with a dilution of L-arginine (Santa Cruz Biotechnology, Santa Cruz, USA), according to the required concentration (1.244 mg for 10%, 1.97 mg for 15% and 2.8 mg for 20%), with 10 mL of distilled water until a homogeneous consistency was achieved. Then, 0.5 mL of acetic acid and 0.2 mL of glycerol were added and mixed with 0.5 mg of low molecular weight chitosan (Sigma-Aldrich, St. Louis, USA). The hydrogel was kept refrigerated and used for experimentation within a week of fabrication.

Physicochemical characterization

The physicochemical characterization was done in the Materials Engineering and Chemistry Laboratory of the University of Valle (Cali, Colombia) after the different hydrogels were dried and processed. Gel samples were dried at 60°C for 72 h, and their chemical composition was studied using Fourier-transform infrared spectroscopy in attenuated total internal reflectance mode (ATR-FTIR) (Perkin-Elmer, Waltham, USA) with Shimadzu equipment (Spectrophotometer FT-IR-8400; Shimadzu Corp., Kyoto, Japan). A Fisherbrand Accumet™ AB150 pH (Thermo Fisher Scientific, Waltham, USA) meter measured pH using a pH/ATC electrode with a refillable epoxy body, previously calibrated with buffer solutions of pH at 4, 7 and 10. Density was determined with a 25 cm³ pycnometer (Brand, Wertheim, Germany). The amount of each sample required to fill the pycnometer was weighed, and the density was calculated as mass/volume.

Cytotoxicity and cell viability tests

To perform the cytotoxicity tests, we used the HeLa cell line available at the *in vitro* cell culture laboratory of the Department of Pharmacology of the University of Valle. Six evaluation groups were determined according to the percentage of L-arginine:

- cells in medium alone (negative control);
- cells seeded in chitosan gel with 0% L-arginine;
- cells seeded in chitosan gel with 10% L-arginine;
- cells seeded in chitosan gel with 15% L-arginine;
- cells seeded in chitosan gel with 20% L-arginine;
- cells with cisplatin (positive control).

For the hydrogel treatment, each group was seeded in 96-mug plates under a humidified atmosphere of 5% CO₂ at 37°C for 24 h and allowed to proliferate. Thirty thousand (30,000) cells per mug were achieved following the protocol of the 3-(4,5-dimethylthiazol-2-yl)-2,5-diphenyltetrazolium bromide (MTT) assay manufacturer. Subsequently, the mugs were brought to a final volume of 200 µL using Hank's balanced salt solution (HBSS) without fetal bovine serum (FBS) since the formazan crystals of the MTT assay were not formed. We added 20 µL of hydrogel to each mug and incubated them for 24 h. Cell viability analysis was then carried out.

MTT feasibility assay

Cell viability was evaluated using the MTT Cell Proliferation Assay Kit (Abcam ab211091; Abcam, Cambridge, UK), which is based on the conversion of the water-soluble component MTT to an insoluble formazan product. Viable cells with active metabolism convert MTT to formazan, while dead cells lose their metabolic capacity and do not show any signal. A spectrophotometer was used to analyze the absorbance once the formazan crystallization process was completed to evaluate whether there was cell death. The absorbance measurement at optical density (OD) 590 nm is proportional to the number of viable cells.^{27–29} To make the data more easily interpreted, the following equation was used³⁰:

$$\% \text{ viability} = (\text{OD treated cells} / \text{OD control cells}) \times 100$$

Artemia salina assay

Artemia salina culture was performed for 3 days within a sterile saline medium with a pH of 8.5 using 0.1 N NaOH under constant oxygenation and artificial light to simulate a natural and controlled saline environment. The specimens were harvested once the newly hatched nauplii were available. Samples in culture dishes were divided into 6 groups: 0%, 10%, 15%, and 20% L-arginine hydrogel, negative control with the same saline medium, and positive control with an enzymatic soap. Each group was analyzed in 5 dishes with 10 *Artemia salina* specimens in each mug to guarantee enough replicates for each treatment.

Once the number of samples per group was achieved, the hydrogels were introduced to the culture dishes for 24 h and 48 h, with 20 μL of hydrogel added to each mug. Statistical analyses were carried out according to the number of *Artemia salina* specimens not seen alive under an optical microscope (Primo Star; Carl Zeiss AG, Jena, Germany) at $\times 4$ magnification.

HeLa cell culture assay

The viability data of each hydrogel concentration was recorded in Microsoft Excel 2019 sheets (Microsoft Corp., Redmond, USA) and later analyzed in GraphPad Prism v. 9.11 (GraphPad, San Diego, USA). The analysis consisted of calculating measures of central tendency and dispersion of the serial tests for each material. A summary table and graph of mean values with the corresponding standard errors (SEs) were constructed. Viability distributions were compared between pairs of the experimental samples (compared to the positive and negative controls) using Mann–Whitney U test.

Statistical analyses

Culture data were expressed as the mean \pm SE of independent experiments for each condition. Differences

between treatment groups were analyzed with the GraphPad software. Viability distributions were compared between pairs of the experimental samples (compared to the positive and negative controls) using Mann–Whitney U test. A significance level of less than 0.01 was used.

Artemia salina assay data were recorded in Excel and later analyzed in the Stata IC15 program (Stata Corp., College Station, USA). The analysis consisted of calculating measures of central tendency and dispersion of the presence of nauplii for each hydrogel concentration (0%, 10%, 15%, and 20%). A summary table and graph of means with the corresponding SE were constructed. The number of nauplii per pair was compared between 24 h and 48 h using a Wilcoxon paired test. The contrast between groups was performed using the Kruskal–Wallis test and post hoc in pairs with Dunn's test; this analysis excluded the negative control. We used a significance level of 0.05.

Results

Physicochemical characterization

The results showed absorption bands that characterize chitosan in the 3,200–3,600 cm^{-1} region, which are due to stretching of the $-\text{OH}$ and $-\text{NH}$ bonds. The absorption bands near the 2,870 cm^{-1} and 1,404 cm^{-1} region corresponded to the stretching and bending vibration of the C–H single bond in the polymer chain (Fig. 1). The peaks present in the 1,638 cm^{-1} and 1,545 cm^{-1} region corresponded to amide bands I and II, respectively.

For the pH results, there was a difference in acidity that corresponded to the percentage of the amino acid added. For instance, the hydrogel with 0% L-arginine component had a 3.32 score on the acidity scale, while the one with 20% had a more neutral score of 6.60.

Finally, the density presented by the different types of hydrogels was 1.14 g/cm^3 for the 0% hydrogel, 1.18 g/cm^3 for the 10% hydrogel, 1.09 g/cm^3 for the 15% hydrogel, and 1.07 g/cm^3 for the 20% hydrogel.

Artemia salina culture

Microscopic analyses demonstrated a significant decrease in specimens at 24 h in the 0% and 10% hydrogels, while there was no such mortality in the less viscous hydrogels (15% and 20%).

The mean number of nauplii in the hydrogel was higher at the 20% (9.0 \pm 2.24) and 15% (8.2 \pm 1.79) concentrations at 24 h. After 48 h, the number of nauplii decreased, but the same pattern continued, with more *Artemia salina* nauplii at higher hydrogel concentrations. For instance, an average of 7 (\pm 1.73) nauplii were found in the 20% hydrogel, while 6.8 (\pm 1.30) nauplii were found in the 15% hydrogel. The differences were

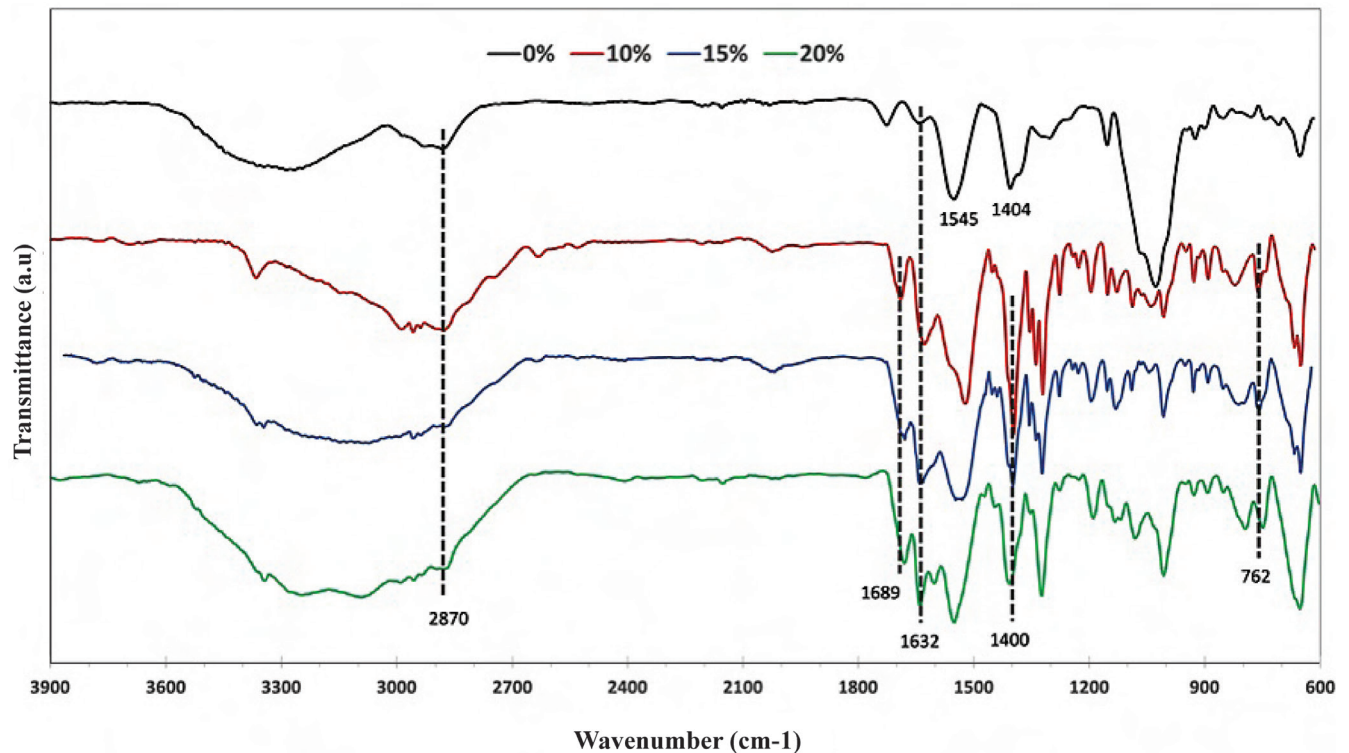


Fig. 1. Infrared Fourier-transform spectra of chitosan and arginine gels

Table 1. The average number of *Artemia salina* nauplii at 24 h and 48 h according to the concentration of the experimental hydrogel

Materials	n	24 h			48 h			p-value
		Mean	SD	SE	Mean	SD	SE	
H-0%	5	2.2	0.84	0.37	0.8	0.84	0.37	0.038
H-10%	5	2.8	0.45	0.2	1.6	0.55	0.24	0.034
H-15%	5	8.2	1.79	0.8	6.8	1.30	0.58	0.038
H-20%	5	9	2.24	1	7	1.73	0.77	0.039
C-	4	6.5	1.29	0.65	6	0.82	0.41	0.157
C+	4	0	0	0	0	0	0	-

SD – standard deviation; SE – standard error; H – hydrogel; C+ – positive control; C- – negative control.

Table 2. P-value of contrast tests by pairs (Dunn's test)

Materials	24 h				48 h			
	C-	H-0%	H-10%	H-15%	C-	H-0%	H-10%	H-15%
H-0%	0.007**	-	-	-	0.011*	-	-	-
H-10%	0.024*	0.309	-	-	0.045*	0.264	-	-
H-15%	0.207	0.000**	0.002**	-	0.349	0.002**	0.014*	-
H-20%	0.439	0.003**	0.012*	0.241	0.120	0.000**	0.001**	0.202

H – hydrogel; C+ – positive control; C- – negative control; *p < 0.05; **p < 0.01.

statistically significant between 24 h and 48 h at all concentrations (Table 1).

When comparing the groups with each other in pairs (Table 2), statistically significant differences were found at 24 h (Kruskal–Wallis $p = 0.001$) and 48 h (Kruskal–Wallis $p = 0.001$) (Fig. 2).

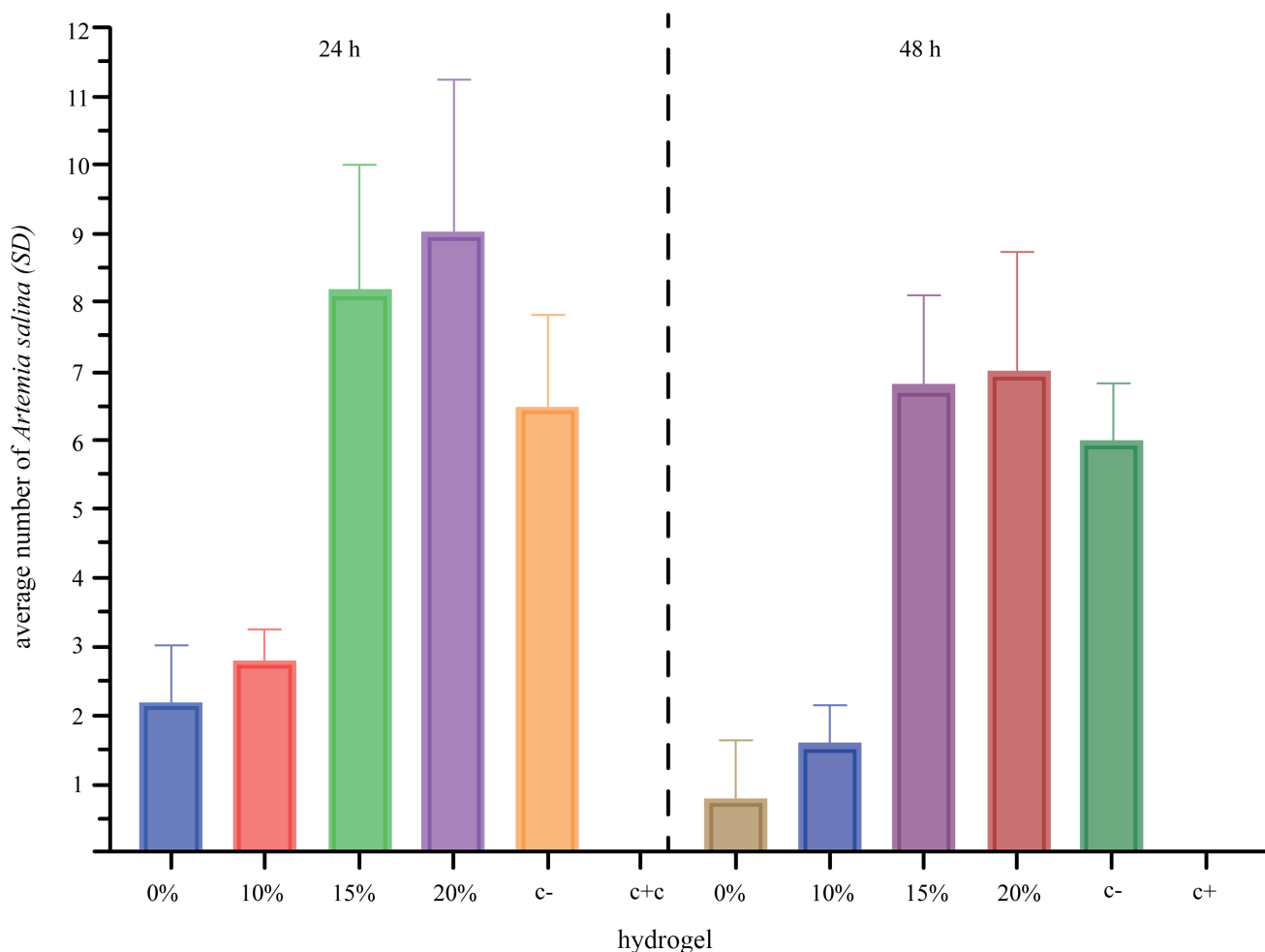
HeLa cell culture assay

Table 3 shows viability distributions between pairs of experimental samples compared to the controls (positive and negative). The bar graph of the mean and SE indicates higher viability in the 10% and 20% hydrogels, with 0.24 ± 0.29 and

Table 3. Spectrophotometric viability analysis of absorbance level

Materials	Mean	SD	SE	H-ABS vs C+	p-value*	H-ABS vs C-	p-value**
C+	0.043	0.001	0.001	–	–	–	–
H-0%	0.065	0.013	0.008	0.021	0.100	0.064	0.100
H-10%	0.245	0.290	0.167	0.201	0.100	0.116	0.600
H-15%	0.114	0.054	0.031	0.070	0.100	0.015	0.600
H-20%	0.158	0.056	0.032	0.115	0.100	0.029	0.600
C-	0.129	0.013	0.008	–	–	–	–
0-ABS	0.042	0.001	0.001	–	–	–	–

SD – standard deviation; SE – standard error; H – hydrogel; ABS – absorbance; C+ – positive control; C- – negative control; *significance of correlation between each hydrogel absorbance and the positive control; **significance of correlation between each hydrogel absorbance and the negative control.

**Fig. 2.** Mean values of *Artemia salina* nauplii at 24 h and 48 h according to experimental hydrogel concentration

SD – standard deviation; C+ – positive control; C- – negative control.

0.16 ± 0.06, respectively). Comparisons between the positive control and the hydrogel at different concentrations showed that the positive control values were lower than the material. The largest absolute difference was obtained by the 10% hydrogel (0.20, in favor of the material), and the same results were obtained with the negative control (0.12). Furthermore, the 0% and the 15% hydrogels had values lower than the negative control. The differences in the data reported in Fig. 3 were not statistically significant.

Discussion

This study aimed to assess the cytotoxicity of chitosan hydrogels on human HeLa cells using different concentrations of L-arginine. Based on our findings, we suggest that adding 10% of L-arginine to hydrogels generates an efficient product that achieves the desired effect, is easy to handle, and reaches optimal levels of cell viability.

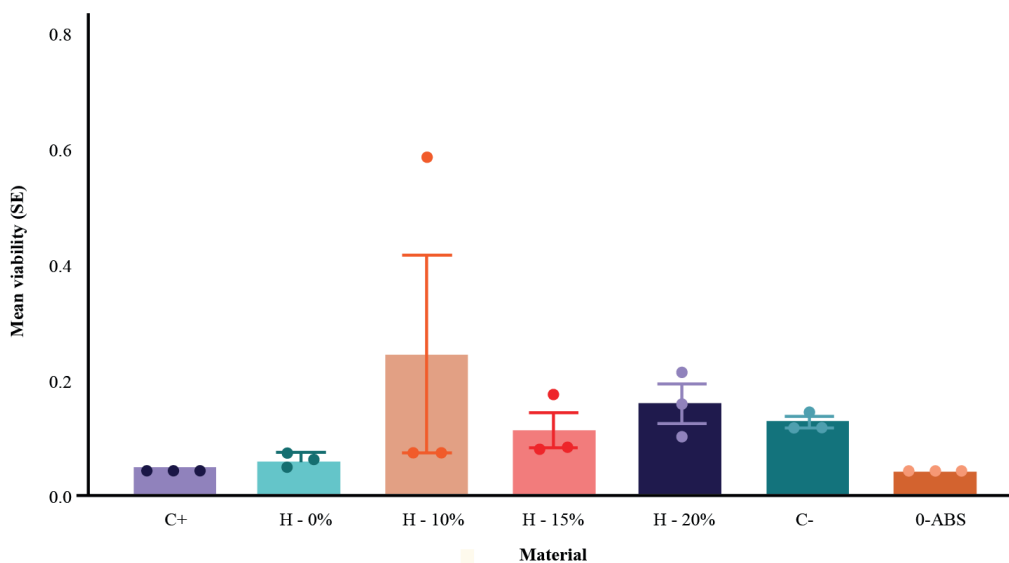


Fig. 3. Mean viability values according to the material used

SE – standard error; H – hydrogel; ABS – absorbance; C+ – positive control; C- – negative control

Artemia salina assay

The *Artemia salina* test is widely used for preliminary material compatibility studies.³¹ The *Artemia salina* culture was done using a saline medium in culture dishes and was impregnated with different hydrogels to assess the viability of the specimens. The MTT and *Artemia salina* assays were performed to validate the method. The hydrogel in the wells of *Artemia salina* was too dense and reduced the movement of the nauplii, and for that reason, the MTT assay was carried out.

Different concentrations of L-arginine were used since it is a precursor of NO synthase and can be found endogenously at a cellular level. Raising the levels of the precursor (L-arginine) increases NO production or synthesis. Chitosan is a vehicle used to transport the amino acid and is stable over time.³²

Pereira et al.³¹ reported a hydrogel with chitosan cross-linked using ceftazidime and modified with acetyl-acetone and ethylenediamine (Cacen) or diethylenetriamine (Cacdien), and carried out cytotoxicity tests with *Artemia salina*, obtaining low mortality (less than 10%). These results showed the non-toxic nature of the chitosan derivate elements. Likewise, Parvez et al.³³ reported low cytotoxicity in an *Artemia salina* assay using a matrix of chitosan and gelatin for healing purposes.

Our results were likely influenced by the viscosity of the hydrogels, which reduced the movement of the specimens, unlike the lower density hydrogels. Similar results were reported by Pereira et al. and Parvez et al.,^{31,33} where several samples died due to the high viscosity that limited the entry of oxygen. A layer of high concentration of the scaffold inhibited the permeability of oxygen, producing sequential death of several specimens.

HeLa cell culture assay

Cytotoxicity analyses ensure the biocompatibility of a material. Rakhshaei et al.³⁴ reported obtaining a gelled chitosan compound cross-linked with zinc nanoparticles and Arg-Gly-Asp. The viability of our analysis at various concentrations achieved a significance greater than 100% at 24 h and increased at 48 h without statistical significance.

Cell dispersion through the scaffold and its pores has been observed from the 2nd day. Meanwhile, Rodriguez et al.³⁵ highlighted the usefulness of low molecular weight chitosan hydrogels with polyvinyl alcohol (PVA) and evaluated the cytotoxicity of the hydrogel at 1, 3 and 7 days in a non-somatic cell line (colorectal adenocarcinoma), obtaining cell viability higher than 80%. However, as a result, there was a decrease in biocompatibility on most of the samples and their dilutions by the 7th day. In our study, cell viability achieved a higher percentage when arginine was applied, with 50% without L-arginine and 190%, 88% and 122% when 10%, 15% and 20% L-arginine were used, respectively. The characteristics of arginine explain this as a NO precursor that increases cellular metabolic capacity.^{36,37}

Govindaraj and Raghavachari³⁸ demonstrated 120% viability in their fibroblast culture with a hydrogel partially cross-linked with succinic acid and urea with genipin. Two chitosan hydrogels have been reported by in vitro studies using human bone carcinoma cells and rodent fibroblast lines, where the hydrogel with polyethylene glycol dimethacrylate (PEDGMA) had the highest cytotoxicity compared with the negative control and the hydrogel in both cell lines.³⁹

A chitosan hydrogel with dopamine-inulin was tested, with acceptable cytotoxicity values in the same fibroblast cell line.¹² In a study by Su et al.,¹³ the same cell line was used to assess their 2 variants of carboxymethyl hydrogels with chitosan/poly(lactide) (CMCS-PLA) and CMCS,

obtaining a viability of 97% after 72 h of evaluation. Other studies used different amino acids to improve physical-chemical properties, mucoadhesion and solubility to develop safe and efficient products.^{11,26}

Physicochemical characterization

Hydrogels can retain liquids in their macrostructure, but their stability and integrity can vary with the addition of other elements, such as amino acids or medications. For this reason, density is a relevant property when supplying hydrogels to patients. As reported by Sanchez et al.,⁴⁰ a chitosan hydrogel was obtained from purified technical shrimp, with this purified hydrogel displaying optimal physical characteristics. However, as described in the in vitro tests and the scanning electron microscopy (SEM) analysis, a better arrangement and distribution of the hydrogel pores was observed when they were cross-linked with external chemical elements such as glutaraldehyde or glyoxal. The purified hydrogel was also compared with non-cross-linked hydrogels, obtaining better water retention, temperature affectation and scaffolding structure. The hydrogels prepared with L-arginine in our research presented an absorption band around 1,632 cm⁻¹, that was assigned to the guanidine group, and a band at 1,689 cm⁻¹, that was associated with the stretching vibration of the carboxy carbonyl group. The bands at 1,400 cm⁻¹ and 762 cm⁻¹ were attributed to symmetric and asymmetric bending of the COO⁻, respectively.^{41,42} The increase in the amide I peak in formulations with arginine suggests that arginine was effectively linked to the chitosan polymer chain.⁴²

Mohandas and Rangasamy⁴³ found the same pH behavior of the hydrogel when they polymerized hydrogels with concentrations of L-arginine between 1.4 mM and 22.9 mM, obtaining a more neutral pH as the concentration of the amino acid increased given the alkaline nature of arginine.

Conclusions

The presence of L-arginine in our chitosan gels increased the viability of HeLa cells compared to the samples without this component, which was caused by an increase in the metabolic capacity of the NO precursors in the cultures.

The physical characteristics of the hydrogel with 10% L-arginine resulted in a better clinical application due to its density ratio and viability levels, with the density likely affecting the viability of *Artemia salina* nauplii. However, it is evident that hydrogels with lower densities were more viable. Based on our results, we suggest that chitosan/L-arginine hydrogels could be used in humans without toxic effects. However, more trials and tests are needed to evaluate tooth movement rate during orthodontic treatment.

ORCID iDs

Santiago Herrera-Guardiola  <https://orcid.org/0000-0002-0877-6909>
 Carlos H. Valencia-Llano  <https://orcid.org/0000-0003-4892-9786>
 Miguel Á. Casillas-Santana  <https://orcid.org/0000-0003-0288-9117>
 Farid A. Dipp-Velázquez  <https://orcid.org/0000-0001-9788-8795>
 Juan F. Aristizábal-Pérez  <https://orcid.org/0000-0003-4391-7188>

References

- Jing D, Xiao J, Li X, Li Y, Zhao Z. The effectiveness of vibrational stimulus to accelerate orthodontic tooth movement: A systematic review. *BMC Oral Health*. 2017;17(1):143. doi:10.1186/s12903-017-0437-7
- Aldosari M. Effects of vibration forces on maxillary expansion and orthodontic tooth movement [doctoral thesis]. Bloomington, USA: Indiana University; 2015. <https://scholarworks.iupui.edu/items/9de936ac-12e7-4230-ab9c-9dc4ac332061>. Accessed September 28, 2023.
- Ellingson L. The effect of mechanical vibration on pain and rate of tooth movement during initial orthodontic alignment [doctoral thesis]. Omaha, USA: University of Nebraska Medical Center; 2017. <https://digitalcommons.unmc.edu/cgi/viewcontent.cgi?article=1242&context=etd>. Accessed September 28, 2023.
- Genc G, Kocadereli İ, Tasar F, Kilinc K, El S, Sarkarati B. Effect of low-level laser therapy (LLL) on orthodontic tooth movement. *Lasers Med Sci*. 2013;28(1):41–47. doi:10.1007/s10103-012-1059-6
- Dominguez Camacho A, Clarkson Lopez A, López Aldana R. An in vitro study of the reaction of periodontal and gingival fibroblasts to low-level laser irradiation. *J Oral Laser Appl*. 2008;8:235–244. http://www.quintpub.com/journals/jola/abstract.php?iss2_id=771&article_id=9014&article=4. Accessed September 28, 2023.
- Wilcko MT, Wilcko WM, Pulver JJ, Bissada NF, Bouquet JE. Accelerated osteogenic orthodontics technique: A 1-stage surgically facilitated rapid orthodontic technique with alveolar augmentation. *J Oral Maxillofac Surg*. 2009;67(10):2149–2159. doi:10.1016/j.joms.2009.04.095
- Raja A, Reddy Y, Sreekanth C, Reddy B, Raj G, Reddy R. Speedy orthodontics: A comprehensive review. *J Oral Health Med Res*. 2016;2(6):121–124. https://www.researchgate.net/profile/Ymuralidhar-Reddy/publication/349214177_Speedy_Orthodontics_A_Comprehensive_Review/links/60253db445851589399aa73d/Speedy-Orthodontics-A-Comprehensive-Review.pdf.
- Aristizábal J. Accelerated orthodontics and express transit orthodontics (ETO)[®], a contemporary concept of high efficiency [in Spanish]. *Rev CES Odont*. 2014;27:56–73. <https://revistas.ces.edu.co/index.php/odontologia/article/view/2782/2136>. Accessed September 28, 2023.
- Iglesias-Linares A, Morford LA, Hartsfield JK. Bone density and dental external apical root resorption. *Curr Osteoporos Rep*. 2016;14(6):292–309. doi:10.1007/s11914-016-0340-1
- Ralston SH, Ho LP, Helfrich MH, Grabowski PS, Johnston PW, Benjamin N. Nitric oxide: A cytokine-induced regulator of bone resorption. *J Bone Miner Res*. 1995;10(7):1040–1049. doi:10.1002/jbmr.5650100708
- Crini G, Badot PM. Application of chitosan, a natural aminopolysaccharide, for dye removal from aqueous solutions by adsorption processes using batch studies: A review of recent literature. *Prog Polym Sci*. 2008;33(4):399–447. doi:10.1016/j.progpolymsci.2007.11.001
- Rahnama H, Nouri Khorasani S, Aminoroaya A, Molavian MR, Allafchian A, Khalili S. Facile preparation of chitosan-dopamine-inulin aldehyde hydrogel for drug delivery application. *Int J Biol Macromol*. 2021;185:716–724. doi:10.1016/j.ijbiomac.2021.06.199
- Su F, Wang Y, Liu X, et al. Biocompatibility and in vivo degradation of chitosan based hydrogels as potential drug carrier. *J Biomater Sci Polym Ed*. 2018;29(13):1515–1528. doi:10.1080/09205063.2017.1412244
- Udhayakumar S, Shankar KG, Sowndarya S, Venkatesh S, Muralidharan C, Rose C. L-arginine intercedes bio-crosslinking of a collagen–chitosan 3D-hybrid scaffold for tissue engineering and regeneration: In silico, in vitro, and in vivo studies. *RSC Adv*. 2017;7(40):25070–25088. doi:10.1039/C7RA02842C
- Sharma JN, Al-Omran A, Parvathy SS. Role of nitric oxide in inflammatory diseases. *Inflammopharmacology*. 2007;15(6):252–259. doi:10.1007/s10787-007-0013-x
- Mollace V, Muscoli C, Masini E, Cuzzocrea S, Salvemini D. Modulation of prostaglandin biosynthesis by nitric oxide and nitric oxide donors. *Pharmacol Rev*. 2005;57(2):217–252. doi:10.1124/pr.57.2.1

17. Collin-Osdoby P, Rothe L, Bekker S, Anderson F, Osdoby P. Decreased nitric oxide levels stimulate osteoclastogenesis and bone resorption both in vitro and in vivo on the chick chorioallantoic membrane in association with neoangiogenesis. *J Bone Miner Res.* 2000;15(3):474–488. doi:10.1359/jbmr.2000.15.3.474
18. Aguirre J, Buttery L, O'Shaughnessy M, et al. Endothelial nitric oxide synthase gene-deficient mice demonstrate marked retardation in postnatal bone formation, reduced bone volume, and defects in osteoblast maturation and activity. *Am J Pathol.* 2001;158(1):247–257. doi:10.1016/S0002-9440(10)63963-6
19. Abdelkarem HM, Fadda LH, El-Sayed EM, Radwan OK. Potential role of L-arginine and vitamin E against bone loss induced by nano-zinc oxide in rats. *J Diet Suppl.* 2018;15(3):300–310. doi:10.1080/19390211.2017.1343889
20. Nilforoushan D, Gramoun A, Glogauer M, Manolson MF. Nitric oxide enhances osteoclastogenesis possibly by mediating cell fusion. *Nitric Oxide.* 2009;21(1):27–36. doi:10.1016/j.niox.2009.04.002
21. Wimalawansa SJ. Nitric oxide and bone. *Ann NY Acad Sci.* 2010;1192(1):391–403. doi:10.1111/j.1749-6632.2009.05230.x
22. Yang J, Tang R, Yi J, et al. Diallyl disulfide alleviates inflammatory osteolysis by suppressing osteoclastogenesis via NF- κ B–NFATc1 signal pathway. *FASEB J.* 2019;33(6):7261–7273. doi:10.1096/fj.201802172R
23. Lee Y, Park Y, Lee S, et al. Tissue engineered bone formation using chitosan/tricalcium phosphate sponges. *J Periodontol.* 2000;71(3):410–417. doi:10.1902/jop.2000.71.3.410
24. Sámano-Valencia C, Martínez-Castañón GA, Martínez-Martínez RE, et al. Bactericide efficiency of a combination of chitosan gel with silver nanoparticles. *Mater Lett.* 2013;106:413–416. doi:10.1016/j.matlet.2013.05.075
25. Sámano-Valencia C, Martínez-Castañón GA, Martínez-Gutiérrez F, et al. Characterization and biocompatibility of chitosan gels with silver and gold nanoparticles. *J Nanomater.* 2014;2014:543419. doi:10.1155/2014/543419
26. Cheng F, Wang B, Xia Y. Synthesis and characterization of O-acetyl-chitosan acetic ester. *Int J Polym Sci.* 2018;2018:4960416. doi:10.1155/2018/4960416
27. Berridge MV, Herst PM, Tan AS. Tetrazolium dyes as tools in cell biology: New insights into their cellular reduction. *Biotechnol Ann Rev.* 2005;11:127–152. doi:10.1016/S1387-2656(05)11004-7
28. Stockert JC, Horobin RW, Colombo LL, Blázquez-Castro A. Tetrazolium salts and formazan products in cell biology: Viability assessment, fluorescence imaging, and labeling perspectives. *Acta Histochem.* 2018;120(3):159–167. doi:10.1016/j.acthis.2018.02.005
29. Mosmann T. Rapid colorimetric assay for cellular growth and survival: Application to proliferation and cytotoxicity assays. *J Immunol Methods.* 1983;65(1–2):55–63. doi:10.1016/0022-1759(83)90303-4
30. Valencia AM, Valencia CH, Zuluaga F, Grande-Tovar CD. Synthesis and fabrication of films including graphene oxide functionalized with chitosan for regenerative medicine applications. *Heliyon.* 2021;7(5):e07058. doi:10.1016/j.heliyon.2021.e07058
31. Pereira LA, Da Silva Reis L, Batista FA, Mendes AN, Osajima JA, Silva-Filho EC. Biological properties of chitosan derivatives associated with the ceftazidime drug. *Carbohydr Polym.* 2019;222:115002. doi:10.1016/j.carbpol.2019.115002
32. Arqub SA, Gandhi V, Iverson MG, et al. The effect of the local administration of biological substances on the rate of orthodontic tooth movement: A systematic review of human studies. *Prog Orthod.* 2021;22(1):5. doi:10.1186/s40510-021-00349-5
33. Parvez S, Rahman MM, Khan MA, et al. Preparation and characterization of artificial skin using chitosan and gelatin composites for potential biomedical application. *Polym Bull.* 2012;69(6):715–731. doi:10.1007/s00289-012-0761-7
34. Rakhshaei R, Namazi H, Hamishehkar H, Kafil HS, Salehi R. In situ synthesized chitosan–gelatin/ZnO nanocomposite scaffold with drug delivery properties: Higher antibacterial and lower cytotoxicity effects. *J Appl Polym Sci.* 2019;136(22):47590. doi:10.1002/app.47590
35. Rodríguez-Rodríguez R, Velasquillo-Martínez C, Knauth P, et al. Sterilized chitosan-based composite hydrogels: Physicochemical characterization and in vitro cytotoxicity. *J Biomed Mater Res A.* 2020;108(1):81–93. doi:10.1002/jbm.a.36794
36. Hecker M, Sessa WC, Harris HJ, Anggård EE, Vane JR. The metabolism of L-arginine and its significance for the biosynthesis of endothelium-derived relaxing factor: Cultured endothelial cells recycle L-citrulline to L-arginine. *Proc Natl Acad Sci U S A.* 1990;87(21):8612–8616. doi:10.1073/pnas.87.21.8612
37. Marzinzig M, Nussler AK, Stadler J, et al. Improved methods to measure end products of nitric oxide in biological fluids: Nitrite, nitrate, and S-nitrosothiols. *Nitric Oxide.* 1997;1(2):177–189. doi:10.1006/niox.1997.0116
38. Govindaraj P, Raghavachari D. Fabrication of macroporous soft hydrogels of chitosan scaffolds by hydrothermal reaction and cytotoxicity to 3T3 L1 cells. *J Polym Res.* 2021;28(3):86. doi:10.1007/s10965-021-02426-z
39. Li Q, Yang D, Ma G, et al. Synthesis and characterization of chitosan-based hydrogels. *Int J Biol Macromol.* 2009;44(2):121–127. doi:10.1016/j.ijbiomac.2008.11.001
40. Sanchez A, Sibaja Ballesteros M, Vega-Baudrit J, Madrigal S. Síntesis y caracterización de hidrogeles de quitosano obtenido a partir del camarón langostino (*Pleuroncodes planipes*) con potenciales aplicaciones biomédicas. *Rev Iberoam Polim.* 2007;8(4):241–267. <https://reviberpol.files.wordpress.com/2019/08/2007-sanchez.pdf>.
41. Wang K, Qi Z, Pan S, et al. Preparation, characterization and evaluation of a new film based on chitosan, arginine and gold nanoparticle derivatives for wound-healing efficacy. *RSC Adv.* 2020;10(35):20886–20899. doi:10.1039/D0RA03704D
42. Antunes BP, Moreira AF, Gaspar VM, Correia IJ. Chitosan/arginine–chitosan polymer blends for assembly of nanofibrous membranes for wound regeneration. *Carbohydr Polym.* 2015;130:104–112. doi:10.1016/j.carbpol.2015.04.072
43. Mohandas A, Rangasamy J. Nanocurcumin and arginine entrapped injectable chitosan hydrogel for restoration of hypoxia induced endothelial dysfunction. *Int J Biol Macromol.* 2021;166:471–482. doi:10.1016/j.ijbiomac.2020.10.205

Solubility of dapsona in deep eutectic solvents: Experimental analysis, molecular insights and machine learning predictions

Rozpuszczalność dapsonu w rozpuszczalnikach głęboko eutektycznych: analiza eksperymentalna, aspekty molekularne i prognozy przy użyciu uczenia maszynowego

Tomasz Jeliński^{1,A–F}, Maciej Przybyłek^{1,B,C,E,F}, Rafał Różalski^{2,B,C,E,F}, Piotr Cysewski^{1,A–F}

¹ Department of Physical Chemistry, Faculty of Pharmacy, Collegium Medicum in Bydgoszcz, Nicolaus Copernicus University in Toruń, Poland

² Department of Clinical Biochemistry, Faculty of Pharmacy, Collegium Medicum in Bydgoszcz, Nicolaus Copernicus University in Toruń, Poland

A – research concept and design; B – collection and/or assembly of data; C – data analysis and interpretation; D – writing the article; E – critical revision of the article; F – final approval of the article

Polymers in Medicine, ISSN 0370-0747 (print), ISSN 2451-2699 (online)

Polim Med. 2024;54(1):15–25

Address for correspondence

Tomasz Jeliński
E-mail: tomasz.jelinski@cm.umk.pl

Funding sources

None declared

Conflict of interest

None declared

Received on November 15, 2023

Reviewed on December 18, 2023

Accepted on December 18, 2023

Published online on January 10, 2024

Cite as

Jeliński T, Przybyłek M, Różalski R, Cysewski P. Solubility of dapsona in deep eutectic solvents: Experimental analysis, molecular insights and machine learning predictions. *Polim Med.* 2024;54(1):15–25. doi:10.17219/pim/177235

DOI

10.17219/pim/177235

Copyright

Copyright by Author(s)

This is an article distributed under the terms of the Creative Commons Attribution 3.0 Unported (CC BY 3.0) (<https://creativecommons.org/licenses/by/3.0/>)

Abstract

Background. Dapsona (DAP) is an anti-inflammatory and antimicrobial active pharmaceutical ingredient used to treat, e.g., AIDS-related diseases. However, low solubility is a feature hampering its efficient use.

Objectives. First, deep eutectic solvents (DES) were used as solubilizing agents for DAP as an alternative to traditional solvents. Second, intermolecular interactions in the systems were described and quantified. Finally, the solubility prediction model, previously created using the machine learning protocol, was extended and improved using new data obtained for eutectic systems.

Material and methods. New DES were created by blending choline chloride (ChCl) with 6 selected polyols. The solubility of DAP in these solvents was measured spectrophotometrically. The impact of water dilution on the solubility curve was investigated. Experimental research was enriched with theoretical interpretations of intermolecular interactions, identifying the most probable pairs in the systems. Dapsona self-association and its ability to interact with components of the analyzed systems were considered. Thermodynamic characteristics of pairs were utilized as molecular descriptors in the machine learning process, predicting solubility in both traditional organic solvents and the newly designed DES.

Results. The newly formulated solvents demonstrated significantly higher efficiency compared to traditional organic solvents, and a small addition of water increased solubility, indicating its role as a co-solvent. The interpretation of the mechanism of DAP solubility highlighted the competitive nature of self-association and pair formation. Thermodynamic parameters characterizing affinity were instrumental in developing an efficient model for theoretical screening across diverse solvent classes. The study emphasized the necessity of retraining models when introducing new experimental data, as exemplified by enriching the model with data from DES.

Conclusions. The research showcased the efficacy of developing new DES for enhancing solubility and creating environmentally and pharmaceutically viable systems, using DAP as an example. Molecular interactions proved valuable in understanding solubility mechanisms and formulating predictive models through machine learning processes.

Keywords: solubility, dapsona, machine learning, intermolecular interactions, deep eutectic solvents

Streszczenie

Wprowadzenie. Dapson jest substancją czynną o działaniu przeciwzapalnym i przeciwbakteryjnym, stosowaną m.in. w leczeniu schorzeń związanych z AIDS. Jednakże jego niska rozpuszczalność to cecha utrudniająca jego efektywne wykorzystanie.

Cel pracy. Po pierwsze, do rozpuszczania dapsonu jako alternatywy dla tradycyjnych rozpuszczalników zastosowano rozpuszczalniki głęboko eutektyczne (DES). Po drugie, opisano i obliczono oddziaływania międzycząsteczkowe w tych układach. Wreszcie, model przewidywania rozpuszczalności, wcześniej opracowany przy użyciu protokołu uczenia maszynowego, został rozszerzony i ulepszony uwzględniając rozpuszczalniki z grupy głębokich eutektyków.

Materiał i metody. Przygotowano nowe rozpuszczalniki należące do grupy głębokich eutektyków (DES) poprzez zmieszanie chlorku choliny oraz jednego z sześciu wybranych polioli. W każdym z zaprojektowanych rozpuszczalników zmierzono rozpuszczalność dapsonu metodą spektrofotometryczną. Przebadano wpływ rozcieńczenia wodą na rozpuszczalność. Badania eksperymentalne wzbogacono o interpretację teoretyczną oddziaływań międzycząsteczkowych i zidentyfikowano najbardziej prawdopodobne pary. Uwzględniono zarówno autoasocjację dapsonu, jak i jego zdolność do oddziaływania ze składnikami analizowanych układów. Charakterystyki termodynamiczne par wykorzystano jako deskryptory molekularne w procesie uczenia maszynowego. Otrzymany model wykorzystano do przewidywania rozpuszczalności zarówno w tradycyjnych rozpuszczalnikach organicznych, jak i nowych głębokich eutektykach.

Wyniki. Potwierdzono znacznie wyższą efektywność nowych rozpuszczalników niż tradycyjnych rozpuszczalników organicznych, a niewielki dodatek wody wywołał wzrost rozpuszczalności, co wskazuje na jej rolę jako współrozpuszczalnika. Interpretacja mechanizmu rozpuszczalności dapsonu wykazała konkurencyjny charakter autoasocjacji oraz tworzenia par ze składnikami analizowanych roztworów. Parametry termodynamiczne charakteryzujące powinowactwo wykorzystano w procesie uczenia maszynowego i opracowano bardzo efektywny model pozwalający na teoretyczne badania przesiewowe w bardzo szerokiej domenie klas rozpuszczalników. Zwrócono uwagę na konieczność ponownego treningu modelu w przypadku rozszerzenia puli danych doświadczalnych o przypadki układów o nowych cechach na przykładzie wzbogacenia modelu o nowe wartości dla DES.

Wnioski. Na przykładzie dapsonu udokumentowano, że projektowanie nowych rozpuszczalników głęboko eutektycznych jest wysoce efektywnym sposobem zwiększania rozpuszczalności prowadzącym do otrzymania ekologicznie i farmaceutycznie akceptowalnych układów. Oddziaływania między molekularne są wartościowym źródłem informacji umożliwiającym nie tylko zrozumienie mechanizmu rozpuszczalności, ale również sformułowania modeli teoretycznych wykorzystujących proces uczenia maszynowego.

Słowa kluczowe: dapson, rozpuszczalność, uczenie maszynowe, oddziaływania międzycząsteczkowe, rozpuszczalniki głęboko eutektyczne.

Background

Dapsone (IUPAC name: 4,4'-Diaminodiphenyl sulfone, abbreviated here as DAP) is a synthetic sulphone known for its anti-inflammatory and antimicrobial properties.¹ Both systematic and topical forms of DAP are used in medicine, and among different diseases addressed by this drug, one can include dermatitis herpetiformis, leprosy, acne, malaria, and also conditions related to AIDS.^{2–5} Dapsone demonstrates its antibacterial activity by competitively inhibiting dihydropteroate synthetase, thereby impeding the biosynthesis of folic acid. This disruption hampers the production of nucleic acids, which are crucial for the survival and multiplication of the affected bacteria.^{2,6} Dapsone's ability to reduce inflammation is associated with its modulation of the production of cytokines.^{7,8} Moreover, its ability to bind with NADPH oxidase results in the inhibition of reactive oxygen species (ROS) and superoxide radical production, thus rendering its antioxidant capacity.⁹ Dapsone is metabolized in the liver via acetylation and hydroxylation, and excreted primarily in urine.^{10,11} Among its adverse effects, hematologic issues and peripheral neuropathy are considered the most important, with the DAP hypersensitivity syndrome being identified as a life-threatening drug reaction.¹² Dapsone is included in class II of drugs according to the Biopharmaceutics

Classification System (BCS), which reflects its limited water solubility as well as its reduced permeability.¹³ Because of the above features, the transdermal delivery route, instead of the oral one, is the preferred way of administering this drug.¹⁴ These limitations were the inspiration for various strategies aimed at resolving the poor aqueous solubility and low bioavailability of DAP.^{15,16}

Solubility, as a fundamental characteristic, holds significant importance in the pharmaceutical realm and plays a crucial role in drug design and formulation.^{17,18} The reactivity, stability and bioavailability of a chemical compound are significantly influenced by its capacity for dissolution in a specific solvent. Investigations into solubility, encompassing both equilibrium and kinetic methodologies, play a vital role in various critical domains, including enhancing liquid dosage,¹⁹ improving bioavailability,²⁰ facilitating crystallization,²¹ aiding pre-formulation,²² and enabling thermodynamic modeling.²³ Based on the above, it can be easily concluded that solvents are extremely important for the pharmaceutical industry. In fact, it can be estimated that they account for even 90% of all chemicals used in this industry.²⁴ Because of the amount of solvents used, it is crucial to focus not only on their effectiveness in dissolving desired compounds but also on their environmental impact. This is why the framework of "green chemistry"^{25,26} has become

widely introduced in the context of solvents.^{27–30} Various properties can be attributed to these green solvents, with non-toxicity, non-flammability and low environmental impact being the most important ones.

When considering the above properties, a particular group of designed solvents comes to mind, namely deep eutectic solvents (DES). They are formed by mixing at least 2 compounds, and their key feature lies in the lowering of the melting point compared to individual constituents of the eutectic mixture.^{31,32} This characteristic enables them to remain in a liquid state even at low temperatures. The DES share many aspects with more traditional ionic liquids; they differ mainly by including non-ionic constituents in their structure.³³ Frequently, DES employ compounds that can be termed primary metabolites derived from plants, including alcohols, sugars, organic acids, and amino acids.^{34,35} The properties of DES are in line with the general requirements for green solvents since these systems are not readily volatile and flammable, they are sustainable and biodegradable, their preparation is simple and cost-efficient, and they can be tailored for user-specific requirements.^{36–39} These desirable properties resulted in the widespread usage of DES, and the pharmaceutical industry is, of course, one of the beneficiaries of this approach.^{40–42} The DES have proven to have the ability to significantly increase the solubility and bioavailability of many active pharmaceutical ingredients.^{43–45} Also our research group has successfully demonstrated the usefulness of using DES for the dissolution of many active substances, including sulfonamides,⁴⁶ curcumin,⁴⁷ caffeine,⁴⁸ and edaravone.⁴⁹ Therefore, it seems natural to apply DES in the case of DAP.

Selecting the right solvent to enhance the solubility of a specific active pharmaceutical ingredient is a challenging and labor-intensive process. The number of experiments is constrained by various factors, including time, financial limitations and the contemporary emphasis on eco-friendly chemical practices. Hence, preliminary screening using diverse computational methods seems imperative before conducting actual experiments. Of notable importance is the use of machine learning to determine pharmaceutical solubility limits, an area that has seen a surge in neural network and deep learning applications.^{50–52} Our previous studies have demonstrated that combining COSMO-RS with machine learning techniques yields highly accurate predictions,^{53–55} also in the case of dapsone.⁵⁶

The current study had 3 primary objectives. First, DAP solubility data was augmented using several designed DES, which were expected to have a greater solubilization potential than traditional organic solvents. Furthermore, the intermolecular interactions within the considered systems were studied in order to gain insight into the observed solubility phenomena. Finally, the model for predicting solubility, previously created using the machine learning protocol, was extended and improved using new data obtained for eutectic systems.

Materials and methods

Materials

Dapsone (CAS No. 80-08-0) was acquired from Sigma-Aldrich (St. Louis, USA) with $\leq 99\%$ purity. The constituents of DES were also obtained from Sigma-Aldrich with the same purity. These constituents include choline chloride (ChCl, CAS No. 67-48-1), as well as 6 polyols, namely glycerol (GLY, CAS No. 56-81-5), ethylene glycol (ETG, CAS No. 107-21-1), diethylene glycol (DEG, CAS No. 111-46-6), triethylene glycol (TEG, CAS No. 112-27-6), 1,2-propanediol (P2D, CAS No. 57-55-6), and 1,3-butanediol (B3D, CAS No. 107-88-0) used as hydrogen bond donors (HBDs). Methanol (CAS No. 67-56-1), used as a solvent throughout the study, was supplied by Avantor Performance Materials (Gliwice, Poland) and had a purity of at least 99%. Prior to use, ChCl was dried, while all the other compounds were used without any initial procedures.

Preparation of the samples and solubility measurements

For DAP solubility determination in the investigated DES, the initial step involved the preparation of a calibration curve. For this purpose, a stock solution of DAP was prepared in methanol and subsequently diluted in 10-mL volumetric flasks. The concentration of solutions used for the preparation of the calibration curve ranged from 0.007 mg/mL to 0.017 mg/mL. An A360 spectrophotometer from AOE Instruments (Shanghai, China) was employed for spectrophotometrical measurements of the solutions. The wavelength corresponding to the maximum absorbance value was found to be 295 nm. Three separate calibration curves were averaged in order to obtain the final curve. The linear regression equation was found to be $A = 113.87 \cdot C + 0.0015$ (A – absorbance, C – concentration expressed in mg/mL). The degree of linearity was found to be satisfactory, with $R^2 = 0.999$.

In the investigation of various DES, ChCl consistently served as one of the constituents. The 2nd component varied and GLY, ETG, DEG, TEG, P2D, or B3D. To formulate the DES, ChCl and the 2nd component were mixed together in sealed test tubes in 1:2 molar ratio. A water bath at 90°C was utilized for creating homogeneous solutions. The resulting DES were used either in their pure form or combined with water to create binary systems with varying water proportions. To obtain saturated solutions of DAP in the studied systems, excess amounts of DAP were added to the test tubes containing both pure DES and binary mixtures with water.

The prepared samples were incubated for 24 h at 25°C in an Orbital Shaker Incubator ES-20/60 from Biosan (Riga, Latvia). The temperature was precisely maintained at 0.1°C, with a variation of $\pm 0.5^\circ\text{C}$ observed over the 24-h cycle. During the mixing process, all samples

were agitated at a speed of 60 rpm. Afterward, the samples were filtered using a syringe combined with a PTFE syringe filter of 0.22 μm pore size. In order to prevent precipitation, the test tubes, syringes, pipette tips, and filters were initially warmed to align with the temperature of the sample.

Ultimately, fixed volumes of the filtered solution were placed in test tubes filled with methanol, and the samples diluted in this way were subjected to spectrophotometric measurements. Additionally, to determine the mole fractions of DAP, 1 mL of each solution was precisely weighed in a 10 mL volumetric flask in order to obtain the density of the sample. Throughout the study, an Eppendorf (Hamburg, Germany) Reference 2 pipette was used with a systematic error of 0.6 μL . The RADWAG (Radom, Poland) AS 110 R2.PLUS analytical balance with a precision of 0.1 mg was also utilized.

The solubility of DAP in the considered solvents was determined based on spectrophotometric measurements of the prepared samples. The wavelength range from 190 nm to 500 nm was used during solubility measurements, and the corresponding resolution was 1 nm. Initially, methanol was used for spectrophotometer calibration, and it was also utilized to dilute the measured samples. Dilution was necessary to ensure that the absorbance values remained within the linear range. Based on the calibration curve, the absorbance values measured at 295 nm were used to calculate DAP solubility, expressed both as its concentration and mole fraction. These values were obtained by averaging the results from 3 separate measurements.

Computations details

Solubility predictions were made using a custom Python model designed to tune the hyperparameters of 36 regressors using various algorithms, which include, among many others, boosting, nearest neighbors, linear models, ensembles, and neural networks. The methodology was already described in our previous studies,^{56–58} and only a brief description is presented here. The exploration of the hyperparameter space was aimed at finding their optimal values throughout 5000 minimization trials with the help of the Optuna framework. The performance of the considered regression models was assessed based on a custom score function combining metrics accounting for model accuracy and generalizability. The ultimate performance assessment of all models relied on the loss values representing both test and validation subsets. The ensemble model definition incorporated the subset of regression models characterized by the lowest values corresponding to both criteria. The final predictions were the results of the averaging of the chosen models. The solubility data from the previous work⁵⁶ was used for model training, and was supplemented with the new measurements presented in this work. The same types of molecular descriptors

were used to characterize the intermolecular interactions in the system, expressed in terms of solute–solvent affinities. These properties were characterized by the Gibbs free energy (ΔG_r) values associated with reactions involving the formation of pairs, namely $X + Y = XY$, with X and Y representing solute and solvent molecules, respectively. For the purpose of machine learning, both the enthalpic and entropic contributions included in the affinities were additionally incorporated into the set of molecular descriptors. Each compound in the form of monomers, dimers or heteromolecular pairs was represented by the set of the most representative conformations selected from a large number of potential geometries optimized using RIDEFT BP86 (B88-VWN-P86) in Turbomole v. 7.5.1 (Turbomole GmbH, Frankfurt am Main, Germany). Highly similar clusters and those exceeding the 2.5 kcal/mol threshold for relative energy were not included in the pool of conformations. All thermodynamic properties were computed using the COSMOtherm program v. 22.0.0 (Dassault Systèmes, Biovia, San Diego, USA).

Results and Discussion

Experimental solubility of DAP in designed solvents

The solubility of DAP was studied in several DES comprising ChCl and 1 of 6 considered polyols, namely GLY, ETG, DEG, TEG, P2D, and B3D. These systems were studied previously for other active pharmaceutical ingredients and proved to be very effective in enhancing their solubility.⁴⁹ Also, based on earlier experiences, the 1:2 molar ratio of DES constituents (i.e., a twofold excess amount of the polyol) was used. The studies encompassed the determination of DAP solubility in neat DES, as well as in binary solvent mixtures of DES and water. In the latter case, different molar proportions of the eutectic and water were used. The results are presented in Fig. 1.

The analysis of the results leads to several interesting observations. First of all, there is a following decreasing trend among the studied neat DES in terms of DAP dissolution effectiveness, namely: TEG > DEG > ETG > GLY > B3D > P2D. At 25°C, the mole fraction solubility of DAP in the neat DES comprising ChCl and TEG equals $x_{\text{DAP}} = 107.50 \cdot 10^{-3}$. Using DEG as a DES constituent yields a slightly smaller solubility of $x_{\text{DAP}} = 96.48 \cdot 10^{-3}$. The next 2 systems, involving ETG and GLY, are responsible for a considerably lower solubility of $x_{\text{DAP}} = 70.96 \cdot 10^{-3}$ and $x_{\text{DAP}} = 65.1 \cdot 10^{-3}$, respectively. Finally, DAP is the least soluble in DES utilizing B3D and P2D, with $x_{\text{DAP}} = 49.36 \cdot 10^{-3}$ and $x_{\text{DAP}} = 46.91 \cdot 10^{-3}$, respectively.

The studied DES systems differ slightly in their behavior when introduced as a part of an aqueous binary solvent. For all studied DES, a cosolvency effect can be observed, which means that at a specific molar composition

of the aqueous binary solvent, the solubility of DAP is higher than for the neat DES. However, the solubility profiles presented in Fig. 1 are not identical among the studied DES. The most important difference comes from the binary mixture composition, which results in the highest DAP solubility. In the case of eutectics comprising ETG, DEG and TEG, the $x_w^* = 0.2$ composition is responsible for the highest solubility of DAP. Meanwhile, for DES utilizing P2D, B3D and GLY, this composition is $x_w^* = 0.3$. The shape of the solubility profiles also differs slightly between the studied systems, although the solubility increase is rather similar and in the range from 1.07 to 1.15 times greater when comparing the optimal binary composition and the neat DES. For example, the most efficient composition for the DES comprising TEG results in the solubility of DAP equals to $x_{\text{DAP}} = 120.96 \cdot 10^{-3}$ at 25°C. Interestingly, there is a deviation from the solubility effectiveness trend observed among the studied neat DES. When the optimal composition is concerned, the eutectic involving GLY turns out to be more effective than the one with ETG, which is the opposite for neat DES.

Of course, it is necessary to put the obtained results in the context of DAP solubility in the neat solvents studied previously.⁵⁶ All the studied DES, as well as most water-DES mixtures, outperform classical organic solvents, including dimethyl sulfoxide (DMSO), DEG and diethylene glycol bis(3-aminopropyl) ether (B3APE), as evidenced in Fig. 1. Even DMSO, a compound that is known to be a very efficient solubilizer, yielded DAP solubility at a level of $x_{\text{DAP}} = 18.95 \cdot 10^{-3}$, which is only around 20% of the solubility of the neat eutectic involving TEG.

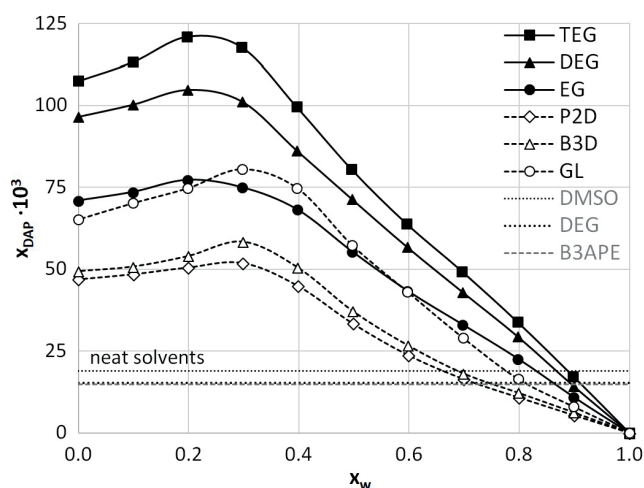


Fig. 1. Solubility of dapsone (DAP) at 25°C in the studied designed solvents, comprising choline chloride (ChCl) with either glycerol (GLY), ethylene glycol (ETG), diethylene glycol (DEG), triethylene glycol (TEG), 1,2-propanediol (P2D), or 1,3-butanediol (B3D). Horizontal lines represent values characterizing saturated solutions of DAP in neat solvents including dimethyl sulfoxide (DMSO), DEG and diethylene glycol bis(3-aminopropyl) ether (B3APE), as documented in a previous study x_w^* – mole fraction of water in solute-free solutions.

Intermolecular interactions of DAP in the studied DES

The characteristics of the intermolecular interactions in saturated solvents studied here are expressed as the collection of the values of ΔG_r of synthesis reactions of homo- and hetero-molecular pairs. This, however, requires the proper representation of the structural diversity of potential intermolecular contacts in considered systems. Hence, an extensive conformational search for potential pair formation was conducted as an initial step. According to the procedure described in the methodology section, each complex is represented by the set of the most stable conformations used for the determination of the affinity values. It is important to note that 2 types of thermodynamic characteristics can be derived using COSMOtherm depending on the way of interpretation of the reaction of the pair formation. For the purpose of the overall stability of the systems, the values of concentration independent ΔG_r were used. Such a way of representing affinity simply utilizes the product of activity coefficients, correcting the values of equilibrium constants determined based on the mole fraction distribution in a given system. The resulting activity equilibrium constants are directly related to the values of the ΔG_r and are related to the temperature, but remain the same independently of the system composition. These values are collected in Fig. 2, quantifying all possible binary contacts of DAP in the studied DES. The graphical representation of the most stable complexes is provided in Fig. 3.

The plots presented in Fig. 2 lead to the conclusion that the self-association of DAP is the most predominant factor of system stability. This suggests that dimer formation might be considered the driving force behind solubility restrictions in any solvent. Indeed, the heteromolecular complexes that characterize the affinity of DAP to any individual DES component are lower compared to DAP-DAP formation. It is worth emphasizing that

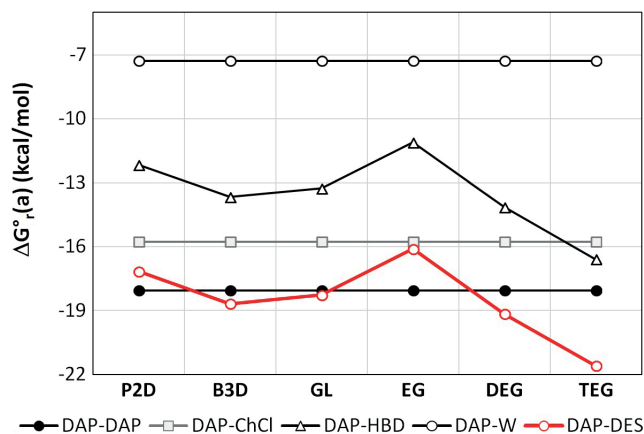


Fig. 2. Collection of solute-solvent and solute-solute affinities characterized by the values of the Gibbs free energy of reactions (ΔG_r): dapsone (DAP) + X = DAP-X, where X stands for either of the deep eutectic solvents (DES) components

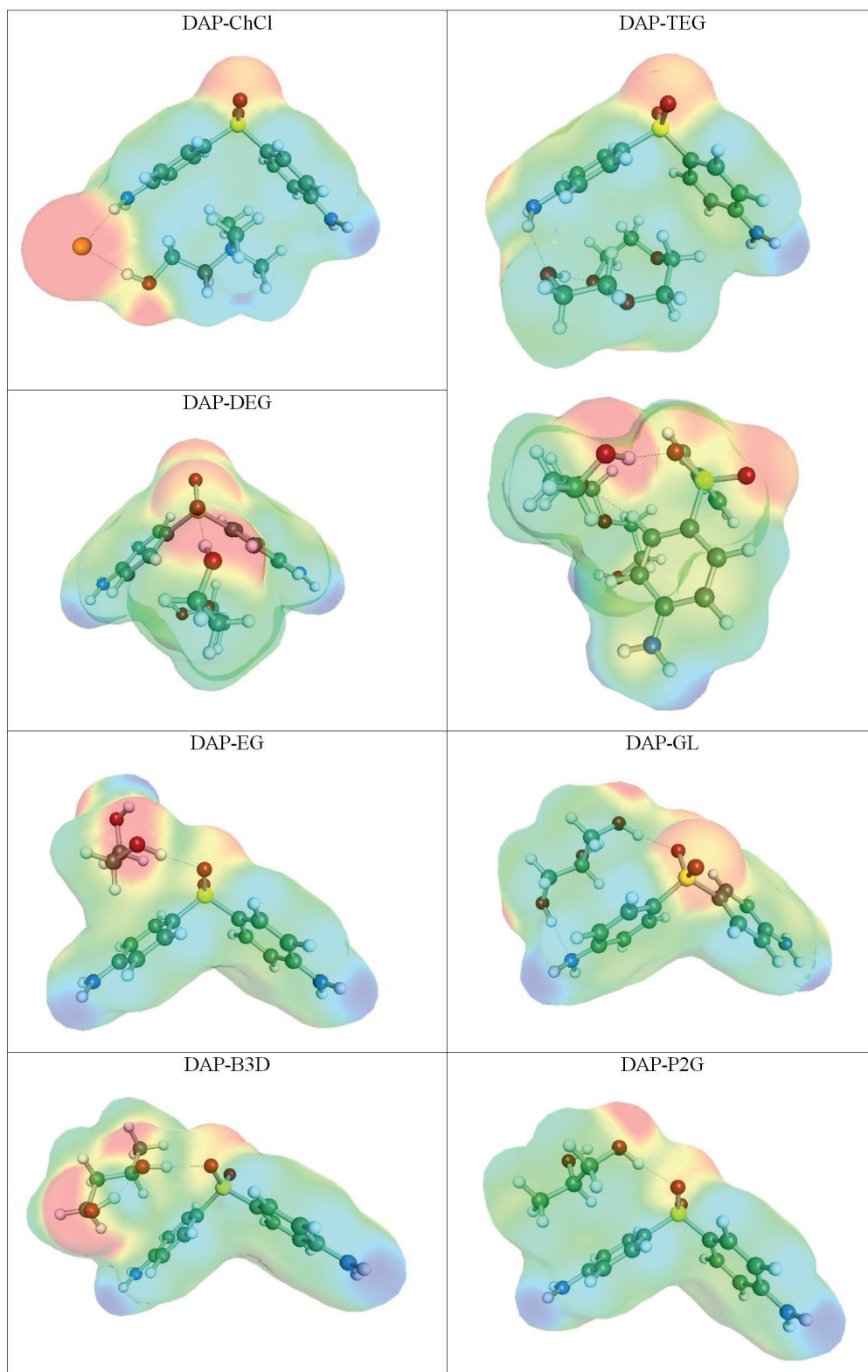


Fig. 3. Representation of the most stable pairs of dapsone (DAP) with deep eutectic solvents (DES) components. The colored clouds represented the charge density

ChCl is a very important component of the system, playing a crucial stabilization role. Indeed, the DAP-ChCl pairs are very stable in all cases. The 2nd factor contributing to the overall system stability comes from DAP-HBD pairs, which are slightly less favorable compared to DAP-ChCl. There is only 1 exception for DAP-TEG, as this pair has stability comparable to the latter. As one might

expect, the hydration of DAP has the smallest contribution to the overall affinity, which might be attributed to the low polarity of the solute. In Fig. 2, the relative solute–solvent affinity was drawn as a thick red line, representing the difference between DAP self-affinity and the sum of affinity to DES components. It is very interesting to observe that there is a correspondence between the order of DAP

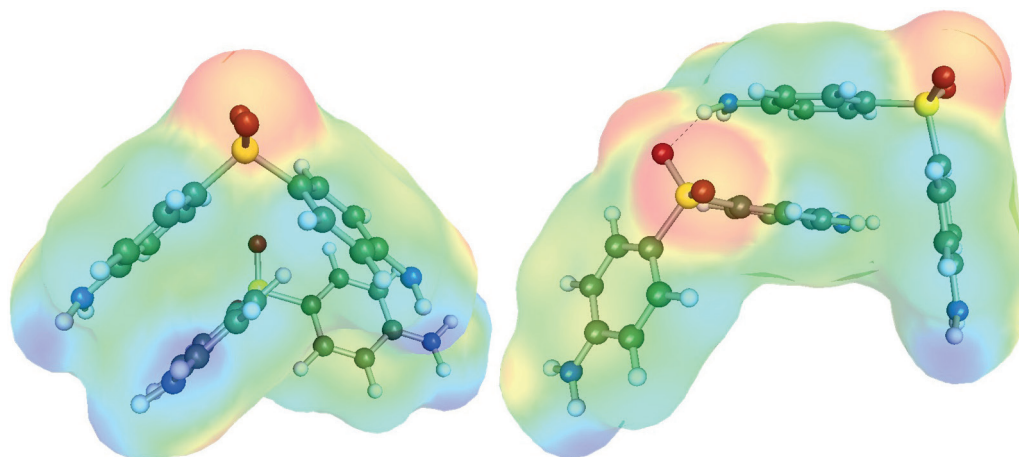


Fig. 4. Graphical representation of 2 types of dapsons (DAP) dimers found in the studied systems

solidity in the studied DES and the relative affinity. Indeed, the highest DAP solubility was observed in the ChCl mixture with TEG. The sequence of solubility reduction in TEG, DEG and ETG is associated with the parallel decrease of $\Delta G_r(AB)$ values. For the rest of the studied HBDs, the trend is not so clear, but solute–solvent interactions are comparable to DAP self-affinity. This conclusion not only qualitatively reveals the mechanism of DAP dissolution in DES but is also a good prognostic for the utilization of intermolecular interaction for machine learning purposes.

It is interesting to note that the structure of DAP allows for 3 types of interactions. The presence of the oxygen centers bound to sulfur atoms stands for acceptors of hydrogen bonding. The amino groups bound to aromatic rings can act as potential donors of hydrogen bonds. Finally, the apolar, aromatic rings can be the source of stabilization via non-covalent dispersive interactions. This general overview suggests that DAP should be easily solvated in a variety of solvents and soluble in diverse solvents. If this simple picture is confronted with the measured data, one can infer a rather more complex behavior of DAP.

Indeed, 3 separate classes of solvents interacting with DAP can be distinguished.⁵⁶ The 1st class comprises systems in which DAP acts as a proton acceptor via the sulfonyl group. This class of solvents encompasses water and aliphatic alcohols. It is anticipated that solubility in these solvents, which donate protons, will generally be at a moderate level due to the potential self-association of DAP. The 2nd group includes systems in which DAP is a proton donor in conjunction with solvents like acetone or DEG. The likelihood of DAP dissolving in these solvents is relatively high, as the non-polar region of DAP is less inclined to self-associate thanks to the obstruction caused by solvent molecules. In the 3rd and final class, solvents can be found that react with DAP through non-hydrogen bond interactions. This includes such solvents as DMSO and N-methyl-2-pyrrolidone, and the potential solubility range of DAP in these compounds is quite extended.

It is important to add that there is another aspect that should be taken into account if the dissolution mechanism is to be described, which is the self-affinity of DAP. As it was documented in Fig. 2, this type of interaction is the strongest among all pairs potentially present in DAP solutions. This holds not only for DES but also for many neat and binary solvents as well.⁵⁶ The dispersive forces are the predominant factor stabilizing the 2 DAP molecules. However, 2 distinct classes of structures were identified in the conformational search, as documented in Fig. 4. Interestingly, the structure of the most stable pair (on the left) is deficient in any type of hydrogen bonding. However, for some stable dimers the active role of both donor and acceptor centers of DAP is evident (on the right). The interplay of DAP self-association and complex formation with solvent molecules of DAP can be regarded as the main factor determining solubility. Solvents whose molecules offer concurrency to DAP dimerization are supposed to be better ones, such as, for example, TEG or DEG. These 2 molecules strongly interact with the non-polar region of DAP, in consequence effectively reducing the self-association. Solvents that can form hydrogen-bonded complexes typically do not impair as seriously the ability of dimerization, which results in more probable self-association leading eventually to aggregation and sedimentation.

Extended model for solubility prediction of DAP

In one of our previous projects,⁵⁶ a model for predicting DAP solubility was developed and validated. The ensemble of regressors with tuned hyperparameters was found to be very accurate in back-computations of DAP mole fraction at saturated conditions in neat solvents and binary solvent mixtures at varying compositions and temperatures. Also, the performed detailed analysis of potential predictive potential proved the ability of the formulated model to reliably predict new cases. The studied solvent space was quite extended and encompassed major types of solvents, including polar-protic, polar-aprotic

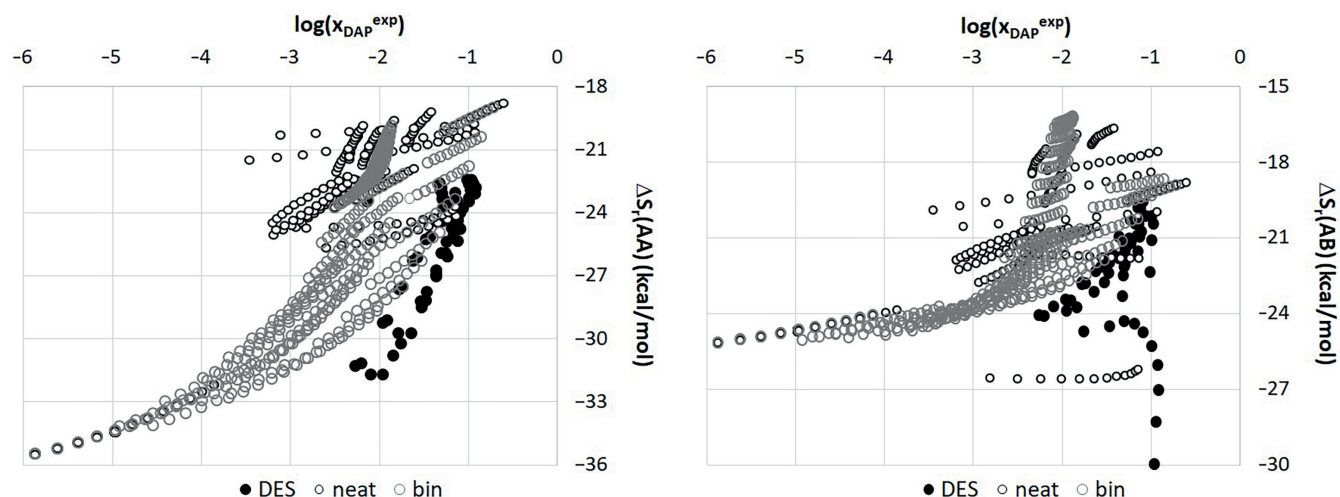


Fig. 5. Distribution of the solute–solute ($\Delta S_r(AA)$ – on the left) and solute–solvent ($\Delta S_r(AB)$ – on the right) entropic contributions to the affinity in the studied systems. Three sets represent the neat solvents (black circles), binary solvent mixtures (grey circles) and studied deep eutectic solvents (DES; black bold circles)

and non-polar ones. It is interesting to see if such a broad range of solvents representatively covers the possible variety of dissolution media. This aspect is especially important from the perspective of the type of solvents studied here, which are very polar, with diverse hydrogen bonding capabilities. Hence, the plots of selected descriptors were prepared for comparison of the coherence of their distributions. The previously developed model,⁵⁶ which optimized the set of the most suitable regressors, utilized intermolecular interactions as molecular descriptors. The detailed analysis of the importance of given descriptors revealed that for the majority of regressors, 2 contributions are dominant. These 2 descriptors characterize the solute–solute ($\Delta S_r(AA)$) and solute–solvent ($\Delta S_r(AB)$) entropic contributions to the affinity in the studied systems. The distributions of these values provided in Fig. 5 are separated into 3 sets, namely pure solvents, binary mixtures and ternary DES systems. The most important conclusion is that the new set of data adds distinct features to the overall characteristics. Although the obtained new results are within the range of solubility data used in the previous machine learning, molecular descriptors have quite distinct distributions. It is worth mentioning that the solubility measurements in DES were done only at room temperature, while the previous dataset included a quite extended range of temperatures from 5°C up to 80°C. It is not surprising that at elevated temperatures, the DAP solubility has been found to be very high, even higher than in the case of the studied DES. Hence, it is not the solubility range that prevents direct utilization of the developed model, but the distinct interactions in new systems. Consequently, it is very unlikely that the previous model can be used for solubility predictions in DES, and the utilization of such a model is not methodologically acceptable as the new pool of data is outside its applicability domain. Hence, it is necessary to extend the model for reliable predictions. The retraining

of the model is characterized in Fig. 6. First of all, the list of the most efficient regressors provided in the caption defines the new ensemble. No additional tuning of weight was performed, as the simple addition of their contributions was quite effective, as documented in the right panel of Fig. 6. The accuracy of back-computed DAP solubility is very high, which is a good prognosis for potential screening for alternative solvents. The fact that the applicability domain is significantly extended by the inclusion of solubility in DES means that the range of potential applications is seriously extended compared to previously formulated ensemble.⁵⁶

Conclusions

The performed multi-aspect analysis of DAP solubility in DES led to a number of conclusions regarding their effectiveness, dissolution mechanism and future screening for new solvents. First of all, the considered eutectic systems outperformed the classical organic solvents studied earlier, including DMSO, with the DES comprising ChCl and TEG being the most effective. It was also found that the addition of a specific amount of water to the DES systems increases DAP solubility even further. Second, the interplay of DAP self-association and the formation of complexes between DAP and solvent molecules can be regarded as the main factor influencing solubility. The self-association of DAP seems to be the most important factor influencing the stability of the systems and thus limiting its solubility. Conversely, the reason for increased solubility in some solvents is the ability of some molecules to strongly interact with the non-polar region of DAP, thus reducing self-association and increasing solubility. Finally, some important considerations have to be made regarding the usage of machine learning for solubility predictions. The general problem of the applicability

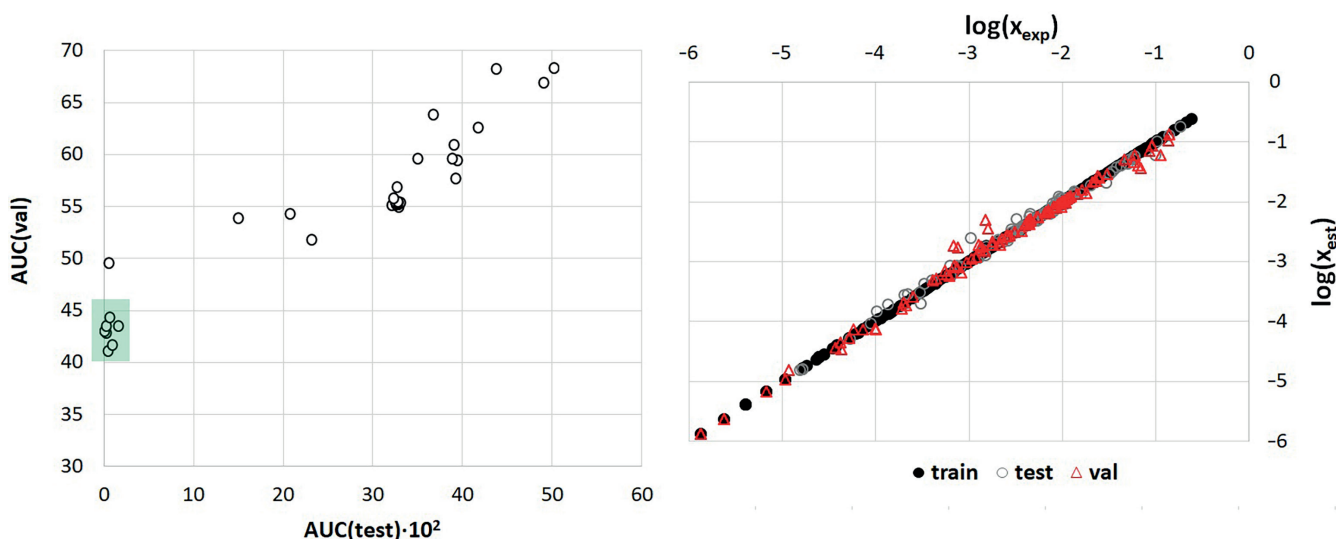


Fig. 6. The ensemble marked with a green rectangle in the left panel is defined by the set of the following regressors: NuSVR, SVR, CatBoostRegressor, RandomForestRegressor, HistGradientBoostingRegressor, LGBMRegressor, and BaggingRegressor. The predictive abilities of this model are provided in the right panel

domain restrictions imposed on any non-linear model developed using machine learning protocols is stressed and exemplified in the case of DAP solubility in DES. According to chemical intuition, the extension of solubility space by the inclusion of new dissolution media can affect the predictive potential of any non-linear model. However, the problem is whether the actual new pool of data resulting from new measurements requires re-formulating the model from scratch.

This paper univocally illustrates the necessity of augmenting the dataset with measurements in DES. The initial model was formulated for a quite extended and diverse set of solvents, which is not a common situation for active pharmaceutical ingredients. Hence, it might seem that the major portion of solvent structural and energetic diversity was already included in the original formulation, and the model can be applied for prediction in a variety of solvents not included in the pool of solvents used for model training. However, DES so seriously differ from organic solvents that retraining was indispensable. Fortunately, after the extension of the solubility data with 6 different solvents, the newly designed and retrained ensemble of regressors was able to capture all the new features of the system and very accurately describe the whole dataset. Since this is also associated with the extension of the applicability domain, its scope of application is broadened. This positive statement is partly mitigated by the fact that retraining is an unavoidable aspect of ensemble development if new data extend the solvent space.

Data availability

The datasets generated and/or analyzed during the current study are available from the corresponding author on reasonable request.

Consent for publication

All the authors give their consent for the publication of their identifiable details in the *Polymers in Medicine* journal.

ORCID iDs

Tomasz Jeliński <https://orcid.org/0000-0002-2359-6260>
 Maciej Przybyłek <https://orcid.org/0000-0002-3399-6129>
 Rafał Różalski <https://orcid.org/0000-0003-2067-9981>
 Piotr Cysewski <https://orcid.org/0000-0001-6220-2634>

References

- Madanipour MR, Fatehi-Zardalou M, Rahimi N, et al. The anti-inflammatory effect of dapsone on ovalbumin-induced allergic rhinitis in balb/c mice. *Life Sci.* 2022;297:120449. doi:10.1016/j.lfs.2022.120449
- Zhu YI, Stiller MJ. Dapsone and sulfones in dermatology: Overview and update. *J Am Acad Dermatol.* 2001;45(3):420–434. doi:10.1067/mjd.2001.114733
- May SM, Motosue MS, Park MA. Dapsone is often tolerated in HIV-infected patients with history of sulfonamide antibiotic intolerance. *J Allergy Clin Immunol Pract.* 2017;5(3):831–833. doi:10.1016/j.jaip.2016.11.011
- Wozel G, Blasum C. Dapsone in dermatology and beyond. *Arch Dermatol Res.* 2014;306(2):103–124. doi:10.1007/s00403-013-1409-7
- Moreno E, Calvo A, Schwartz J, et al. Evaluation of skin permeation and retention of topical dapsone in murine cutaneous leishmaniasis lesions. *Pharmaceutics.* 2019;11(11):607. doi:10.3390/pharmaceutics11110607
- Swain SS, Paidasetty SK, Dehury B, et al. Molecular docking and simulation study for synthesis of alternative dapsone derivative as a newer antileprosy drug in multidrug therapy. *J Cell Biochem.* 2018;119(12):9838–9852. doi:10.1002/jcb.27304
- Roman C, Dima B, Muyschont L, Schurmans T, Gilliaux O. Indications and efficiency of dapsone in IgA vasculitis (Henoch–Schönlein purpura): Case series and a review of the literature. *Eur J Pediatr.* 2019;178(8):1275–1281. doi:10.1007/s00431-019-03409-5
- Ghaoui N, Hanna E, Abbas O, Kibbi A, Kurban M. Update on the use of dapsone in dermatology. *Int J Dermatol.* 2020;59(7):787–795. doi:10.1111/ijd.14761
- Ríos C, Orozco-Suarez S, Salgado-Ceballos H, et al. Anti-apoptotic effects of dapsone after spinal cord injury in rats. *Neurochem Res.* 2015;40(6):1243–1251. doi:10.1007/s11064-015-1588-z

- Tingle MD, Mahmud R, Maggs JL, Pirmohamed M, Park BK. Comparison of the metabolism and toxicity of dapsone in rat, mouse and man. *J Pharmacol Exp Ther.* 1997;283(2):817–823. PMID:9353403.
- Mitra AK, Thummel KE, Kalthorn TF, Kharasch ED, Unadkat JD, Slattery JT. Metabolism of dapsone to its hydroxylamine by CYP2E1 in vitro and in vivo. *Clin Pharmacol Ther.* 1995;58(5):556–566. doi:10.1016/0009-9236(95)90176-0
- Molinelli E, Paolinelli M, Campanati A, Brisigotti V, Offidani A. Metabolic, pharmacokinetic, and toxicological issues surrounding dapsone. *Exp Opin Drug Metab Toxicol.* 2019;15(5):367–379. doi:10.1080/17425255.2019.1600670
- Jouyban A, Rahimpour E, Karimzadeh Z, Zhao H. Simulation of dapsone solubility data in mono- and mixed-solvents at various temperatures. *J Mol Liq.* 2022;345:118223. doi:10.1016/j.molliq.2021.118223
- Schneider-Rauber G, Argenta DF, Caon T. Emerging technologies to target drug delivery to the skin: The role of crystals and carrier-based systems in the case study of dapsone. *Pharm Res.* 2020;37(12):240. doi:10.1007/s11095-020-02951-4
- Wu Y, Hao X, Li J, Guan A, Zhou Z, Guo F. New insight into improving the solubility of poorly soluble drugs by preventing the formation of their hydrogen-bonds: A case of dapsone salts with camphorsulfonic and 5-sulfosalicylic acid. *CrystEngComm.* 2021;23(35):6191–6198. doi:10.1039/D1CE00847A
- Paredes Da Rocha N, De Souza A, Nishitani Yukuyama M, et al. Highly water-soluble dapsone nanocrystals: Towards innovative preparations for an undermined drug. *Int J Pharm.* 2023;630:122428. doi:10.1016/j.ijpharm.2022.122428
- Martínez F, Jouyban A, Acree Jr WE. Pharmaceuticals solubility is still nowadays widely studied everywhere. *Pharm Sci.* 2017;23(1):1–2. doi:10.15171/PS.2017.01
- Savjani KT, Gajjar AK, Savjani JK. Drug solubility: Importance and enhancement techniques. *ISRN Pharmaceutics.* 2012;2012:195727. doi:10.5402/2012/195727
- Kalam MA, Alshamsan A, Alkholief M, et al. Solubility measurement and various solubility parameters of glipizide in different neat solvents. *ACS Omega.* 2020;5(3):1708–1716. doi:10.1021/acsomega.9b04004
- Yang Z, Yang Y, Xia M, Dai W, Zhu B, Mei X. Improving the dissolution behaviors and bioavailability of abiraterone acetate via multi-component crystal forms. *Int J Pharm.* 2022;614:121460. doi:10.1016/j.ijpharm.2022.121460
- Thakur AK, Kumar R, Vipin Kumar VK, Kumar A, Kumar Gaurav G, Naresh Gupta K. A critical review on thermodynamic and hydrodynamic modeling and simulation of liquid antisolvent crystallization of pharmaceutical compounds. *J Mol Liq.* 2022;362:119663. doi:10.1016/j.molliq.2022.119663
- Kim HS, Kim CM, Jo AN, Kim JE. Studies on preformulation and formulation of JIN-001 liquid tablet with enhanced solubility. *Pharmaceutics (Basel).* 2022;15(4):412. doi:10.3390/ph15040412
- Anwer MdK, Muqtader M, Iqbal M, et al. Estimating the solubility, solution thermodynamics, and molecular interaction of aliskiren hemifumarate in alkylimidazolium-based ionic liquids. *Molecules.* 2019;24(15):2807. doi:10.3390/molecules24152807
- Constable DJC, Jimenez-Gonzalez C, Henderson RK. Perspective on solvent use in the pharmaceutical industry. *Org Process Res Dev.* 2007;11(1):133–137. doi:10.1021/op060170h
- Anastas PT, Williamson T. Green chemistry: An overview. In: Anastas PT, Williamson TC, eds. *Green Chemistry: Designing Chemistry for the Environment.* Vol. 626. ACS Symposium Series. Washington, DC, USA: American Chemical Society; 1996:691–697. doi:10.1021/bk-1996-0626
- Becker J, Manske C, Randl S. Green chemistry and sustainability metrics in the pharmaceutical manufacturing sector. *Curr Opin Green Sust Chem.* 2022;33:100562. doi:10.1016/j.cogsc.2021.100562
- DeSimone JM. Practical approaches to green solvents. *Science.* 2002;297(5582):799–803. doi:10.1126/science.1069622
- Jessop PG. Searching for green solvents. *Green Chem.* 2011;13(6):1391. doi:10.1039/c0gc00797h
- Cvjetko Bubalo M, Vidović S, Radojčić Redovniković I, Jokić S. Green solvents for green technologies. *J Chem Technol Biotechnol.* 2015;90(9):1631–1639. doi:10.1002/jctb.4668
- Häckl K, Kunz W. Some aspects of green solvents. *Comptes Rendus Chimie.* 2018;21(6):572–580. doi:10.1016/j.crci.2018.03.010
- Abbott AP, Ahmed EI, Harris RC, Ryder KS. Evaluating water miscible deep eutectic solvents (DESS) and ionic liquids as potential lubricants. *Green Chem.* 2014;16(9):4156–4161. doi:10.1039/C4GC00952E
- Omar KA, Sadeghi R. Physicochemical properties of deep eutectic solvents: A review. *J Mol Liq.* 2022;360:119524. doi:10.1016/j.molliq.2022.119524
- Zhang Q, De Oliveira Vigier K, Royer S, Jérôme F. Deep eutectic solvents: Syntheses, properties and applications. *Chem Soc Rev.* 2012;41(21):7108. doi:10.1039/c2cs35178a
- Choi YH, Van Spronsen J, Dai Y, et al. Are natural deep eutectic solvents the missing link in understanding cellular metabolism and physiology? *Plant Physiol.* 2011;156(4):1701–1705. doi:10.1104/pp.111.178426
- Dai Y, Van Spronsen J, Witkamp GJ, Verpoorte R, Choi YH. Natural deep eutectic solvents as new potential media for green technology. *Anal Chim Acta.* 2013;766:61–68. doi:10.1016/j.aca.2012.12.019
- Espino M, De Los Angeles Fernández M, Gomez FJV, Silva MF. Natural designer solvents for greening analytical chemistry. *Trends Anal Chem.* 2016;76:126–136. doi:10.1016/j.trac.2015.11.006
- Xu G, Shi M, Zhang P, et al. Tuning the composition of deep eutectic solvents consisting of tetrabutylammonium chloride and n-decanoic acid for adjustable separation of ethylene and ethane. *Separ Purif Technol.* 2022;298:121680. doi:10.1016/j.seppur.2022.121680
- Paiva A, Craveiro R, Aroso I, Martins M, Reis RL, Duarte ARC. Natural deep eutectic solvents: Solvents for the 21st century. *ACS Sust Chem Eng.* 2014;2(5):1063–1071. doi:10.1021/sc500096j
- Cao Y, Tao X, Jiang S, Gao N, Sun Z. Tuning thermodynamic properties of deep eutectic solvents for achieving highly efficient photothermal sensor. *J Mol Liq.* 2020;308:113163. doi:10.1016/j.molliq.2020.113163
- Nguyen CH, Augis L, Fourmentin S, Barratt G, Legrand FX. Deep eutectic solvents for innovative pharmaceutical formulations. In: Fourmentin S, Costa Gomes M, Lichtfouse E, eds. *Deep Eutectic Solvents for Medicine, Gas Solubilization and Extraction of Natural Substances.* Vol. 56. Environmental Chemistry for a Sustainable World. Cham, Switzerland: Springer International Publishing; 2021:41–102. doi:10.1007/978-3-030-53069-3_2
- Liu Y, Wu Y, Liu J, Wang W, Yang Q, Yang G. Deep eutectic solvents: Recent advances in fabrication approaches and pharmaceutical applications. *Int J Pharm.* 2022;622:121811. doi:10.1016/j.ijpharm.2022.121811
- Pedro SN, Freire CSR, Silvestre AJD, Freire MG. Deep eutectic solvents and pharmaceuticals. *Encyclopedia.* 2021;1(3):942–963. doi:10.3390/encyclopedia1030072
- Duarte ARC, Ferreira ASD, Barreiros S, Cabrita E, Reis RL, Paiva A. A comparison between pure active pharmaceutical ingredients and therapeutic deep eutectic solvents: Solubility and permeability studies. *Eur J Pharm Biopharm.* 2017;114:296–304. doi:10.1016/j.ejpb.2017.02.003
- Pedro SN, Freire MG, Freire CSR, Silvestre AJD. Deep eutectic solvents comprising active pharmaceutical ingredients in the development of drug delivery systems. *Exp Opin Drug Deliv.* 2019;16(5):497–506. doi:10.1080/17425247.2019.1604680
- Bazzo GC, Pezzini BR, Stulzer HK. Eutectic mixtures as an approach to enhance solubility, dissolution rate and oral bioavailability of poorly water-soluble drugs. *Int J Pharm.* 2020;588:119741. doi:10.1016/j.ijpharm.2020.119741
- Jeliński T, Przybyłek M, Cysewski P. Solubility advantage of sulfanilamide and sulfacetamide in natural deep eutectic systems: Experimental and theoretical investigations. *Drug Dev Ind Pharm.* 2019;45(7):1120–1129. doi:10.1080/03639045.2019.1597104
- Jeliński T, Przybyłek M, Cysewski P. Natural deep eutectic solvents as agents for improving solubility, stability and delivery of curcumin. *Pharm Res.* 2019;36(8):116. doi:10.1007/s11095-019-2643-2
- Jeliński T, Cysewski P. Quantification of caffeine interactions in choline chloride natural deep eutectic solvents: Solubility measurements and COSMO-RS-DARE interpretation. *Int J Mol Sci.* 2022;23(14):7832. doi:10.3390/ijms23147832
- Cysewski P, Jeliński T, Przybyłek M. Intermolecular interactions of edaravone in aqueous solutions of ethaline and glyciline inferred from experiments and quantum chemistry computations. *Molecules.* 2023;28(2):629. doi:10.3390/molecules28020629
- Lee S, Lee M, Gyak KW, Kim SD, Kim MJ, Min K. Novel solubility prediction models: Molecular fingerprints and physicochemical features vs graph convolutional neural networks. *ACS Omega.* 2022;7(14):12268–12277. doi:10.1021/acsomega.2c00697

51. Panapitiya G, Girard M, Hollas A, et al. Evaluation of deep learning architectures for aqueous solubility prediction. *ACS Omega*. 2022; 7(18):15695–15710. doi:10.1021/acsomega.2c00642
52. Vermeire FH, Chung Y, Green WH. Predicting solubility limits of organic solutes for a wide range of solvents and temperatures. *J Am Chem Soc*. 2022;144(24):10785–10797. doi:10.1021/jacs.2c01768
53. Cysewski P, Jeliński T, Przybytek M. Finding the right solvent: A novel screening protocol for identifying environmentally friendly and cost-effective options for benzenesulfonamide. *Molecules*. 2023;28(13): 5008. doi:10.3390/molecules28135008
54. Cysewski P, Jeliński T, Przybytek M, Nowak W, Olczak M. Solubility characteristics of acetaminophen and phenacetin in binary mixtures of aqueous organic solvents: Experimental and deep machine learning screening of green dissolution media. *Pharmaceutics*. 2022; 14(12):2828. doi:10.3390/pharmaceutics14122828
55. Cysewski P, Przybytek M, Rozalski R. Experimental and theoretical screening for green solvents improving sulfamethizole solubility. *Materials (Basel)*. 2021;14(20):5915. doi:10.3390/ma14205915
56. Cysewski P, Przybytek M, Jeliński T. Intermolecular interactions as a measure of dapsone solubility in neat solvents and binary solvent mixtures. *Materials (Basel)*. 2023;16(18):6336. doi:10.3390/ma16186336
57. Jeliński T, Kubsik M, Cysewski P. Application of the solute–solvent intermolecular interactions as indicator of caffeine solubility in aqueous binary aprotic and proton acceptor solvents: Measurements and quantum chemistry computations. *Materials (Basel)*. 2022;15(7):2472. doi:10.3390/ma15072472
58. Cysewski P, Jeliński T, Cymerman P, Przybytek M. Solvent screening for solubility enhancement of theophylline in neat, binary and ternary NADES solvents: New measurements and ensemble machine learning. *Int J Mol Sci*. 2021;22(14):7347. doi:10.3390/ijms22147347

Predicting sulfanilamide solubility in the binary mixtures using a reference solvent approach

Przewidywanie rozpuszczalności sulfanilamidu w mieszaninach dwuskładnikowych z wykorzystaniem metodyki rozpuszczalnika referencyjnego

Piotr Cysewski^{A–F}, Maciej Przybyłek^{B–F}, Tomasz Jeliński^{B–F}

Department of Physical Chemistry, Faculty of Pharmacy, Ludwik Rydygier Collegium Medicum in Bydgoszcz, Nicolaus Copernicus University in Toruń, Poland

A – research concept and design; B – collection and/or assembly of data; C – data analysis and interpretation; D – writing the article; E – critical revision of the article; F – final approval of the article

Polymers in Medicine, ISSN 0370-0747 (print), ISSN 2451-2699 (online)

Polim Med. 2024;54(1):27–34

Address for correspondence

Piotr Cysewski
E-mail: piotr.cysewski@cm.umk.pl

Funding sources

None declared

Conflict of interest

None declared

Received on November 19, 2023

Reviewed on December 19, 2023

Accepted on January 5, 2024

Published online on February 2, 2024

Cite as

Cysewski P, Przybyłek M, Jeliński T. Predicting sulfanilamide solubility in the binary mixtures using a reference solvent approach. *Polim Med.* 2024;54(1):27–34. doi:10.17219/pim/178284

DOI

10.17219/pim/178284

Copyright

Copyright by Author(s)

This is an article distributed under the terms of the Creative Commons Attribution 3.0 Unported (CC BY 3.0) (<https://creativecommons.org/licenses/by/3.0/>)

Abstract

Background. Solubility is a fundamental physicochemical property of active pharmaceutical ingredients. The optimization of a dissolution medium aims not only to increase solubility and other aspects are to be included such as environmental impact, toxicity degree, availability, and costs. Obtaining comprehensive solubility characteristics of chemical compounds is a non-trivial and demanding process. Therefore, support from theoretical approaches is of practical importance.

Objectives. This study aims to examine the accuracy of the reference solubility approach in the case of sulfanilamide dissolution in a variety of binary solvents. This pharmaceutically active substance has been extensively studied, and a substantial amount of solubility data is available. Unfortunately, using this set of data directly for theoretical modeling is impeded by noticeable inconsistencies in the published solubility data. Hence, this aspect is addressed by data curation using theoretical and experimental confirmations.

Materials and methods. In the experimental part of our study, the popular shake-flask method combined with ultraviolet (UV) spectrophotometric measurements was applied for solubility determination. The computational phase utilized the conductor-like screening model for real solvents (COSMO-RS) approach.

Results. The analysis of the results of solubility calculations for sulfonamide in binary solvents revealed abnormally high error values for acetone-ethyl acetate mixtures, which were further confirmed with experimental measurements. Additional confirmation was obtained by extending the solubility measurements to a series of homologous acetate esters.

Conclusions. Our study addresses the crucial issue of coherence of solubility data used for many theoretical inquiries, including parameter fitting of semi-empirical models, in-depth thermodynamic interpretations and application of machine learning protocols. The effectiveness of the proposed methodology for dataset curation was demonstrated for sulfanilamide solubility in binary mixtures. This approach enabled not only the formulation of a consistent dataset of sulfanilamide solubility binary solvent mixtures, but also its implementation as a qualitative tool guiding rationale solvent selection for experimental solubility screening.

Key words: *in silico*, solubility, sulfanilamide, binary solvents, COSMO-RS

Streszczenie

Wprowadzenie. Rozpuszczalność jest jedną z najbardziej fundamentalnych charakterystyk fizykochemicznych substancji aktywnych farmaceutycznie. Optymalizacja medium rozpuszczalnikowego jest złożonym problemem obejmującym nie tylko wyznaczenie samej rozpuszczalności ale również takie aspekty jak wpływ na środowisko, toksyczność, dostępność i koszt zakupu oraz utylizacji rozpuszczalników. Ponieważ uzyskanie kompleksowej charakterystyki rozpuszczalności nie jest trywialna, a często wiąże się z kosztownym i czasochłonnym procesem, badania teoretyczne stanowią istotne wsparcie.

Cel pracy. Celem pracy jest ilościowa ocena efektywności obliczania rozpuszczalności w mieszaninach dwuskładnikowych w oparciu o metodologię referencyjnego rozpuszczalnika. Z uwagi na duże zainteresowanie tym związkiem dostępna jest znaczna ilość danych doświadczalnych umożliwiających szczegółową analizę teoretyczną. Niestety, wykorzystanie tego zestawu bezpośrednio do modelowania teoretycznego jest utrudnione przez zaobserwowane niespójności. Ten problem został szczegółowo przeanalizowanych w oparciu o rozważania teoretyczną oraz przeprowadzone eksperymenty.

Materiał i metody. Część doświadczalna badań obejmowała równowagowy pomiar rozpuszczalności z wykorzystaniem metody spektrofotometrycznej w zakresie UV. Badania teoretyczne zostały zrealizowane z wykorzystaniem modelu COSMO-RS.

Wyniki. Analiza wyników przeprowadzonych obliczeń rozpuszczalności sulfonamidu w binarnych rozpuszczalnikach ujawniła anomalnie wysokie wartości błędów dla przypadku mieszanin aceton-octan etylu, co zostało zweryfikowane poprzez nowe pomiary eksperymentalne. Dodatkowego potwierdzenia dostarczyło rozszerzenie pomiarów rozpuszczalności o serie homologicznych estrów octanowych. Ponowne obliczenie rozpuszczalności w oparciu o metodykę rozpuszczalnika referencyjnego doprowadziło do znaczącej mniejszej rozbieżności pomiędzy obliczonymi oraz zmierzonymi wartościami ułamków molowych.

Wnioski. Niniejszy raport porusza kluczową kwestię zapewnienia spójności danych rozpuszczalności, które częstokroć są wykorzystywane w rozważaniach teoretycznych, takich jak interpretacja rozpuszczalności w oparciu o modele empiryczne czy półempiryczne oraz termodynamicznej charakterystyce procesów rozpuszczania. Zastosowanie metodyki obliczania rozpuszczalności w mieszaninach dwuskładnikowych na podstawie danych dla czystych rozpuszczalników pozwoliło nie tylko na identyfikację niespójności danych ale również na potencjalne badania przesiewowe.

Słowa kluczowe: *in silico*, rozpuszczalność, sulfonamid, COSMO-RS

Background

Sulfonamides are a highly important class of active pharmaceutical ingredients (APIs). This group of antimicrobial substances has a broad spectrum of applications, including the treatment of various bacterial and fungal infections and diabetes therapy.^{1,2} Sulfanilamide (SA; $C_6H_8N_2O_2S$; CAS:63-74-1, DrugBank: DB00259) is a precursor of sulfonamides used as topical anti-infectives.³ Furthermore, besides its conventional applications, SA has been employed in the synthesis of functional polymers with potential biomedical and pharmaceutical significance.^{4–6}

The solubility of a particular API is a fundamental physicochemical property routinely determined at the early stages of drug development. Moreover, the optimization of the dissolution media is often required to fulfill the criterion of solubilization effectiveness and additional requirements such as ecological issues, toxicity, availability, and costs. However, due to the enormously large solvent space, the practical realization of this step poses serious challenges. Hence, multiple theoretical approaches have been developed for the estimation of the properties of saturated solutions. Among the many available methods, the conductor-like screening model for real solvents (COSMO-RS)^{7,8} is one of the most ambitious theoretical approaches, aiming to determine the comprehensive characteristics of liquids exclusively from molecular structure. This particular approach harnesses the first principle

of quantum chemistry computations augmented with statistical thermodynamics. This 2-step procedure results in full temperature-dependent thermodynamics for bulk systems, even with complex compositions. A unique feature is its theoretical framework that explicitly includes the structural and energetic diversity of the liquid systems by allowing the molecular representation by the set of the most probable conformers. There is considerable evidence of the successful application of this method to a wide range of chemical problems. Some reported examples include solubility modeling of rutin in natural deep eutectic solvents (NADES),⁹ halogenated hydrocarbons in ionic liquids¹⁰ or cellulose in ionic liquids.¹¹ Notably, according to a recent report by Klajmon,¹² the COSMO-RS model is generally significantly more accurate for modeling the solubility of various pharmaceuticals in conventional solvents compared to the popular perturbed-chain statistical associating fluid theory (PC-SAFT) method.

Importantly, COSMO-RS is a theory of bulk liquids, and the characteristics of the solid-liquid equilibria (SLE) require taking into account the Gibbs free energy values of fusion of the solute (ΔG_{fus}). This thermodynamic property considers the transfer of the compound from the crystalline state into an unordered liquid and is typically determined experimentally using differential scanning calorimetry (DSC) measurements, including melting temperature (T_m), heat of fusion (ΔH_{fus}), and heat capacity change upon melting. Although many solids have been fully

characterized in these respects,^{13,14} such thermodynamic data are not available for numerous active pharmaceutical ingredients. The reasons for this are related to the thermal instabilities and decomposition below the melting point. Additionally, the complex polymorphic behavior, which is often observed for many solids, requires further determination of thermodynamic equilibria between the different polymorphs. Occasionally,¹⁵ the polymorph dissolved under the experimental conditions of solubility measurements differs from the crystal form stable at the melting point. Also, sulfanilamide is considered a problematic solid. In the Cambridge Structural Database (CSD), sulfanilamide solid structure is deposited in 4 sets of records documenting distinct polymorphic forms, namely α (Pbca), β (P21/c), γ (P 21/c), and δ (Pbca). It has been reported^{16,17} that both α and β forms during the heating process undergo a transition to the γ form, which is the only existing form under melting conditions. The 4th form is metastable and does not melt. The β -polymorph is the most stable one under ambient conditions and is usually commercially available.¹⁸ This complicates the theoretical computations of solubility since the experimental fusion data are unavailable. Moreover, proper characteristics of the fusion require the determination of the temperature-related heat capacities of the solid and liquid states, which often exceed the melting conditions. Therefore, the melting and fusion terms are often distinguishable. The former is used to depict the solid-liquid phase transition at the melting state, while the latter is reserved for solid transfer into a sub-cooled liquid state at any other temperature. Furthermore, the possibility of solvate formation should be considered. Fortunately, for sulfanilamide, no solvent inclusion occurs after crystallization.^{16,19} The reported DSC thermograms¹⁹ provide a consistent picture where the thermograms' shapes are preserved irrespective of the recrystallization from many solvents. This is evident by the observed small endothermic peak corresponding to the polymorphic transition and the large endothermic peak associated with the melting of the γ form.

The above information suggests that solubility computation is not a straightforward and trivial task, even in conjunction with the first-principle approach. Hence, many simplifications have been proposed by some authors, but criticized by others.²⁰ However, the lack of consensus regarding the appropriate way of including fusion thermodynamics in solubility predictions should not be a prohibiting factor. Indeed, in the COSMOtherm program (Dassault Systèmes, Biovia, San Diego, USA), which practically implements the COSMO-RS theory, it is possible to compute solid solubility by indirectly defining necessary fusion data. This is achieved by providing experimental data for a given solute in a given solvent or mixture at a given temperature as input data for computing solubility in different media. This approach refers to the reference solubility method. Furthermore, using the value of ΔG_{fus} determined in such a manner reproduces the solubility of the solutes

given as the reference. Hence, this method is very flexible, providing the reference solubility at conditions different from those of the solubility predictions. Particularly, it is possible to generate several reference solubility values or a variety of temperatures. The former option is utilized in our study by providing the 2 reference solubility data, which were experimentally determined for neat solvents for computing the solubility in the binary mixture at the given temperature. This reference solvent procedure was previously used with varying effectiveness, depending on the system under consideration.²¹ In general, the proper selection of a reference solvent can provide a reasonable solubility estimate. Such a solvent is commonly referred to as a consonance solvent.^{15,21} It is interesting to note that this approach is not utilized for the practical prediction of solubility in solvent mixtures.

Herein, we analyzed the accuracy of the aforementioned approach for sulfanilamide dissolved in a variety of binary solvent mixtures. This particular solute was extensively studied, and the available solubility data were large enough for theoretical analysis.

Materials and methods

Analytical grade sulfanilamide ($\geq 98\%$, SA, CAS: 63-74-1), ethyl acetate (99.5%, CAS: 141-78-6), n-propyl acetate ($\geq 99.5\%$, CAS: 109-60-4), n-butyl acetate (99.7%, CAS: 123-86-4), and methanol ($\geq 99.8\%$, CAS: 67-56-1) were obtained from Sigma-Aldrich (Saint Louis, USA) and used as received. Nitrogen (99.999%) for DSC analyses was supplied by Linde (Warsaw, Poland).

Solubility measurements

In this study, the shake-flask solubility determination procedure was applied. It is worth noting that the protocol has been previously employed for various organic compounds and validated in literature data.^{19,22–27} To determine the concentration of the saturated solutions of sulfanilamide in the considered set of solvents, the samples containing undissolved excess of active substances were incubated with mixing (60 rpm) at 25°C. The mixtures were prepared by dissolving sulfanilamide in a solvent in glass tubes (10 mL). Then, the test tubes were placed in an incubator (Orbital Shaker ES-20/60; Biosan, Riga, Latvia). After allowing the undissolved precipitate to settle for 1 h at 25°C, the mixture and the sediment were separated by filtration using a syringe equipped with a 0.22 μm PTFE filter. Spectrophotometric measurements were taken using 0.1 mL of the filtered solution, which was immediately diluted with 2 mL of methanol. Rapid dilution of the samples was essential to avoid crystallization during subsequent analytical procedures for concentration determination. For the same reason, i.e., to avoid crystallization, the equipment employed at the filtration and dilution steps

(syringes, filters, test tubes for filtrates, and pipette tips) was preheated at 25°C before use. For density determination, 1 mL of the filtrate was immediately transferred using an automatic pipette (Eppendorf Reference 2; Eppendorf, Hamburg, Germany) with a preheated tip to the tared 10 mL glass flask and weighted using an analytical balance (RADWAG AS 110 R2.PLUS; Radwag, Radom, Poland).

The quantification of SA in filtrates was ascertained using a spectrophotometric method ($\lambda_{\max} = 262 \text{ nm}$). To establish the calibration curve, the absorbance values were determined for a series of dilutions of the stock sulfanilamide solution (1.78×10^{-5} – $6.68 \times 10^{-5} \text{ M}$). All spectrophotometric measurements were performed using the A360 UV-VIS device (AOE Instruments, Shanghai, China).

Thermal analysis

After the shake-flask procedure, SA solid residues were air-dried and subjected to DSC analysis using a DSC 6000 PerkinElmer calorimeter (PerkinElmer, Waltham, USA). Heating rate was set to 5 K/min, while the nitrogen flow was 20 mL/min. The samples were measured in standard aluminum pans. The heat flow and temperature calibration were performed using zinc and indium standards supplied by the DSC device manufacturer.

Solubility dataset

An extensive literature review revealed sulfanilamide solubility of 18 different binary mixtures, including water-propylene glycol,²⁸ 1,4-dioxane-water,²⁹ water-methanol,³⁰ acetone-ethanol,³¹ acetone-methanol,³¹ acetone-toluene,³¹ methanol-toluene,³² ethanol-toluene,³² methanol-chloroform,³² ethanol-chloroform,³² methanol-ethanol,³² 1,4-dioxane-water,¹⁹ ethanol-water,¹⁹ dimethyl sulfoxide (DMSO)-water,¹⁹ dimethylformamide (DMF)-water,¹⁹ acetonitrile-water,¹⁹ and 4-formylmorpholine-water.¹⁹

This collection included 13 solvents used for binary mixtures' preparation in broad ranges of compositions and temperatures. The total number of datapoints was equal to $n = 1171$.

COSMO-RS computations

The COSMO-RS quantum chemistry approach^{7,8} was used for solubility predictions, as implemented in the COSMOtherm software.³³ A standard procedure for conformer generation was adopted, using the COSMOconf program (Dassault Systèmes, Biovia, San Diego, USA)³⁴ at the highest parametrization level available (BP_TZVPD_FINE_21.ctd). The most stable conformer is shown in Fig. 1.

The solubility computations relied on a thermodynamic equation defining the general solid-liquid equilibria in the following form (Equation 1):

$$\ln(y_i \cdot x_1^{\text{id}}) = \frac{\Delta H_{\text{fus}}}{R} \left(\frac{1}{T_m} - \frac{1}{T} \right) - \frac{1}{RT} \int_{T_m}^T \Delta C_{p,\text{fus}} dT + \frac{1}{R} \int_{T_m}^T \frac{\Delta C_{p,\text{fus}}}{T} dT \quad (1)$$

where the left side defines the solute activity $a_i = y_i \cdot x_1^{\text{id}}$ at saturated conditions, T_m stands for melting temperature, ΔH_{fus} represents heat of fusion, $\Delta C_{p,\text{fus}}$ denotes heat capacity change upon melting, and R is the gas constant. The fusion data indispensable for direct solubility computations in the COSMOtherm were taken as the average of available values,¹³ namely heat of fusion $\Delta H_{\text{fus}} = 23.40 \pm 0.38 \text{ kJ/mol}$ (average of reported 23.28 kJ/mol,³⁵ 23.30 kJ/mol,^{35,36} 24.02 kJ/mol,³⁷ 23.0 kJ/mol,³⁸ and 23.42 kJ/mol³²) and melting point $T_m = 437.3 \pm 1.84 \text{ K}$ (mean value of reported 435.35,³⁵ 435.4 K,^{35,36} 439.3K,³⁷ 438.7 K,³⁸ and 437.7 K³²). The application of this equation for any solid solute is often simplified by assuming the temperature independence of $\Delta C_{p,\text{fus}}$. There are 2 common alternatives, which suffer

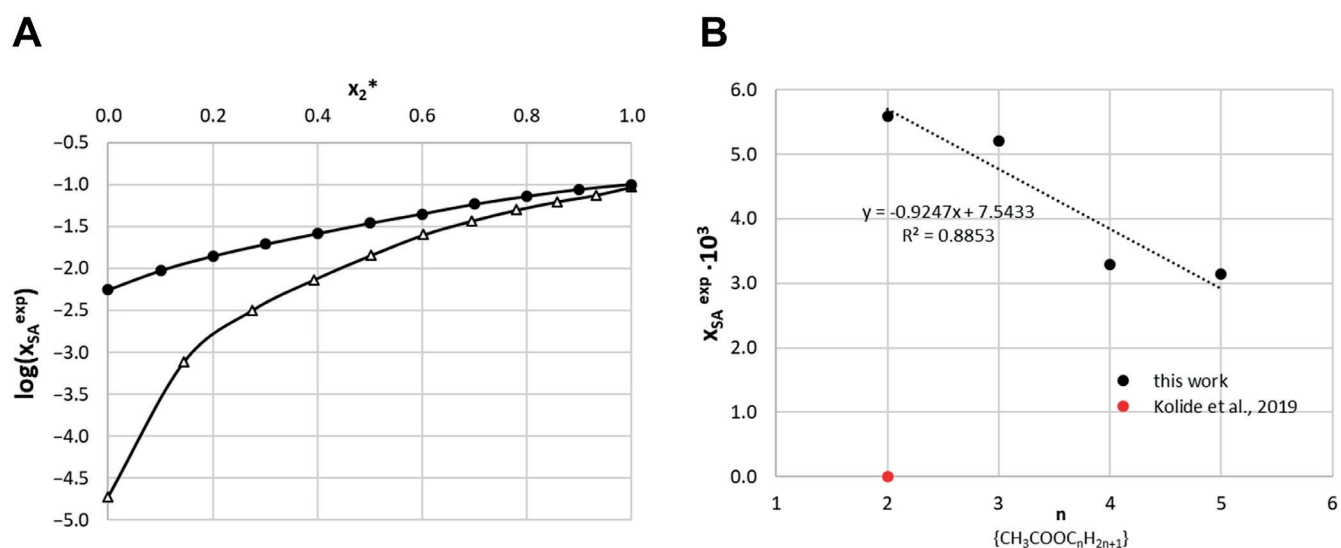


Fig. 1. A graphical representation of the structure and charge density distribution of the most stable conformer of sulfanilamide

from different inaccuracies depending on the studied system. The crudest simplification ignores heat capacity by setting $\Delta C_{p,\text{fus}} = 0$, which is often quite acceptable and was denoted as COSMO-RS in our study. Alternatively, one can assume $\Delta C_{p,\text{fus}} \approx S_{\text{fus}} = \Delta H_{\text{fus}}/T_m$ referred to below as CSOMO-RS(2). It is worth mentioning that these fusion data were used for computing the solubility in binary mixtures only for comparisons with reference solubility computations. The latter did not require fusion thermodynamics, since they were computed using the COSMOtherm program from the provided reference solubility data. The solubility values were computed by completely solving the SLE problem, utilizing a sequence of the following options in the input file “SLESOL solub screening”. For every reference solvent computation, actual values of neat solvent solubility were declared using the “ref_sol_x_log10” option along with the binary mixture composition, “x_ref_sol”, and temperature, “T_ref_sol”, keywords.

Results and discussion

The solubility of sulfanilamide in binary solvent mixtures was computed using the reference solvent approach. The experimental mole fractions of the saturated solutions were collected from the literature for systems listed in the methodology section. The computed values of SA solubility for the whole dataset are shown in Fig. 2, which comprises of 4 sets of results. The 1st set consisted of the prediction of SA solubility in binary mixtures derived directly from solving SLE within the COSMO-RS framework, and was displayed as the distribution of gray crosses. It was visible that this method provided a very raw estimate of the experimental solubility data.

However, reports have stated that COSMO-RS performs poorly in solubility prediction for various systems,^{22,39} although there are cases where the computed values are in good agreement with the experimental ones.²⁴ This was not the case for SA dissolved in the binary solvent mixtures, and we did not rely on such values for screening purposes, due to the back-computed values suffering from serious inaccuracies. The value of the mean absolute percentage error (MAPE) of mole fractions was as high as 1,310% (or 100% of the mean absolute logarithmic error), and cases arose that predicted value deviates by 3 orders of magnitude with respect to the measured ones. This was found for SA dissolution in chloroform, DMSO, DMF, and 4-formylmorpholine. Fortunately, the reference solvent procedure significantly increased the accuracy of the overall performance, since MAPE was reduced to about 40%. Although this was not a qualitative prediction, it offered rational estimates directing solvent selection for further experiments, if screening was needed. This was a very practical result, since only about 10% of the systems were studied experimentally within the whole solubility space formed by all possible combinations of the 13 neat solvents involved in the collected dataset of SA. Additionally, by performing measurements of SA in new neat solvents, the procedure enabled the estimation of solubility in virtually any combinations forming new binary mixtures.

Apart from the above determinations, additional interesting aspects emerged after performing reference solvent computations. Unexpected and anomalous behavior of acetone-ethyl acetate binary systems can be observed.³¹ This occasionally occurs where the reported solubilities were incongruent²³ and should be used with reserve. Herein, the highly inaccurate values of SA solubility in the mentioned binary mixture computed using

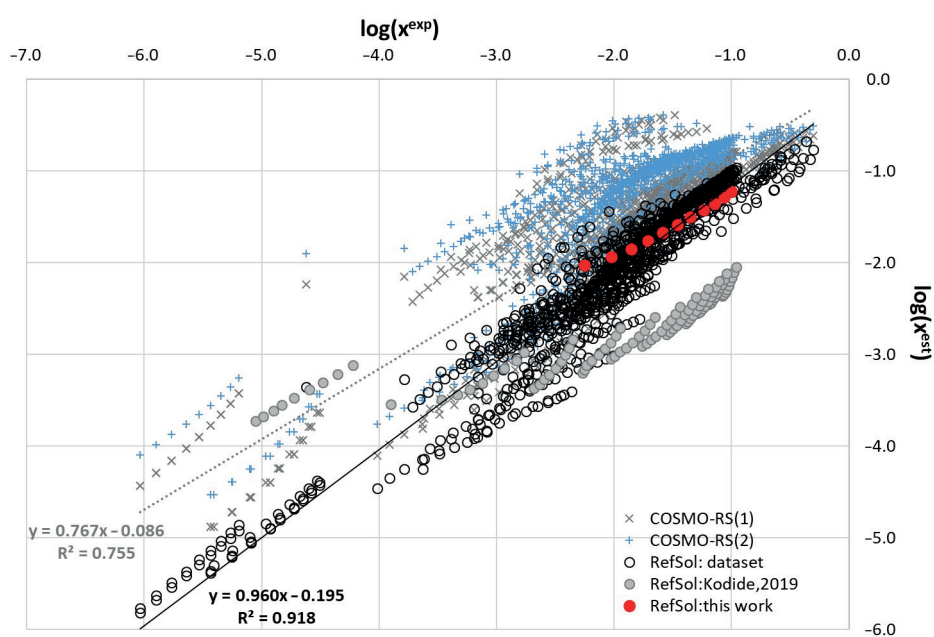


Fig. 2. Distribution of the computed values of sulfanilamide solubility in 18 binary mixtures confronted with experimentally determined ones. The circles represent the results of reference solubility computations and are denoted in the legend as the RefSol series. The distribution obtained for the whole dataset (open black circles) is overlapped with data described by Kodide et al.³¹ (gray circles) and measurements from the present study work (red circles). Additionally, results of the solubility computed using the COSMO-RS approach are provided, assuming $\Delta C_p = 0$ (gray crosses, COSMO-RS(1)) and $\Delta C_p = \Delta H_{\text{fus}}/T_m$ (blue pluses, COSMO-RS(2)). In both cases, the following fusion data are used: $\Delta H_{\text{fus}} = 23.40$ kJ/mol and $T_m = 437.3$ K

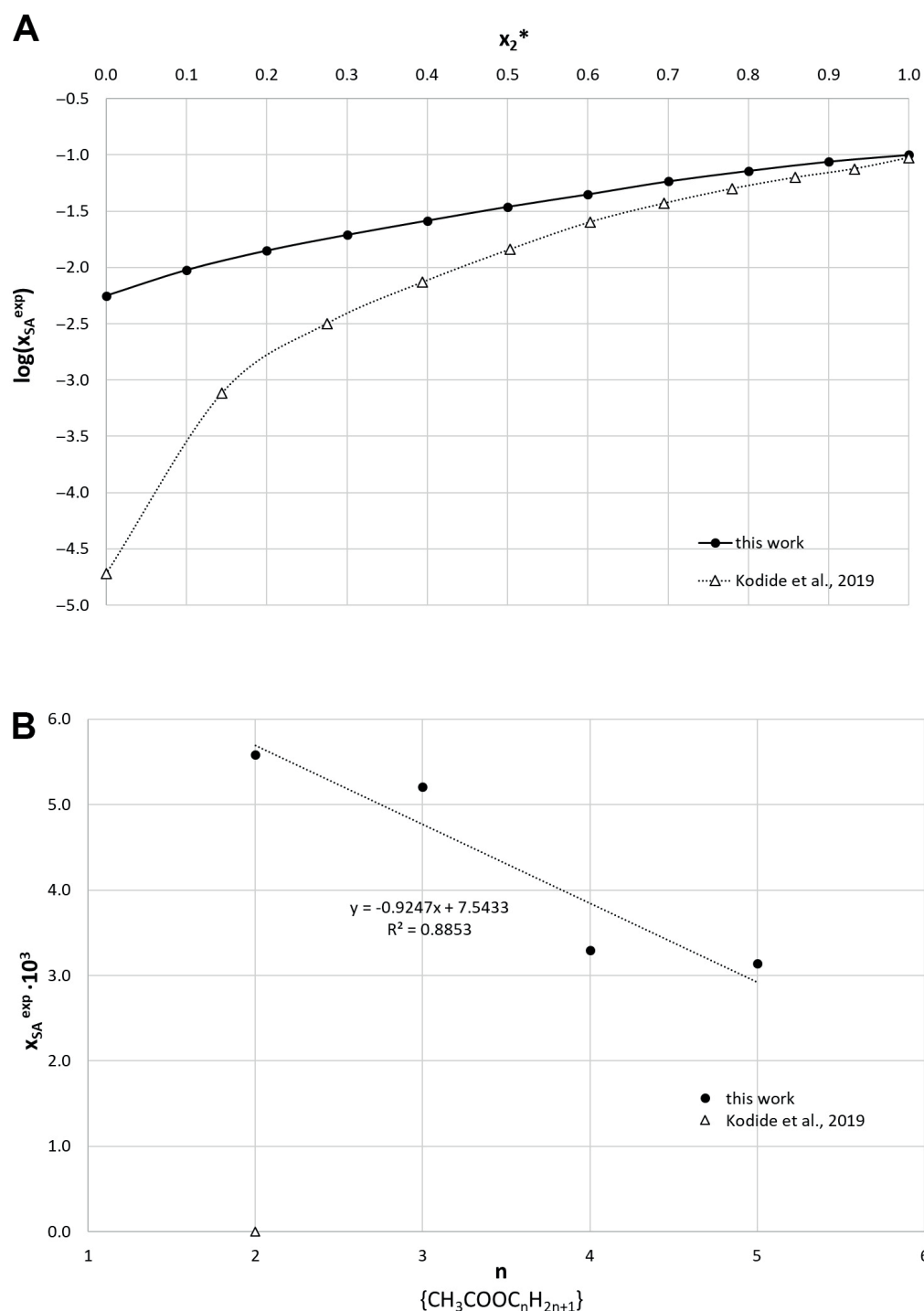


Fig. 3. Results of solubility determination ($T = 298.15\text{K}$) of sulfanilamide (SA) in (a) acetone (2) – ethyl acetate (3) as a function of acetone composition in solute-free solutions and (b) homology series of acetate esters, where n denotes carbon atoms of the alcohol part (2 for ethyl acetate, 3 for n-propyl acetate, 4 for n-butyl acetate, and 5 for n-amyl acetate)

the reference solvent approach are highlighted in Fig. 2 as gray circles distribution. Reports suggest a similarity in the solubility of SA in toluene and ethyl acetate.³¹ However, due to the differences in the polarity of both solvents, the opposite is expected. Notably, Asadi et al.⁴⁰ showed relatively high deviations for SA solubility in the acetone-ethyl acetate system if interpreted using different solubility equations. Hence, extremely inaccurate predictions using reference solvent approaches for this system should not be attributed to theoretical issues. To resolve this problem and univocally address the observed discrepancy, 2 series

of new measurements were performed. In the 1st trial, the solubility of SA was measured in 9 compositions of acetone and ethyl acetate at room temperature. To further confirm the solubility trend, the solubility of SA was determined in a series of ester homologs. The results of these 2 series of experiments are provided in Fig. 3. The obtained data highlighted the problem of the reported SA solubility in acetone-ethyl acetate binary mixtures and provided a comprehensive and convincing resolution.

First, the left panel confirms the serious discrepancy between our measurements and those reported

in the literature.³¹ Interestingly, the application of the reference solvent method to these new solubility data resulted in a very accurate prediction. Indeed, as shown in Fig. 2, the red circles representing the values for SA in acetone-ethyl acetate mixtures were the same as the overall trend and similar to the experimental data. Hence, this conducted analysis confirmed the higher reliability of the new measurements collected in Fig. 3A over those previously reported.³¹ To further support our observations, additional confirmation was offered by the results of new experimental solubility measurements (Fig. 3B). It was reasonable to expect that for a homolog series of solvents, a type of smooth trend of solubility should be observed. As shown in Fig. 3B, this was the case for a series of 4 acetate esters. A linear trend was found between the number of carbon atoms in the alcohol part and SA solubility in the corresponding acetate esters. The literature values were beyond that of the measured trend.

Undoubtedly, factors related to the characteristics of the solid, such as purity and polymorphism, have an impact on the results of solubility measurements. Therefore, calorimetric studies could provide valuable insight. Importantly, DSC measurement results of the sediments collected after the shake-flask procedure in neat solvents did not differ significantly from the pure sulfanilamide measured in this study (Fig. 4) and those reported in the literature.³¹ For all thermograms, a small peak corresponding to the polymorphic transformation and an intense γ form melting peak was observed. The onset values for the polymorphic and solid-liquid phase transitions of pure SA were

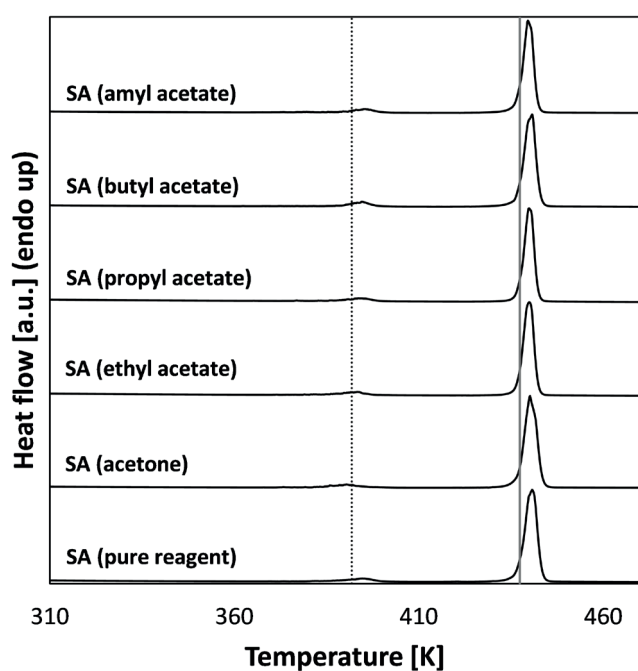


Fig. 4. Differential scanning calorimetry (DSC) analysis of solid residues from selected shake-flask experiments and pure sulfanilamide (SA). The dotted black and solid gray lines denote the onset values of the polymorphic transformation, and γ forms the melting point

391.84 K and 437.41 K, with corresponding enthalpy values of 1.89 kJ/mol and 24.17 kJ/mol. Notably, the melting point obtained in our study was similar to that reported by Koldide et al. for SA powder used for solubility measurements ($T_m = 437.78$ K).³¹

Conclusions

In this report, we addressed an important problem of solubility data coherence. The accuracy of this data is crucial as it is often used for further theoretical investigations, such as fitting parameters of empirical or semi-empirical solubility equations, solubility thermodynamics interpretation or more sophisticated inquiries, such as local composition determinations. Furthermore, the development of non-linear models using machine learning methodology also requires a reliable and consistent dataset for parameter hypertuning. Hence, data curation for solubility collections is a vital and valuable step.

This study displayed a straightforward methodology for the curation of certain subsets of the solubility data available in the published resources. The well-known saying “garbage in – garbage out” was exemplified for the solubility computations using the reference solvent approach. The accuracy of computed values in mixed solvents was inherently dependent on the reliability of solubility in neat solvents, as shown for sulfanilamide dissolved in binary mixtures of acetone and ethyl acetate. The replacement of suspicious solubility in neat solvents promoted an increase in the overall accuracy of solubility computations. This method is a reliable way to test the consistency of solid solutes in mixed dissolution media at various temperatures, including sulfanilamide.

Although qualitatively accurate, the reference solvent solubility values are still not accurate enough and cannot replace actual measurements. However, machine learning protocols may be implemented to further increase the accuracy of predicted solubility. The cured dataset, which encompasses congruent and coherent data, will be used in our next project for this purpose.

Data availability

The datasets generated and/or analyzed during the current study are available from the corresponding author upon reasonable request.

ORCID iDs

Piotr Cysewski <https://orcid.org/0000-0001-6220-2634>

Maciej Przybyłek <https://orcid.org/0000-0002-3399-6129>

Tomasz Jeliński <https://orcid.org/0000-0002-2359-6260>

References

1. Ovung A, Bhattacharyya J. Sulfonamide drugs: Structure, antibacterial property, toxicity, and biophysical interactions. *Biophys Rev.* 2021;13(2):259–272. doi:10.1007/s12551-021-00795-9

2. Hegazy WAH, Rajab AAH, Abu Lila AS, Abbas HA. Anti-diabetics and antimicrobials: Harmony of mutual interplay. *World J Diabetes*. 2021; 12(11):1832–1855. doi:10.4239/wjd.v12.i11.1832
3. Drugbank Online. Sulfanilamide. Drugbank Online; 2023. <https://go.drugbank.com/drugs/DB00259>. Accessed November 15, 2023.
4. Odnoroh M, Marty JD, Bourdon V, Coutelier O, Destarac M. Primary sulfonamide-functional polymers with controlled chain architectures by RAFT polymerisation. *Polym Chem*. 2023;14(33):3821–3826. doi:10.1039/D3PY00629H
5. Erol I. Synthesis and characterization of novel sulfonamide functionalized maleimide polymers: Conventional kinetic analysis, antimicrobial activity and dielectric properties. *J Mol Struct*. 2022;1255:132362. doi:10.1016/j.molstruc.2022.132362
6. Reddy CU, Amalraj A, Reddy BSR, Arun A. Polymeric drug based on sulfanilamide: Synthesis, antimicrobial and drug releasing studies. *J Pharm Pharmacol*. 2010;59(9):1207–1213. doi:10.1211/jpp.59.9.0004
7. Eckert F, Klamt A. Fast solvent screening via quantum chemistry: COSMO-RS approach. *AIChE J*. 2002;48(2):369–385. doi:10.1002/aic.690480220
8. Klamt A, Schüürmann G. COSMO: A new approach to dielectric screening in solvents with explicit expressions for the screening energy and its gradient. *J Chem Soc Perkin Trans 2*. 1993;5:799–805. doi:10.1039/P29930000799
9. Popović BM, Uka D, Alioui O, Ždero Pavlović R, Benguerba Y. Experimental and COSMO-RS theoretical exploration of rutin formulations in natural deep eutectic solvents: Solubility, stability, antioxidant activity, and bioaccessibility. *J Mol Liq*. 2022;359:119266. doi:10.1016/j.molliq.2022.119266
10. AlSaleem SS, Zahid WM, AlNashef IM, Hadj-Kali MK. Solubility of halogenated hydrocarbons in hydrophobic ionic liquids: Experimental study and COSMO-RS prediction. *J Chem Eng Data*. 2015;60(10):2926–2936. doi:10.1021/acs.jced.5b00310
11. Kahlen J, Masuch K, Leonhard K. Modelling cellulose solubilities in ionic liquids using COSMO-RS. *Green Chem*. 2010;12(12):2172. doi:10.1039/c0gc00200c
12. Klajmon M. Purely predicting the pharmaceutical solubility: What to expect from PC-SAFT and COSMO-RS? *Mol Pharm*. 2022;19(11):4212–4232. doi:10.1021/acs.molpharmaceut.2c00573
13. Acree W, Chickos JS. Phase transition enthalpy measurements of organic and organometallic compounds: Sublimation, vaporization and fusion enthalpies from 1880 to 2015. Part 1: C₁–C₁₀. *J Phys Chem Ref*. 2016;45(3):033101. doi:10.1063/1.4948363
14. Acree W, Chickos JS. Phase transition enthalpy measurements of organic and organometallic compounds and ionic liquids: Sublimation, vaporization, and fusion enthalpies from 1880 to 2015. Part 2: C₁₁–C₁₉₂. *J Phys Chem Ref*. 2017;46(1):013104. doi:10.1063/1.4970519
15. Cysewski P, Przybyłek M, Jeliński T. Intermolecular interactions as a measure of dapsone solubility in neat solvents and binary solvent mixtures. *Materials (Basel)*. 2023;16(18):6336. doi:10.3390/ma16186336
16. Toscani S, Thorén S, Agafonov V, Céolin R, Dugué J. Thermodynamic study of sulfanilamide polymorphism: (I) Monotropy of the α -variety. *Pharm Res*. 1995;12(10):1453–1456. doi:10.1023/A:1016271017802
17. Trontelj Z, Lužnik J, Pirnat J, Jazbinšek V, Lavrič Z, Srčič S. Polymorphism in sulfanilamide: 14N nuclear quadrupole resonance study. *J Pharm Sci*. 2019;108(9):2865–2870. doi:10.1016/j.xphs.2019.05.015
18. Toscani S, Dzyabchenko A, Agafonov V, Dugué J, Céolin R. Polymorphism of sulfanilamide: (II) Stability hierarchy of α -, β - and γ - forms from energy calculations by the atom–atom potential method and from the construction of the p,T phase diagram. *Pharm Res*. 1996; 13(1):151–154. doi:10.1023/A:1016058123659
19. Jeliński T, Bugalska N, Koszucka K, Przybyłek M, Cysewski P. Solubility of sulfanilamide in binary solvents containing water: Measurements and prediction using Buchowski–Ksiazczak solubility model. *J Mol Liq*. 2020;319:114342. doi:10.1016/j.molliq.2020.114342
20. Abbott S. *Solubility: Principles and Practice*. Ipswich, UK: Steven Abbott TCNF Ltd; 2017. https://www.stevenabbott.co.uk/_downloads/Solubility%20Science%20Principles%20and%20Practice.pdf. Accessed December 1, 2023.
21. Cysewski P. Application of the consonance solvent concept for accurate prediction of Buckminster solubility in 180 net solvents using COSMO-RS approach. *Symmetry*. 2019;11(6):828. doi:10.3390/sym11060828
22. Cysewski P, Jeliński T, Cymerman P, Przybyłek M. Solvent screening for solubility enhancement of theophylline in neat, binary and ternary NADES solvents: New measurements and ensemble machine learning. *Int J Mol Sci*. 2021;22(14):7347. doi:10.3390/ijms22147347
23. Cysewski P, Jeliński T, Przybyłek M. Application of COSMO-RS-DARE as a tool for testing consistency of solubility data: Case of coumarin in neat alcohols. *Molecules*. 2022;27(16):5274. doi:10.3390/molecules27165274
24. Przybyłek M, Miernicka A, Nowak M, Cysewski P. New screening protocol for effective green solvents selection of benzamide, salicylamide and ethenzamide. *Molecules*. 2022;27(10):3323. doi:10.3390/molecules27103323
25. Cysewski P, Przybyłek M, Rozalski R. Experimental and theoretical screening for green solvents improving sulfamethizole solubility. *Materials (Basel)*. 2021;14(20):5915. doi:10.3390/ma14205915
26. Cysewski P, Przybyłek M, Kowalska A, Tymorek N. Thermodynamics and intermolecular interactions of nicotinamide in neat and binary solutions: Experimental measurements and COSMO-RS concentration dependent reactions investigations. *Int J Mol Sci*. 2021; 22(14):7365. doi:10.3390/ijms22147365
27. Przybyłek M, Kowalska A, Tymorek N, Dziarn T, Cysewski P. Thermodynamic characteristics of phenacetin in solid state and saturated solutions in several neat and binary solvents. *Molecules*. 2021; 26(13):4078. doi:10.3390/molecules26134078
28. Delgado DR, Romdhani A, Martínez F. Thermodynamics of sulfanilamide solubility in propylene glycol + water mixtures. *Lat Am J Pharm*. 2011;30(10):2024. http://www.lamajpharm.org/resumenes/30/10/LAJOP_30_10_1_23.pdf. Accessed November 15, 2023.
29. Delgado DR, Peña Fernández MÁ, Martínez F. Preferential solvation of some sulfonamides in 1,4-dioxane + water co-solvent mixtures at 298.15 K according to the inverse Kirkwood–Buff integrals method. *Rev la Acad Colomb ciencias exactas, físicas y Nat*. 2014;38(146): 104–114. <https://raccefyn.co/index.php/raccefyn/article/view/44>. Accessed November 15, 2023.
30. Cárdenas ZJ, Jiménez DM, Almanza OA, Jouyban A, Martínez F, Acree WE. Solubility and preferential solvation of sulfanilamide, sulfamethizole and sulfapyridine in methanol+water mixtures at 298.15 K. *J Solution Chem*. 2016;45(10):1479–1503. doi:10.1007/s10953-016-0513-7
31. Kodide K, Asadi P, Thati J. Solubility and thermodynamic modeling of sulfanilamide in 12 mono solvents and 4 binary solvent mixtures from 278.15 to 318.15 K. *J Chem Eng Data*. 2019;64(12):5196–5209. doi:10.1021/acs.jced.9b00411
32. Asadi P, Kodide K, Kota M, Thati J. Determination and correlation of solubility and solution thermodynamics of 4-aminobenzenesulfonamide in five binary solvent mixtures from 278.15 to 318.15 K. *J Mol Liq*. 2020;303:112670. doi:10.1016/j.molliq.2020.112670
33. Dassault Systèmes. COSMOtherm. Dassault Systèmes, Biovia, San Diego, USA; 2022. <https://www.3ds.com/products/biovia/cosmo-rs/cosmotherm>. Accessed November 15, 2023.
34. Dassault Systèmes. COSMOconf. Dassault Systèmes, Biovia, San Diego, USA; 2022. <https://www.3ds.com/products/biovia>. Accessed November 15, 2023.
35. Martínez F, Gómez A. Thermodynamic study of the solubility of some sulfonamides in octanol, water, and the mutually saturated solvents. *J Solution Chem*. 2001;30(10):909–923. doi:10.1023/A:1012723731104
36. Martínez F, Gomez A. Estimation of the solubility of sulfonamides in aqueous media from partition coefficients and entropies of fusion. *Phys Chem Liq*. 2002;40(4):411–420. doi:10.1080/0031910021000017735
37. Ciocazanu I, Meltzer V. Etude thermodynamique de certains médicaments. *J Ther Anal*. 1996;47(6):1755–1758. doi:10.1007/BF01980921
38. Ohm A, Lippold BC. Surface tension of solid drugs and its correlation with solubility. *Int J Pharm Technol Prod Manuf*. 1985;6(4):1–6.
39. Cysewski P. Prediction of ethenzamide solubility in organic solvents by explicit inclusions of intermolecular interactions within the framework of COSMO-RS-DARE. *J Mol Liq*. 2019;290:111163. doi:10.1016/j.molliq.2019.111163
40. Asadi P, Kodide K, Thati J, Busi MR. Predicting sulfanilamide solubility in mixed solvents: A comparative analysis of computational models. *Fluid Phase Equilibria*. 2024;577:113966. doi:10.1016/j.fluid.2023.113966

Alteration of zeta potential and cell viability in rat-derived L6 skeletal muscle cells and H9c2 cardiomyocytes: A study with submicron polystyrene particles

Zmiany potencjału zeta oraz żywotności komórek mięśni szkieletowych L6 oraz kardiomiocytów H9c2: badania z submikronowymi cząstkami polistyrenowymi

Joanna Kotyńska^{1,A,C,D,F}, Marcin Zajęc^{2,B–D,F}, Agnieszka Mikłosz^{3,B,C,F}, Adrian Chabowski^{3,E,F}, Monika Naumowicz^{1,A,C–F}

¹ Department of Physical Chemistry, Faculty of Chemistry, University of Białystok, Poland

² Doctoral School of Exact and Natural Sciences, University of Białystok, Poland

³ Department of Physiology, Medical University of Białystok, Poland

A – research concept and design; B – collection and/or assembly of data; C – data analysis and interpretation; D – writing the article; E – critical revision of the article; F – final approval of the article

Polymers in Medicine, ISSN 0370-0747 (print), ISSN 2451-2699 (online)

Polim Med. 2024;54(1):35–43

Address for correspondence

Monika Naumowicz
E-mail: monikan@uwb.edu.pl

Funding sources

None declared

Conflict of interest

None declared

Received on November 20, 2023

Reviewed on December 15, 2023

Accepted on December 15, 2023

Published online on January 17, 2024

Cite as

Kotyńska J, Zajęc M, Mikłosz A, Chabowski A, Naumowicz M. Alteration of zeta potential and cell viability in rat-derived L6 skeletal muscle cells and H9c2 cardiomyocytes: A study with submicron polystyrene particles. *Polim Med.* 2024;54(1):35–43. doi:10.17219/pim/177127

DOI

10.17219/pim/177127

Copyright

Copyright by Author(s)

This is an article distributed under the terms of the Creative Commons Attribution 3.0 Unported (CC BY 3.0) (<https://creativecommons.org/licenses/by/3.0/>)

Abstract

Background. Micro- and nanoplastics pollution can cause substantial damage to ecosystems. Since scientists have focused mainly on their impact on aquatic environments, less attention has been paid to the accumulation of polymer particles in terrestrial organisms.

Objectives. We checked if submicron (<5 μm) polystyrene (PS) particles, which can accumulate in living organisms, lead to changes in the physicochemical properties of mammalian cell membranes.

Materials and methods. The influence of submicron PS particles on the properties of rat-derived L6 myocytes and H9c2 cardiomyocytes was analyzed. Non-functionalized and amine-functionalized PS particles of 100 nm and 200 nm in diameter were used. The MTT assay was performed to evaluate the viability of the polymers-treated cells. The effect of short (6 h) and prolonged (48 h) incubation with different concentrations of PS particles on the cell's zeta (ζ) potential was examined with the electrophoretic light scattering technique (ELS). Polystyrene particles' physicochemical characteristics (size and stability) were performed using dynamic light scattering (DLS) and electrophoretic light scattering methods.

Results. The results show that submicron PS particles affect cell viability and cause changes in the physicochemical parameters of rat cell membranes. Differences were observed depending on the origin of the cells. We observed dose- and time-dependent alterations in the studied parameters after submicron PS particle incubation in L6 myotubes and H9c2 cardiomyocytes.

Conclusions. The size and modification of PS particle surfaces determine the extent to which they affect the analyzed properties of rat cardiomyocytes and myocytes membranes.

Keywords: physicochemical properties, zeta potential, cardiomyocyte, myotubes, submicron polystyrene particles

Streszczenie

Wprowadzenie. Zanieczyszczenia mikro- i nanoplastikami mogą powodować znaczne szkody w ekosystemach. Ze względu na to, że naukowcy skupili się głównie na wpływie polimerów na środowisko wodne, mniej uwagi w literaturze poświęcono problemowi akumulacji ich cząstek w organizmach lądowych.

Cel pracy. Zbadano, czy submikronowe (< 5 mm) cząstki polistyrenowe, które mogą kumulować się w organizmach żywych, powodują zmiany właściwości fizykochemicznych błon komórkowych ssaków.

Materiał i metody. Przeanalizowano wpływ submikronowych cząstek polistyrenowych na właściwości szczurzych komórek mięśni szkieletowych L6 oraz kardiomiocytów H9c2. Zastosowano cząstki polistyrenu niesfunkcjonalizowanego i sfunkcjonalizowanego grupą aminową –NH₂ o średnicy 100 i 200 nm. W celu oceny żywotności komórek traktowanych polimerami przeprowadzono testy MTT. Wpływ krótko- (6 godzin) i długotrwałej (48 godzin) inkubacji z różnymi stężeniami cząstek polistyrenu na wartość potencjału zeta (ζ) zbadano techniką elektroforetycznego rozpraszania światła (ELS, ang. Electrophoretic Light Scattering). Charakterystykę fizykochemiczną (wielkość i stabilność) analizowanych cząstek polistyrenu określono metodami dynamicznego rozpraszania światła (DLS, ang. Dynamic Light Scattering) oraz ELS.

Wyniki. Uzyskane dane wykazały, że submikronowe cząstki polistyrenowe wpływają na żywotność szczurzych komórek mięśni szkieletowych oraz komórek mięśnia sercowego, a także powodują zmiany parametrów fizykochemicznych ich błon. Odnotowano różnice w zależności od rodzaju tkanki z której pochodzą komórki (mięśnie szkieletowe/mięsień sercowy). Uzyskane wyniki zależą od rodzaju i dawki polistyrenu, a także od czasu inkubacji.

Wnioski. Wielkość i modyfikacja powierzchni cząstek polistyrenu jest istotna dla stopnia w jakim wpływają one na właściwości fizykochemiczne błon szczurzych miotub oraz kardiomiocytów.

Słowa kluczowe: właściwości fizykochemiczne, submikronowe cząstki polistyrenowe, potencjał zeta, kardiomiocyty, komórki mięśni szkieletowych

Background

The main components of plastics are natural or synthetic polymers.¹ In the past, it was believed that plastics were the material of the future, making everyday life easier. However, due to their inappropriate use and management, they are now considered a severe environmental issue worldwide.^{2,3} The raw material used in the production of plastics is polystyrene (PS), a crucial compound, e.g., during the COVID-19 pandemic since most of the packaging in which meals were delivered to households was made from PS.⁴ This polymer is not biodegradable, and its disposal is a complicated and expensive process, the price of which exceeds the cost of producing the raw material.⁵ In addition to the improper utilization of plastic waste, which is essential for the future of our environment, the accumulation of plastics in living organisms is a fundamental issue. Submicron particles (smaller than 5 mm) may accumulate in the living organism. The particles are formed by the degradation of plastics into smaller and smaller materials,⁶ which may come from intentional production (primary plastics) or may be the products of the fragmentation of larger pieces (secondary plastics).⁷ Most polymer particles are classified as secondary plastics, and their fragmentation can occur as a result of exposure to O₂, temperature, ultraviolet (UV) radiation, or mechanical abrasion.⁸ Polymer particles are categorized as anthropogenic pollutants that are present all over the Earth, found in waters,⁹ soils¹⁰ and air.¹¹ Plastic pollution can cause substantial damage to ecosystems. Since scientists have focused mainly

on their impact on aquatic environments,^{12,13} less attention has been paid to the accumulation of polymer particles in terrestrial organisms. The literature reports the adverse effects of microplastics on mammals, such as impaired reproduction or changes in metabolism.^{14–16} Polymer particles can bioaccumulate in the organism and exhibit various levels of toxicity that can be attributed to their physicochemical characteristics (size, shape, surface chemistry), which may allow them to enter cells and interact with their components. This process can lead to nanoparticle-induced biophysical and/or biochemical changes.¹⁷

Objectives

A crucial issue worth focusing on is the effect of polymer particles on changes occurring within the biological membranes of organisms. *Rattus norvegicus* is used in biomedical research and remains the model of choice for chemical toxicity studies.¹⁸ Rat cells (L6 skeletal muscle cells and H9c2 cardiomyocytes) were chosen as an in vitro model system to investigate how anthropogenic pollutants, such as plastics, affect the properties of mammalian cell membranes. Since PS is one of the polymers that mainly pollute our environment and does not form in reactive forms in which cells occur (thus not damaging the membrane due to oxidative stress), its particles were chosen for the study.¹⁹ Non-functionalized (pristine) PS and amine-functionalized PS-NH₂ particles of 100 nm and 200 nm in diameter were used. Rat L6 myotubes and H9c2

cardiomyocytes were exposed to 6 h and 48 h of incubation with PS particles at concentrations ranging from 2 µg/mL to 1000 µg/mL.

In order to investigate the cytotoxic activity of PS particles toward L6 and H9c2 cells, the MTT (3-(4,5-dimethylthiazol-2-yl)-2,5-diphenyltetrazolium bromide) biochemical assays were performed. Electrochemical techniques were used to examine the effect of PS particles on the electrical parameters characterizing the cell membranes after conducting biological tests. A significant parameter describing biological cells is the zeta potential (electrokinetic potential (ζ)) – an essential and credible index of the membrane's surface charge. Its value is characteristic of a membrane composition and knowledge of ζ makes it possible to determine the system's stability.²⁰ This parameter depends on viscosity, temperature and pH, so even slight modifications of the analyzed system may affect its value.²¹

Materials and methods

Materials

Cell culture

The study was conducted on the L6 skeletal muscle cells and H9c2 cardiomyocytes obtained from the American Type Culture Collection (ATCC; Manassas, USA). Cells were cultured in Dulbecco's modified Eagle's medium (DMEM; PAN-Biotech, Aidenbach, Germany) with the addition of 10% fetal bovine serum (FBS; Thermo Fisher Scientific, Waltham, USA) and 1% solution of antibiotics (PAN-Biotech) in a humidified atmosphere containing 5% CO₂ at 37°C. Confluent cells were then cultured in differentiation medium containing DMEM and 2% horse serum (HS; Thermo Fisher Scientific) for L6 cells and DMEM enriched with 1% of FBS for H9c2 myoblasts. After 2 weeks, myoblasts were fully differentiated into elongated, multinucleated myotubes. Thereafter, myotubes were exposed to PS nanoparticles (PS/PS-NH₂) of 100 nm or 200 nm in diameter at concentrations ranging from 2 µg/mL to 1000 µg/mL and incubated for 6 h and 48 h. Myotubes cultured without PS/PS-NH₂ were used as a control.

Polymers

Pristine 100-nm and 200-nm PS (Sigma-Aldrich, Saint Louis, USA), amine-functionalized 100-nm (Polysciences, Hirschberg an der Bergstrasse, Germany) and 200-nm (Bang Laboratories, Fishers, USA) PS-NH₂ were used to treat L6 and H9c2 cells. The amount of dose and the time of treatment with the PS particles were chosen in the pre-study. The PS molecules were diluted to the required concentration with 155 mmol/L NaCl, in which the cells were also suspended.

Methods

Cell viability assay

Cytotoxicity of PS nanoparticles was assessed with MTT viability assay (Sigma-Aldrich). Briefly, L6 and H9c2 cells were cultured on 96-well plates at a density of 4×10³ cells/well. Fully differentiated myotubes were incubated with different concentrations of PS/PS-NH₂ ranging from 2 µg/mL to 1000 µg/mL for 6 h and 48 h. Cells were then rinsed 2 times with PBS and incubated with 200 µl of MTT solution (5 mg/mL in PBS) for 4 h. After removing the medium, the purple precipitate was dissolved in 200 µL of dimethyl sulfoxide (DMSO; Sigma-Aldrich). The absorbance of the resulting formazan solution was measured at 570 nm using a microplate reader (Synergy H1 Hybrid Reader; BioTek Instruments, Winooski, USA). The viability of pristine PS/PS-NH₂-treated cells was calculated as the percentage of untreated cells.

Dynamic light scattering

The dynamic light scattering (DLS) technique was used to estimate the diameter of DMEM-suspended polymer particles (pH = 7.4, T = 25°C). Measurements were made with the Zetasizer Nano ZS analyzer (Malvern Instruments Ltd, Malvern, UK). Applying the Stokes–Einstein equation, the particle velocity caused by Brownian motion is transformed into a particle size distribution. Using a non-invasive backscattering technique, in which the detector is angled at 173°, particle size detection can be done. The derived data were error-laden, represented as standard deviation.

Electrophoretic light scattering

Zetasizer Nano ZS analyzer uses the electrophoretic light scattering (ELS) method to determine the ζ potential of the PS particles and cells. In the first step, the parameter for both 100-nm and 200-nm PS/PS-NH₂ was measured (DMEM, pH = 7.4, T = 25°C). In the next step, L6 and H9c2 cells were treated with both pristine and amine-functionalized PS particles (2 µg/mL, 10 µg/mL and 100 µg/mL) for 6 h and 48 h in 155 mmol/L NaCl, and ζ potential was measured as a function of pH (pH range 2.5–10). The microelectrophoretic measurements were also performed for control samples – L6 and H9c2 cells suspended in 155 mmol/L NaCl untreated with PS. At least 3 repeated measurements on each sample were taken to check for result repeatability.

Statistical analyses

GraphPad Prism 9 software (GraphPad Software, San Diego, USA) was applied to statistically analyze the data derived from the MTT test. The data that fulfilled normality

and homogeneity assumptions were analyzed using a one-way analysis of variance (ANOVA). If the abovementioned assumptions were not fulfilled, we applied the Kruskal–Wallis test. As a post hoc test, Dunnett's multiple comparisons test (parametric test) or Dunn's multiple comparisons test (non-parametric test) were used. Statistical significance was defined as * $p < 0.05$; ** $p < 0.01$; *** $p < 0.001$; **** $p < 0.0001$.

Data obtained from the DLS and ELS studies were given as means \pm standard deviation ($M \pm SD$). The data were evaluated with standard statistical analyses, namely one-way ANOVA with Scheffe's F test for multiple comparisons to detect significance between the various groups. Values of $p < 0.05$ were assumed to be relevant.

Results and discussion

The size and stability of submicron polystyrene particles

Measurements of both DLS and ELS have been used to evaluate the PS particle changes in size, charge (ζ potential) and particle size distribution (polydispersity index (PDI)) in DMEM (a medium in which L6 and H9c2 cells were cultured). During the experiments, 100-nm and 200-nm non-modified (PS-100 and PS-200) and amino-functionalized PS particles (PS-NH₂-100 and PS-NH₂-200) were analyzed.

Particle size distribution curves (by number and intensity) are presented in Fig. 1. As can be seen from Table 1, the sizes by number of PS-NH₂ (both 100-nm and 200-nm) are consistent with the commercially stated values and comparable to results obtained in 155 mmol/L NaCl.²² Analyzing the data registered for non-modified PS submicron particles, we can see that PS with 200 nm in diameter dispersed in DMEM deviate from the commercially stated values and are equal to 297.70 ± 118.90 nm (size by number) and 387.40 ± 147.00 nm (size by intensity). The obtained differences may be caused by the stronger dispersion of PS particles in DMEM than in sodium chloride.²³ Moreover, PS-100 suspended in DMEM exhibits a bimodal size distribution profile (Fig. 1), with PDI = 0.328, indicating that pristine PS particles are polydisperse. This proves the tendency of PS-100 to form aggregates in DMEM, a common phenomenon characterizing PS nanoparticles.

The ζ -potential characterizes the electrokinetic potential of nanoparticles in solutions, which is a factor that alters the stability of particles and thus their possible absorption or toxicity.²⁴ In general, if ζ is higher than 30 mV, negative or positive, it suggests high physical stability of the system because of the electrostatic repulsion of the particles.²⁵ A ζ value between -30 mV and $+30$ mV usually suggests flocculation and/or aggregation of the particles.²⁶ From the data summarized in Table 1, it may be deduced that amine-modified PS particles show lower stability than native particles. Non-functionalized PS particles have

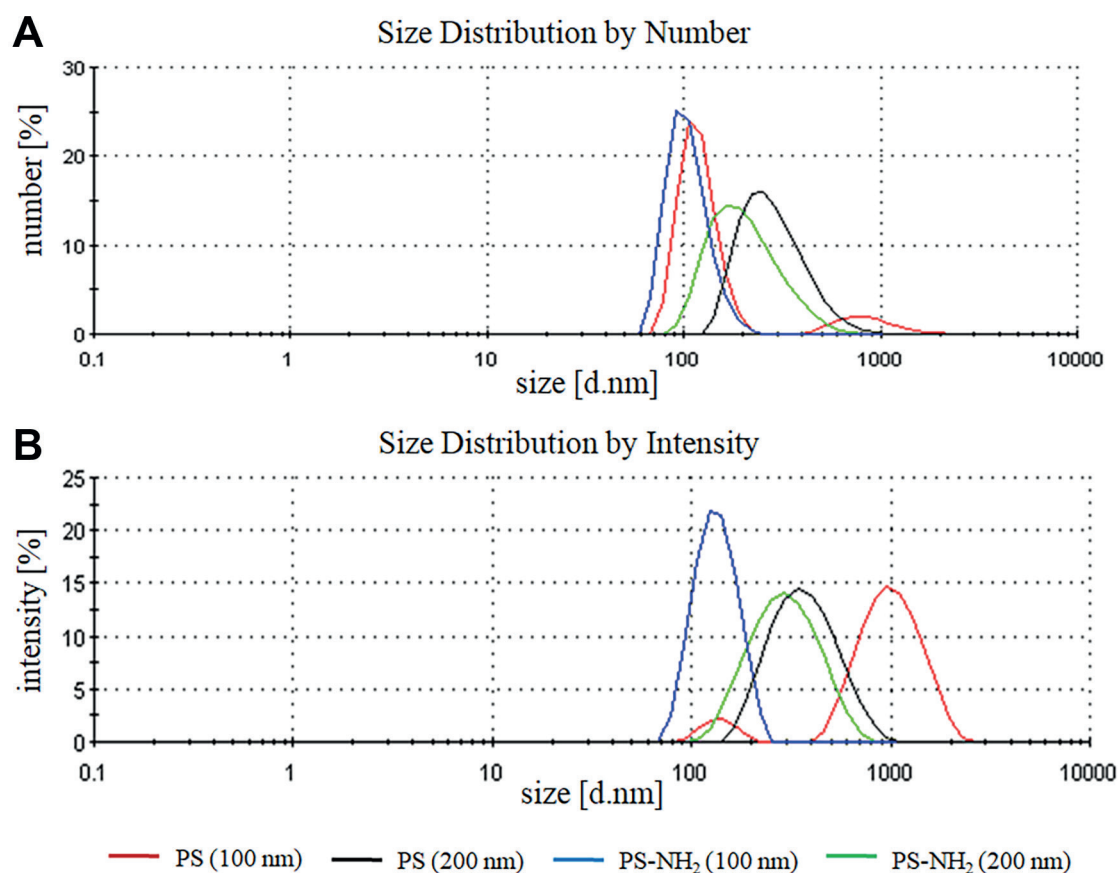


Fig. 1. Polystyrene (PS) size distribution by (A) number and (B) intensity in Dulbecco's modified Eagle's medium (DMEM; $C_{PS} = 100 \mu\text{g/mL}$, $\text{pH} = 7.4$)

Table 1. Polymers physicochemical characteristics (DMEM, $C_{PS} = 100 \mu\text{g/mL}$, $\text{pH} = 7.4$)

Polymer	Size by number [nm]	Size by intensity [nm]	PDI	ζ potential [mV]
PS (100-nm)	119.40 \pm 25.90	139.00 \pm 26.61	0.328	-22.08 \pm 0.68
PS (200-nm)	297.70 \pm 118.90	387.40 \pm 147.00	0.183	-31.18 \pm 1.06
PS-NH ₂ (100-nm)	106.70 \pm 26.69	135.40 \pm 32.44	0.250	-9.62 \pm 0.42
PS-NH ₂ (200-nm)	215.80 \pm 94.18	310.30 \pm 119.70	0.126	-15.73 \pm 0.72

DMEM – Dulbecco's modified Eagle's medium; PDI – polydispersity index; PS – polystyrene.

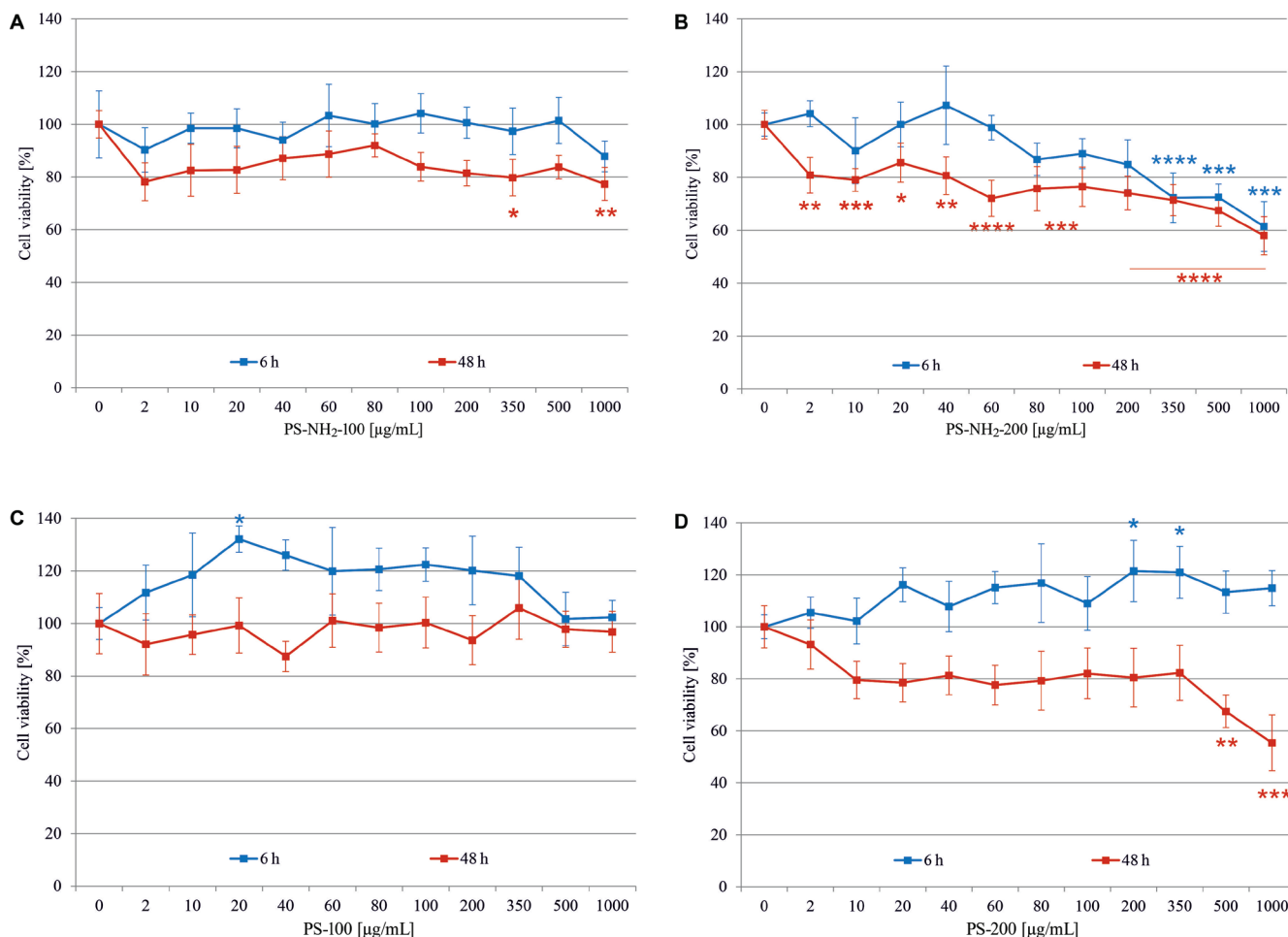


Fig. 2. The effect of different types of polystyrene (PS) particles on the viability of L6 cells. Cells were incubated for 6 h and 48 h with the indicated particle concentrations. Data are represented as the percentage of counted cells relative to the untreated control. Statistical significance was defined as * $p < 0.05$; ** $p < 0.01$; *** $p < 0.001$; **** $p < 0.0001$

more negative ζ -potential of -31.18 ± 1.06 mV (PS-200) and -22.08 ± 0.68 mV (PS-100) compared to amine-modified ones (-15.73 ± 0.72 mV (PS-NH₂-200) and -9.62 ± 0.42 mV (PS-NH₂-100)). This can be explained by the fact that the presence of amino groups causes their interactions with the medium. This confirms that the presence of -NH₂ groups in the system increases its tendency to combine into larger assemblies.²⁷ Moreover, both pristine and amine-functionalized PS particles show significantly lower stability when dispersed in DMEM than in 155 mmol/L NaCl, directly increasing the chances of the particles to form aggregates, which was shown in the case of 100-nm pristine PS.²²

The influence of submicron polymer particles on cell viability

The cytotoxic effect of submicron PS particles on rat L6 myotubes and H9c2 cardiomyocytes was assessed using MTT assay. Cells were incubated with native and amine-functionalized 2 sized PS molecules (100-nm and 200-nm) at concentrations ranging from 2 $\mu\text{g/mL}$ to 1000 $\mu\text{g/mL}$ for 6 h and 48 h. The results for the L6 cell line are presented in Fig. 2, and data obtained for the H9c2 line are collected in the Supplementary data.

As shown in Fig. 2A, incubation of the cells with PS-NH₂-100 did not induce cytotoxicity at least up

to concentrations of 350 $\mu\text{g/mL}$ and 1000 $\mu\text{g/mL}$ after 48 h of incubation. PS-NH₂-200 (Fig. 2B) exerted the most severe cytotoxic effect on L6 cells, especially after 48 h of treatment. The lowest dose of PS-NH₂-200 induced a mild cytotoxic impact reaching 80% cell viability. Incubation with increasing concentrations of PS-NH₂-200 (i.e., 350 $\mu\text{g/mL}$, 500 $\mu\text{g/mL}$ and 1000 $\mu\text{g/mL}$) exhibited more pronounced cytotoxic effects, approaching 28.6%, 32.5% and 42% non-viable cells after 48 h, respectively. Similarly, incubation for 6 h with the highest concentrations of PS-NH₂-200 led to a decrease in L6 cell survival, reaching from 27.7% to 38.5% of non-viable cells (Fig. 2B). This is presumably because particles containing amino groups in their structure affect cell signaling pathways, thereby influencing proliferation and accelerating the process of apoptosis.²⁸ Many biochemical processes describing signals from outside the cell leading to these changes have not yet been thoroughly investigated and reported in the literature.²⁹ Polystyrene particles containing -NH₂ groups with 100 nm in diameter affect cell proliferation to a lesser extent.

Moreover, PS-100 had a relatively low ability to limit cell viability and even had a growth-promoting effect after 6 h of incubation (Fig. 2C). Pristine 200-nm PS also had a growth-stimulatory impact at 6 h; however, a cytotoxic effect was observed for 500 $\mu\text{g/mL}$ and 1000 $\mu\text{g/mL}$ at 48 h (Fig. 2D). This is confirmed by a few *in vitro* studies where the cytotoxic effects of PS particles were compared in mammalian cell culture systems representing organs belonging to different potential entry pathways. It has been reported that amine-modified molecules show higher toxicity in various cell lines, inducing reactive oxygen species (ROS), cell death, the damage of mitochondria, and genotoxicity, while no cytotoxicity was observed with unmodified molecules.^{30–32}

On the other hand, H9c2 cardiomyocytes exposed to both unmodified or amine-modified PS nanoparticles showed significantly greater viability than L6 cells (Supplementary Fig. 1). The cytotoxic effect was observed solely for the highest concentration (1000 $\mu\text{g/mL}$) of tested PS nanoparticles, except PS-100, after 48 h of incubation.

Our results revealed that mainly 200-nm NH₂-modified nanoparticles induced severe toxicity after 48 h of incubation, albeit only to L6 cells. Moreover, the dose-dependent loss of viability was most pronounced in this case.

The influence of submicron polymer particles on the ζ potential of rat cells

The ELS experiment was intended to indicate possible changes in the ζ potential of rat cells treated with PS particles compared to the control samples. The measurements were performed after 6-h and 48-h incubation of L6 cells with PS particles. The effect of both pristine and amino-functionalized 100-nm and 200-nm PS particles on ζ of L6 cells in a function of pH of electrolyte (155 mmol/L NaCl) was analyzed. The data obtained for L6 cell line are presented in Fig. 3, 4, and for H9c2 cell line – in Supplementary

Fig. 2 and Supplementary Fig. 3. Furthermore, in the Supplementary data, a statistical analysis of the results obtained for L6 cell line treated with PS-NH₂ is presented (Supplementary Table 1 and Supplementary Table 2).

The profiles of all curves collected in Fig. 3 are similar: positive ζ values are observed in an acidic environment, and negative ζ values are observed in an alkaline environment. The most visible changes in the electrokinetic potential values were observed after exposure of the cells to PS-NH₂-100 (100 $\mu\text{g/mL}$) compared to untreated ones. After 6-h incubation (Fig. 3A), a decrease in ζ potential values was observed in acidic pH (pH = 2.5–4.5), where the ζ potential reached the highest value (compared to control) of 13.10 ± 0.74 mV. Slight changes in ζ in pH range of 6.5–10.0 were noted. In the same pH range, a more pronounced decrease in negative ζ value was observed after 48 h of exposure of skeletal muscle cells to PS-NH₂-100 particles (Fig. 3B). Furthermore, after both 6 h and 48 h of the cell's exposure to 100 $\mu\text{g/mL}$ PS-NH₂-200 particles, in an acidic pH (2.5–4.0) statistically significant changes in ζ potential values were noted (Supplementary Table 2). In general, due to the treatment of analyzed cells with both PS-NH₂-100 and PS-NH₂-200, more significant changes in ζ were observed after 48 h of incubation of the L6 cells with polymer particles, which may suggest that amine-modified PS particles do not penetrate the cell membrane after 48 h but adsorb on their surface. The surface charge is the parameter that can explain the changes occurring on the membrane surface. The surface of animal cell membranes is negatively charged as a result of the occurrence of, among others, sialic acid residues in membrane-building carbohydrate chains.³³ Cationic groups, such as amino groups, have been proven to interact with the negatively charged membrane.³⁴ The interactions lead to electrostatic attraction in the system and cause lysis of the cell membrane, allowing positively charged particles to penetrate the membranes more easily. Moreover, inert particles were found to penetrate the membrane to a lesser extent.^{34,35}

The effect of PS-100 and PS-200 on the ζ potential of L6 cells in a function of pH was also analyzed; experimental curves are presented in Fig. 4. The profiles of curves presented in Fig. 4 are similar to those obtained for PS-NH₂ particles (Fig. 3). Based on the data obtained, it was concluded that no statistically relevant alterations were observed in the ζ potential of the cells over the entire pH range for the PS-200 treatment. However, incubations of the cells with PS-100 lead to slight changes in ζ potential values both in acidic and basic pH after 6 h and in acidic media after 48 h. It is worth noting, however, that changes in a strongly acidic environment can be due to the membrane structure destruction caused by the concentration of H₃O⁺ ions.

The electrokinetic potential depends on the level of ionization of functional groups of particles like amino groups (-NH₂).³⁶ On the other hand, the degree of ionization of amino groups depends on the pH and ionic strength of the electrolyte. The amino groups are positively charged

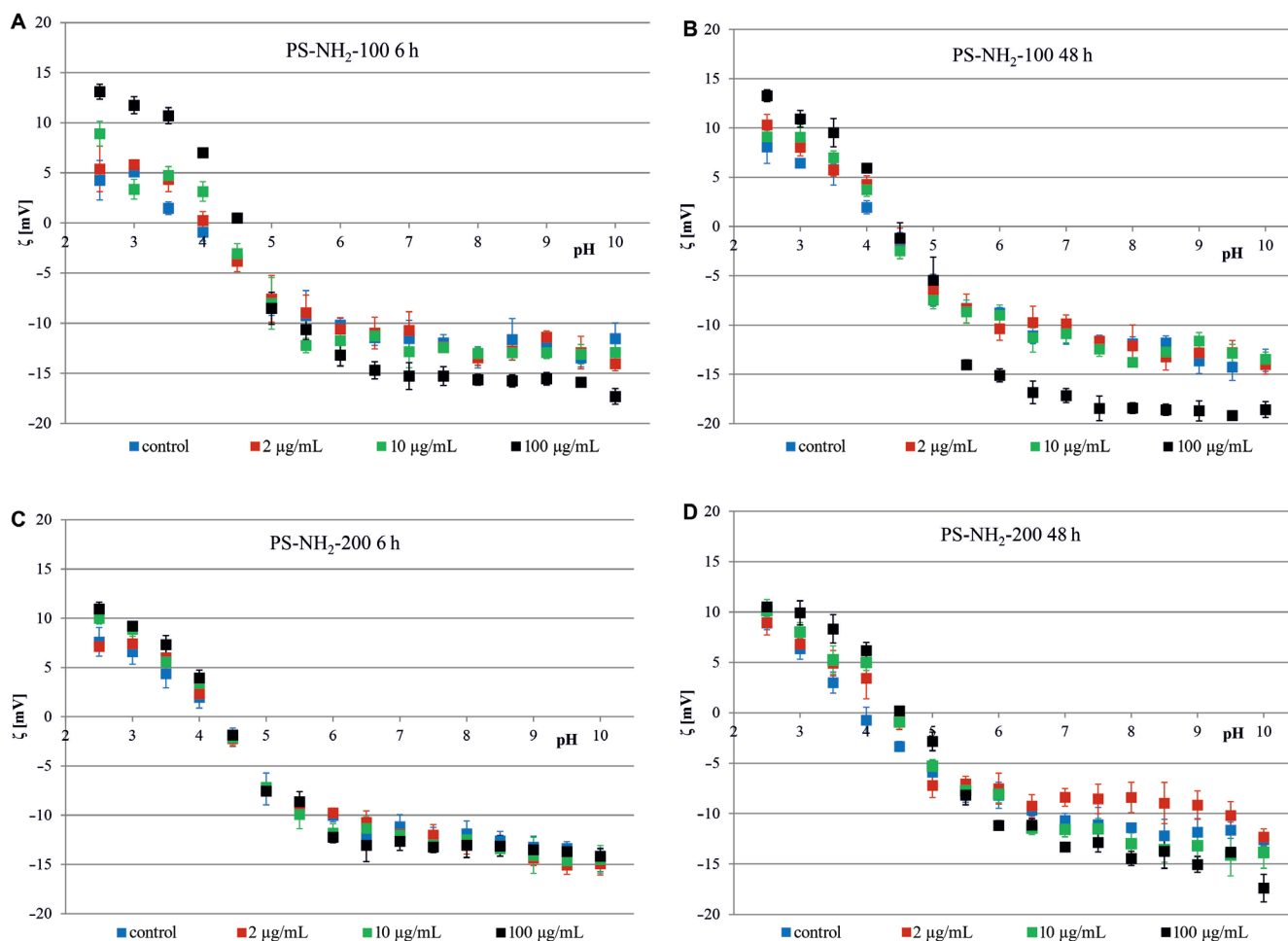


Fig. 3. The zeta (ζ) potential of L6 cells as a function of the pH of the electrolyte solution. Control cells and cells treated with 2 $\mu\text{g/mL}$, 10 $\mu\text{g/mL}$ and 100 $\mu\text{g/mL}$ of polystyrene (PS) and after various times of incubation of the cells in the presence of polymer particles: A. PS-NH₂-100, 6 h; B. PS-NH₂-100, 48 h; C. PS-NH₂-200, 6 h; and (D) PS-NH₂-200, 48 h. Statistical analysis is presented in Supplementary Table 1

(-NH₃⁺) at pH below the isoelectric point. Above the isoelectric point, the groups become largely neutral (-NH₂), and ζ tends to decrease as the OH⁻ ions begin to react with the neutral amino groups, leading to a negative charge in the solution.^{37,38} Such variations cause variations in ζ values due to electrostatic shielding and the binding ion effect.³⁹

Interactions of polymer particles with cell membranes are an extremely complex phenomenon that depends on the size and shape of particles, the surface composition of the components that make up the system, or the surface charge that forms on membrane surfaces.^{37,38} Various behaviors of PS particles in relation to biological structures have been described in the literature. Polymers can interact with each other by several mechanisms, such as hydrogen bonds, hydrophobic interactions or van der Waals forces.^{40,41}

Conclusions

Nowadays, there is a strong necessity to understand how polymer particles affect the properties of living cells. The physicochemical properties of nanomaterials, including

polymers, contribute to their behavior within the biological milieu. Surface charge and particle size are the most frequently cited factors responsible for various biological effects of nanoparticles, including toxicity or cellular uptake. We have shown that PS particles influence rat cardiomyocytes and myotubes' viability and ζ potential. Moreover, our studies indicate that the polymer particles' size and surface modifications (amine-functionalized) define the extent to which they influence the physicochemical behavior of cell membranes. The results also depend on the polymer particle concentration and the time the cells are incubated with PS. It should be emphasized that, in recent years, studies on the influence of submicron polymer particles on laboratory animals are becoming more frequent. Polymer molecules can overcome the organism's barriers and therefore penetrate and accumulate in organs and tissues. The physicochemical properties, surface modifications of PS submicron particles and their large surface area promote their interaction with cell membranes, leading to internalization of the polymer by cells. We hope that our research may provide evidence for the behavior of the PS particles in rat cells, and contribute to a better understanding of their potential

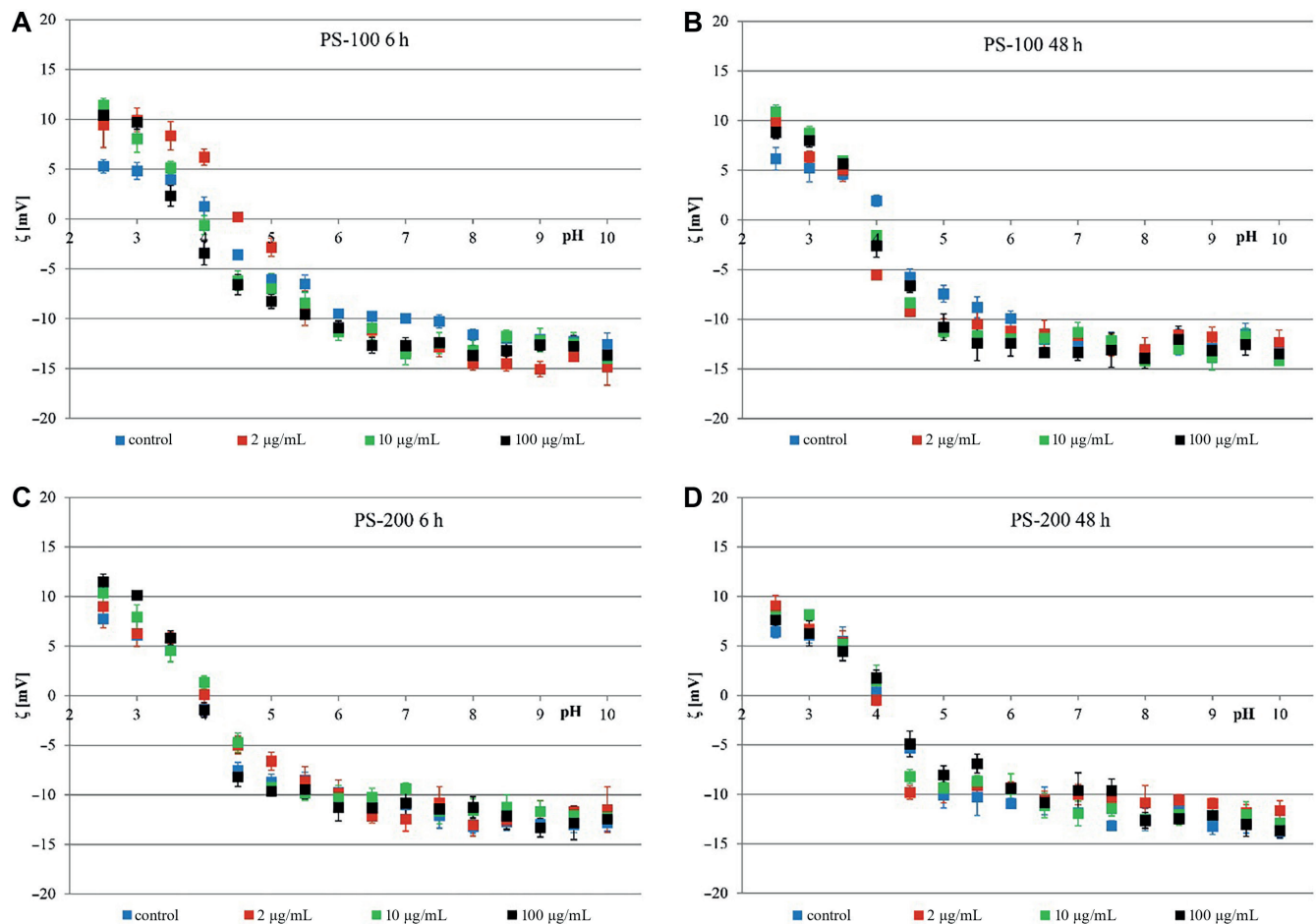


Fig. 4. The zeta (ζ) potential of L6 cells as a function of the pH of the electrolyte solution. Control cells and cells treated with 2 $\mu\text{g/mL}$, 10 $\mu\text{g/mL}$ and 100 $\mu\text{g/mL}$ of polystyrene (PS) and after various times of incubation of the cells in the presence of polymer particles: A. PS-100, 6 h; B. PS-100, 48 h; C. PS-200, 6 h; and (D) PS-200, 48 h. Statistical analysis is presented in Supplementary Table 2

harm to organisms to avoid the risk of some diseases. Nevertheless, more in-depth studies are needed to further elucidate the mechanisms of interaction between PS particles and the cell membrane of animals.

Supplementary data

The Supplementary materials are available at <https://doi.org/10.5281/zenodo.10401147>. The package includes the following files:

Supplementary Fig. 1. The effect of different PS particles on the viability of H9c2 cells.

Supplementary Fig. 2. The ζ potential of H9c2 cells treated with amine-functionalized PS particles in a function of pH.

Supplementary Fig. 3. The ζ potential of H9c2 cells treated with pristine PS particles in a function of pH.

Supplementary Table 1. The ζ potential of the L6 cells after exposure to PS-NH2-100. Measurements were performed after 6 h and 48 h.

Supplementary Table 2. The ζ potential of the L6 cells after exposure to PS-NH2-200. Measurements were performed after 6 h and 48 h.

Data availability

The datasets generated and/or analyzed during the current study are available from the corresponding author on reasonable request.

Consent for publication

Not applicable.

ORCID iDs

Joanna Kotyńska <https://orcid.org/0000-0003-2532-4856>

Marcin Zajac <https://orcid.org/0000-0002-8934-4218>

Agnieszka Mikłosz <https://orcid.org/0000-0003-4936-3120>

Adrian Chabowski <https://orcid.org/0000-0002-7407-8156>

Monika Naumowicz <https://orcid.org/0000-0001-5229-1805>

References

1. Tabasum S, Younas M, Zaeem MA, et al. A review on blending of corn starch with natural and synthetic polymers, and inorganic nanoparticles with mathematical modeling. *Int J Biol Macromol.* 2019;122: 969–996. doi:10.1016/j.ijbiomac.2018.10.092
2. Sol D, Laca A, Laca A, Diaz M. Approaching the environmental problem of microplastics: Importance of WWTP treatments. *Sci Total Environ.* 2020;740:140016. doi:10.1016/j.scitotenv.2020.140016

3. Prata JC, Silva ALP, Da Costa JP, et al. Solutions and integrated strategies for the control and mitigation of plastic and microplastic pollution. *Int J Environ Res Public Health*. 2019;16(13):2411. doi:10.3390/ijerph16132411
4. Dharmaraj S, Ashokkumar V, Pandiyan R, et al. Pyrolysis: An effective technique for degradation of COVID-19 medical wastes. *Chemosphere*. 2021;275:130092. doi:10.1016/j.chemosphere.2021.130092
5. Ho BT, Roberts TK, Lucas S. An overview on biodegradation of polystyrene and modified polystyrene: The microbial approach. *Crit Rev Biotechnol*. 2018;38(2):308–320. doi:10.1080/07388551.2017.1355293
6. Manivannan B, Eltzov E, Borisover M. Submicron polymer particles may mask the presence of toxicants in wastewater effluents probed by reporter gene containing bacteria. *Sci Rep*. 2021;11(1):7424. doi:10.1038/s41598-021-86672-7
7. Xu B, Liu F, Cryder Z, et al. Microplastics in the soil environment: Occurrence, risks, interactions and fate. A review. *Crit Rev Environ Sci Technol*. 2020;50(21):2175–2222. doi:10.1080/10643389.2019.1694822
8. Andrady AL. The plastic in microplastics: A review. *Mar Pollut Bull*. 2017;119(1):12–22. doi:10.1016/j.marpolbul.2017.01.082
9. Cai M, He H, Liu M, et al. Lost but can't be neglected: Huge quantities of small microplastics hide in the South China Sea. *Sci Total Environ*. 2018;633:1206–1216. doi:10.1016/j.scitotenv.2018.03.197
10. Wang T, Li B, Zou X, et al. Emission of primary microplastics in mainland China: Invisible but not negligible. *Water Res*. 2019;162:214–224. doi:10.1016/j.watres.2019.06.042
11. Chen G, Feng Q, Wang J. Mini-review of microplastics in the atmosphere and their risks to humans. *Sci Total Environ*. 2020;703:135504. doi:10.1016/j.scitotenv.2019.135504
12. Di Renzo L, Mascilongo G, Berti M, et al. Potential impact of microplastics and additives on the health status of loggerhead turtles (*Caretta caretta*) stranded along the Central Adriatic Coast. *Water Air Soil Pollut*. 2021;232(3):98. doi:10.1007/s11270-021-04994-8
13. Sequeira IF, Prata JC, Da Costa JP, Duarte AC, Rocha-Santos T. Worldwide contamination of fish with microplastics: A brief global overview. *Mar Pollut Bull*. 2020;160:111681. doi:10.1016/j.marpolbul.2020.111681
14. Kannan K, Vimalkumar K. A review of human exposure to microplastics and insights into microplastics as obesogens. *Front Endocrinol (Lausanne)*. 2021;12:724989. doi:10.3389/fendo.2021.724989
15. Prata JC, Da Costa JP, Lopes I, Duarte AC, Rocha-Santos T. Environmental exposure to microplastics: An overview on possible human health effects. *Sci Total Environ*. 2020;702:134455. doi:10.1016/j.scitotenv.2019.134455
16. Sangkham S, Faikhaw O, Munkong N, et al. A review on microplastics and nanoplastics in the environment: Their occurrence, exposure routes, toxic studies, and potential effects on human health. *Mar Pollut Bull*. 2022;181:113832. doi:10.1016/j.marpolbul.2022.113832
17. Verma A, Stellacci F. Effect of surface properties on nanoparticle-cell interactions. *Small*. 2010;6(1):12–21. doi:10.1002/smll.200901158
18. Smith JR, Bolton ER, Dwinell MR. The rat: A model used in biomedical research. *Methods Mol Biol*. 2018;2018:1–41. doi:10.1007/978-1-4939-9581-3_1
19. Wang ML, Hauschka PV, Tuan RS, Steinbeck MJ. Exposure to particles stimulates superoxide production by human THP-1 macrophages and avian HD-11EM osteoclasts activated by tumor necrosis factor- α and PMA. *J Arthroplasty*. 2002;17(3):335–346. doi:10.1054/arth.2002.30416
20. Lowry GV, Hill RJ, Harper S, et al. Guidance to improve the scientific value of zeta-potential measurements in nanoEHS. *Environ Sci Nano*. 2016;3(5):953–965. doi:10.1039/C6EN00136J
21. Marsalek R, Kotyrba M, Volna E, Jarusek R. Neural network modeling for prediction of zeta potential. *Mathematics*. 2021;9(23):3089. doi:10.3390/math9233089
22. Zając M, Kotyńska J, Worobiczuk M, Breczko J, Naumowicz M. The effect of submicron polystyrene on the electrokinetic potential of cell membranes of red blood cells and platelets. *Membranes (Basel)*. 2022;12(4):366. doi:10.3390/membranes12040366
23. Souza TGF, Ciminelli VST, Mohallem NDS. A comparison of TEM and DLS methods to characterize size distribution of ceramic nanoparticles. *J Phys Conf Ser*. 2016;733:012039. doi:10.1088/1742-6596/733/1/012039
24. Clogston JD, Patri AK. Zeta potential measurement. *Methods Mol Biol*. 2011;2011:63–70. doi:10.1007/978-1-60327-198-1_6
25. Esteban PP, Jenkins ATA, Arnot TC. Elucidation of the mechanisms of action of Bacteriophage K/nano-emulsion formulations against *S. aureus* via measurement of particle size and zeta potential. *Colloids Surf Biointerfaces*. 2016;139:87–94. doi:10.1016/j.colsurfb.2015.11.030
26. Li X, He E, Xia B, et al. Impact of CeO₂ nanoparticles on the aggregation kinetics and stability of polystyrene nanoplastics: Importance of surface functionalization and solution chemistry. *Water Res*. 2020;186:116324. doi:10.1016/j.watres.2020.116324
27. Bagwe RP, Hilliard LR, Tan W. Surface modification of silica nanoparticles to reduce aggregation and nonspecific binding. *Langmuir*. 2006;22(9):4357–4362. doi:10.1021/la052797j
28. Hochreiter R, Weiger TM, Colombatto S, et al. Long chain diamines inhibit growth of C6 glioma cells according to their hydrophobicity: An in vitro and molecular modeling study. *Naunyn Schmiedeberg Arch Pharmacol*. 2000;361(3):235–246. doi:10.1007/s002109900188
29. Hegemann D, Hanselmann B, Guimond S, Fortunato G, Giraud MN, Guex AG. Considering the degradation effects of amino-functional plasma polymer coatings for biomedical application. *Surf Coat Technol*. 2014;255:90–95. doi:10.1016/j.surfcoat.2014.01.054
30. Anguissola S, Garry D, Salvati A, O'Brien PJ, Dawson KA. High content analysis provides mechanistic insights on the pathways of toxicity induced by amine-modified polystyrene nanoparticles. *PLoS One*. 2014;9(9):e108025. doi:10.1371/journal.pone.0108025
31. Busch T, Bruce-Clark P, Derwall J, et al. Impact investments: A call for (re)orientation. *SN Bus Econ*. 2021;1(2):33. doi:10.1007/s43546-020-00033-6
32. Schröter L, Ventura N. Nanoplastic toxicity: Insights and challenges from experimental model systems. *Small*. 2022;18(31):2201680. doi:10.1002/smll.202201680
33. Loufakis DN, Cao Z, Ma S, Mittelman D, Lu C. Focusing of mammalian cells under an ultrahigh pH gradient created by unidirectional electropulsion in a confined microchamber. *Chem Sci*. 2014;5(8):3331–3337. doi:10.1039/C4SC00319E
34. Rojanasakul Y, Wang L, Bhat M, Glover DD, Malanga CJ, Ma JKH. The transport barrier of epithelia: A comparative study on membrane permeability and charge selectivity in the rabbit. *Pharm Res*. 1992;9(8):1029–1034. doi:10.1023/A:1015802427428
35. Bandi SP, Kumbhar YS, Venuganti VVK. Effect of particle size and surface charge of nanoparticles in penetration through intestinal mucus barrier. *J Nanopart Res*. 2020;22(3):62. doi:10.1007/s11051-020-04785-y
36. Sriprabhom J, Luangpituksa P, Wongkongkatep J, Pongtharangkul T, Suphantharika M. Influence of pH and ionic strength on the physical and rheological properties and stability of whey protein stabilized o/w emulsions containing xanthan gum. *J Food Eng*. 2019;242:141–152. doi:10.1016/j.jfoodeng.2018.08.031
37. Chambers E, Mitragotri S. Prolonged circulation of large polymeric nanoparticles by non-covalent adsorption on erythrocytes. *J Control Release*. 2004;100(1):111–119. doi:10.1016/j.jconrel.2004.08.005
38. Dwivedi MV, Harishchandra RK, Koshkina O, Maskom M, Galla HJ. Size influences the effect of hydrophobic nanoparticles on lung surfactant model systems. *Biophys J*. 2014;106(1):289–298. doi:10.1016/j.bpj.2013.10.036
39. Kulmyrzaev AA, Schubert H. Influence of KCl on the physicochemical properties of whey protein stabilized emulsions. *Food Hydrocolloids*. 2004;18(1):13–19. doi:10.1016/S0268-005X(03)00037-7
40. Geiser M, Rothen-Rutishauser B, Kapp N, et al. Ultrafine particles cross cellular membranes by nonphagocytic mechanisms in lungs and in cultured cells. *Environ Health Perspect*. 2005;113(11):1555–1560. doi:10.1289/ehp.8006
41. Rothen-Rutishauser BM, Schürch S, Haenni B, Kapp N, Gehr P. Interaction of fine particles and nanoparticles with red blood cells visualized with advanced microscopic techniques. *Environ Sci Technol*. 2006;40(14):4353–4359. doi:10.1021/es0522635

L version of the transformed Kedem–Katchalsky equations for membrane transport of electrolyte solutions and internal energy conversion

Wersja L przekształconych równań Kedem-Katchalskiego dla membranowego transportu roztworów elektrolitów oraz transformacji energii wewnętrznej

Andrzej Ślęzak^{1,A–F}, Sławomir M. Grzegorzczyn^{2,E,F}

¹ Collegium Medicum, Jan Długosz University, Częstochowa, Poland

² Department of Biophysics, Faculty of Medical Sciences in Zabrze, Medical University of Silesia, Poland

A – research concept and design; B – collection and/or assembly of data; C – data analysis and interpretation; D – writing the article; E – critical revision of the article; F – final approval of the article

Polymers in Medicine, ISSN 0370-0747 (print), ISSN 2451-2699 (online)

Polim Med. 2024;54(1):45–57

Address for correspondence

Sławomir M. Grzegorzczyn

E-mail: grzegorzczyn@sum.edu.pl

Funding sources

None declared

Conflict of interest

None declared

Received on November 22, 2023

Reviewed on November 26, 2023

Accepted on November 27, 2023

Published online on February 2, 2024

Cite as

Ślęzak A, Grzegorzczyn SM. L version of the transformed Kedem–Katchalsky equations for membrane transport of electrolyte solutions and internal energy conversion. *Polim Med.* 2024;54(1):45–57. doi:10.17219/pim/175949

DOI

10.17219/pim/175949

Copyright

Copyright by Author(s)

This is an article distributed under the terms of the Creative Commons Attribution 3.0 Unported (CC BY 3.0) (<https://creativecommons.org/licenses/by/3.0/>)

Abstract

Background. One of the important formalisms of non-equilibrium thermodynamics is Peusner network thermodynamics. The description of the energy conversion in membrane processes, i.e., the conversion of the internal energy of the system into the dissipated energy and the free energy used for the work associated with the transport of solution components, allows us to describe the relationship between these energies and the thermodynamic forces acting in the membrane system.

Objectives. The aim of this study was to develop a procedure to transform the Kedem–Katchalsky equations for the transport of binary electrolytic solutions across a membrane into the Kedem–Katchalsky–Peusner equations based on Peusner network thermodynamics. The conversion of electrochemical energy to free energy in the membrane system was also determined.

Materials and methods. The nanobiocellulose biomembranes (Biofill) were the subject of the study with experimentally determined transport parameters for aqueous NaCl solutions. The research method is the Kedem–Katchalsky–Peusner formalism for binary electrolyte solutions with introduced Peusner coefficients.

Results. The coefficients of the L version of the membrane transport equations and the Peusner coupling coefficients were derived as functions of NaCl concentration in the membrane. Based on these coefficients, the fluxes of internal energy of the system, energy dissipated to the surroundings and free energy related to the transport of electrolyte across the membrane were calculated and presented as functions of the osmotic and electric forces on the membrane.

Conclusions. The Peusner coefficients obtained from the transformations of the coefficients of the Kedem–Katchalsky formalism for the transport of electrolyte solutions through the Biofill membrane were used to calculate the coupling coefficients of the membrane processes and the dissipative energy flux. The dissipative energy flux takes the form of a quadratic form due to the thermodynamic forces on the membrane – second degree curves are obtained. Moreover, the dissipative energy flux as a function of thermodynamic forces allowed us to examine the energy conversion in transport processes in the membrane system.

Key words: membrane transport, Kedem–Katchalsky–Peusner equations, bacterial cellulose membrane, Peusner transport coefficients, internal energy conversion

Streszczenie

Wprowadzenie. Jednym z ważnych formalizmów termodynamiki nierównowagowej jest termodynamika sieciowa Peusnera. Opis transformacji energii w procesach membranowych t.j. energii wewnętrznej układu na energię dyssypowaną w otoczeniu i swobodną wykorzystywaną na pracę związaną z transportem składników roztworu pozwala uchwycić związek tych energii z siłami termodynamicznymi działającymi w układzie membranowym.

Cel pracy. Celem pracy było opracowanie procedury transformacji równań Kedem–Katchalsky’ego dla transportu binarnych roztworów elektrolitycznych przez membranę do równań Kedem–Katchalsky’ego–Peusnera w oparciu o formalizm termodynamiki sieciowej Peusnera. Ponadto, określono konwersję energii elektrochemicznej do energii swobodnej w układzie membranowym.

Materiał i metody. Przedmiotem badań były biomembrany nanobiocelulozowe (Biofill) o eksperymentalnie wyznaczonych parametrach transportu dla wodnych roztworów NaCl. Metodą badawczą jest formalizm Kedem–Katchalsky’ego–Peusnera dla binarnych roztworów elektrolitów, z wprowadzonymi współczynnikami Peusnera.

Wyniki. Współczynniki wersji L równań transportu oraz współczynniki sprzężenia Peusnera zostały wyprowadzone jako zależne od stężenia NaCl w membranie. W oparciu o te współczynniki wyliczone zostały strumienie energii wewnętrznej układu, energii dyssypowanej w otoczeniu i energii swobodnej związanej z transportem elektrolitu przez membranę i przedstawione jako funkcje termodynamicznych bodźców na membranie: stężeniowego i elektrycznego.

Wnioski. Otrzymane współczynniki Peusnera z przekształceń współczynników formalizmu Kedem–Katchalsky’ego dla transportu roztworów elektrolitowych przez membranę Biofill posłużyły do obliczenia współczynników sprzężenia procesów membranowych oraz obliczenia strumienia energii dyssypatywnej. Strumień energii dyssypatywnej przyjmuje postać formy kwadratowej od bodźców termodynamicznych na membranie – krzywe drugiego stopnia. Ponadto, strumień energii dyssypatywnej jako funkcja bodźców termodynamicznych pozwolił zbadać konwersję energii w procesach transportowych w układzie membranowym.

Słowa kluczowe: transport membranowy, równania Kedem–Katchalsky’ego–Peusnera, membrana z celulozy bakteryjnej, współczynniki transportu Peusnera, konwersja energii wewnętrznej

Background

Membrane transport is one of the fundamental non-equilibrium processes that occur at all levels of organization of all physicochemical systems, including biological systems.¹ Many of these processes can be carried out on a different scale in physicochemical systems containing artificial polymeric membranes.² The study of membrane transport processes in such systems is important in many areas of human activity of a cognitive and utilitarian nature, e.g., in science, technology and biomedicine.^{3,4} The controlled drug release systems, membrane dressings to support the healing of chronic wounds, bioreactors for testing strategies to combat bacterial infections using lytic phage application in combination with established and novel antibacterial agents, etc.,^{4,5} are the main examples of biomedical applications. In these systems, the membrane is a selective barrier that ensures the separation of the phases it separates. This role is played by polymeric membranes of various structure and composition, made of polyvinyl chloride, bacterial cellulose, graphene cellulose acetate, etc.^{3–9}

The physical quantity that characterizes non-equilibrium systems is thermodynamic entropy (S-entropy).^{10,11} It plays a fundamental role in the study of non-equilibrium processes, since it numerically characterizes the degree of irreversibility of physico-chemical processes, including biological processes. It is well-known that these processes are subject to the law of entropy growth. Accordingly,

the production of S-entropy is a consequence of irreversible processes of mass, charge, energy, and momentum transport in various types of systems, including membrane systems.¹¹

Formalisms and research tools developed in the context of non-equilibrium thermodynamics and/or network thermodynamics have been used to describe membrane transport.^{12,13} These methods include the Kedem–Katchalsky (K–K)¹² and Kedem–Katchalsky–Peusner (K–K–P)¹³ formalisms, along with modifications and extensions.^{14–19} The starting point for deriving the equations for membrane transport and also energy conversion is the determination of the energy dispersion function, which is the product of entropy production and absolute temperature.^{12,13} The temporal change in entropy production is reflected in disease processes and in the aging processes of biological organisms.^{10,20}

Previous studies have presented procedures for transforming the classical equations into *L*, *R*, *H* and *P* versions using Peusner network thermodynamics methods for membrane transport of homogeneous or heterogeneous non-electrolyte solutions.^{16–19,21} Chemical energy conversion procedures using *L*, *R*, *H* and *P* versions of the transformed K–K equations are presented. These procedures use thermodynamic forces (hydrostatic pressure and osmotic pressure gradients) and volume and solute fluxes. In this study, in addition to the above forces and fluxes, the electrical potential difference and the ionic flux were used.

Accordingly, the purpose of this paper is to develop a procedure for transforming the K–K equations for

binary electrolyte solutions into the K–K–P equations using the formalism developed in the context of Peusner's network thermodynamics. Using the obtained L -version of the K–K–P equations, a method was developed to evaluate the conversion of electrochemical energy into free energy in a membrane system containing aqueous electrolyte solutions with a concentration field and an electric field superimposed on them. The 1st part of this paper is an introduction. The 2nd part presents the procedure for deriving L -versions of the K–K–P equations describing the membrane transport of homogeneous electrolyte solutions and the equations representing L -versions of the transport parameters L_{ij} of the coupling coefficients l_{ij} and $(Q_L)_{ij}$ and the energy conversion efficiency coefficient $[(e_{ij})_L]_{max}$, where $(i, j \in \{1, 2, 3\})$. In this section, we also present mathematical equations for the S -energy dissipation function $(\Phi_S)_L$ derived from the K–K–P formalism describing the energy dissipation function as a function of thermodynamic forces. The equations obtained were used to calculate the characteristics: $(\Phi_S)_L = f[(\Delta P - \Delta\pi_s), (\Delta\pi_s/C_s), E]$, $[(\Phi_F)_L]_{ij} = f[(\Delta P - \Delta\pi_s), (\Delta\pi_s/C_s), E]$, and $[(\Phi_{U})_L]_{ij} = f[(\Delta P - \Delta\pi_s), (\Delta\pi_s/C_s), E]$, based on the characteristics $L_{ij} = f(C_s)$ and $l_{ij} = f(C_s)$, for the bacterial cellulose membrane Biofill. The values of the coupling parameter and the coefficient of energy conversion efficiency $[(e_{ij})_L]_{max}$ were used to evaluate electrochemical energy conversion.

Materials and methods

Membrane system

The membrane transport measurement system is illustrated schematically in Fig. 1. This system consists of a membrane (M), located in the vertical plane and separating 2 aqueous NaCl solutions with concentrations at the initial moment C_h and $C_l = \text{const.}$ ($C_h \geq C_l$). The density of solutions with concentrations of C_h and C_l fulfilled the condition $P_h \leq P_l = \text{constant}$. In this system there are 3 driving forces ($\Delta P = P_h - P_l$, $\Delta\pi = RT(C_h - C_l)$, $E = E_h - E_l$), which generate 3 fluxes (J_v, J_s, I).

According to the K–K formalism, the transport parameters of a membrane are determined by 6 coefficients: hydraulic permeability (L_p), reflection (σ_s), diffusion permeability (ω_s), electroosmotic permeability (β), transference number (τ_c), and conductance (κ).

L -version of the Kedem–Katchalsky–Peusner equations for electrolyte solutions

The L -versions of the K–K–P equations for homogeneous electrolyte solutions are obtained by appropriate transformation of the classical K–K equations.¹² Two alternative sets of these equations can be used for this purpose. In this study, the following form of these equations is used:

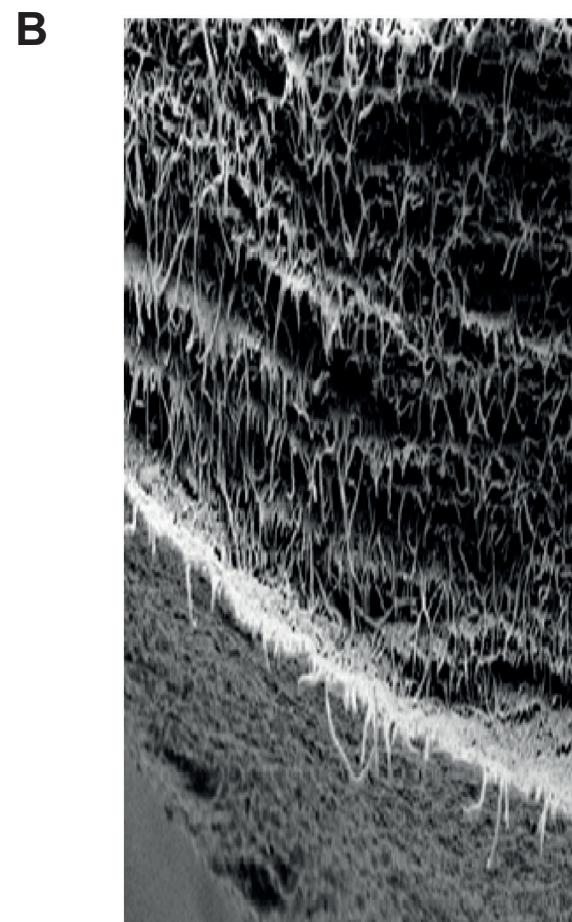
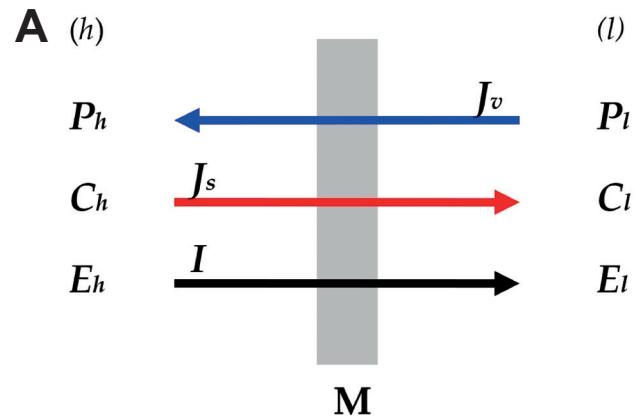


Fig. 1. A. Model of a single-membrane system; M – membrane; P_h and P_l – mechanical pressures; C_h and C_l – total solution concentrations ($C_h > C_l$); C_s^A , J_v – volume flux; J_s – solute flux; I – ionic electric current; E_h and E_l – electrode potentials; B. Cross-sectional image of the Biofill membrane obtained with a scanning microscope at $\times 10,000$ magnification

$$J_v = L_p [(\Delta P - \Delta\pi_i) - \sigma_s \Delta\pi_s + \beta I] \quad (1)$$

$$J_s = C_s (1 - \sigma_s) J_v + \omega_s \Delta\pi_s + \frac{\tau_c}{z_c F} I \quad (2)$$

$$I = \kappa \left(\frac{\tau_c}{z_c F} \frac{\Delta\pi_s}{C_s} - \beta J_v + E \right) \quad (3)$$

where: L_p – hydraulic permeability coefficient, σ_s – reflection coefficient, ω_s – coefficient of diffusion permeability,

J_v – volume flux, J_s – solute flux, I – ionic electric current, $\Delta\pi = RT\Delta C$ – osmotic pressure difference, RT – the product of the gas constant and the absolute temperature, $\Delta C = C_h - C_l$ ($C_h > C_l$) – concentration difference on the membrane, $C_s = (C_h - C_l)(\ln C_h C_l^{-1})^{-1} = \Delta\pi(RT \ln C_h C_l^{-1})^{-1}$ – average concentration of the solution in the membrane, $\Delta\pi_i$ – osmotic pressure difference generated by solute molecules that do not penetrate the membrane, E – the potential difference across the membrane, β – electroosmotic permeability coefficient, τ_c – transference number, F – Faraday constant, and κ – the conductance coefficient.

The phenomenological coefficients appearing in equations (1)–(3) are defined by the following expressions:

$$L_p = \left(\frac{\tau_c}{\Delta P - \Delta\pi_i} \right)_{\Delta\pi_s=0, I=0} \quad (4)$$

$$\sigma_s = \left(\frac{\Delta P - \Delta\pi_i}{\Delta\pi_s} \right)_{J_v=0, I=0} \quad (5)$$

$$\omega_s = \left(\frac{J_s}{\Delta\pi_s} \right)_{J_v=0, I=0} \quad (6)$$

$$\beta = \frac{1}{L_p} \left(\frac{J_v}{I} \right)_{\Delta P - \Delta\pi_i=0, \Delta\pi_s=0} \quad (7)$$

$$\kappa = \left(\frac{I}{E} \right)_{J_v=0, \Delta\pi_s=0} \quad (8)$$

$$\kappa = z_c F \left(\frac{J_s}{I} \right)_{J_v=0, \Delta\pi_s=0} \quad (9)$$

To obtain the L -version of the K–K–P equations for electrolyte solutions, we will transform Equations (1)–(3) using Peusner's network thermodynamics methods. Considering Equations (2) and (3) in Equation (1), we get the L -version of Equation (1):

$$J_v = L_{11}(\Delta P - \Delta\pi_s) + L_{12} \frac{\Delta\pi_s}{C_s} + L_{13}E \quad (10)$$

$$\text{where } L_{11} = \frac{L_p}{1 + L_p\beta^2\kappa}, \quad L_{12} = \frac{L_p[\beta\tau_c\kappa + C_s(1 - \sigma_s)z_cF]}{z_cF(1 + L_p\beta^2\kappa)},$$

$$L_{13} = \frac{\kappa\beta L_p}{1 + L_p\beta^2\kappa}.$$

In turn, considering Equations (10) and (3) in Equation (2), we get the L -version of Equation (2):

$$J_s = L_{21}(\Delta P - \Delta\pi_s) + L_{22} \frac{\Delta\pi_s}{C_s} + L_{23}E \quad (11)$$

$$\text{where } L_{21} = \frac{L_p[C_s(1 - \sigma_s)z_cF + \beta\tau_c\kappa]}{z_cF(1 + L_p\beta^2\kappa)},$$

$$L_{22} = \frac{C_s z_s^2 F^2 [\omega_s(1 + L_p\beta^2\kappa) + L_p C_s(1 - \sigma_s)^2] + \tau_c^2 \kappa}{z_c^2 F^2 (1 + L_p\beta^2\kappa)},$$

$$L_{23} = \frac{\kappa[\tau_c + C_s(1 - \sigma_s)z_c F L_p \beta]}{z_c^2 F^2 (1 + L_p\beta^2\kappa)}$$

To get the L version of Equation (3), one must transform Equation (3) with Equation (10). As a result of these operations, we get:

$$I = L_{31}(\Delta P - \Delta\pi_s) + L_{32} \frac{\Delta\pi_s}{C_s} + L_{33}E \quad (12)$$

$$\text{where } L_{31} = \frac{L_p\beta\kappa}{1 + L_p\beta^2\kappa}, \quad L_{32} = \frac{\kappa[\tau_c - L_p\beta C_s(1 - \sigma_s)z_cF]}{z_cF(1 + L_p\beta^2\kappa)},$$

$$L_{33} = \frac{\kappa}{1 + L_p\beta^2\kappa}.$$

Equations (10)–(12) can also be written in a matrix form:

$$\begin{bmatrix} J_v \\ J_s \\ I \end{bmatrix} = \begin{bmatrix} L_{11} & L_{12} & L_{13} \\ L_{21} & L_{22} & L_{23} \\ L_{31} & L_{32} & L_{33} \end{bmatrix} \begin{bmatrix} \Delta P - \Delta\pi_s \\ \frac{\Delta\pi_s}{C_s} \\ E \end{bmatrix} = [L] \begin{bmatrix} \Delta P - \Delta\pi_s \\ \frac{\Delta\pi_s}{C_s} \\ E \end{bmatrix} \quad (13)$$

where: $[L]$ is a matrix of Peusner coefficients L_{ij} ($i, j \in \{1, 2, 3\}$) for binary homogeneous electrolyte solutions. Equations (11)–(13) are one of the forms of the K–K equations obtained by means of the symmetrical transformation of Peusner network thermodynamics. The comparison of Equations (10)–(13) shows that for nondiagonal coefficients $L_{12} \neq L_{21}$, $L_{13} \neq L_{31}$ and $L_{23} \neq L_{32}$. In turn, the determinant of the matrix $[L]$ $\det[L] \equiv L_{det}$ can be written as:

$$L_{det} = C_s L_p \kappa \quad (14)$$

Cross coefficients $L_{ij(i \neq j)}$ describe the relationship between different irreversible processes. The expression

$$l_{ij} = \frac{L_{ij}}{\sqrt{L_{ii}L_{jj}}}, \quad i, j \in \{1, 2, 3\}, \quad (15)$$

formed from these coefficients determines the degree of coupling. This means that the coefficient l_{ij} is a measure of the degree of coupling. If $L_{ij} = 0$, the irreversible processes are independent, while when $l_{ij} = \pm 1$, the irreversible processes are maximally coupled.

Using Peusner's definition,¹³ the energy coupling parameter Q can be written in the following form:

$$(Q_L)_{ij} = \frac{2|L_{ij}L_{ji}|}{4L_{ii}L_{jj} - 2L_{ij}L_{ji}} = \frac{l_{ij}l_{ji}}{2 - l_{ij}l_{ji}} = (Q_L)_{ij}, \quad i, j \in \{1, 2, 3\} \quad (16)$$

This parameter can be used to study the efficiency and stability of physico-chemical and biological energy conversion systems.

The concept of the degree of coupling was used to determine the energy conversion efficiency $(e_{ij})_L$, $0 \leq (e_{ij})_L \leq 1$. The maximum value of this coefficient is determined by the expression:

$$\begin{aligned} [(e_{ij})_L]_{\max} &= \frac{L_{ij}L_{ji}}{L_{ij}L_{ji} \left(1 + \sqrt{1 - \frac{L_{ij}L_{ji}}{L_{ii}L_{jj}}} \right)^2} \\ &= \frac{2(Q_L)_{ij}}{(1 + Q_{ji}) \left(1 + \sqrt{1 - \frac{2(Q_L)_{ij}}{1 - (Q_L)_{ij}}} \right)^2}, \quad j \in \{1, 2, 3\} \end{aligned} \quad (17)$$

Equation (17) illustrates the relationship between the degree of coupling and the maximum efficiency of energy conversion. It is worth mentioning that full coupling ($l_{ij} = 1$) occurs at $(e_{ij})_l = 1$. This means that the stationary states of flows characterized by minimum entropy production are identical to the state with maximum efficiency.

Mathematical model of energy conversion in the membrane system

The measure of S -energy dissipation is the so-called dissipation function Φ_s , which is equal to the product of absolute temperature (T) and S -entropy production ($d_i S/dt$). To obtain mathematical expressions for S -energy dissipation in a system in which a membrane separates 2 homogeneous electrolytic solutions of different concentrations, we will use the procedure described in previous papers.^{21,22} In stationary state, the membrane transport of homogeneous electrolytic solutions containing 1 solute (s) and solvent (w) is caused by thermodynamic forces, $\Delta\pi$ (osmotic pressure difference), ΔP (hydrostatic pressure difference) and E (electromotive force); then

$$(\Phi_s)_L = J_w \bar{V}_w (\Delta P - \Delta\pi_s) + J_s \left(\bar{V}_s \Delta P + \frac{\Delta\pi_s}{C_s} \right) + IE \quad (18)$$

where: \bar{V}_s and \bar{V}_w denote the partial molar volumes of the s -th and w -th component of the solution, J_s and J_w – fluxes of solute and solvent respectively, I – ionic electric current $C_s = (C_h - C_l) [\ln(C_h C_l^{-1})]^{-1}$, C_h and C_l ($C_h > C_l$) – solute concentrations, $\Delta\pi_s = RT(C_h - C_l)$ – osmotic pressure difference, RT – the product of the gas constant and the absolute temperature, and $E = E_h - E_l$ – the potential difference across the membrane.

Taking into consideration the expressions: $J_s \bar{V}_s + J_w \bar{V}_w \equiv J_v$ and $J_s C_s^{-1} - J_w \bar{V}_w \equiv J_D$ (J_v – volume flux, J_D – diffusive flux) we can write Equation (18) in the form:

$$(\Phi_s)_L = J_v (\Delta P - \Delta\pi_s) + J_s \left(\frac{1}{C_s} + \bar{V}_s \right) \Delta\pi_s + IE \quad (19)$$

Assuming for NaCl $C_h = 100 \text{ mol m}^{-3}$ and $C_l = 0.01 \text{ mol m}^{-3}$, we get $C_s = 10.86 \text{ mol m}^{-3}$ and $1/C_s = 0.092 \text{ m}^3 \text{ mol}^{-1}$. On the other hand, $\bar{V}_s = 2.3 \times 10^{-5} \text{ m}^3 \text{ mol}^{-1}$. This means that $(1/C_s) \gg \bar{V}_s$, so Equation (19) can be written as follows:

$$(\Phi_s)_L = J_v (\Delta P - \Delta\pi_s) + J_s \frac{\Delta\pi_s}{C_s} + IE \quad (20)$$

We will now calculate the $(\Phi_s)_L$ of Equation (20), using the L -versions of the K–K–P equations.

In thermodynamic systems, including membrane systems, the internal energy (U -energy) can be converted into free energy (F -energy) and the dissipated energy (S -energy).^{21,22} The fluxes of these energies satisfy the following equation:

$$[(\Phi_U)_L]_{ij} = [(\Phi_F)_L]_{ij} + (\Phi_s)_L \quad (21)$$

where: $(\Phi_U)_L = A^{-1} dU/dt$ is the flux of U -energy, $(\Phi_F)_L = A^{-1} dF/dt$ is the flux of F -energy, $(\Phi_s)_L = TA^{-1} d_i S/dt$ – the flux of dissipated energy (S -energy), $d_i S/dt$ – the rate of entropy creation in the membrane system by irreversible processes (flux of cumulative entropy creation), T – absolute temperature, and A – the membrane surface area.

If the solutions contain a solvent and 1 dissolved substance, then the L -version of the dissipated energy for the homogeneous solution conditions denoted by $(\Phi_s)_L$ is described by the following equation:

$$(\Phi_s)_L = (\Phi_s)_{J_v} + (\Phi_s)_{J_s} = J_s (\Delta P - \Delta\pi_s) + J_s \frac{\Delta\pi_s}{C_s} + IE \quad (22)$$

where: $(\Phi_s)_L$ is the L -version of the dissipated energy, $(\Phi_s)_{J_v}$ – the dissipated energy produced by J_v , $(\Phi_s)_{J_s}$ – the dissipated energy produced by J_s , $(\Phi_s)_l$ – the dissipated energy produced by I , J_v and J_s – the volume and solute fluxes, respectively; I is the ionic current.

Taking into consideration Equations (10)–(12) into Equation (22), we get:

$$\begin{aligned} (\Phi_s)_L = & L_{11} (\Delta P - \Delta\pi_s)^2 + (L_{12} + L_{21}) \frac{\Delta\pi_s}{C_s} (\Delta P - \Delta\pi_s) \\ & + (L_{13} + L_{31}) E (\Delta P - \Delta\pi_s) + \\ & + (L_{23} + L_{32}) \frac{\Delta\pi_s}{C_s} E + L_{22} \left(\frac{\Delta\pi_s}{C_s} \right)^2 + L_{33} E^2 \end{aligned} \quad (23)$$

The Equation (23) shows the L -version of the S -energy dissipation. The $(\Phi_s)_L$ is the dissipated energy flux, i.e., the time change of energy per unit area of the membrane expressed in W/m^2 . We can calculate the $(\Phi_F)_L$ and $(\Phi_U)_L$ for the concentration polarization conditions using the following equation^{21,22}:

$$[(e_L^r)_{ij}]_{\max} = \frac{[(\Phi_F)_L]_{ij}}{(\Phi_U)_L} = \frac{[(\Phi_F)_L]_{ij}}{[(\Phi_F)_L]_{ij} + (\Phi_s)_L} \quad (24)$$

Transforming Equation (24), we get:

$$[(\Phi_F)_L]_{ij} = \frac{[(e_L)_{ij}]_{\max}}{1 - [(e_L)_{ij}]_{\max}} (\Phi_s)_L \quad (25)$$

where: $[(e_L)_{ij}]_{\max}$ is the energy conversion efficiency defined by means of Kedem–Caplan–Peusner coefficients and can be presented in the following form:

$$[(e_L)_{ij}]_{\max} = \frac{l_{ij} l_{ji}}{(1 + \sqrt{1 - l_{ij} l_{ji}})^2} = [(e_L)_{ji}]_{\max} \quad (26)$$

From a formal point of view, the cases of $\phi(F)_L = 0$ and $\phi(U)_L = 0$ are excluded, because in order for the denominator of Equations (25) and (26) to be different from 0, the condition $[(e_L)_{ij}]_{\max} \neq 1$ must be satisfied.

The values of $[(e_L)_{ij}]_{\max}$ coefficients are limited by the relations $0 \leq [(e_L)_{ij}]_{\max} \leq 1$; $[(e_L)_{ij}]_{\max} = 0$ when $L_{12}L_{21} = 0$ or $l_{12}l_{21} = 0$ and $[(e_L)_{ij}]_{\max} = 1$, when $L_{12}L_{21} = L_{11}L_{22}$, and, $L_{12}L_{21} = 1$. Taking into account the Equation (26) in (25), we get:

$$\begin{aligned}
[(\Phi_F)_L]_{ij} &= \frac{L_{ij}L_{ji}}{L_{ii}L_{jj} \left(1 + \sqrt{1 - \frac{L_{ij}L_{ji}}{L_{ii}L_{jj}}} \right)^2 - L_{ij}L_{ji}} (\Phi_S)_L \\
&= \frac{[(e_L)_{ij}]_{\max}}{1 - [(e_L)_{ij}]_{\max}} (\Phi_S)_L
\end{aligned} \quad (27)$$

To obtain the equation for $[(\Phi_U)_L]_{ij}$, it is necessary to take into consideration Equation (26) in Equation (24). After performing the necessary transformations, we get:

$$[(\Phi_U)_L]_{ij} = \frac{L_{ij}L_{ji}\mathcal{L}^2}{L_{ii}L_{jj}\mathcal{L}^2 - L_{ij}L_{ji}} (\Phi_S)_L = \frac{1}{1 - [(e_L)_{ij}]_{\max}} (\Phi_S)_L \quad (28)$$

where $\mathcal{L} = 1 + \sqrt{1 - \frac{L_{ij}L_{ji}}{L_{ii}L_{jj}}}$.

From the above procedure, based on the Equations (24)–(28), we can calculate the amount of available F -energy that can be converted into useful work and the total internal U -energy.

Biomembrane characteristics

The nanobiocellulose as a main component of the Biofill membrane (Biofill Produtos Biotecnológicos S.A., Curitiba, Brazil) is produced by *Acetobacter xylinum*.^{23–26} Studies using a scanning microscope (Zeiss Supra 35; Carl Zeiss AG, Jena, Germany) have shown that the structure of the Biofill membrane is made up of fibers interwoven into a network that is no more than 130-nm thick, consisting of micro-fibers with a cross section of 0.1–0.2 μm arranged in layers.²⁶ The thickness of the membrane in its hydrated state is about 20 μm . The Bioprocess membrane is symmetric, isotropic and electrically neutral.

The values of transport coefficients (L_{pp} , σ_s , ω_s , β , κ , t_c) of the Biofill membrane, appearing in Equations (1)–(3) and defined by Equations (4)–(9), were taken from the previous work.²⁶ This paper describes the methodology for determining these coefficients in a series of independent experiments. The values of transport coefficients L_{pp} , σ_s and

ω_s in the studied range of NaCl concentrations are constant and amount to $L_{pp} = 6.5 \times 10^{-11}$ [m^3/Ns], $\sigma_s = 0.36 \times 10^{-3}$ and $\omega_s = 17.1 \times 10^{-10}$ [mol/Ns]. In turn, the values of transport coefficients β , κ and t_c in the studied range of NaCl concentrations are concentration-dependent. The dependencies $\beta = f(C_s)$, $\kappa = f(C_s)$ and $t_c = f(C_s)$ are summarized in Table 1.

Bacterial cellulose membranes are used for both biomedical and non-medical purposes. For biomedical purposes, they are used as dressings in the healing process of burns and venous leg ulcers, and in the manufacture of prosthetic blood vessels and as a selective barrier in the controlled release of drugs.^{9,23–25}

Results

Characteristics of $L_{ij} = f(C_s)$ ($i, j \in \{1, 2, 3\}$) and $L_{det} = f(C_s)$

Calculations of the coefficients $L_{ij} = f(C_s)$ ($i, j \in \{1, 2, 3\}$) and $L_{det} = f(C_s)$ were performed for the following data: $R = 8.31$ J/mol K, $T = 295$ K and $F = 9.65 \times 10^4$ C/mol, and $C_s = 0.06 \div 15$ mol/ m^3 , $C_l = 0.01$ mol/ m^3 and $C_h = 0.2 \div 144$ mol/ m^3 . To calculate the dependencies $L_{ij} = f(C_s)$, ($i, j \in \{1, 2, 3\}$) and $L_{det} = f(C_s)$, the Equations (13)–(17) were used. The results of the calculations are presented in Fig. 2A–F. They show that the coefficient L_{11} is independent on C_s . Therefore, its value is constant and amounts to $L_{11} = 6.49 \times 10^{-11}$ m^3/Ns .

The values of coefficients $L_{ij} = f(C_s)$ ($i, j \in \{1, 2, 3\}$) and $L_{det} = f(C_s)$ are dependent on C_s as is illustrated in Fig. 2A–F. Most of the calculated flux-force coupling coefficients (L_{ij}) in general depend non-linearly on the concentration of the substance in the membrane, except the coefficients $L_{12} = L_{21}$ (showing linear dependence on concentration) and the almost linear dependence of the coefficient L_{22} on the NaCl concentration in the membrane. The values of these coefficients are positive except for the L_{31} coefficient, which is negative in the entire range of considered concentrations. Figure 2A shows that the values of coefficients $L_{12} \approx L_{21}$ are positive and increase with increasing value of C_s . Figure 2B demonstrates that the characteristics $L_{13} \neq L_{31} = f(C_s)$ are nonlinear. The values of coefficient L_{13} are positive and decrease with increasing value of C_s . In contrast, the absolute values of coefficient L_{31} decrease with increase of C_s . A positive coefficient L_{ij} means that an increase in the corresponding thermodynamic force j causes an increase in the corresponding flux i . The absolute values of coefficients L_{13} and L_{31} decrease as the concentration of the substance in the membrane increases. In turn, the remaining coefficients (except L_{23} and L_{32} , which show extreme values) increase with increasing concentration in the membrane. The linear increase of the L_{ij} coefficient with the concentration in the membrane means that a change in the corresponding thermodynamic force

Table 1. Dependencies $\beta = f(C_s)$, $\kappa = f(C_s)$, and $t_c = f(C_s)$ for Biofill bacterial cellulose membrane and aqueous NaCl solutions

C_s [mol/ m^3]	$\beta \times 10^{-3}$ [N/A]	κ [1/ Ωm^2]	t_c
0.06	8.5	0.45	0.4
0.1	6.0	0.5	0.5
0.6	2.0	0.9	0.4
1	1.2	1.3	0.3
3	0.5	1.5	0.22
5	0.4	1.7	0.18
7	0.2	2.0	0.15
10	0.02	2.4	0.12
15	0.01	7.0	0.1

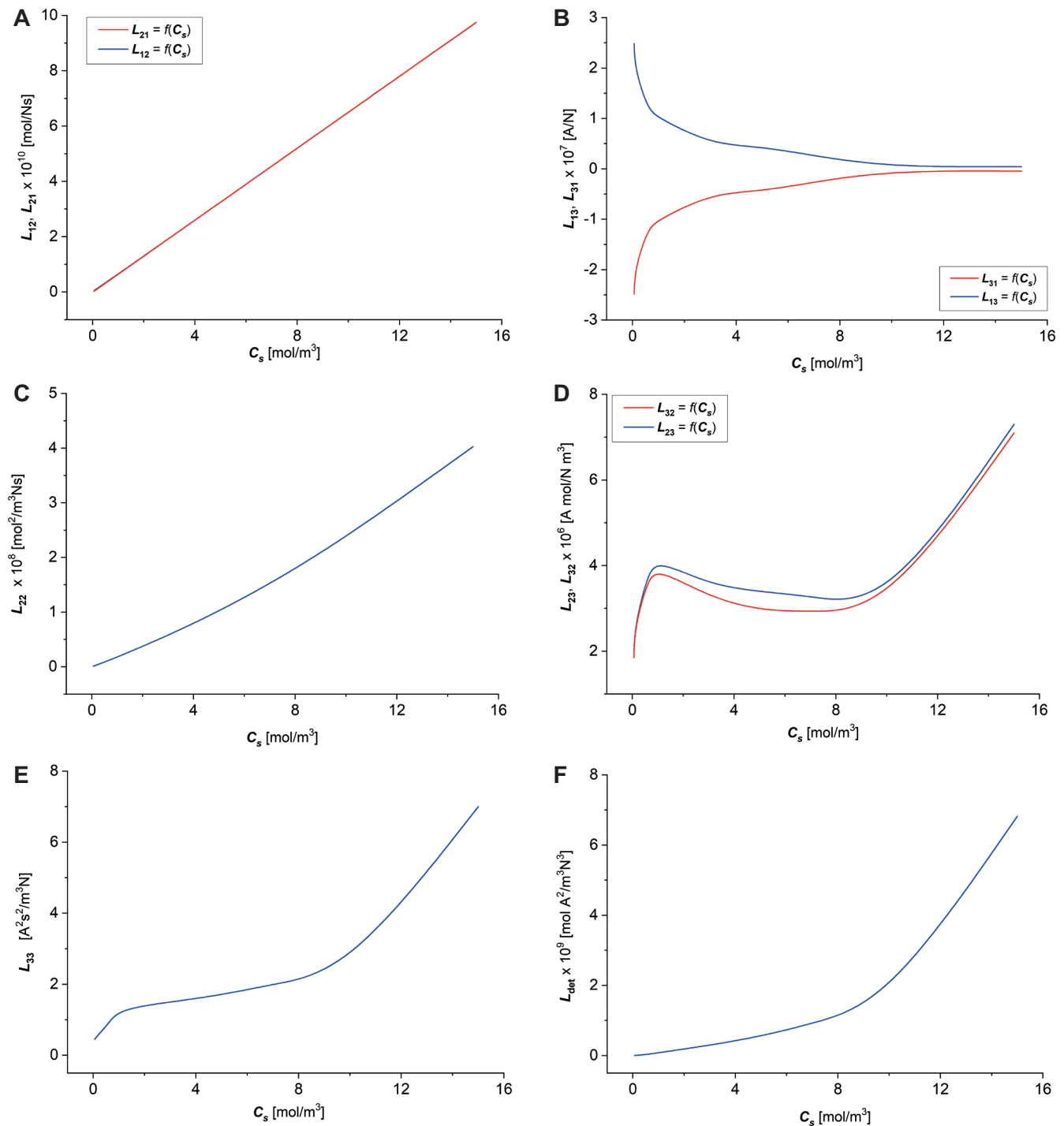


Fig. 2. Graphical representation of the dependencies $L_{ij} = f(C_s)$ ($i, j \in \{1, 2, 3\}$) and $L_{det} = f(C_s)$ for aqueous NaCl solutions. A. $L_{12} = L_{21} = f(C_s)$; B. $L_{13} \neq L_{31} = f(C_s)$; C. $L_{22} = f(C_s)$; D. $L_{23} \neq L_{32} = f(C_s)$; E. $L_{33} = f(C_s)$; F. $L_{det} = f(C_s)$

on the membrane (j) causes a proportional increase in the corresponding flux (i). Non-linear changes of the L_{ij} coefficient make the force-flux relationship more complicated. The greater the slope of the L_{ij} – concentration dependence (i.e. the greater the derivative of L_{ij} with respect to concentration), the greater an influence of given thermodynamic force on the relevant flux. The most interesting dependence on concentration is observed for the coefficients L_{23} and L_{32} , which, after a large increase in the narrow range of low concentrations (up to a concentration

of about 1 mol/m³), show a slight reduction or even stabilization of the coefficient in the concentration range from 1 mol/m³ to about 10 mol/m³. Above the concentration of 10 mol/m³, increase of the concentration in the membrane causes a further non-linear increase in the L_{23} and L_{32} coefficients, but smaller than that observed in the low concentration range (up to 1 mol/m³). These nonlinear dependencies of the coefficients on concentration are related to the structure of the membrane itself and its impact on individual transported substances, and thus

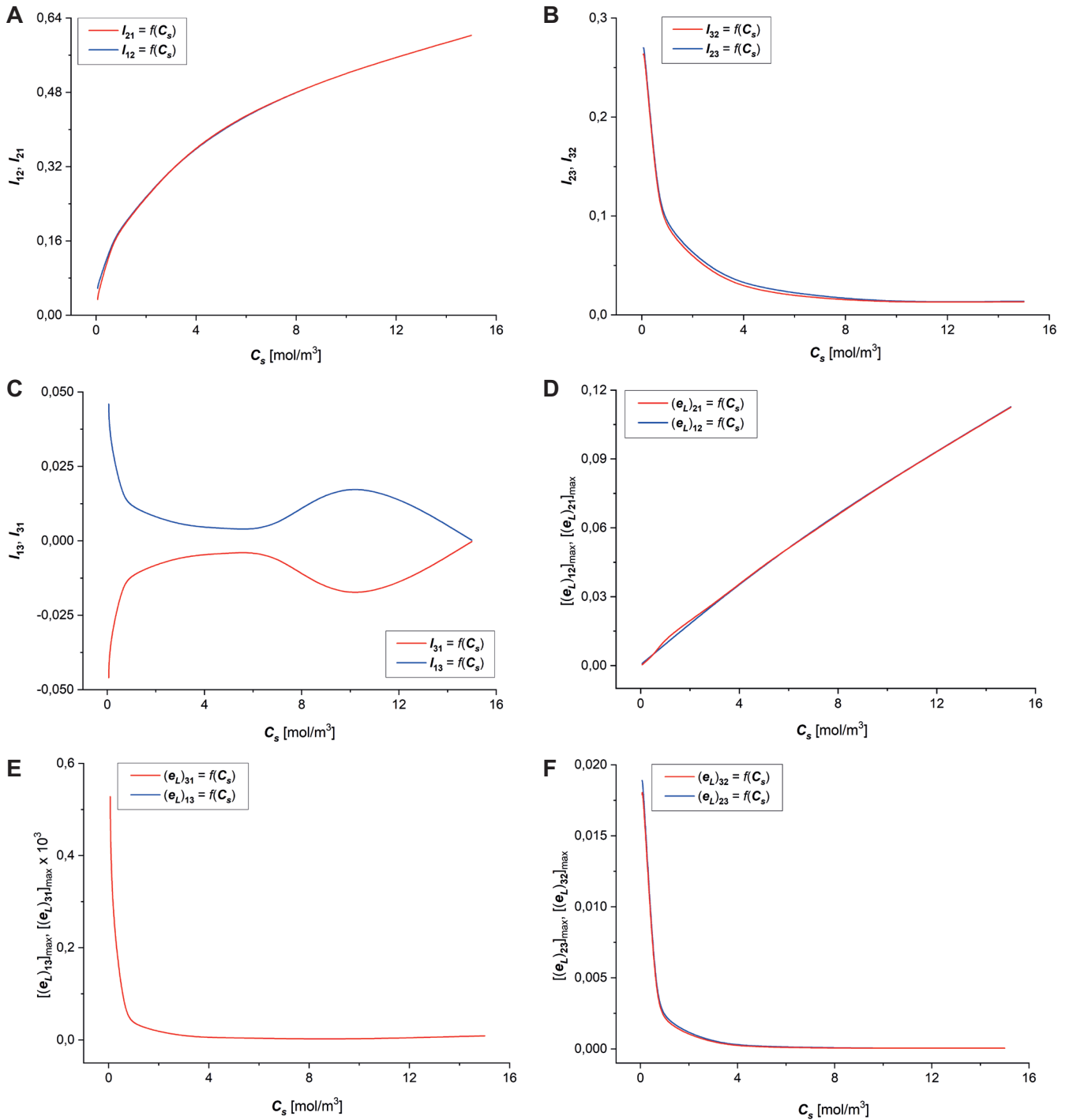


Fig. 3. Graphical representation of the dependencies $l_{ij} = f(C_s)$ ($i, j \in \{1, 2, 3\}$) and $(e_l)_{ij,max} = f(C_s)$, for aqueous NaCl solutions. A. $l_{12} = l_{21} = f(C_s)$; B. $L_{23} = L_{32} = f(C_s)$; C. $L_{13} \neq L_{31} = f(C_s)$; D. $(e_l)_{12,max} = (e_l)_{21,max} = f(C_s)$; E. $(e_l)_{23,max} = (e_l)_{32,max} = f(C_s)$ and $(e_l)_{13,max} = (e_l)_{31,max} = f(C_s)$

indirectly on the interaction of substances transported through the membrane.

Figure 2C shows that the characteristic $L_{22} = f(C_s)$ is nonlinear and values of L_{22} are positive. Figure 2D demonstrates that the characteristics $L_{23} \neq L_{32} = f(C_s)$ are nonlinear and values both L_{23} and L_{32} are positive. The curve shown in Fig. 2E shows that the $L_{33} = f(C_s)$ characteristics are nonlinear and the L_{33} values are positive. $L_{det} = f(C_s)$ characteristics are also nonlinear and L_{det} values are positive.

Characteristics $l_{ij} = f(C_s)$ and $[(e_l)_{ij}]_{max} = f(C_s)$ ($i, j \in \{1, 2, 3\}$)

Taking into account the results of calculations obtained for dependencies $L_{ij} = f(C_s)$, ($i, j \in \{1, 2, 3\}$) shown in Fig. 3A–C in the Equation (15), the dependencies $l_{ij} = f(C_s)$ were calculated and presented in Fig. 3A–E.

The curves presented in Fig. 3A show that the characteristics $l_{12} = f(C_s)$ and $l_{21} = f(C_s)$ are nonlinearly dependent on concentration, besides $l_{12} = l_{21}$, and these curves are

of saturation type. Figure 3B shows the characteristics of the $l_{13} = f(C_s)$ and $l_{31} = f(C_s)$. Figure 3B illustrates also that the values of l_{13} are positive and l_{31} are negative. Moreover, these characteristics are symmetrical about the axis passing through the point of zero concentration. The $l_{23} = f(C_s)$ and $l_{32} = f(C_s)$ characteristics shown in Fig. 3C are also nonlinear. These characteristics are of hyperbolic type. In addition, $l_{23} = l_{32}$ in whole range of studied concentrations. A comparison of Fig. 3A, 3B and 3C shows that $l_{12} = l_{21} > l_{23} = l_{32} > l_{13} > l_{31}$. The coupling coefficients l_{ij} between processes occurring in the membrane have values ranging from 0 (no coupling) to 1 (complete coupling). Coupling coefficients with the same indexes (the same process) l_{ij} are equal to 1. The coefficients l_{12} (characterizing coupling of processes $\ll J_v | \Delta p - \Delta \pi_i \gg \Leftrightarrow \ll J_s | \Delta \pi_s / C_s \gg$ suitably) and l_{21} increase with increasing concentration in the membrane, which indicates greater coupling of these processes with increasing concentration. This may indicate an increasing role of the membrane in the interaction between these processes as the concentration of substances in the membrane increases. In turn, the coefficients l_{23} and l_{32} (coupling of processes $\ll J_s | \Delta \pi_s / C_s \gg \Leftrightarrow \ll I | E \gg$ respectively) reach higher values at low concentrations (high coupling) and gradually decrease with increasing concentration in the membrane to a value close to 0 (no coupling) for concentrations higher than 8 mol/m³.

Considering the $l_{ij} = f(C_s)$ dependencies shown in Fig. 3A–C, and Equation (17), the dependencies $[(e_L)_{ij}]_{max} = f(C_s)$ were calculated. The coefficients $(e_L)_{ij}$, characterize the efficiency of energy conversion in the membrane. The curves presented in Fig. 3D show that the characteristics $[(e_L)_{12}]_{max} = f(C_s)$ and $[(e_L)_{21}]_{max} = f(C_s)$ are linear and $[(e_L)_{12}]_{max} = [(e_L)_{21}]_{max}$. These coefficients increase linearly from 0 (inefficient energy conversion) for low concentrations to values of approx. 0.12 for a concentration in the membrane of 15 mol/m³. Figure 3E shows the characteristics $[(e_L)_{23}]_{max} = f(C_s)$ and $[(e_L)_{32}]_{max} = f(C_s)$. These characteristics are nonlinear and are of hyperbolic type. In addition, Fig. 3E shows that $[(e_L)_{23}]_{max} = [(e_L)_{32}]_{max}$. Similarly,

the characteristics $[(e_L)_{13}]_{max} = f(C_s)$ and $[(e_L)_{31}]_{max} = f(C_s)$, illustrated in Fig. 3F are of hyperbolic type. In addition, Fig. 3F shows that $[(e_L)_{13}]_{max} = [(e_L)_{31}]_{max}$. A comparison of Fig. 3D, Fig. 3E and Fig. 3F shows that $[(e_L)_{12}]_{max} = [(e_L)_{21}]_{max} > [(e_L)_{23}]_{max} = [(e_L)_{32}]_{max} > [(e_L)_{13}]_{max} = [(e_L)_{31}]_{max}$. The coefficients presented in Fig. 3E,F, characterize energy conversion in the membrane decrease with increasing concentration, with the highest rate of coefficient reduction being observed in the concentration range from 0 to approx. 1 mol/m³. For concentrations greater than 2 mol/m³, the values of these coefficients are almost equal to 0 (inefficient energy conversion processes in the membrane).

**Characteristics $(\Phi_S)_L = f[(\Delta P - \Delta \pi_s), (\Delta \pi_s / C_s), E]$,
 $[(\Phi_F)_L]_{ij} = f[(\Delta P - \Delta \pi_s), (\Delta \pi_s / C_s), E]$
and $[(\Phi_U)_L]_{ij} = f[(\Delta P - \Delta \pi_s), (\Delta \pi_s / C_s), E]$**

Taking into account the results of the calculations obtained for $L_{ij} = f(\Delta \pi)$, ($i, j \in \{1, 2\}$) (Fig. 2A–E) in Equation (23), the dependencies $(\Phi_S)_L = f(\Delta \pi_s / C_s)_{E=const.}$ and $(\Phi_S)_L = f(E)_{\Delta \pi_s / C_s=const.}$ were calculated. The results of calculations are presented in Fig. 4A,B. The graphs shown in Fig. 2A–E are 2nd degree curves.

From Fig. 4A,B, it can be seen that $(\Phi_S)_L$ increases both with the increase of $\Delta \pi_s / C_s$ at a fixed value of E and with the increase of E at a fixed value of $\Delta \pi_s / C_s$. It should be noted that $\Delta P - \Delta \pi_s$ had no effect on $(\Phi_S)_L$, as the values of $\Delta P - \Delta \pi_s$ were chosen so that $\Delta P - \Delta \pi_s = 0$. The function $(\Phi_S)_L$ as the flux of energy dissipated in membrane processes allows to estimate the part of the energy required for membrane transport that is dissipated in the environment as heat. In the analysed cases, this function is nonlinearly dependent on both thermodynamic forces on the membrane and symmetrical with respect to zero value of thermodynamic force. In the case of small concentrations (or small electric fields), the energy dissipated is small and increases as the thermodynamic force increases. The increase of this function is larger for the greater thermodynamic force. The shape of the curves resembles parabolas. For

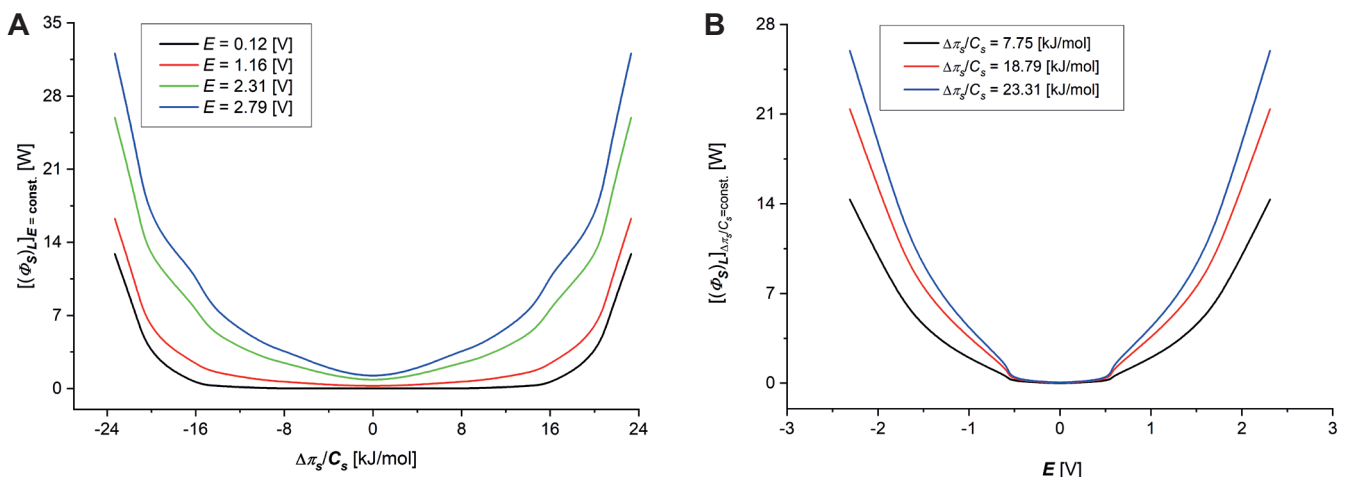


Fig. 4. Graphical representation of the dependencies $[\Phi(S)]_{E=const.} = f(\Delta \pi_s / C_s)$ ($i, j \in \{1, 2, 3\}$) and $[\Phi(S)]_{\Delta \pi_s / C_s=const.} = f(E)$, for aqueous NaCl solutions

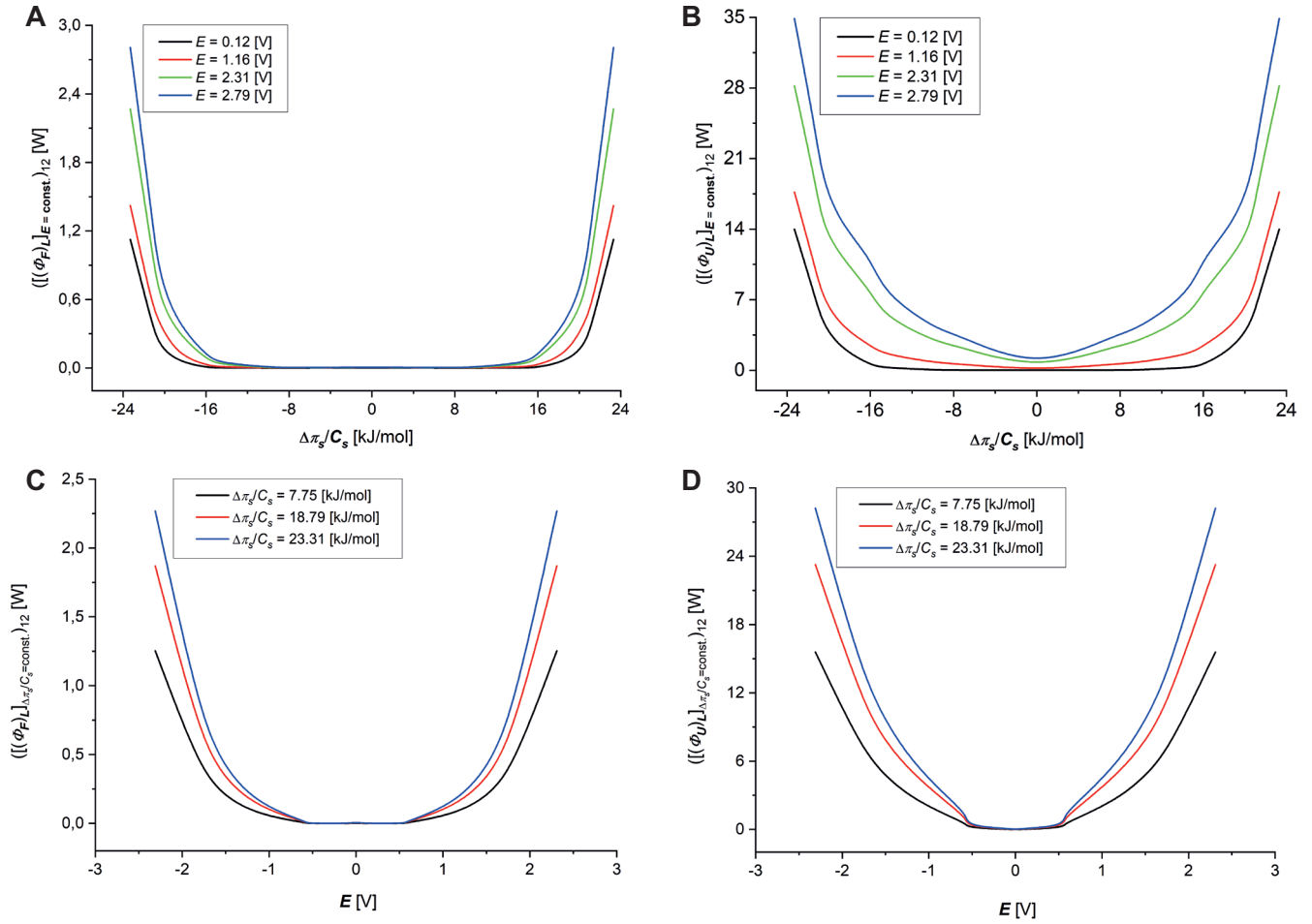


Fig. 5. Graphical representation of the dependencies $((\Phi_F)_L)_{E=const.} = f(\Delta\pi_s/C_s)$ (A), $((\Phi_U)_L)_{E=const.} = f(\Delta\pi_s/C_s)$ (B), $((\Phi_F)_L)_{\Delta\pi_s/C_s=const.} = f(E)$ (C) and $((\Phi_U)_L)_{\Delta\pi_s/C_s=const.} = f(E)$ (D), for aqueous NaCl solutions

the thermodynamic force $\Delta\pi_s/C_s$ (Fig. 4A), large changes in the dissipated energy flux are observed above 16 kJ/mol, while for greater established 2nd thermodynamic force E , significant changes in $\Phi(S)_L$ are observed for greater values of $\Delta\pi_s/C_s$. The dependence $\Phi(S)_L = f(E)$ is analogous when $\Delta\pi_s/C_s$ is constant, but for E values lower than 0.5 V, $\Phi(S)_L$ increases slightly and only above this value changes of $\Phi(S)_L$ are significant, is larger for greater osmotic pressure difference ($\Delta\pi_s/C_s$). This indicates that the amount of energy dissipated in membrane processes increases with increasing thermodynamic force on the membrane, due to the fact that at small forces, the influence of the membrane on the transported substances and at the same time on the energy dissipated in this transport is small. Increasing thermodynamic forces, especially osmotic force, cause a higher concentration of substances in the membrane and a greater influence of the membrane on transport of substances and cause greater dissipation of energy in membrane.

Taking into account the results of calculations obtained for dependencies $(e_L)_{12,max}$ (shown in Fig. 3D) in Equations (27) and (28), and dependencies $[\Phi(S)_L]_{E=const.} = f(\Delta\pi_s/C_s)$, $[(\Phi_S)_L]_{\Delta\pi_s/C_s=const.} = f(E)$ presented in Fig. 4A,B, the dependencies $[(\Phi_F)_L]_{E=const.} = f(\Delta\pi_s/C_s)$, $[(\Phi_U)_L]_{E=const.} = f(\Delta\pi_s/C_s)$, $[(\Phi_F)_L]_{\Delta\pi_s/C_s=const.} = f(E)$, $[(\Phi_U)_L]_{\Delta\pi_s/C_s=const.} = f(E)$ were calculated.

The results of calculations are presented in Fig. 5A–D. Comparing the data for $[(\Phi_F)_L]_{E=const.} = f(\Delta\pi_s/C_s)$ and $[(\Phi_U)_L]_{E=const.} = f(\Delta\pi_s/C_s)$ shown in Fig. 5A,B and the data for $[(\Phi_F)_L]_{\Delta\pi_s/C_s=const.} = f(E)$ and $[(\Phi_U)_L]_{\Delta\pi_s/C_s=const.} = f(E)$ shown in Fig. 5C,D, it can be seen that $[(\Phi_F)_L]_{12} \approx 0.1 \cdot [(\Phi_U)_L]_{12}$.

As shown in Fig. 5A–D, both the internal energy flow $(\Phi_U)_L$ and the free energy flow $(\Phi_F)_L$ are symmetrical with respect to the 0 values of both thermodynamic forces $\Delta\pi_s/C_s$ with a fixed $E = const.$, and E with a fixed thermodynamic force $\Delta\pi_s/C_s = const.$ As one of the thermodynamic forces increases, regardless of its direction, the values of both energy fluxes increase nonlinearly. The larger the value of the thermodynamic force, the larger the energy fluxes are observed. This may result, as in the previous cases, from the increased influence of the membrane on the transport processes for larger thermodynamic forces. As could be expected, the values of the internal energy flux are much higher than the values of free energy flux converted into mechanical work related to the transported substances. Taking into account Equation (21), which combines the considered energies, and the corresponding Fig. 4,5, it can be concluded that the flux of released internal energy $(\Phi_U)_L$ in membrane

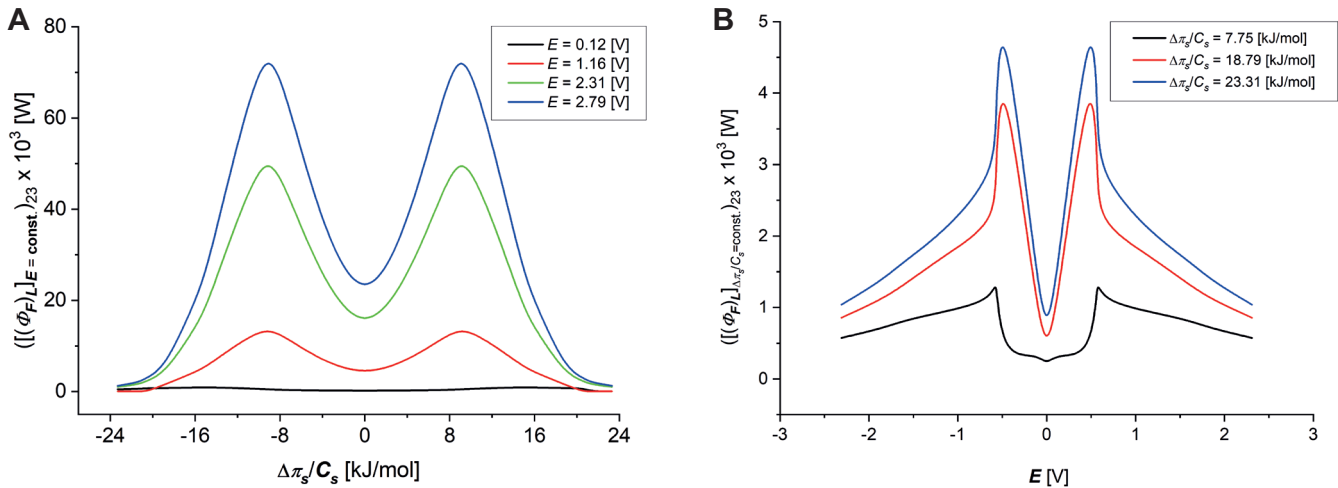


Fig. 6. Graphical representation of the dependencies $((\Phi_F)_{L23})_{E=const.} = f(\Delta\pi_s/C_s)$ and $((\Phi_F)_{L12})_{\Delta\pi_s/C_s=const.} = f(E)$, for aqueous NaCl solutions

processes is converted into 2 fluxes: of free energy $(\Phi_F)_L$ and dissipated as heat $(\Phi_S)_L$. For the membrane processes considered, the energy flux dissipated in the form of heat $(\Phi_S)_L$ is about 10 times larger than the free energy flux $(\Phi_F)_L$. By comparing $(\Phi_F)_L$ to $(\Phi_U)_L$, the average efficiency of the observed processes can be estimated and is approx. $1/11 = 9.1\%$.

Taking into account the results of calculations obtained for dependencies $[(e_L)_{23}]_{max}$ (shown in Fig. 3E) in Equations (27) and (28), and dependencies $[(\Phi_S)_L]_{E=const.} = f(\Delta\pi_s/C_s)$ and $[(\Phi_S)_L]_{\Delta\pi_s/C_s=const.} = f(E)$ presented in Fig. 3A,B, the dependencies $((\Phi_F)_{L23})_{E=const.} = f(\Delta\pi_s/C_s)$ and $((\Phi_F)_{L23})_{\Delta\pi_s/C_s=const.} = f(E)$, were calculated. The results of calculations are presented in Fig. 6A,B.

The comparison of the data presented in Fig. 5A, Fig. 6A, Fig. 5C, and Fig. 6B shows that $((\Phi_F)_{L12})_{E=const.}$ is 3 orders of magnitude larger than $((\Phi_F)_{L23})_{E=const.}$, while $((\Phi_F)_{L12})_{\Delta\pi_s/C_s=const.}$ is 2 orders of magnitude larger than $((\Phi_F)_{L23})_{\Delta\pi_s/C_s=const.}$. Therefore, $((\Phi_U)_{L12})_{E=const.} \approx ((\Phi_S)_{L23})_{E=const.}$ and $((\Phi_U)_{L12})_{\Delta\pi_s/C_s=const.} \approx ((\Phi_S)_{L23})_{\Delta\pi_s/C_s=const.}$.

Similar reasoning can be done for $((\Phi_F)_{L12})_{E=const.}$, $((\Phi_F)_{L13})_{E=const.}$, $((\Phi_U)_{L12})_{E=const.}$ and $((\Phi_U)_{L13})_{\Delta\pi_s/C_s=const.}$. Due to the fact that $[(e_L)_{12}]_{max} \gg [(e_L)_{13}]_{max}$ so $((\Phi_F)_{L13})_{E=const.} \ll ((\Phi_F)_{L12})_{E=const.}$. This means that $((\Phi_U)_{L12})_{E=const.} \approx ((\Phi_S)_{L13})_{E=const.}$ and $((\Phi_U)_{L12})_{\Delta\pi_s/C_s=const.} \approx ((\Phi_S)_{L13})_{\Delta\pi_s/C_s=const.}$.

Discussion

According to the Peusner network formalism, appropriate transformations of the classical K–K equations for electrolyte solutions lead to L versions of the K–K–P equations for electrolyte solutions for 3 thermodynamic forces (ΔP , $\Delta\pi_s$ and E) and 3 fluxes (J_v , J_s and I). The resulting equations include the Peusner coefficients L_{ij} ($i, j \in \{1, 2, 3\}$) and L_{det} , which characterize the transport properties of any membrane. There are 9 coefficients in these equations – that is, the 3rd thermodynamic

force (E) introduces 5 additional coefficients: L_{13} , L_{31} , L_{23} , L_{32} , and L_{33} . The Peusner coefficients are useful for calculating the degree of coupling, which is determined by the coefficients l_{12} , l_{21} , l_{13} , l_{31} , l_{23} , and l_{32} . It is well known that when $l_{ij} = 0$, the irreversible processes are independent, whereas when $l_{ij} = \pm 1$, the irreversible processes are maximally coupled.

The data presented in Fig. 3A show that, in the concentration range $0 < C_s \leq 15 \text{ mol/m}^3$, the coupling coefficients l_{12} and l_{21} take values in the range $0 < l_{12} = l_{21} \leq 0.64$. This means that the irreversible processes in membrane, measured using the fluxes J_v and J_s , are strongly coupled to each other and that the coupling increases with increasing C_s . In contrast, the data presented in Fig. 3B show that, in the same C_s concentration range, the coupling coefficients l_{13} and l_{31} take the values in the ranges: $0.046 \geq l_{13} \geq 2.1 \times 10^{-4}$ and $-0.046 \leq l_{13} \leq 2.1 \times 10^{-4}$. This means that the irreversible processes, whose measures are the fluxes J_v and I , are weakly coupled to each other. The data presented in Fig. 3C show that in the concentration range $0 < C_s \leq 15 \text{ mol/m}^3$, the coupling coefficients l_{13} and l_{32} take values in the range $0.27 \geq l_{23} = l_{32} \geq 0.014$. This means that the irreversible processes, whose measures are the fluxes J_s and I , are coupled to each other, but this coupling decreases nonlinearly with increasing solute concentration.

According to the procedure proposed by Peusner,^{13,27,28} the coefficients l_{12} , l_{21} , l_{13} , l_{31} , l_{23} , and l_{32} can be grouped into the coefficient $(Q_L)_{ij}$ expressed by Equation (16). From this equation, $0 \leq (Q_L)_{ij} \leq 1$. The concentration dependence of $(Q_L)_{ij}$ coefficients are presented in Fig. 7.

From Fig. 7A, it can be seen that in the concentration range $0 < C_s \leq 15 \text{ mol/m}^3$, $(Q_L)_{12}$ takes the values in the range $0 < (Q_L)_{12} \leq 0.22$. This means that the irreversible processes associated with the fluxes J_v and J_s are coupled. Figure 7B shows that in the same concentration range $(Q_L)_{13}$ satisfies condition $0.106 \times 10^{-2} \geq (Q_L)_{13} \geq 2 \times 10^{-4}$ and $(Q_L)_{23}$ satisfies condition $3.68 \times 10^{-2} \geq (Q_L)_{13} \geq 0.92 \times 10^{-4}$. This means that

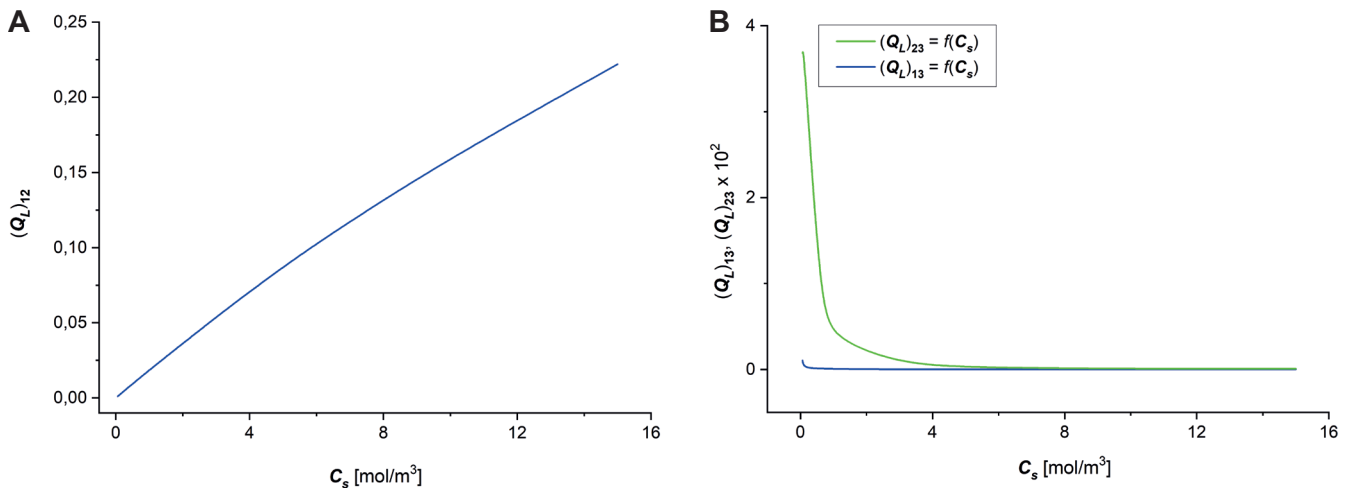


Fig. 7. Graphical representation of the dependencies $(Q_L)_{ij} = f(C_s)$ for aqueous NaCl solutions: $(Q_L)_{12} = f(C_s)$ (A), $(Q_L)_{13} = f(C_s)$ and $(Q_L)_{23} = f(C_s)$ (B)

the irreversible processes associated with J_v and I fluxes and J_s and I fluxes are decoupled.

The conversion of electrochemical energy is a significant natural process. Internal energy, also known as U -energy, is not a usable form of energy.^{27–30} Instead, free energy or F -energy is the useful form.

The electrochemical energy conversion evaluation method presented in this study uses dissipative energy (S -energy), the measure of which is the dispersion function $(\Phi_S)_L$ and the energy conversion efficiency factor $[(e_L)_{ij}]_{max}$. The measure of F -energy is $[(\Phi_F)_L]_{ij}$ and of U -energy is $[(\Phi_U)_L]_{ij}$. The pioneering work of Kedem, Caplan and Peusner is one of the premises for the development of Peusner's network thermodynamics.^{13,27–30}

Conclusions

The L version of the K–K–P equations presented in this study, which contains 3 fluxes (J_v , J_s , I) and 3 thermodynamic forces ($\Delta\pi$, $\Delta\pi_s$, E), introduces 10 Peusner coefficients L_{ij} ($i, j \in \{1, 2, 3\}$) and L_{det} . These coefficients can be calculated using the transport parameters L_p , σ_s and ω_s , which determine the fluxes J_v and J_s , and the transport parameters β , τ_c and κ determining the flux I . Five of them (L_{13} , L_{31} , L_{23} , L_{32} , and L_{33}) are a consequence of considering the additional thermodynamic force E and flux I . The coefficients L_{12} , L_{13} , L_{31} , L_{33} , and L_{32} are necessary to define the 3 groups of coefficients: l_{12} , l_{21} , l_{13} , l_{31} , l_{23} , and l_{32} ; $(Q_L)_{12}$, $(Q_L)_{13}$ and $(Q_L)_{23}$; $[(e_L)_{12}]_{max}$, $[(e_L)_{21}]_{max}$, $[(e_L)_{23}]_{max}$, $[(e_L)_{32}]_{max}$, $[(e_L)_{13}]_{max}$, and $[(e_L)_{31}]_{max}$. The coefficients L_{ij} ($i, j \in \{1, 2, 3\}$) are needed to calculate the energy dissipation $(\Phi_S)_L$.

The equations describing the energy dissipation $(\Phi_S)_L$ take the form of equations that are the sum of quadratic equations of 3 variables: ΔP , $\Delta\pi$ and E . The characteristics $[\Phi(S)_L]_{E=const.} = f(\Delta\pi_s/C_s)$ ($i, j \in \{1, 2, 3\}$) and $[\Phi(S)_L]_{\Delta\pi_s/C_s=const.} = f(E)$ are 2nd degree curves located in the 1st and 2nd quadrants of the coordinate system. Equations for $(\Phi_S)_L$ and for $[(e_L)_{12}]_{max}$, $[(e_L)_{21}]_{max}$, $[(e_L)_{23}]_{max}$, $[(e_L)_{32}]_{max}$, $[(e_L)_{13}]_{max}$,

or $[(e_L)_{31}]_{max}$ are required to examine the energy conversion, and calculate the characteristics $[(\Phi_F)_L]_{12} E=const. = f(\Delta\pi_s/C_s)$, $[(\Phi_F)_L]_{12} \Delta\pi_s/C_s=const. = f(E)$, $[(\Phi_U)_L]_{12} E=const. = f(\Delta\pi_s/C_s)$, and $[(\Phi_U)_L]_{12} \Delta\pi_s/C_s=const. = f(E)$.

ORCID iDs

Andrzej Ślęzak <https://orcid.org/0000-0001-6818-2099>

Sławomir M. Grzegorzczyn <https://orcid.org/0000-0002-5248-3505>

References

- Demirel Y. *Nonequilibrium Thermodynamics: Transport and Rate Processes in Physical, Chemical and Biological Systems*. 2nd ed. Amsterdam, the Netherlands-Heidelberg, Germany: Elsevier; 2007. ISBN:978-0-444-53079-0.
- Gerbaud V, Shcherbakova N, Da Cunha S. A nonequilibrium thermodynamics perspective on nature-inspired chemical engineering processes. *Chem End Res Des*. 2020;15(4):316–330. doi:10.1016/j.cherd.2019.10.037
- Baker RW. *Membrane Technology and Applications*. Hoboken, USA: Wiley; 2012. doi:10.1002/9781118359686
- Radu ER, Voicu SI, Thakur VK. Polymeric membranes for biomedical applications. *Polymers (Basel)*. 2023;15(3):619. doi:10.3390/polym15030619
- Dorotkiewicz-Jach A, Markwitz P, Rachuna J, Arabski M, Drulis-Kawa Z. The impact of agarose immobilization on the activity of lytic *Pseudomonas aeruginosa* phages combined with chemicals. *Appl Microbiol Biotechnol*. 2023;107(2–3):897–913. doi:10.1007/s00253-022-12349-4
- Anton-Sales I, D'Antin JC, Fernández-Engroba J, et al. Bacterial nanocellulose as a corneal bandage material: A comparison with amniotic membrane. *Biomater Sci*. 2020;8(10):2921–2930. doi:10.1039/D0BM00083C
- Richter T, Keipert S. In vitro permeation studies comparing bovine nasal mucosa, porcine cornea and artificial membrane: Androstenedione in microemulsions and their components. *Eur J Pharm Biopharm*. 2004;58(1):137–143. doi:10.1016/j.ejpb.2004.03.010
- Twardowski ZJ. History of hemodialyzers' designs. *Hemodialysis Int*. 2008;12(2):173–210. doi:10.1111/j.1542-4758.2008.00253.x
- Harma B, Gül M, Demircan M. The efficacy of five different wound dressings on some histological parameters in children with partial-thickness burns. *J Burn Care Res*. 2020;41(6):1179–1187. doi:10.1093/jbcr/iraa063
- Highfield R, Coveney P. *The Arrow of Time: A Voyage Through Science to Solve Time's Greatest Mystery*. New York, USA: Ballantine Books; 1991. ISBN:978-0-449-90723-8.
- Kondepudi D. *Introduction to Modern Thermodynamics*. Hoboken, USA: Wiley; 2008. ISBN:978-0-470-98649-3.
- Katchalsky A, Curran PF. *Nonequilibrium Thermodynamics in Biophysics*. Harvard, USA: Harvard University Press; 1965. doi:10.4159/harvard.9780674494121

13. Peusner L. *Studies in Network Thermodynamics*. Amsterdam, the Netherlands–New York, USA: Elsevier; 1986. ISBN:978-0-444-42580-5.
14. Ślęzak A. Irreversible thermodynamic model equations of the transport across a horizontally mounted membrane. *Biophys Chem*. 1989; 34(2):91–102. doi:10.1016/0301-4622(89)80047-X
15. Ślęzak A. A model equation for the gravielectric effect in electrochemical cells. *Biophys Chem*. 1990;38(3):189–199. doi:10.1016/0301-4622(90)87001-2
16. Batko KM, Ślęzak-Prochazka I, Grzegorzczyn S, Ślęzak A. Membrane transport in concentration polarization conditions: Network thermodynamics model equations. *J Por Media*. 2014;17(7):573–586. doi:10.1615/JPorMedia.v17.i7.20
17. Ślęzak A, Grzegorzczyn S, Batko KM. Resistance coefficients of polymer membrane with concentration polarization. *Transp Porous Med*. 2012;95(1):151–170. doi:10.1007/s11242-012-0038-5
18. Batko KM, Ślęzak-Prochazka I, Ślęzak A. Network hybrid form of the Kedem–Katchalsky equations for non-homogenous binary non-electrolyte solutions: Evaluation of P_{ij}^* Peusner's tensor coefficients. *Transp Porous Med*. 2015;106(1):1–20. doi:10.1007/s11242-014-0352-1
19. Ślęzak-Prochazka I, Batko KM, Wąsik S, Ślęzak A. H^* Peusner's form of the Kedem–Katchalsky equations for non-homogeneous non-electrolyte binary solutions. *Transp Porous Med*. 2016;111(2):457–477. doi:10.1007/s11242-015-0604-8
20. Klimek R. Biology of cancer: Thermodynamic answers to some questions. *Neuro Endocrinol Lett*. 2001;22(6):413–416. PMID:11781537.
21. Ślęzak A, Grzegorzczyn SM, Pilis A, Ślęzak-Prochazka I. A method for evaluating the transport and energy conversion properties of polymer biomembranes using the Kedem–Katchalsky–Peusner equations. *Polim Med*. 2023;53(1):25–36. doi:10.17219/pim/161743
22. Batko KM, Ślęzak-Prochazka I, Ślęzak A, Bajdur WM, Włodarczyk-Makula M. Management of energy conversion processes in membrane systems. *Energies*. 2022;15(5):1661. doi:10.3390/en15051661
23. Ahmed J, Gultekinoglu M, Edirisinghe M. Bacterial cellulose micro-nano fibres for wound healing applications. *Biotechnol Adv*. 2020;41:107549. doi:10.1016/j.biotechadv.2020.107549
24. Czaja WK, Young DJ, Kawecki M, Brown RM. The future prospects of microbial cellulose in biomedical applications. *Biomacromolecules*. 2007;8(1):1–12. doi:10.1021/bm060620d
25. Jadczyk K, Ochędzan-Siodłak W. Bacterial cellulose: Biopolymer with novel medical applications. *J Biomater Appl*. 2023;38(1):51–63. doi:10.1177/08853282231184734
26. Grzegorzczyn S. *Effects of Concentration Polarization of Flat Bacterial Cellulose Membranes* [in Polish]. Katowice, Poland: Silesian Medical Academy Press; 2006.
27. Peusner L. Hierarchies of irreversible energy conversion systems: A network thermodynamic approach. I. Linear steady state without storage. *J Ther Biol*. 1983;102(1):7–39. doi:10.1016/0022-5193(83)90260-6
28. Peusner L. Hierarchies of irreversible energy conversion systems. II. Network derivation of linear transport equations. *J Ther Biol*. 1985;115(3):319–335. doi:10.1016/S0022-5193(85)80195-8
29. Kedem O, Caplan SR. Degree of coupling and its relation to efficiency of energy conversion. *Trans Faraday Soc*. 1965;61:1897. doi:10.1039/tf9656101897
30. Caplan SR. Nonequilibrium thermodynamics and its application to bioenergetics. *Curr Top Bioenerg*. 1971;4:1–79. doi:10.1016/B978-0-12-152504-0.50008-3

Enzymatic synthesis of furan-based copolymers: Material characterization and potential for biomedical applications

Synteza enzymatyczna kopolimerów furanowych: charakterystyka materiałów i potencjał do zastosowań medycznych

Martyna Sokołowska^{B–D}, Moein Zarei^{B,C}, Mirosława El Fray^{A,D–F}

Department of Polymer and Biomaterials Science, West Pomeranian University of Technology, Szczecin, Poland

A – research concept and design; B – collection and/or assembly of data; C – data analysis and interpretation; D – writing the article; E – critical revision of the article; F – final approval of the article

Polymers in Medicine, ISSN 0370-0747 (print), ISSN 2451-2699 (online)

Polim Med. 2024;54(1):59–69

Address for correspondence

Mirosława El Fray
Email: mirfray@zut.edu.pl

Funding sources

This work has received funding from the European Union's Horizon 2020 research and innovation program under the Marie Skłodowska-Curie grant agreement No. 872152 (GREEN MAP). An international project co-financed by the program of the Minister of Science and Higher Education entitled "PMW" in the years 2000–2023; contract No. 5091/H2020/2020/2 is acknowledged.

Conflict of interest

None declared

Received on December 26, 2023

Reviewed on February 20, 2024

Accepted on February 20, 2024

Published online on March 27, 2024

Cite as

Sokołowska M, Zarei M, El Fray M. Enzymatic synthesis of furan-based copolymers: Material characterization and potential for biomedical applications. *Polim Med.* 2024;54(1):59–69. doi:10.17219/pim/184535

DOI

10.17219/pim/184535

Copyright

Copyright by Author(s)

This is an article distributed under the terms of the Creative Commons Attribution 3.0 Unported (CC BY 3.0) (<https://creativecommons.org/licenses/by/3.0/>)

Abstract

Background. Today's growing demand for advanced and sustainable polyester materials is driven by an increasing awareness of the environmental impact of traditional materials, emphasizing the need for eco-friendly alternatives. Sustainability has become central in materials development, including the biomedical area, where biobased and environmentally friendly solutions are a rapidly growing field.

Objectives. This research aims to comprehensively evaluate a new enzymatically catalyzed furan-based copolymer, poly(decamethylene furanoate)-*co*-(dilinoleic furanoate) (PDF-DLF), with a 70–30 wt% hard-to-soft segment ratio. Then, its performance across medical applications is explored, with a particular focus on its potential as a nanofibrous scaffolding material.

Materials and methods. PDF-DLF was synthesized from biobased monomers using *Candida antarctica* lipase B (CAL-B) as the biocatalyst. Material characterization included dynamic mechanical thermal analysis (DMTA) to assess the mechanical behavior and thermal properties. Enzymatic degradation studies determined biodegradability, while cytotoxicity tests established in vitro biocompatibility. The copolymer was electrospun into nanofibers, with scanning electron microscopy (SEM) employed to analyze their morphology.

Results. PDF-DLF displays mechanical and thermal properties indicating high storage modulus and 2 main temperature transitions. Enzymatic degradation studies and cytotoxicity assessments confirm biodegradability and in vitro biocompatibility. Electrospinning successfully transformed the copolymer into nanofibers with diameters ranging from 500 nm to 700 nm.

Conclusions. This study significantly advances our understanding of sustainable polyesters with versatile processing capabilities. The successful electrospinning highlights its potential as a biodegradable scaffold for medical engineering, supported by biocompatibility and sufficient mechanical properties. It opens new opportunities for sustainable materials in critical biomedical industries, including tissue engineering.

Key words: 2,5-furandicarboxylate, enzymatic synthesis, bio-based monomers, CAL-B, block copolymers

Streszczenie

Wprowadzenie. Współcześnie rośnie zapotrzebowanie na zaawansowane materiały poliestrowe, które nie tylko wykazują nowatorskie właściwości funkcjonalne, ale także spełniają podwyższone standardy zrównoważonego rozwoju. Wymagania te stają się kluczowe dla rozwoju materiałów, z inżynierią biomateriałów włącznie, gdzie rozwiązania oparte na naturalnych i zrównoważonych surowcach stają się dynamicznie rozwijającym obszarem.

Cel pracy. Celem badań jest ocena i charakterystyka katalizowanego enzymatycznie kopolimeru – poli(furanianu dekametyleny)-co-(furanianu dilynolu) (PDF-DLF) o stosunku segmentów sztywnych do giętkich 70–30 wag% oraz zbadanie jego potencjału w zastosowaniach biomedycznych jako nanowłókniste skafoldy.

Materiał i metody. PDF-DLF został zsyntetyzowany z monomerów pochodzących z biomasy na drodze dwuetapowej syntezy w eterze difenylu, wykorzystując lipazę B *Candida antarctica* jako biokatalizator. Termiczna analiza dynamicznych właściwości mechanicznych (DMTA) pozwoliła na ocenę właściwości mechanicznych i termicznych. Badania degradacji enzymatycznej określiły podatność materiału na biodegradację, a ocena cytotoksyczności in vitro umożliwiła ocenę biokompatybilności. Kopolimer został poddany procesowi elektroprzędzenia w celu wytworzenia nanowłókien, których morfologię oceniono za pomocą skaningowego mikroskopu elektronowego (SEM).

Wyniki. PDF-DLF wykazuje interesujące właściwości mechaniczne i termiczne, wskazujące na wysoki moduł zachowawczy i dwie przemiany temperaturowe. Badania degradacji enzymatycznej i ocena cytotoksyczności potwierdziły biodegradowalność i biokompatybilność materiału. Stosując metodę elektroprzędzenia wytworzono nanowłókna o średnicy mieszczącej się w zakresie od 500 do 700 nm.

Wnioski. Przeprowadzone badania wskazują na szerokie możliwości przetwórcze nowego kopolimeru. Otrzymany materiał jest biodegradowalny, biokompatybilny oraz posiada odpowiednie właściwości mechaniczne oraz termiczne. Co więcej, możliwość przekształcenia materiału w nanowłókna podkreśla jego potencjał zastosowania w inżynierii biomedycznej jako rusztowania dla inżynierii tkankowej.

Słowa kluczowe: kopolimery blokowe, synteza enzymatyczna, bio-pochodne monomery, CAL-B, kwas furanodiakarboksylowy

Background

In the ever-evolving field of biomedical engineering, the quest for sustainable materials that are both environmentally friendly and functionally versatile has never been more necessary. Traditional polymers often rely on petroleum-derived compounds, which not only contribute to environmental pollution but also raise concerns regarding their biocompatibility in biomedical applications.^{1,2}

In this context, 2,5-furandicarboxylic acid (FDCA) emerges as a promising candidate with its unique potential derived from natural resources, offering an alternative to petrochemical monomers.^{3,4} The FDCA is a carbohydrate compound within the furfural group, derived from polysaccharides, starch or lignocellulose. Its chemical structure bears resemblance to terephthalic acid (TPA), the primary petrochemical monomer for the synthesis of semicrystalline aromatic polyesters like poly(ethylene terephthalate) (PET) or poly(butylene terephthalate) (PBT).^{5–8} Notably, numerous publications have demonstrated FDCA's capacity to yield materials with superior properties and enhanced polymer chain orientation compared to their TPA analogs, which imparts significant advantages.^{9–12} Such attributes are particularly critical in the field of tissue engineering, where the mechanical properties of the material must often align with the specific tissue being repaired or replaced.

Interestingly, the versatility of copolymers containing both hard and soft segments offers the advantage of tailoring the final properties to meet the precise requirements of different tissue engineering applications.¹³

A growing interest in the conversion and utilization of biomass, coupled with rapid developments in the biorefinery industry, has introduced a wide spectrum of opportunities in the production of novel monomers and polymers from renewable sources.^{14–19} However, questions persist about the selection of the best and most selective catalyst. Conventionally, PET material is produced in melt processes using antimony-based catalysts in the form of oxide or acetate, known for their high performance and ability to withstand elevated temperatures. Nevertheless, a significant drawback arises from the presence of residual metals within the polymeric material, which is challenging to remove due to strong metal–ester interactions. This can lead to material discoloration and raise environmental concerns upon disposal, potentially disqualifying the polymer's use in various applications, including the medical industry.^{16,20}

To address this issue, we used enzymes that have emerged as a compelling alternative catalyst derived from natural resources. Among these enzymes, *Candida antarctica* lipase B (CAL-B) stands out due to its stability and high reactivity, with its unique structure enabling high region-, enantio- and stereoselectivity, and the ability to function under mild reaction conditions.^{21–24} As confirmed in previous studies, enzymatic catalysis results in a more regular structure in copolyesters compared to metal-catalyzed processes.^{25,26} This feature opens up opportunities to obtain optically pure materials with well-defined chemical structures, particularly valuable in the pharmaceutical industry. The CAL-B-induced polymerization has already been successfully applied to various polymer types,

including polyesters based on 2,5-bis(hydroxymethyl)furan, vegetable oils, sugars, and 3,6-dianhydrohexitol.^{17,27–30} By using monomers and catalysts originating from biomass resources, it is possible to provide sustainable and safe materials for biomedical applications.

Advances in the tissue engineering field have brought much attention regarding scaffold fabrication, such as with biodegradable polyester nanofibers. The justification for using nanofibers for tissue engineering is that the non-woven polymeric meshwork is a close representation of the nanoscale protein fiber meshwork in the native extracellular matrix (ECM).³¹ The electrospinning technique is a promising way to fabricate a controllable, continuous nanofiber scaffold mimicking the ECM structure. Electrospun nanofibers provide a high surface-to-volume ratio and high porosity as a promising scaffold for tissue engineering. Because the degradation behaviors of scaffolds significantly affect new tissue regeneration, the degradation of the material becomes one of the crucial factors when considering using polyester nanofibers as tissue engineering scaffolds.

Objectives

Therefore, we focused on a comprehensive exploration of furan-based copolymers, investigating their potential as scaffolds in the dynamic field of biomedical engineering, and emphasizing their ecological advantages and the integration of enzymatic catalysis for improved sustainability. Our focus extends to the electrospinning technique applied to poly(decamethylene furanoate-dilinoleic furanoate) (PDF-DLF) with 70 wt% PDF segments, introducing a groundbreaking avenue for the creation of sustainable biomaterials. This innovative approach aims to not only assess the biocompatibility and biodegradation profile of the manufactured material but also to evaluate its suitability for processing into nanofibers.

Materials and methods

Materials

The following chemicals were purchased from Sigma-Aldrich (Poznań, Poland): diphenyl ether (DE; ≥99%), mouse fibroblasts L929 EACC, Dulbecco's modified Eagle's medium (DMEM), Dulbecco's phosphate-buffered saline (DPBS), resazurin, penicillin, streptomycin, fetal bovine serum (FBS), and L-glutamine. Polycaprolactone CAPA 6430 was purchased from Perstop (Warrington, UK). 1,10-decanediol (DDO; ≥99%) was acquired from Acros Organics (Geel, Belgium). Dimethyl 2,5-furandicarboxylate (DMFDCA; ≥99%) was obtained from Fluorochem (Łódź, Poland). Dilinoleic diol (DLD; ≥96.5%) (trade name Pripol™ 2033) was obtained from Cargill Bioindustrials

(Gouda, the Netherlands). Chloroform (≥98.5%) was purchased from Chempur (Piekary Śląskie, Poland), and methanol (≥99.8%) was acquired from Stanlab (Lublin, Poland). CAL-B covalently immobilized on polyacrylate beads (300–500 μm, ≥95%; Fermase CALB™ 10000), with a nominal activity of 10 000 PLU/g (propyl laurate units per gram dry weight) was purchased from Fermenta Biotech Ltd (Mumbai, India) and Enzyme Catalyzed Polymers LLC (Akron, USA). Before use, CAL-B was pre-dried under vacuum for 24 h at 40°C, and diphenyl ether was stored over 4 Å molecular sieves. The remaining chemicals were used as received.

CAL-B catalyzed polycondensation

To produce poly(decamethylene furanoate)-*co*-(dilinoleic furanoate) (PDF-DLF) copolyester with a 70–30 wt% hard to soft segment ratio, a 2-step polycondensation reaction was carried out in diphenyl ether at different temperatures, following the protocol outlined in our prior study.³²

Dynamic mechanical thermal analysis

To determine the storage and loss modulus, a PDF-DLF sample for dynamic mechanical thermal analysis (DMTA) was fabricated by melt-pressing within a temperature of 110°C. The specimen had dimensions of 100 μm in thickness, 1 mm in width and 50 mm in length. The measurements were carried out in tensile mode using the DMA Q800 apparatus (TA Instruments, New Castle, USA). The analysis was conducted at a constant frequency of 1 Hz, a heating rate of 2°C/min and an amplitude of 60.

Enzymatic degradation

Enzymatic degradation studies were conducted on melt-pressed films (prepared according to the same protocol as for DMTA studies) using lipase produced by *Pseudomonas cepacia* bacteria. The enzyme was prepared in DPBS sterile buffer with a concentration of 25 U/mL and a pH of 7.25. Sodium azide (0.02%) was added to prevent the bacteria from multiplying. Degradation was carried out at a temperature of 37°C for 35 days, and measuring points were scheduled every 7 days. The degradation medium was replaced every 48 h to maintain enzyme activity. Each measuring point consisted of 4 samples, which were subjected to weight, microscopic and size exclusion chromatography (SEC) analysis. Enzymatic degradation was performed on discs of the test material (6 mm in diameter and 100 μm in thickness). To ensure sterile conditions during the enzymatic degradation tests, all operations were performed under a laminar airflow chamber. The discs of both the test and reference materials were sterilized with UVC radiation for 30 min on each side.

To monitor the enzymatic degradation progress, the samples underwent analysis for mass loss, molecular weight, morphology, and structural changes. Mass loss was quantified using Equation (1), where m_0 is the sample mass before degradation and m_d is the mass of the vacuum-dried sample (37°C, -60 kPa, 48 h) after degradation. Molecular weight analysis was performed via SEC using a Thermo Fisher (HLC-8320) system (Thermo Fisher Scientific, Waltham, USA) equipped with 4 detection systems: a dual absorbance UV (UV; Waters 2487; Waters Corporation, Santa Barbara, USA; wavelength $\lambda = 254\text{--}280$ nm), multi-angle laser light scattering (MALLS, Wyatt DAWN; Waters Corporation), a refractive index detector (RI; Wyatt Optilab®; Waters Corporation), and a viscometer (VIS; Wyatt ViscoStar®; Waters Corporation) detectors. The determination of average molar (apparent) mass (M_n , M_w) and dispersity (D , M_w/M_n) was carried out through gel chromatography. The mobile phase used was CHCl_3 (HPLC grade; Alfa Aesar, Haverhill, USA) at a flow rate of 1 mL/min, a sample concentration of 15 mg/mL and an injected volume of 50 μL . Before injection onto the column, the sample solutions underwent filtering using a 0.20 μm sulphate removal plant (SRP; to extract the sulphates from prior to injection) 20 filter. Absolute molecular masses were derived by processing the data with ASTRA v. 8.1.2 software (Waters Corporation), assuming 100% recovery from the columns.

Structural alterations were evaluated through attenuated total reflection–Fourier-transform infrared (ATR–FTIR) spectra, recorded on a Bruker ALPHA spectrometer (Bruker Corporation, Billerica, USA) within the spectral range of 400–4000 cm^{-1} , employing a resolution of 2 cm^{-1} . Notably, 32 scans were conducted for each sample. Morphological changes were examined utilizing a scanning electron microscope (SEM) equipped with ultra-high resolution (UHR; Hitachi SU8020; Hitachi Ltd., Chiyoda, Tokyo, Japan).

$$\text{Mass loss} = (m_0 - m_d)/m_0 \times 100\% \quad (1)$$

Cytotoxicity assessment

The cytotoxic potential and growth-inhibitory effects of the PDF-DLF copolyester were assessed in cell culture using L929 mouse fibroblasts, following ISO 1993-5 guidelines. L929 cells (passages 9–11) were cultured in growth media consisting of DMEM, 10% FBS, 2 mM L-glutamine, 100 U/mL penicillin, and 100 $\mu\text{g}/\text{mL}$ streptomycin in T25 flasks. For the experiments, sub-confluent T25 culture flasks of L929 cells were trypsinized, and 1×10^4 cells were seeded per well in a 96-well plate. Simultaneously, 100- μm -thick films of PBF-DLF copolyester and a reference material (polycaprolactone PCL CAPA® 6430; Pertrop, Warrington, UK) were cut into three 6 cm^2 samples, which were then sterilized under UV-C light for 15 min on each side. Subsequently, the material samples ($n = 3$)

were sectioned into smaller pieces and placed in a 24-well plate, with 1 mL of medium added to each well. The plates were incubated for 24 h at 37°C in a 5% CO_2 environment to allow the cells to adhere and spread. After incubation, the media was aspirated, and 100 μL of growth media containing extracts from the tested materials were added to the wells (with 6 technical replicates performed for each material). A sham control was prepared by adding 100 μL of pure growth media. The plate was incubated for an additional 24 h, after which cell viability was evaluated using an inverted light microscope (Delta Optical IB-100; Delta Optical, Mińsk Mazowiecki, Poland) and a resazurin viability assay.²³ The assay was conducted with a fluorescent plate reader (Biotek Synergy HTX; BioTek, Winooski, USA) at an excitation wavelength of 540 nm and an emission wavelength of 590 nm. During the resazurin viability assay, complete growth media was added to an empty well without cells to serve as the blank. The results obtained were expressed as the percentage of normalized cell viability (CV%), calculated using Equation (2)³³:

$$\text{CV}\% = (\text{FL}_s - \text{FL}_b)/(\text{FL}_c - \text{FL}_b) \times 100\% \quad (2)$$

where FL is the fluorescence intensity and indices s , b and c refer to sample, blank and control, respectively.

Electrospinning

A systematic exploration of key parameters was conducted to optimize the electrospinning process for the synthesis of our novel polymer. The homemade electrospinning setup employed in this study comprised a syringe pump, a high-voltage power supply and a collector. Various parameters, namely needle diameter, applied voltage, flow rate, distance between the needle tip and the collector, and polymer solution concentration, were subjected to meticulous optimization. The distance between the needle tip and the collector varied at 10 cm, 15 cm and 20 cm, while the applied voltage ranged from 10 kV to 20 kV. Simultaneously, the flow rate of the polymer solution was adjusted at 2 mL/h, 5 mL/h and 10 mL/h. A high-purity solvent, chloroform, was utilized for the polymer solution, and concentrations spanning from 1% to 50% were explored, with observations facilitated using a light microscope Delta Optical Evolution 300 (Delta Optical). The morphology of resulting fibers was examined using a SEM on a Hitachi SU8020 (Hitachi Ltd.) apparatus with UHR.

Results and discussion

Fully biobased PDF-DLF copolymer containing 70 wt% PDF as the hard segments and 30 wt% DLF as the soft segments were successfully synthesized employing temperature-varied 2-step method in diphenyl ether using CAL-B as biocatalyst according to the protocol described in our previous paper³² and as presented in Fig. 1.

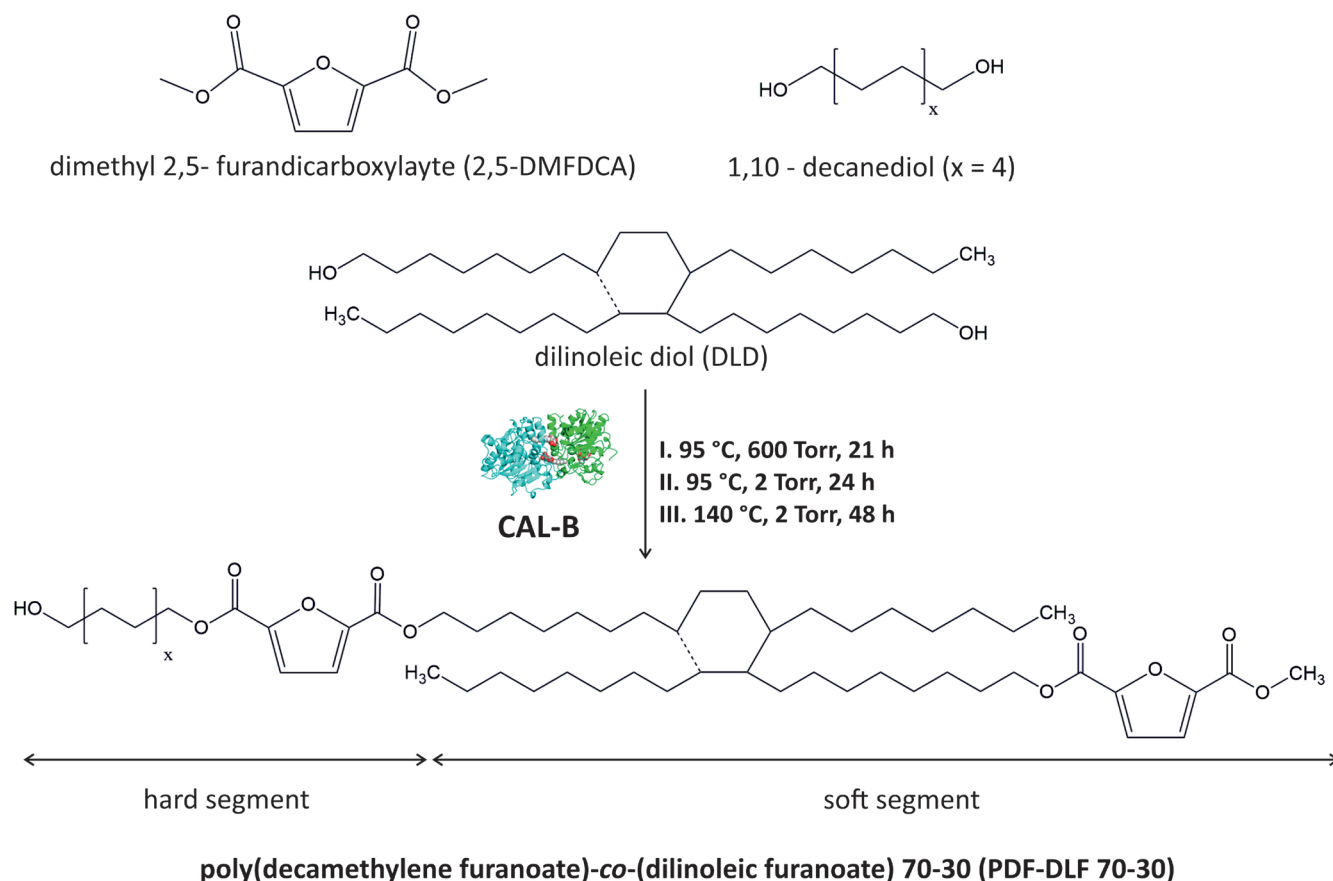


Fig. 1. General scheme of *Candida antarctica* lipase B (CAL-B) catalyzed synthesis of poly(decamethylene furanoate)-co-(dilinoic furanoate) (PDF-DLF) copolyesters via the temperature-varied 2-stage method in diphenyl ether. Adapted from Sokolowska et al.³²

Table 1. Physico-chemical characteristics of poly(decamethylene furanoate)-co-(dilinoic furanoate) (PDF-DLF) copolyester

¹ H NMR ^a	DSC ^a					
	Composition wt% [mol%]	T_g [°C]	T_m [°C]	ΔH_m [J/g]	T_c [°C]	ΔH_c [J/g]
70.0–30.0 (84.0–16.0)	–20	95	34.40	27	30.77	17.4

T_g – glass transition temperature; ΔH_m – melting enthalpy of the hard segments; T_m – melting temperature; T_c – crystallization temperature; ΔH_c – crystallization enthalpy; X_c – total crystalline phase content in the polymer; DSC – differential scanning calorimetry; ^a values provided from Sokolowska et al.³²

In the aforementioned study, we also conducted a comprehensive assessment of the chemical structure, molecular weight, as well as thermal and crystalline properties. A summary of the essential material parameters is given in Table 1. Within the context of this research, we continued our investigation of the PDF-DLF material, with a particular emphasis on evaluating additional critical characteristics that are essential in determining the feasibility of utilizing furan-based copolymers in the biomedical sector.

Dynamic mechanical thermal analysis was performed to assess the mechanical properties of the PDF-DLF material (Fig. 2). The DMTA measurements indicate the viscoelastic characteristics of furan-based copolyesters, shedding light on their thermo-mechanical dynamics. Below the glass transition temperature (T_g), the copolyesters exhibited a consistently stable storage modulus. This stability

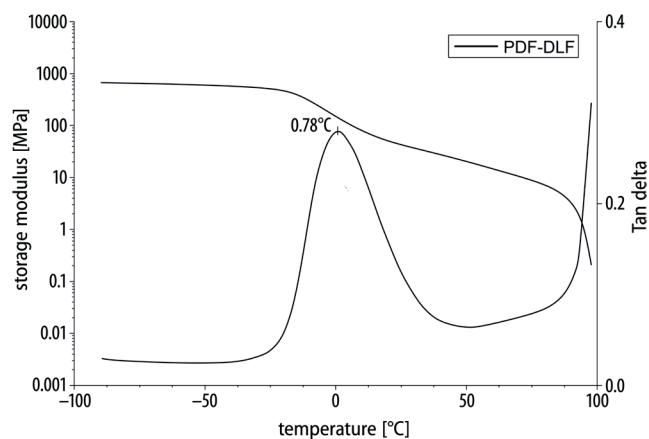


Fig. 2. Dynamic mechanical thermal analysis (DMTA) of poly(decamethylene furanoate)-co-(dilinoic furanoate) (PDF-DLF) copolyester

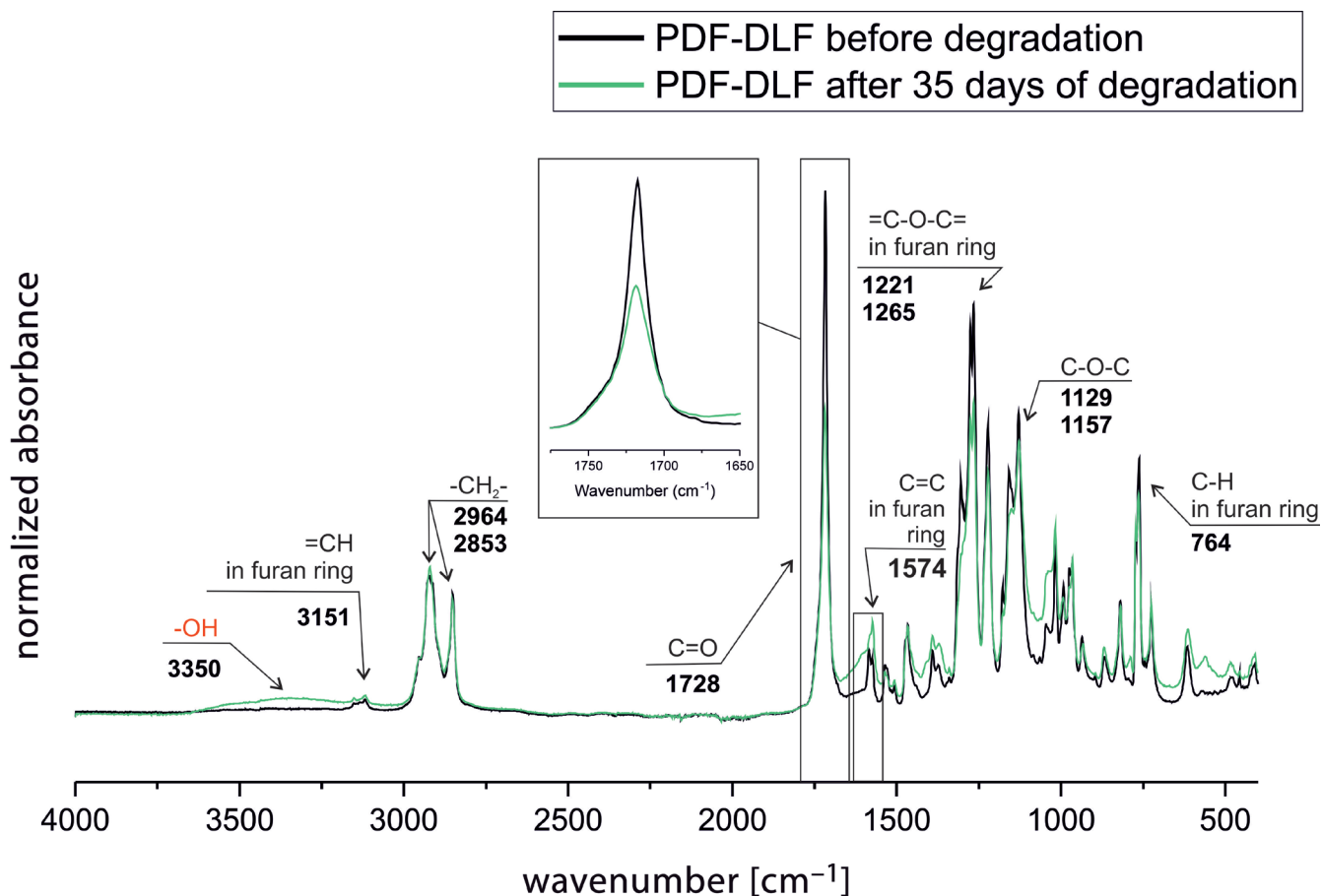


Fig. 3. Fourier-transform infrared (FTIR) spectra of poly(decamethylene furanoate)-*co*-(dilinoleic furanoate) (PDF-DLF) copolymer before and after 35 days of enzymatic degradation

indicates a solid and rigid nature within this temperature range, emphasizing the material's ability to maintain structural integrity and stiffness. Upon reaching the T_g , an evident decline in the storage modulus values was observed. This transition denotes a shift in molecular mobility, typically associated with a reduction in stiffness. The material undergoes a transformation toward increased flexibility, accompanied by heightened molecular movement, influencing its mechanical behavior. This particular aspect is pertinent in applications where flexibility is a critical parameter. As the temperature continued to rise, the storage modulus gradually decreased until reaching the melting temperature (T_m). This gradual reduction in modulus values signified a transition from a more solid to a more liquid-like state.

Enzymatic degradation played a pivotal role in assessing the suitability of the PDF-DLF copolymer for biomedical applications. The material, subjected to lipase from *P. cepacia* in a DPBS solution, aimed to simulate physiological conditions within the human body. Understanding how the polymer undergoes enzymatic breakdown was essential for ensuring its compatibility with biological systems.

The FTIR analysis before and after degradation revealed changes in intensities and shifts in peaks of characteristic functional groups (Fig. 3). A clear decrease in intensity

Table 2. Molecular weight of poly(decamethylene furanoate)-*co*-(dilinoleic furanoate) (PDF-DLF) copolyester before and after degradation

Material	SEC		
	M_n [g/mol]	M_w [g/mol]	\mathcal{D}
PDF-DLF before degradation	12,200	43,600	3.6
PDF-DLF after 35 days of degradation	7,800	30,700	4.0

M_n – number average molecular mass, M_w – weight average molecular mass, \mathcal{D} – dispersity index.

is visible in the carbonyl group region (C=O), potentially indicating hydrolysis of ester bonds and monomer formation. This is further supported by the appearance of a peak arising from –OH groups. Additionally, changes are noted in the region where C=C bonds in the furan ring appear. These structural alterations suggest that the material undergoes disintegration under the influence of the enzyme.

To verify changes in the molecular weight, SEC measurements were conducted on materials both before and after 35 days of degradation. The observed molar mass changes (Table 2), along with the increased dispersity index, suggest that the material has undergone enzymatic degradation. The degradation of polyesters with semi-aromatic structures is typically known to be relatively inefficient. However, in this case, it appears that the enzyme is targeting

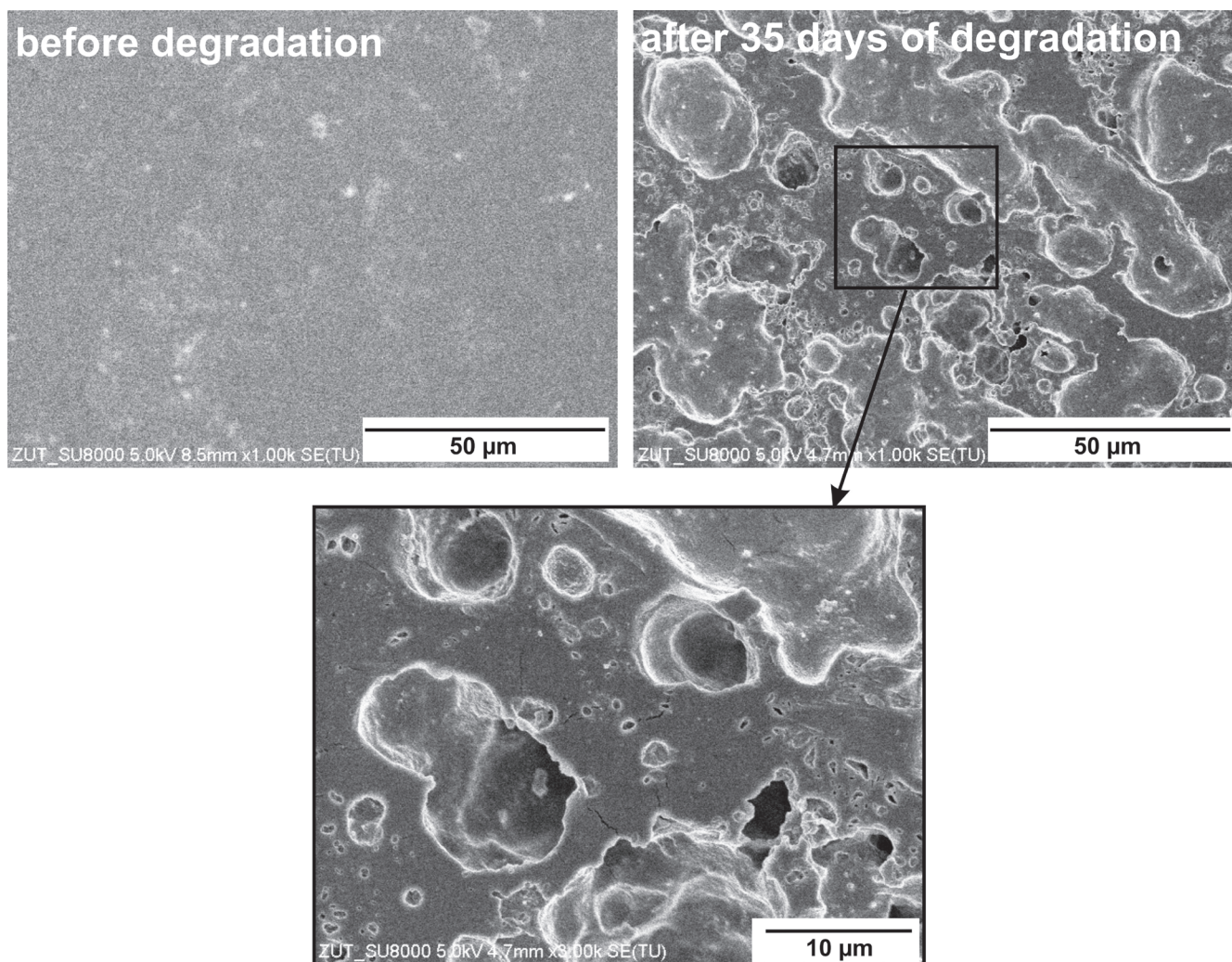


Fig. 4. Scanning electron microscopy (SEM) images of poly(decamethylene furanoate)-co-(dilinoic furanoate) (PDF-DLF) copolyester before and after 35 days of enzymatic degradation using lipase from *Pseudomonas cepacia*

the amorphous regions, specifically the DLF soft segments. The visible alterations in molecular weight serve as a clear indicator of ester bond cleavage. This phenomenon is significant as it highlights the susceptibility of specific regions to enzymatic attack, contributing to the molecular rearrangement and changes observed.

Interestingly, SEM analysis displayed noticeable surface changes, including breaks and holes following degradation. Figure 4 illustrates these alterations on the material surface, indicating a localized impact. The results suggest that enzymatic degradation likely occurs through a surface erosion mechanism rather than extensive bulk breakdown.

Finally, the detected mass loss of slightly over 2% during the 35 days indicated relatively slow enzymatic degradation (Fig. 5). This behavior is typical of the first phase of enzyme-assisted chemical hydrolysis, and only after this is usually followed by metabolizing the fragments and rapid loss of polymer mass.

All these factors collectively suggest that PDF-DLF is susceptible to enzyme-assisted chemical hydrolysis, despite no significant mass loss. However, further in-depth

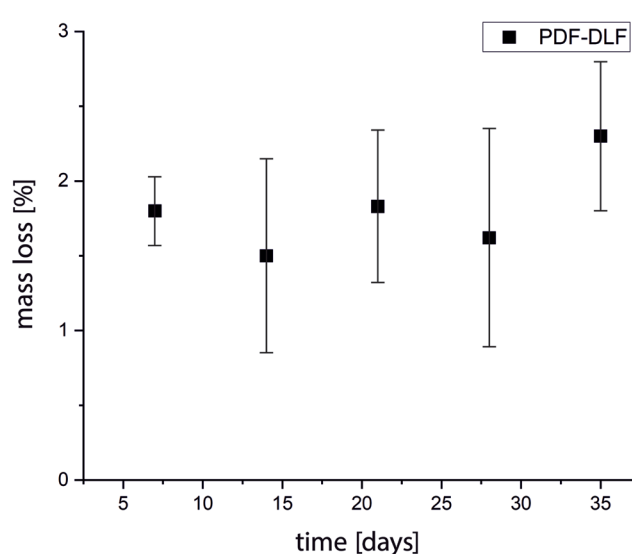


Fig. 5. Mass loss of poly(decamethylene furanoate)-co-(dilinoic furanoate) (PDF-DLF) copolyester during enzymatic degradation

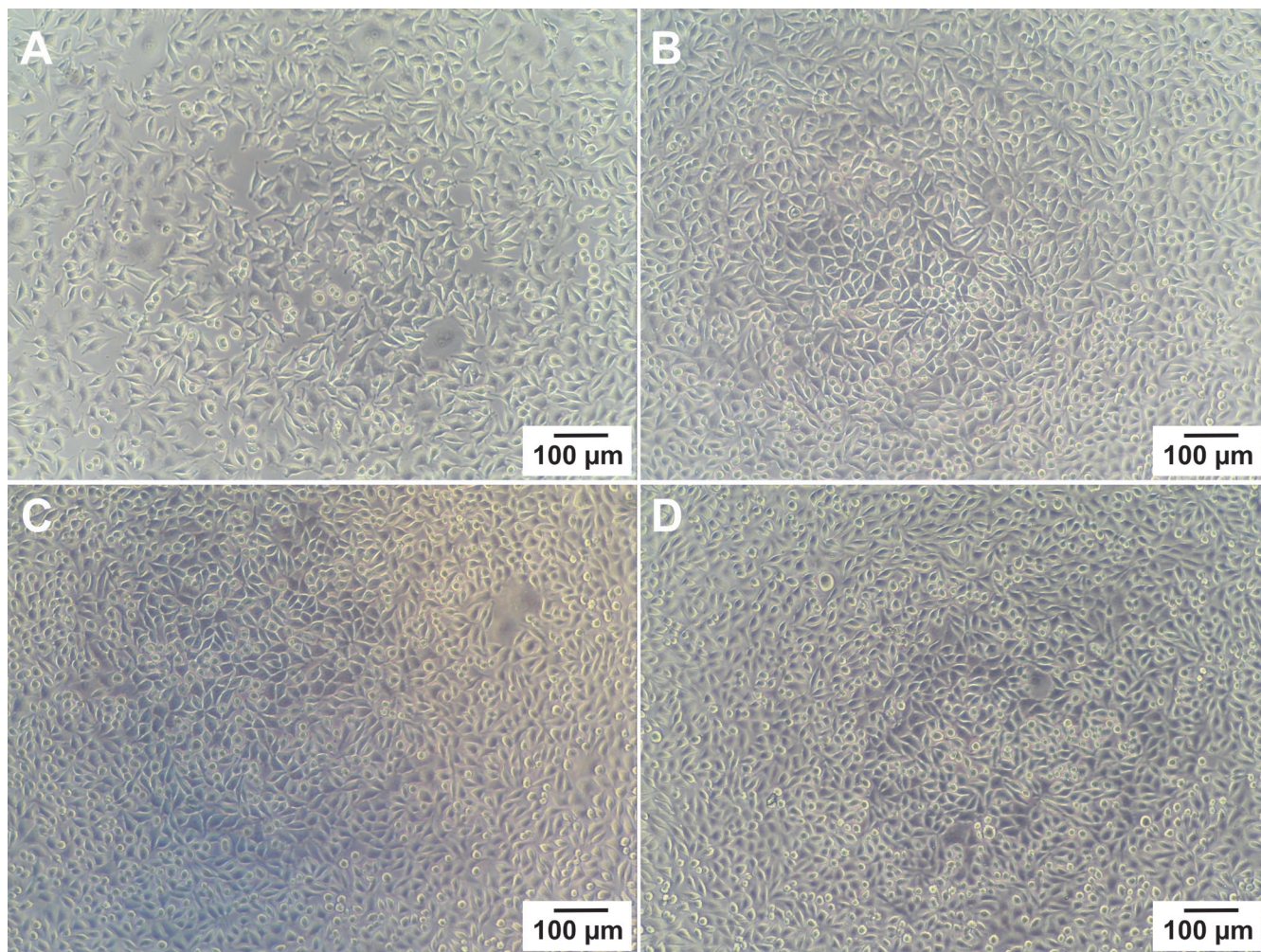


Fig. 6. Representative micrographs of L929 cells seeded at 10,000 cells per well. A. Cells 24 h after seeding; B. Cells 48 h of culture without extracts. Cells were cultured for 24 h with extracts from tested poly(decamethylene furanoate)-co-(dilinoleic furanoate) (PDF-DLF) material (C) and reference material (PCL sample) (D)

investigation and research in this matter are necessary, potentially involving the use of different enzymes. For example, enzymatic degradation was also studied utilizing recombinant *Thermobifida cellulosilytica* cutinase 1 (Thc_Cut1), cutinase from *Humicola insolens* (HiC) and lipase from *Porcine pancreas* (LPP) on poly(ethylene furanoate) (PEF), revealing promising results and correlations.^{34–38} Thc_Cut1 exhibited higher activity on higher molecular weight PEF powders, releasing 13 mM of FDCA after 72 h.³⁶ Crystallinity significantly impacted degradation rates, accelerating hydrolysis in cases of lower crystallinity. Conversely, HiC demonstrated greater activity than Thc_Cut1 on the highly crystalline forms of PEF, thereby slowing enzymatic hydrolysis.³⁴

Moreover, a recent study by Kim et al. explored the enzymatic degradation of poly(butylene adipate)-co-(butylene furanoate) (PBAF) copolymers with varying furan ring fractions (50 mol% and 70 mol%) using *Thermomyces lanuginosus* lipase (TLL), a highly selective catalyst.³⁹ The study revealed that PBAF with a 50 mol% furan ring fraction experienced a mass loss exceeding

80% within a few days, while PBAF with a 70 mol% furan ring fraction exhibited only around 1–2% mass loss over the same period. These findings align with our research, indicating that a higher proportion of furan units in the copolymer results in a slower rate of degradation. Hence, careful design considerations for such materials are essential to accelerate this process, particularly when attempting to meet the requirements for medical applications. All enzymes used for the enzymatic degradation studies acknowledged above were in their native form (not immobilized).

Given the potential application of the copolymer in the biomedical field, specifically in contact with the body, it became imperative to assess the material's biocompatibility. To investigate any potential cytotoxic or growth-inhibitory effects of the PDF-DLF copolyester, an *in vitro* indirect contact assay was conducted using L929 murine fibroblasts. Over 24 h, cells were exposed to extracts from both the reference material (PCL) and the PDF-DLF samples, and cell viability was assessed with light microscopy and a resazurin viability assay. Following

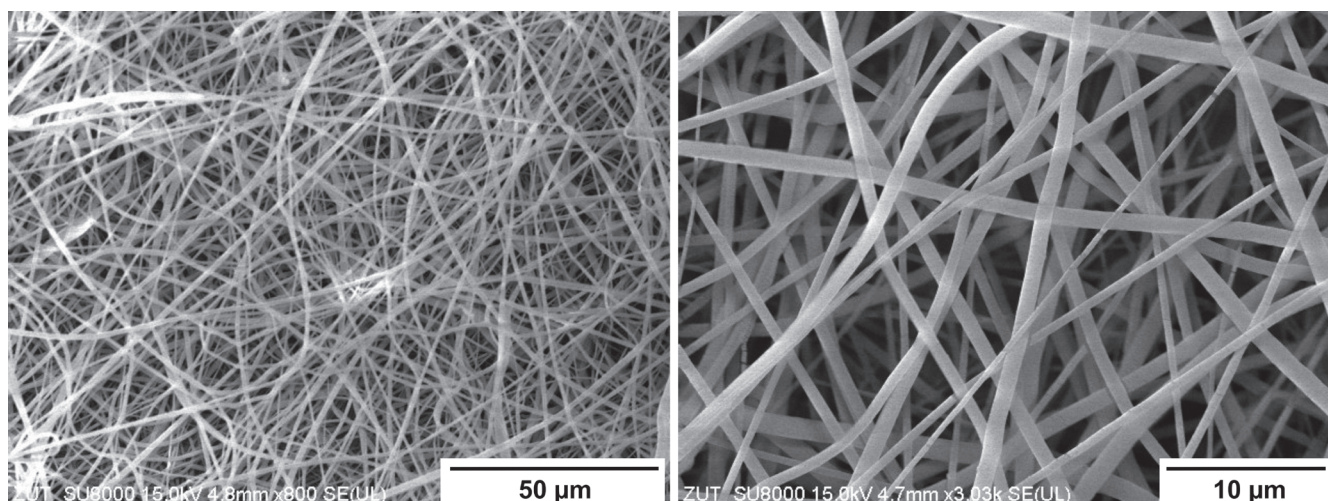


Fig. 7. Scanning electron microscopy (SEM) micrographs of the obtained fibers from poly(decamethylene furanoate)-*co*-(dilinoleic furanoate) (PDF-DLF) copolymer using CHCl_3 as the solvent with 30% wt/vol% concentration

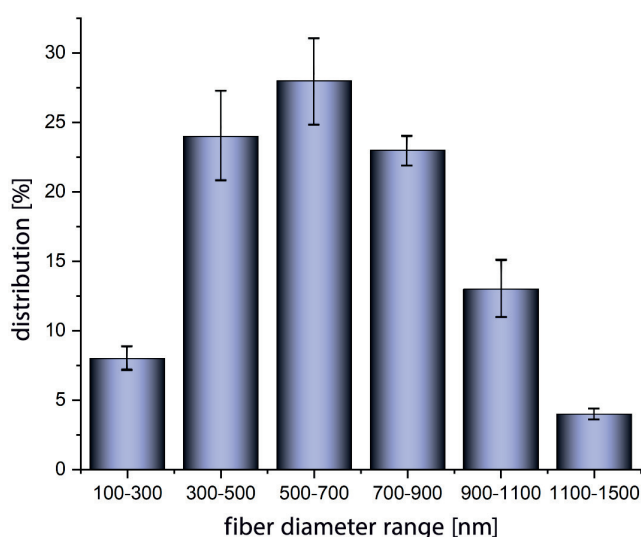


Fig. 8. Fiber diameter distribution was obtained from scanning electron microscopy (SEM) micrographs of the copolymer using ImageJ software

the 24-h incubation, noticeable adverse effects of both PCL and PDF-DLF materials were observed (Fig. 6). Importantly, the absence of toxic contaminants was confirmed by the robust growth and typical cell morphology observed when cells were treated with extracts from control, reference and tested materials. The microscopic observations were supported by the results of the resazurin viability assay, from which normalized viability values were calculated. These values were in accordance with the visual evaluation. Considering the typical doubling time of L929 cells is approx. 20–22 h, viability values below 70% are indicative of cytotoxicity according to ISO10993. The average values of normalized cell viability (CV%) for PCL and PDF-DLF were $97 \pm 5\%$ and $95 \pm 7\%$, respectively.

Ultimately, PDF-DLF underwent a preliminary study involving electrospinning to assess its processability and suitability for application in the field of tissue engineering as scaffolds.

In the course of our investigations, it was observed that polymer concentrations below 20% resulted in electro-spraying, revealing inadequate fiber formation, while a concentration of 50% led to the formation of a bulk structure. This was attributed to the solvent evaporation rate on crystalline phase formation of the polymer during electrospinning, which can be irrespective of polymer drawing forces.⁴⁰

Subsequent experimental studies identified that the optimum polymer concentration of 30%, coupled with a 24-gauge needle, yielded the most favorable electrospinning outcomes. The fine-tuning process extended beyond concentration adjustment and encompassed modifications to key electrospinning parameters, including the distance between the needle tip and the collector, applied voltage and polymer solution flow rate. Through systematic adjustments, the following optimal parameters were identified; a distance of 20 cm, a flow rate of 5 mL/h and an applied voltage of 15 kV. The establishment of these conditions not only enabled the reproducibility of the electrospinning process but also underscored the importance of optimal parameters in governing the morphological characteristics of the resulting fibers.

Figure 7 presents the SEM images of the obtained fibers through the optimized parameters of the electrospinning. The acquired fibers exhibit structural homogeneity and uniform distribution. Given the utilization of a flat aluminum collector during the electrospinning process, the resulting fibers exhibit a random orientation. Figure 8 presents a comprehensive analysis of fiber diameters and their distribution, conducted through ImageJ software (National Institutes of Health (NIH), Bethesda, USA). The findings reveal that, for the copolymer under investigation, the majority of fiber diameters fall within the range of 500–700 nm. This outcome underscores the electrospinning potential of the polymer, showcasing characteristics similar to the ECM.^{41,42} The versatility of these fibers extends their applicability to diverse domains, including, but not only limited to, tissue engineering.

Conclusions

In response to the increasing demand for sustainable materials, particularly in the polyester domain, this research has been dedicated to the comprehensive evaluation of a furan-based copolymer, PDF-DLF. This copolymer, with a 70–30 wt% hard-to-soft segment ratio, was examined for its potential in medical applications, with a specific emphasis on its viability as a scaffolding material for tissue engineering.


The results underscore the significant steps made in the development of sustainable materials with versatile processing capabilities. PDF-DLF exhibited promising mechanical and thermal properties. It was successfully electrospun into nanofibers, with diameters ranging from 500 nm to 700 nm, holding promise for the creation of biodegradable scaffolds for medical engineering.

Furthermore, biocompatibility assessments revealed promising results. In vitro studies using L929 murine fibroblasts demonstrated a high cell viability, indicating the material's compatibility and lack of cytotoxic effects. Enzymatic degradation studies revealed structural and molecular changes, as well as localized impact on the polymer's surfaces. Although registered mass loss is not significant, it suggests material susceptibility to enzymatic degradation. However, while this study has unveiled promising aspects of PDF-DLF, further research is imperative. Deeper research on enzymatic degradation mechanisms, which could utilize different enzymes, is recommended.

In conclusion, the findings of this research not only contribute to the expanding knowledge of sustainable materials but also open new avenues for PDF-DLF in critical industries, particularly in the ever-evolving field of biomedical engineering. The convergence of biocompatibility, mechanical properties and processing capabilities in PDF-DLF suggests a multifaceted solution to environmental and engineering challenges, warranting continued exploration and refinement.

ORCID iDs

Martyna Sokołowska  <https://orcid.org/0000-0002-7432-1662>

Moein Zarei  <https://orcid.org/0000-0002-0391-8322>

Mirosława El Fray  <https://orcid.org/0000-0002-2474-3517>

References

- Eerhart AJE, Faaij APC, Patel MK. Replacing fossil based PET with bio-based PEF: Process analysis, energy and GHG balance. *Energy Environ Sci*. 2012;5(4):6407. doi:10.1039/c2ee02480b
- Abdolmohammadi S, Ganseboom D, Goyal S, et al. Analysis of the amorphous and interphase influence of comonomer loading on polymer properties toward forwarding bioadvantaged copolyamides. *Macromolecules*. 2021;54(17):7910–7924. doi:10.1021/acs.macromol.1c00651
- Sousa AF, Vilela C, Fonseca AC, et al. Biobased polyesters and other polymers from 2,5-furandicarboxylic acid: A tribute to furan excellence. *Polym Chem*. 2015;6(33):5961–5983. doi:10.1039/C5PY00686D
- Esteban J, Yustos P, Ladero M. Catalytic processes from biomass-derived hexoses and pentoses: A recent literature overview. *Catalysts*. 2018;8(12):637. doi:10.3390/catal8120637
- Kwiatkowska M, Kowalczyk I, Kwiatkowski K, Szymczyk A, Roslaniec Z. Fully biobased multiblock copolymers of furan-aromatic polyester and dimerized fatty acid: Synthesis and characterization. *Polymer*. 2016;99:503–512. doi:10.1016/j.polymer.2016.07.060
- Bozell JJ, Petersen GR. Technology development for the production of biobased products from biorefinery carbohydrates: The US Department of Energy's "Top 10" revisited. *Green Chem*. 2010;12(4):539. doi:10.1039/b922014c
- Zhu J, Cai J, Xie W, et al. Poly(butylene 2,5-furan dicarboxylate), a biobased alternative to PBT: Synthesis, physical properties, and crystal structure. *Macromolecules*. 2013;46(3):796–804. doi:10.1021/ma3023298
- Zhou W, Zhang Y, Xu Y, et al. Synthesis and characterization of bio-based poly(butylene furandicarboxylate)-b-poly(tetramethylene glycol) copolymers. *Polym Degrad Stab*. 2014;109:21–26. doi:10.1016/j.polymdegradstab.2014.06.018
- Ma J, Pang Y, Wang M, Xu J, Ma H, Nie X. The copolymerization reactivity of diols with 2,5-furandicarboxylic acid for furan-based copolyester materials. *J Mater Chem*. 2012;22(8):3457. doi:10.1039/c2jm15457a
- Bianchi E, Soccio M, Siracusa V, Gazzano M, Thiyagarajan S, Lotti N. Poly(butylene 2,4-furanoate), an added member to the class of smart furan-based polyesters for sustainable packaging: Structural isomerism as a key to tune the final properties. *ACS Sust Chem Eng*. 2021;9(35):11937–11949. doi:10.1021/acssuschemeng.1c04104
- Papageorgiou GZ, Papageorgiou DG, Tsanaktis V, Bikiaris DN. Synthesis of the bio-based polyester poly(propylene 2,5-furan dicarboxylate): Comparison of thermal behavior and solid state structure with its terephthalate and naphthalate homologues. *Polymer*. 2015;62:28–38. doi:10.1016/j.polymer.2015.01.080
- Jiang M, Liu Q, Zhang Q, Ye C, Zhou G. A series of furan-aromatic polyesters synthesized via direct esterification method based on renewable resources. *J Polym Sci A Polym Chem*. 2012;50(5):1026–1036. doi:10.1002/pola.25859
- Manuel HJ, Gaymans RJ. Segmented block copolymers based on poly(butylene terephthalate) and telechelic polyesters and polyamides of dimerized fatty acids. *Polymer*. 1993;34(20):4325–4329. doi:10.1016/0032-3861(93)90196-H
- Mathers RT. How well can renewable resources mimic commodity monomers and polymers? *J Polym Sci A Polym Chem*. 2012;50(1):1–15. doi:10.1002/pola.24939
- Jiang Y, Woortman A, Van Ekenstein G, Loos K. Enzyme-catalyzed synthesis of unsaturated aliphatic polyesters based on green monomers from renewable resources. *Biomolecules*. 2013;3(4):461–480. doi:10.3390/biom3030461
- Jiang Y, Woortman AJJ, Alberda Van Ekenstein GOR, Loos K. Environmentally benign synthesis of saturated and unsaturated aliphatic polyesters via enzymatic polymerization of biobased monomers derived from renewable resources. *Polym Chem*. 2015;6(30):5451–5463. doi:10.1039/C5PY00660K
- Jiang Y, Loos K. Enzymatic Synthesis of biobased polyesters and polyamides. *Polymers (Basel)*. 2016;8(7):243. doi:10.3390/polym8070243
- Fei X, Wang J, Zhu J, Wang X, Liu X. Biobased poly(ethylene 2,5-furanoate): No longer an alternative, but an irreplaceable polyester in the polymer industry. *ACS Sust Chem Eng*. 2020;8(23):8471–8485. doi:10.1021/acssuschemeng.0c01862
- Jiang Y, Woortman AJJ, Alberda Van Ekenstein GOR, Petrović DM, Loos K. Enzymatic synthesis of biobased polyesters using 2,5-Bis(hydroxymethyl)furan as the building block. *Biomacromolecules*. 2014;15(7):2482–2493. doi:10.1021/bm500340w
- Douka A, Vouyiouka S, Papaspyridi LM, Papaspyrides CD. A review on enzymatic polymerization to produce polycondensation polymers: The case of aliphatic polyesters, polyamides and polyesteramides. *Prog Polym Sci*. 2018;79:1–25. doi:10.1016/j.progpolymsci.2017.10.001
- Puskas JE, Sen MY, Seo KS. Green polymer chemistry using nature's catalysts, enzymes. *J Polym Sci A Polym Chem*. 2009;47(12):2959–2976. doi:10.1002/pola.23351
- Kobayashi S. Lipase-catalyzed polyester synthesis: A green polymer chemistry. *Proc Jpn Acad Ser B Phys Biol Sci*. 2010;86(4):338–365. doi:10.2183/pjab.86.338
- Kobayashi S. Enzymatic polymerization: A new method of polymer synthesis. *J Polym Sci A Polym Chem*. 1999;37(16):3041–3056. doi:10.1002/(SICI)1099-0518(19990815)37:16<3041::AID-POLA1>3.0.CO;2-V

24. Kobayashi S, Uyama H, Kimura S. Enzymatic polymerization. *Chem Rev.* 2001;101(12):3793–3818. doi:10.1021/cr990121I
25. Sokołowska M, Nowak-Grzebyta J, Stachowska E, El Fray M. Enzymatic catalysis in favor of blocky structure and higher crystallinity of poly(butylene succinate)-co-(dilinoic succinate) (PBS-DLS) copolymers of variable segmental composition. *Materials (Basel).* 2022;15(3):1132. doi:10.3390/ma15031132
26. Sokołowska M, Stachowska E, Czaplicka M, El Fray M. Effect of enzymatic versus titanium dioxide/silicon dioxide catalyst on crystal structure of 'green' poly[(butylene succinate)-co-(dilinoic succinate)] copolymers. *Polym Int.* 2021;70(5):514–526. doi:10.1002/pi.6104
27. Skoczinski P, Espinoza Cangahuala MK, Maniar D, Albach RW, Bittner N, Loos K. Biocatalytic synthesis of furan-based oligomer diols with enhanced end-group fidelity. *ACS Sust Chem Eng.* 2020;8(2):1068–1086. doi:10.1021/acsschemeng.9b05874
28. Tsujimoto T, Uyama H, Kobayashi S. Enzymatic synthesis of cross-linkable polyesters from renewable resources. *Biomacromolecules.* 2001;2(1):29–31. doi:10.1021/bm000097h
29. Japu C, Martínez De Ilarduya A, Alla A, Jiang Y, Loos K, Muñoz-Guerra S. Copolyesters made from 1,4-butanediol, sebacic acid and D-glucose by melt and enzymatic polycondensation. *Biomacromolecules.* 2015;16(3):868–879. doi:10.1021/bm501771e
30. Juais D, Naves AF, Li C, Gross RA, Catalani LH. Isosorbide polyesters from enzymatic catalysis. *Macromolecules.* 2010;43(24):10315–10319. doi:10.1021/ma1013176
31. Dong Y, Liao S, Ngiam M, Chan CK, Ramakrishna S. Degradation behaviors of electrospun resorbable polyester nanofibers. *Tissue Eng Part B Rev.* 2009;15(3):333–351. doi:10.1089/ten.teb.2008.0619
32. Sokołowska M, Nowak-Grzebyta J, Stachowska E, et al. Enzymatically catalyzed furan-based copolyesters containing dilinoic diol as a building block. *RSC Adv.* 2023;13(32):22234–22249. doi:10.1039/D3RA03885H
33. Ciecholewska-Juśko D, Żywicka A, Junka A, et al. Superabsorbent cross-linked bacterial cellulose biomaterials for chronic wound dressings. *Carbohydr Polym.* 2021;253:117247. doi:10.1016/j.carbpol.2020.117247
34. Weinberger S, Haernvall K, Scaini D, et al. Enzymatic surface hydrolysis of poly(ethylene furanoate) thin films of various crystallinities. *Green Chem.* 2017;19(22):5381–5384. doi:10.1039/C7GC02905E
35. Weinberger S, Canadell J, Quartinello F, et al. Enzymatic degradation of poly(ethylene 2,5-furanoate) powders and amorphous films. *Catalysts.* 2017;7(11):318. doi:10.3390/catal7110318
36. Pellis A, Haernvall K, Pichler CM, Ghazaryan G, Breinbauer R, Guebitz GM. Enzymatic hydrolysis of poly(ethylene furanoate). *J Biotechnol.* 2016;235:47–53. doi:10.1016/j.jbiotec.2016.02.006
37. Gigli M, Quartinello F, Soccio M, et al. Enzymatic hydrolysis of poly(1,4-butylene 2,5-thiophenedicarboxylate) (PBTF) and poly(1,4-butylene 2,5-furandicarboxylate) (PBF) films: A comparison of mechanisms. *Environ Int.* 2019;130:104852. doi:10.1016/j.envint.2019.05.046
38. Lalanne L, Nyanhongo GS, Guebitz GM, Pellis A. Biotechnological production and high potential of furan-based renewable monomers and polymers. *Biotechnol Adv.* 2021;48:107707. doi:10.1016/j.biotechadv.2021.107707
39. Kim H, Kim T, Choi S, et al. Remarkable elasticity and enzymatic degradation of bio-based poly(butylene adipate-co-furanoate): Replacing terephthalate. *Green Chem.* 2020;22(22):7778–7787. doi:10.1039/D0GC01688H
40. Costa LMM, Bretas RES, Gregorio R. Effect of solution concentration on the electrospray/electrospinning transition and on the crystalline phase of PVDF. *Mater Sci Appl.* 2010;01(4):247–252. doi:10.4236/msa.2010.14036
41. Zarei M, Żwir MJ, Wiśniewska E, Michalkiewicz B, El Fray M. Melt and solution processability of poly(butylene succinate-dilinoic succinate) copolymers modified with poly(ethylene glycol) using 3D printing and electrospinning. *Polym Adv Technol.* 2023;34(11):3586–3602. doi:10.1002/pat.6159
42. Wei Q, Tao D, Xu Y. Nanofibers: principles and manufacture. In: Wei Q, ed. *Functional Nanofibers and Their Applications.* Amsterdam, the Netherlands–New York, USA: Elsevier; 2012:3–21. doi:10.1533/9780857095640.1.1

A review on topical ophthalmic drug delivery system: Reference to viscosity enhancer

Pravin Kondiba Pawar^C, Raju Dubaji Rathod^{B,D}, Satyajeet Ramesh Jagadale^{B,D}

Department of Pharmaceutics, Dr. Shivajirao Kadam College of Pharmacy, Kasabe Digranj, Sangli, Affiliated to Shivaji University, Kolhapur

A – research concept and design; B – collection and/or assembly of data; C – data analysis and interpretation; D – writing the article; E – critical revision of the article; F – final approval of the article

Polymers in Medicine, ISSN 0370-0747 (print), ISSN 2451-2699 (online)

Polim Med. 2024;54(1):71–84

Address for correspondence

Pravin Kondiba Pawar
E-mail: pkpawar80@yahoo.com

Funding sources

None declared

Conflict of interest

None declared

Acknowledgements

The authors would like to thank Prof. D.D. Chougule, a Director of Dr. Shivajirao Kadam College of Pharmacy (Kasabe Digranj, Sangli) for providing infrastructure and facilities to complete this review.

Received on April 6, 2023

Reviewed on May 18, 2023

Accepted on May 22, 2023

Published online on March 27, 2024

Abstract

The eye is the most accessible site for topical drug delivery. Drug's ocular bioavailability is quite low when administered topically as eye drops. Viscosity enhancers are used to increase ocular bioavailability by extending the precorneal residence time of the drug at the ocular site. Cellulose, polyalcohol and polyacrylic acid are examples of hydrophilic viscosity enhancers. The addition of viscosity modifiers increases the amount of time the drug is in contact with the ocular surface. Several polysaccharides have been studied as excipients and viscosity boosters for ocular formulations, including cellulose derivatives such as chitosan (CS), xyloglucan and arabinogalactan (methylcellulose, hydroxyethylcellulose, hydroxypropylmethylcellulose (HPMC), and sodium carboxymethylcellulose). Viscosity-increasing substances reduce the surface tension, extend the corneal contact time, slow the drainage, and improve the bioavailability. Chitosan is a viscosity enhancer that was originally thought to open tight junction barrier cells in the epithelium. Chitosan thickens the medication solution and allows it to penetrate deeper. Alginate is an anionic polymer with carboxyl end groups that has the highest mucoadhesive strength and is used to improve penetration. Carboxymethylcellulose (CMC), a polysaccharide with a high molecular weight, is one of the most common viscous polymers used in artificial tears to achieve their longer ocular surface residence period. Hyaluronic acid (HA) is biocompatible and biodegradable in nature, and it is available in ocular sustained-release dose forms. A polymer known as xanthan gum is used to increase viscosity. At 0.2% concentration, carbomer forms a highly viscous gel.

Key words: polysaccharides, mucoadhesive strength, retinal bioavailability, viscosity enhancer

Cite as

Pawar PK, Rathod RD, Jagadale SR. A review on topical ophthalmic drug delivery system: Reference to viscosity enhancer. *Polim Med.* 2024;54(1):71–84.
doi:10.17219/pim/166413

DOI

10.17219/pim/166413

Copyright

Copyright by Author(s)

This is an article distributed under the terms of the Creative Commons Attribution 3.0 Unported (CC BY 3.0) (<https://creativecommons.org/licenses/by/3.0/>)

Introduction

Topical administration to the eye is the method most frequently used for the treatment of different eye conditions. Ocular medications are only partially absorbed due to the eye's strong defensive mechanisms. Some of the processes that clear debris from the surface of the eye include drainage, baseline lachrymation, reflex lachrymation, and blinking. Drug absorption is further aided by the cornea's physiology, composition and barrier performance. Toxic side effects or prolonged contact with very concentrated liquids may cause eye damage. The use of a mucoadhesive, which has been helpful in mucosa and oral applications, was another technique for refining the ocular dose form. One investigation focused on the interaction of mucins with natural and synthetic polymers. Interactions with the ocular structures or mucus layer required longer pre-corneal preparation. Several mucoadhesive polymers were found to enhance drug absorption, accelerate wound healing and safeguard epithelial cells.¹

The eye is an extensive organ with unique structure and physiology that obstructs the entry of medicines into the intended ocular locations. Researchers have been interested in effective topical administration for many years. Their goal has been to increase medication residence time and achieve proper ocular penetration.² Precorneal, corneal and blood–corneal barriers, among others, prevent the effective transport of drugs to the ocular regions. Topical, intravitreal, intraocular, juxtasclear, subconjunctival, intracameral, and retrobulbar delivery methods are available for ocular administration. More than 95% of commercially available ophthalmic formulations are in liquid state.³

Although many medications are effective in treating the majority of ocular diseases, there are numerous ocular barriers, including tear film, corneal, conjunctival, and blood–ocular barriers, which limit the therapeutic efficiency of these medications. Both tear production and blinking deplete conventional eye drops. The bioavailability of these drugs is thereby reduced by 90%. As per ocular delivery concern, the first rate-limiting step is cornea. Therefore, to achieve higher bioavailability of therapeutic agent at any dose, the minimal penetration is achieved through the cornea. The cornea is made up of epithelium, stroma and endothelium. Only tiny, lipophilic medications can pass through epithelium, but hydrophilic medications can flow through the stroma. The endothelium protects the corneal transparency and allows for the targeted entrance of hydrophilic medicines and macromolecules into the aqueous humour.^{4,5} Comparatively speaking, the conjunctiva has less of an impact on drug absorption than the cornea, yet specific macromolecular nanomedicines, peptides and oligonucleotides easily reach the deep layers of the eye through these tissues. Xenobiotic substances cannot enter the bloodstream because of the blood–ocular barriers. The blood–aqueous barrier (BAB) is found in the anterior portion of the eye, and the blood–retinal barrier (BRB) is found in the posterior segment.

The goal of this review is to discuss different viscosity-enhancing agents that are used for improving ocular bioavailability. To achieve and maintain an optimal medication concentration with the least amount of the active therapeutic component, successful ocular absorption requires both effective precorneal residence time and appropriate corneal penetration.

In accordance with several literature reviews, this study focused on a few additional properties of viscosity-enhancing agents that enhance residence duration and improve corneal permeability in the ocular region and are useful for formulation issues.

Current review intends to summarize the existing conventional formulations for ocular delivery and their advancements, followed by polymers that are used in the ocular drug delivery system based on the formulation developments.

Gap between the ocular regions

This review aimed to fill in the gaps left by earlier studies that have been published on the viscosity-enhancing agents used in the administration of ocular medication. Various anatomical features of the eye, various ocular diseases, barriers to ocular delivery, various methods of ocular administration, classification of dosage forms, numerous nanostructured platforms, characterization approaches, strategies to improve ocular delivery, and future technologies were just some of the topics covered in a thorough description of ocular drug delivery from various directions.

Anatomy and physiology

The eyeball's 3 layers are an inner coat, a uveal coat, and the sclera and the cornea on the outside (retina). The sclera is made up of sphere-like structures, and the cornea and sclera are both made up of fibers. The flexible front section of the eyelids shields the eye's outer surface. The sclera fissure can open and close based on how rapidly the fragile skin of the eyelids folds over the eyeball.

One can close their eyes either intentionally or involuntarily (via reflex and spontaneous blinking). Sclera fissure provides an optically smooth surface to the cornea by distributing tear fluid throughout the eye. The translucent cornea of the eye extends forward and has an approximately spherical shape. The eyelids, tears, blinking, and lashes are considered ocular defense mechanisms. Blinking often occurs to keep the ocular surface moist using tears secreted by the lachrymal gland and clean the mucus. The blink reflex closes the eyelids to protect them from damage, and the eyelashes trap anything that might fly in while they do so. Tears, because of their antibacterial properties, soothe irritations and protect the body from infections. The defensive mechanisms of the eyelids and

cornea ensure that any substance injected into the eye is quickly removed through the lachrymal system. It is not a modest volume unless it is chemo- and physio-compatible with surface tissues.⁶

Structure of the eye

Along with the extrinsic eye muscles, the lachrymal system (which produces tears) develops. The components of the lachrymal apparatus produce and discharge lachrymal fluid, sometimes known as tears.

The vitreous chamber, the largest of the 3 chambers, is filled with a translucent, jelly-like fluid called vitreous humor. As a result, the health of the eyeball, lens, retina, intraocular pressure, and light refraction within the eye are all protected. Layers of the eye are made up of vascular, fibrous and neuronal tissues. The cornea and sclera are the 2 fibrous outermost layers of the eye. The choroid, ciliary body and iris are examples of intermediate vascular layer structures (Fig. 1).

Fibrous layers of the eye

The cornea

The cornea, a fibrous layer that is external and transparent, makes up 1/6 of the eyeball. The endothelium, stroma, Descemet's membrane, Bowman's membrane, and epithelial membrane are the 5 structural layers of the cornea. There are 5 sublayers and a 50–100- μm thick outer epithelium

of the human cornea. The epithelium's lipophilic character accounts for around 90% of the barrier to hydrophilic drug entry, whereas hydrophobic drug entry accounts for just 10% of the barrier. The Bowman's membrane is considerably thinner than the epithelium, with a thickness range of 8–14 μm . This layer serves as a barrier to prevent medications from entering the cornea, despite the fact that it cannot be regenerated if it is damaged. Mucopolysaccharides, collagen and other proteins make up the 20% of the stroma's dry weight that is not made up primarily of water. Therefore, it is believed that the stroma is responsible for preventing the absorption of lipophilic medicines across the cornea. The membrane that follows is known as the Descemet's membrane. Studies revealed that the 6- μm layer, a thin regeneration membrane, has little impact on how well ocular medications are absorbed. The posterior corneal surface is enveloped by a cell layer resembling the endothelium. These cells, linked by gap junctions, exhibit a permeability 200 times greater than that of the epithelial layer. This structure facilitates active fluid drainage and efficient fluid removal.

The sclera

The sclera, or "white of the eye," covers 5/6 of the eyeball. The stiff, collagenous connective tissue and elastic fibers give it a white, opaque look. It develops the eyeball, shields the internal organs and tissues of the eye, and protects the eye. According to research, the sclera has a strong molecular radius dependence and is highly permeable to hydrophilic medicines. Water-soluble substances with a reduced molecular weight can thus more efficiently penetrate the pores and cytosol of the sclera.

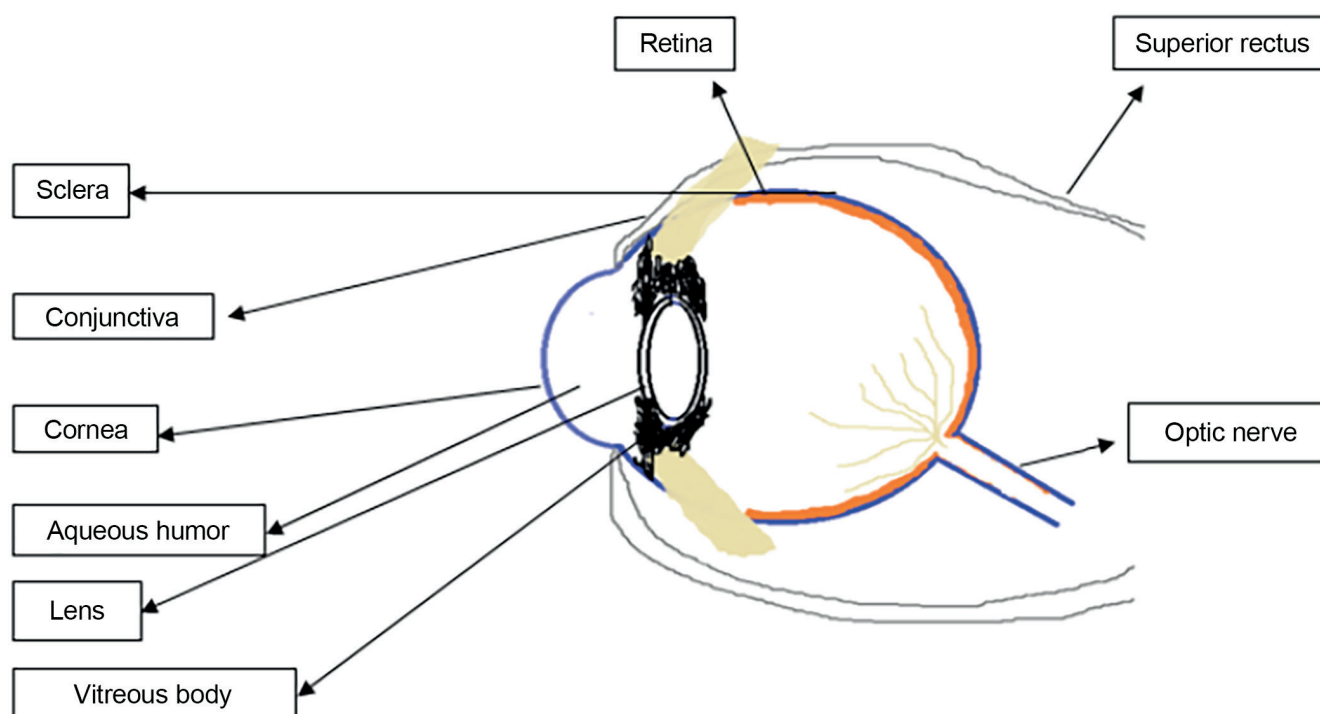


Fig. 1. Structure of the eye

The conjunctiva

This double or triple epithelial layer is made up of 3 major cell types: neurogenic epithelium, relevant epithelium integration and anterior epithelium. Despite their near proximity, these cells are more permeable to hydrophilic chemicals than the cornea. Greater permeability is caused by larger paracellular epithelial holes and an increase in epithelial pores.

The neural layer of the eye

The retina is located in the ocular layer, which is the eyeball's innermost layer. Layers of pigmented cuboidal cells and light-sensitive neurons line the inside and outside of the retina, respectively. This layer of the brain also comprises 6–7- μm photoreceptor cone cells and 120- μm photoreceptor rod cells. The macula and fovea of the retina are both illuminated. The fovea of the retina has more photoreceptors than any other portion of the retina, thus when light is concentrated there, visual acuity is at its peak. The optical disc has a "blind spot" because it lacks photoreceptor cells. The retinal artery and vein enter and leave here.

The vascular layer of the eye

Melanin pigments, which are mostly located in the vascular layer's cells, are responsible for the dark color of the layer. The ophthalmic artery branches and the tiny ciliary arteries that wrap around the optic nerve vascularize the eye. The vascular layer of the eye, in addition to the choroid, ciliary body and iris, includes the majority of the blood vessels. The choroid, the circulatory layer's deepest layer, lines the sclera's inner surface. This layer creates the blood–ocular barrier, which strictly regulates the passage of chemicals from the blood into the eye.⁷

Ophthalmic disorders

Conjunctivitis

Bacteria, viruses, allergens like pollen and dust, smoking, and pollution can all cause ocular inflammation. It distinguishes itself from other conjunctivitis by its capacity to secrete and infiltrate cells. *Staphylococcus aureus* is the most prevalent cause of bacterial conjunctivitis and blepharitis. Furthermore, *Haemophilus influenzae* and *Streptococcus pneumoniae* can cause conjunctivitis.

Glaucoma

Inadequate aqueous humor outflow causes pressure to build up in the front and posterior chambers of the choroid layers. Glaucoma can cause permanent eyesight loss as well as severe and irreversible visual loss, if left untreated.

Keratitis

Keratitis is an eye infection caused by viruses, bacteria or fungi. Bacterial corneal ulcers are more frequently caused by viral infections. The most common causes of corneal ulcers are *S. aureus*, *Pseudomonas pyocyanea*, *Escherichia coli*, and *Proteus mirabilis*.

Dry eye syndrome

The area around the eyes has extremely dry skin. The characteristic of dry eye syndrome, sometimes referred to as keratoconjunctivitis sicca, is inflammation of the lachrymal glands and ocular surface.

Iritis

The usual acute side effects include inflammation and eye irritation. Aside from that, chalazas, ophthalmic rosacea variations, and blepharitis (lid edge inflammation) are also medical conditions (meibomian cysts of the eye lid).⁸

Ocular drug delivery system

Medication of specific impact above surface or interior of the eye is regularly delivered to the ocular system. Topically applied medications, such as eye drops, have a limited bioavailability. The nasolachrymal system is used to inject a dose into the nasopharynx in order to improve the duration of therapeutic activity and ocular bioavailability. Despite improving corneal contact length to varying degrees, these devices have not been widely adopted because of eye pain (ointments), poor patient compliance (inserts) and lid sticking (gels). Their place has been replaced by ointments, gels and polymeric implants. Because of eye irritation (ointments), poor patient compliance (inserts) and lid sticking, all of these technologies extend the duration of corneal contact to varying degrees (Fig. 2). Recently, it was shown that pH- and temperature-induced in situ forming systems, such as carbopol and cellulose acetate phthalate, can keep ocular drugs administered. These in situ gel production strategies may improve ocular bioavailability by increasing a drug's precorneal residence duration. Drugs with low bioavailability due to poor permeability and solubility can be made more accessible by utilizing a variety of techniques. Increased drug absorption and longer ocular residence times are being worked on in order to increase topical bioavailability and therapeutic responsiveness of ophthalmic medicines. The formulation viscosity was increased to improve ocular bioavailability and the drug's precorneal residence duration at the ocular site. Hydrophilic viscosity enhancers such as cellulose, polyalcohol and polyacrylic acid are examples. Sodium carboxymethyl cellulose is the most important mucoadhesive polymer with strong adherence. The addition

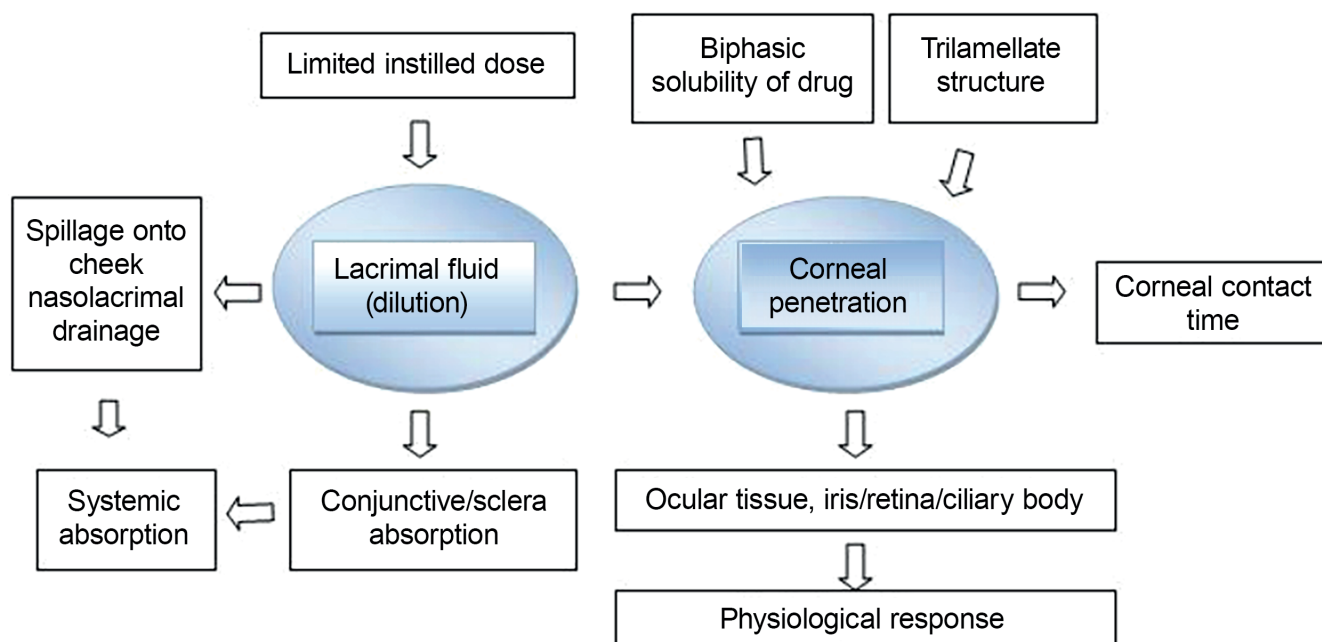


Fig. 2. Ocular drug delivery system

of carbomer increases the viscosity of liquid and semisolid solutions. Because it binds form and has mucoadhesive properties, hydrogel aids in drug delivery system maintenance. Hyaluronic acid (HA) is a naturally occurring substance that is both biocompatible and biodegradable. It is available in dose formulations that provide a sustained release for the eyes. The polysaccharide xanthan gum can be used to enhance viscosity. A viscosity vehicle increases contact time and improves ocular absorption. A viscosity enhancer can be added to an ophthalmic solution vehicle to lower the size of the injected drop while increasing the viscosity of the solution in order to improve ocular absorption, increase the viscosity of the solution and add a viscosity enhancer to an ophthalmic solution vehicle. Poorly absorbed medications can be more successfully absorbed by improving ocular absorption. Using viscosity modifiers to extend the time the medicine is in contact with the ocular surface, for example, can assist increase drug bioavailability. Other techniques include particle retention at the site of administration following ocular delivery, polymer breakdown, diffusion-based drug release, chemical reaction processes, and drug release. Particulate medicine delivery techniques utilize the nanoparticles and microspheres. Chitosan (CS) is a bioadhesive carrier that is suitable for ocular formulation owing to its intrinsic biological properties, which include biodegradability, nontoxicity and biocompatibility.⁹ Salicylic acid reacts ionically with its opposing charges because of its positive charge and neutral pH. Carrageenan and xanthan are both bioadhesive polysaccharides. When surface tension is reduced, longer corneal contact durations result in slower drainage and greater absorption. This is the fundamental purpose of viscosity-increasing compounds.^{9,10} (Fig. 3.)

Viscosity enhancers used in ocular drug delivery system

Viscosity modifiers are chemicals that are used to alter the thickness or texture of medicinal substances. Thickeners, texturizers, gelation agents, and stiffening agents are examples of viscosity modifiers. Table 1 presents viscosity profiles of selected viscosity-enhancing agents.

Chitosan

Chitosan is a positively charged mucopolysaccharide found in the shells of insects and crustaceans that is produced through chitin deacetylation. It contains both N-acetylglucosamine and glucosamine. Chitosan's acetylation level has a substantial impact on its solubility; the higher the acetylation level, the more CS is affected. The amine group in CS has a pKa of about 6.5 and is soluble at acidic pHs but insoluble at neutral pHs. Chitosan, a viscosity enhancer, was considered to open epithelial tight junction barrier cells and intracellular cells. Chitosan increases cell permeability without impairing viability. Because of this increased permeability, more drugs are transported across the cornea. It is also naturally biodegradable and has mucoadhesive properties. The majority of organic acidic solutions, such as citric, formic, acetic, and tartaric acids, are dissolved by CS. Phosphoric and sulfuric acids are not dissolved with CS. It is highly soluble in organic acids due to its ability to generate protonated amines and exhibit polycationic properties at pH values lower than 6. Chitosan concentration can be increased by cutting it into quarters to produce trimethyl CS. It is soluble in both neutral and basic pH ranges.¹¹

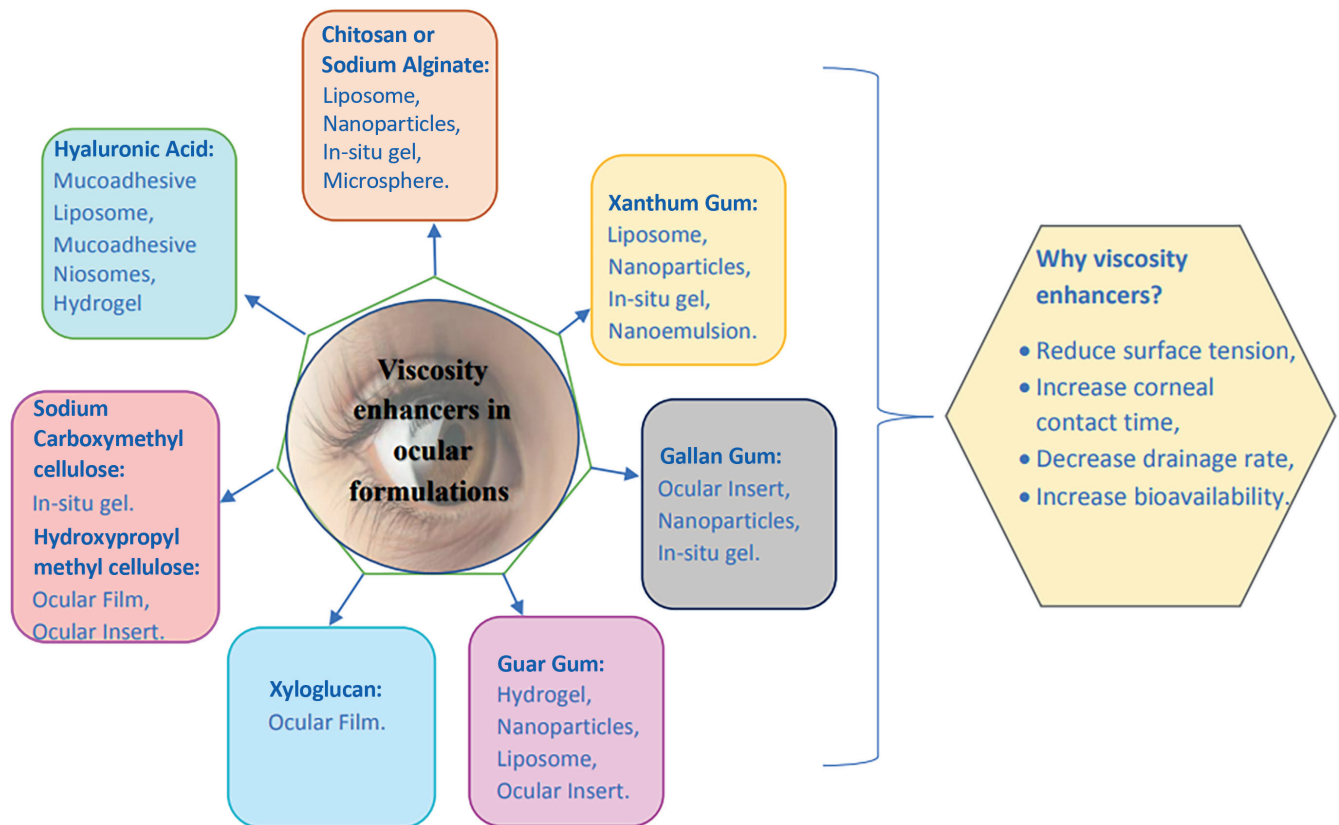


Fig. 3. Viscosity enhancers in ocular formulations

Table 1. Viscosity profile of selected viscosity enhancing agent

Polymer*	Charge	Viscosity profile range (cps)	References
carbomer	anionic	40,000–60,000	[9]
chitosan	cationic	1000–2000	[13]
scleroglucan	anionic	2500–4000	[15]
sodium alginate	anionic	20–400	[28]
xanthan gum	anionic	1350	[35]
gellan gum	anionic	2000–4000	[42]
sodium carboxymethylcellulose	anionic	1500–3000	[62]
hydroxypropylmethylcellulose	non-ionic	3000–5000	[70]

*All polymer viscosity agent concentrations are $\leq 1\%$ w/v.

At pH values above approx. 6.5, CS amines become reactive and deprotonated, encouraging polymer connections and the formation of fibers and networks (i.e., film and gel). Chitosan's structure has been altered to improve properties such as mucoadhesion and penetration. Chitosan penetration capability is improved when given a thiol group by creating disulfide linkages with the cysteine residues on mucin. Several eye disorders could possibly be addressed by using these effects. Chitosan improves faster corneal repair by hastening kerocyte migration, which accelerates wound healing and collagen synthesis. According to Gurtler et al., the optimal CS dose for topical ophthalmology is 1.5% when compared with CS that has a low molecular weight range of 500–800 kDa.

Chitosan-based formulations

Chitosan nanoparticle

The use of CS nanoparticles enhanced drug bioavailability to the ocular mucosa. Tighter contact benefits such systems, and distribution to the outside ocular tissues should be increased without jeopardizing the inner ocular structures.^{12,13} Chitosan nanoparticles were researched to evaluate if they could be used to deliver ocular drugs in vivo; their toxicity in conjunctival cell cultures was also examined. The fluorescent nanoparticles were generated using the ionotropic gelation process.^{14,15} To test the particle stability in the presence of lysozyme, the size, viscosity of the mucin dispersion and particle interaction

with mucin were all examined. The *in vivo* interactions of CS-fluorescent (FL) (CS-FL) nanoparticles with rabbit cornea and conjunctiva were investigated using spectrofluorimetry and confocal imaging. Chitosan nanoparticles are promising medication delivery platforms for the eye.^{16,17}

Chitosan microspheres

Microspheres enable precise and controlled drug administration. The incorporation of penetration enhancers, such as CS, into microspheres has the advantages, such as the bioavailability and improved retention time due to much closer contact with the mucus layer, and accurate targeting of medications to the ocular region.¹⁸ The use of CS microspheres enables prolonged *in-vivo* ocular medication release. Chitosan is useful for drug release control due to its mucoadhesive characteristics. Overall, each particle system provides a feasible technique for improving drug bioavailability in the eye.¹⁹

Chitosan of *in situ* gelling system

In situ gel combines the advantages of liquid and gel. It is precise and easy to operate. Before administration, the medicine was in the solution form; during administration, it was in the gel form. As a result, less medication is lost and the drug remains in the precornea of the eye for longer. Also, the medicine is more bioavailable.^{20,21} Temperature and pH fluctuations can activate *in situ* gelling processes. Chitosan, a polymer sensitive to pH changes, has the capability to enhance the viscosity of a substance. By combining CS *in situ* gel with poloxamer, the resulting gel's mechanical strength surpasses that of either component on its own, making this combination especially advantageous for ocular delivery.²²

Chitosan solutions

When administered topically, polycationic CS compounds that are soluble at the physiological pH of tear fluid enhance penetration. The precorneal residence was extended by tobramycin and CS solutions. The therapeutic solution's viscosity and permeability have increased as a result.²³

Chitosan liposomes

Liposomes, which are colloidal drug delivery techniques, have better ocular bioavailability than standard liquid formulations. Although they have some advantages, such as ease of administration, better bioavailability and no effect on vision, there are also some disadvantages. Drugs leak due to their rapid fusion or disintegration while being stored or administered.²⁴ To address these issues, liposomes were coated with low-molecular-weight CS. Because of the CS coating, the liposomes have high penetration and a positive charge. Chitosan coating improves precorneal retention compared to liposomes without a coating. Chitosan coating increased transcorneal medication absorption through modulating CS influence on drug penetration.²⁵

Sodium alginate

Due to its high degree of hydrophobicity, biocompatibility and low cost, alginate is a popular pharmaceutical delivery alternative. *In situ* gelling system that is based on polymers appears to be a better drug delivery strategy. Most mucoadhesive polymers are found in the form of sodium alginate, an anionic polymer containing a carboxyl end group. When alginate is slowly dissolved in water, it creates a gel. The solution has permeated high viscosity.^{26,27}

Sodium alginate-based formulations

Sodium alginate nanoparticle

Sodium alginate, an interesting polysaccharide, has found applications in diverse ocular delivery systems, both independently and in combination with other substances. Innovative nanoparticles have been created using sodium alginate encapsulation, facilitating gradual medication transport to the ocular mucosa.²⁸ Because of its excellent biological properties, such as renewability and non-toxicity, sodium alginate was chosen as an ocular formulation carrier. Alginic acid formulations with a prolonged precorneal stay were sought after due to their mucoadhesive properties and the ability to gel in the eye.

Sodium alginate microsphere

The sodium alginate technique was devised to deliver gatifloxacin to the ocular mucosa over time. The combination of biocompatible and biodegradable properties protects the encapsulated chemical and prevents its release more effectively than alginate or CS alone. It is a promising technique of drug release because of its properties, such as mild gelation conditions, biocompatibility, biodegradability, and pH dependence.²⁹

Sodium alginate *in situ* gelling system

The porosity of these hydrogels, the initial viscosity of the alginate solution, the ratios between guluronic acid and mannuronic acid, the concentration of the ionic cross-linker – all these factors play a crucial role. Calcium serves as the initial cross-linker in the alginate solution. Calcium cross-linked polymers can physically capture and stimulate the release of a variety of compounds, even at low polymer solution concentrations.³⁰ This phase shift occurs in the *in situ* gel conjunctiva of the eye. In the literature, numerous physiologic circumstances have been employed to document the sol–gel transition of various gels. These include CS, carbopol, sodium alginate, poloxamers, Pluronic® (Shilpa ChemSpe, Mumbai India), Gelrite (Opal Biotech, Mumbai, Maharashtra, India), xanthan, and polymeric copolymers. Many synthetic and organic polymers have the potential to improve drug bioavailability by extending the time drugs stay in the body.³¹ Aside from safety, biocompatibility and biodegradability, an excellent polymer-fabricated delivery system should be able to load medications and have a longer residence length at target tissues.

Xanthan gum

Higher quantities of locust bean gum produce soft, elastic and thermally reversible gels. At 1% or higher concentrations, xanthan gum solutions virtually appear gel-like at repose, yet they pour readily and provide little mixing or pumping issues. These properties are present at 0.1–0.3% of normal use levels. Xanthan gum solutions can help colloidal systems stay stable over time due to their high viscosity at low shear rates.³²

Because xanthan gum solutions are significantly more viscous than sodium alginate or carboxymethylcellulose (CMC) at low shear rates and roughly 15 times more viscous than guar gum at high shear rates, they are more effective at stabilizing suspensions. Because of chemical forces such as van der Waals interactions, xanthan gum has a double-stranded helix structure and a low ionic strength in an aqueous dispersion. To properly link with the co-synergist, the conformation of the xanthan gum molecule must be pushed over if it is in an ordered state at the time of mixing. The physicochemical features of xanthan gum, as well as variations in molecular conformation, have an effect on the substance's capacity to attach to mucous membranes. Secondary bonds formed between double-stranded helices increase polymer concentration and elastic characteristics.³³ Mucin must be present in substantial quantities for xanthan gum to interact. To keep the scattered granules from settling, the liquid must be constantly swirled after being added to the xanthan gum solution until it is completely dissolved. Xanthan gum is a carrier for a number of eye diseases, including proliferative uveitis and choroiditis. Proliferation of tumors causes uveitis.³⁴ Retinopathy of prematurity, posterior segment trauma and retinal vascular pathology are all names used to characterize inflammatory retinal diseases. According to the *in vivo* trial with healthy volunteers, xanthan gum solutions of greater viscosity take longer to clear following injection. Therefore, xanthan gum outperforms poly(vinyl alcohol), hydroxyethylcellulose and hydroxypropylmethylcellulose (HPMC) as a viscosifying agent. But, particularly at later time points, the gelation process of gellan gum performs better than that of xanthan gum.^{35,36}

Xanthan gum-based formulation

Xanthan gum *in situ* gelling

Devices that gel upon ion activation offer 2 advantages: they prompt gel formation on the ocular surface and extend the duration of corneal contact with the surface. The recent investigation of this *in situ* gelling system indicates high cost alongside compatibility considerations.³⁷

Xanthan gum nanoemulsion

Angiogenesis inhibitor-containing targeted vesicles were administered intraocularly and greatly reduced choroidal neovascularization when compared to a placebo injection. Nanoparticle medication has emerged as a feasible

option for cutting-edge ocular ailment therapy as a result of recent improvements in ocular drug delivery system research that have provided new insights into drug composition. Nanoemulsion (NE)-based topical formulations have the potential to create new options for clinical translation in ocular therapy by designing NEs for effective loading and delivery of ocular drugs to achieve the desired therapeutic effects or to behave in a specific ocular state.³⁸

Gellan gum

Nanoparticle drug delivery has become a promising approach for cutting-edge ocular sickness treatment as a result of recent advancements in ocular drug delivery system research that new insights into drug creation.

Gellan gum is a recognized polysaccharide derived from an aerobic Gram-negative bacterium that serves as an energy source. Its structure comprises glucuronic acid, rhamnose and glucose in a 2:1:1 ratio, resulting in a repeat unit of tetrasaccharide through their combination.³⁹ Gelrite, a commercial product, completely de-esters the native polysaccharide after being exposed to alkali, whereas L-glycerate and acetate only partially esterify the polymer. Gellan gum contains the following molecules: O-acetyl, rhamnose, glucose, and glucuronic acid. Gellan gum is easily hydrated and dissolves in both hot and cold deionized water; however, when employed with cold distilled water, it generates viscous solutions. When soluble salts are present, gellan gum can be utilized to form a strong gel at low concentrations. At high temperatures, gellan polymers exist in an arrangement known as an unorganized random coil in aqueous solutions.⁴⁰ When polymers are cooled until they gel, double helices form and assemble to form junction zones. Cations stabilize the double helices and junction zones, resulting in a 3D gel network. Gellan gum is classified into 3 groups based on its structural composition: those with a high polysaccharide content, those with a high protein content, and those with a high polysaccharide O-acetyl replacement content. Indomethacin is gelled *in situ* using gellan gum. When this approach is applied in a test tube to generate sustained drug release for 8 h, there is no harm to the eye tissues. A novel ophthalmic carrier called Gelrite[®] gellan gum hardens when it comes into touch with monovalent or divalent cations in the lachrymal fluid.⁴¹

Gelrite is a better transporter than xanthan gum due to its inclination to gel. Gelation is characterized by the creation of an orderly state of gellan chains.⁴²

Gellan gum-based formulations

System for *in situ* gelling of gellan gum

In situ gelling is used as a delivery strategy in one of the most promising ocular dosage forms. Liquid instillation facilitates administration while simultaneously increasing safety and frequency. Industrial preparation and manufacture are also simplified when compared to solid

and traditional semi-solid forms. The most significant advancement of these smart hydrogels is a solution-to-gel phase transition induced by physiologically relevant ocular surface stimuli such as temperature, pH or ionic strength. These 2 chemicals, hydroxyethylcellulose-based and gellan gum, are used in in situ gelling delivery methods. Many gellan gum-based formulations have been shown to have prolonged in vivo ocular surface residence durations and the propensity to promote ocular gelling.^{43,44} Hydroxyethyl cellulose (HEC) was used to enhance viscosity, mucoadhesion and release properties while decreasing polymer concentration. In comparison to other cellulosic polymers, HEC is well tolerated and possesses the appropriate viscosity and lubricating qualities. All formulations are free of the majority of dangerous eye drop preservatives, such as benzalkonium chloride. Market trends, patient and practitioner expectations and the increasing number of publications on the issue support the effectiveness of polymers like gellan gum (Table 2).

Gellan gum ocular inserts

There are few insert goods on the market due to the difficulties of self-insertion and the perception of a foreign body. Because the production of gels is an extreme form of raising viscosity through the use of viscosity enhancers, the dosage can be reduced to once daily. Droppable gel is made by using modern gel production techniques. They transform from liquid to viscoelastic gel in the ocular cul-de-sac. For effective causation, 3 ways have been devised: pH change, temperature change and ionic activation phase transition in the ocular surface. Eye drops, ointments and lotions are some of the most commonly used topical medications for ocular delivery.^{45,46} Because just a small percentage of the medicine is therapeutically helpful, dosage must be done on a regular basis. Gellan gum ocular inserts irritate the eye and obstruct vision, among other problems.

Guar gum

Guar gum is utilized in the pharmaceutical industry as a solid dosage form binder and disintegrant to improve the cohesiveness of prescription powders, as well as a suspending, thickening and stabilizing agent in oral and topical therapies. Guar gum is a common controlled-release component in medications due to its fast hydration. It is composed of galactose and mannose carbohydrates.⁴⁷ Guar gum is insoluble in the vast majority of organic solvents, but it dissolves efficiently in both cold and warm organic solvents.

Guar gum-based formulations

Guar gum nanoparticle

The lack of stability required for a dependable drug administration strategy is the main drawback in the production of nanosized carboxymethyl guar gum nanoparticles by nanoprecipitation and sonication. Sodium trimetaphosphate (STMP), a non-toxic cyclic triphosphate, is extensively used to cross-link hydrogels and microspheres for therapeutic uses.^{48,49} However, the nanoparticles must be cross-linked to avoid dissolving at different pH levels, which would deplete some of the free functional groups.

Guar gum-based liposome

Liposomes are water-filled containers with a membrane or bilayer covering. As opposed to phospholipid-based liposomes, they feature a core-shell arrangement in drug delivery systems, allowing for a superior encapsulating technique for extended drug release. Hydrophilic medications can be encapsulated by watery phospholipid-based liposomes, whereas hydrophobic drugs can be contained inside the lipid membrane. As a result, the liposomal smart design allows for the inclusion of both hydrophilic and hydrophobic medications.⁵⁰

Table 2. Classification of polymers acting as viscosity enhancers: ocular mucoadhesive capacity

No.	Polymer	Natural viscosity enhancer	Synthetic viscosity enhancer	Semi-synthetic viscosity enhancer
1.	chitosan	+	–	–
2.	sodium alginate	+	–	–
3.	poly(vinyl alcohol)	–	+	–
4.	gellan gum	+	–	–
5.	guar gum	+	–	–
6.	xanthan gum	+	–	–
7.	xyloglucan	+	–	–
8.	sodium carboxymethylcellulose	–	–	+
9.	arabinogalactan	+	–	–
10.	carbomer	–	+	–
11.	hyaluronic acid	+	–	–
12.	scleroglucan	+	–	–
13.	HPMC	–	–	+

HPMC – hydroxypropyl methylcellulose.

Guar gum-based ocular insert

Guar gum is used to strengthen the cohesiveness of the medicinal powder, as a binder and disintegrant in solid dosage forms, and as a suspending, thickening and stabilizing agent in oral and topical therapies. To address the limitations of existing ophthalmic dose forms, ofloxacin and guar gum (a biodegradable polymer) are being developed as ocular inserts with zero order kinetics (eye drops and suspensions).⁵¹ By altering the guar gum content, the release of ofloxacin from inserts was examined (polymer matrix).

Xyloglucan

The sugars arabinose, xylose, glucose, and galactose are mixed in the ratios of 4:3.4:1.5:0.3 to create xyloglucan, a galactoxyloglucan with a molecular weight of 720–880 kDa. The cell walls of higher plants are made up of xyloglucans, a type of linear polysaccharide. The xyloglucan's viscosity is affected by the number of glycosyl and non-glycosyl subunits, the backbone molecular weight and the molecular weight. *Tamarindus indica* L. plants produce tamarind seed unionic and neutral carbohydrate xyloglucan (TSX), a tamarind seed sticky polymer.^{52,53} Tamarind seed polysaccharide (TSP) is a compound with mucoadhesive, bio-adhesive, viscosity-increasing, and mucomimetic properties. At the O-6 position, the 14-linked glucan backbone chain of TSX is significantly replaced by d-xylose. These xylose residues have been found in O-2⁵⁴ in some cases.

Despite the fact that xyloglucan's hydrophilic and hydrophobic characteristics make it soluble in water, aggregated species are present in the solution because individual macromolecules do not fully hydrate. They can be found in extremely diluted liquids. Thus, structure and function are interwoven in xyloglucan aqueous solutions. The xyloglucan content and inherent viscosity have the biggest influence on the random coil overlap and entanglement of the polymer backbone, respectively. When the concentration of xyloglucan in aqueous solutions increases, the random-coil structure appears. Carboxymethylation was used to change the properties of 55 TSPs.^{55,56} The biodegradation of TSP is slowed by carboxymethylation, which also renders TSP more soluble in cold water and stable around bacteria. Even with a longer interval between doses of the medication, polysaccharide still enables prolonged reduction of *S. aureus* in the cornea. Tamarind seed polysaccharide increased drug accumulation in the cornea and prolonged antibiotic precorneal residence duration, most likely by lowering drug washout after topical administration.⁵⁷

Gel-forming ocular film based on xyloglucan

The material's major properties include its high drug retention, mucoadhesivity, biocompatibility, high thermal stability, and lack of carcinogens.⁵⁸ Solvent casting

was utilized to create an ocular film containing xyloglucan, which was then evaluated. Xyloglucan may produce a film with outstanding properties. The characterization outcome, which emphasizes the substance's specific physical and mechanical properties, provides a clear indicator of its filmmaking potential. According to the research, ciprofloxacin could be given to the eye in an effective and consistent manner utilizing xyloglucan ocular films.⁵⁹

Sodium carboxymethyl cellulose

Carboxymethylcellulose, a high-molecular-weight polysaccharide, is one of the most commonly used viscous polymers in synthetic tears to accomplish the prolonged ocular surface residency length. Because of its viscosity and mucoadhesiveness, CMC has a long retention time on the ocular surface. It is made by pretreatment of cellulose with sodium hydroxide, combining chloroacetic acid, and adding an alkali catalyst. The molecular weights of this material, however, range from 90,000 to 2,000,000 g/mol. As a viscosity modifier, emulsifier, stabilizing agent, and lubricant, sodium carboxymethylcellulose (SCMC) is frequently employed in the manufacturing of medicinal dosage forms. In addition to being secure for use in medicine, it is inexpensive, abundant, and has a high-water bonding capacity.⁶⁰

Sodium carboxymethyl cellulose-based formulations

SCMC-based in situ gel

After being injected into the eye and subjected to physiological conditions, a viscous liquid known as an in situ active gel forming system transforms into gels or solid phase. In situ gelation combines the precision and ease of solutions and gels, as well as the latter's prolonged precorneal retention.⁶¹

We created the formulation with the most potential for sustained azithromycin release and effectiveness using pectin and SCMC at 0.5% w/v. Similar to polyacrylic acid, the cellulose ether SCMC exhibits mucoadhesive characteristics. In order to promote ocular bioavailability via mucoadhesion and aid in the creation of the in situ gel, SCMC, a viscosity enhancer, is used. Pectin-based in situ gels may be utilized to extend azithromycin's duration of action or contact time in the ocular region.⁶²

Hyaluronic acid

The extracellular matrix contains HA, a polymer with a high molecular weight. This non-immunogenic glycosaminoglycan is utilized in ophthalmic medicine for a variety of objectives, including protecting corneal endothelial cells during intraocular surgery, treating dry eyes by replacing tears for vitreous humor, and lengthening the precorneal residence duration of various pharmaceuticals. Diluted sodium hyaluronate solutions, which act as a substitute for tears, have been used successfully to treat severe dry

eye conditions. Their primary advantages are their biophysical characteristics that resemble mucin and viscoelasticity, which allow long-lasting hydration and retention. The eye's surface is also well moisturized. Along with its ability to promote corneal epithelial cell proliferation, HA has also been related to inflammation and wound healing.⁶³

When given topically to the eye, HA stimulates keratocyte proliferation and corneal epithelial migration, which speeds up wound healing. Topical eye drops must be applied on a regular basis. The viscosity required to ensure good efficacy and an extended residence period while delaying the commencement of ocular surface drainage. However, in order to eliminate optical haze and to speed up the production process, which includes sterile filtration, the solutions should not be excessively viscous.⁶⁴

Hyaluronic acid-based formulations

Hyaluronic acid-modified mucoadhesive liposomes

For more than a decade, liposomes, a type of closed vesicle composed of an aqueous phase and a phospholipid bilayer, have been used to treat eye problems. This approach resulted in regulated medication release and lowered membrane permeability. Liposomes modified with HA function as an eye therapy. Because HA-modified liposomes can be given more often and at lower doses, and because HA-coated vehicles have a longer retention time on the surface of the eye, ocular drug bioavailability is increased.

Hyaluronic acid-based mucoadhesive niosomes

Niosomes, which are non-ionic, self-assembling vesicles, outperformed the replacement system in the following ways: they offer high compatibility, chemical stability, low toxicity, ease of production, and increased solubility and permeability due to the use of surfactants. Mucoadhesion niosomes with HA coatings are being developed. The HA coating aided niosome adherence to mucin. The HA-coated niosomes surpassed solution- or uncoated niosomes in terms of ocular bioavailability and aqueous humor pharmacokinetics. They also improved tacrolimus retention *in vivo*.⁶⁵

Oxidized hyaluronic acid-based hydrogel

A hydrogel can be created by combining oxidized HA, CS and glycol. In this study, researchers developed a hydrogel film that can deliver the eye drugs dexamethasone and levofloxacin at the same time. The swelling ratio of the hydrogel films reduced as the oxidized hyaluronic acid (OHA) oxidation level increased. Many bacterial strains were inhibited in their development when exposed to hydrogel sheets containing levofloxacin.⁶⁶

Hydroxypropylmethylcellulose

According to research, while having a lower viscosity than carbomer, this substance has better mucoadhesive

qualities. The gelling capabilities of HPMC and carboxypol 980 NF were merged to create a pH-responsive *in situ* gelling vehicle, serving as a gelling agent for administering drugs to the eye. Additionally, the laboratory examined how hydroxypropyl- β -cyclodextrin (HP- β -CD) impacted puerarin solubility in water and its penetration into the cornea.⁶⁷ The substance is composed of glucose molecule chain. However, instead of the hydrogen, the material is composed with methoxy and hydroxypropyl side chains of the hydroxyl groups. It is a cellulose ether that is commonly used as a first-line treatment for dry eyes and other ocular surface problems.^{68,69}

HPMC-based formulations

Ocular film using HPMC

Following the method for administering diclofenac sodium to the eye, CS-based nanoparticles are dispersed on an HPMC-based film. The CS-HA nanoparticles' zeta potential was discovered to have a negative charge. Encapsulation efficiency was 70%, and the particles were nanometer in size. The diclofenac film viscosity/polymer concentration had a higher viscosity and a slower rate of drug release. When nanoparticles were added to HPMC films, the drug was released gradually and constantly. Drug release and corneal penetration studies demonstrated that diclofenac-loaded nanoparticles have a slower- or longer-lasting drug release.⁷⁰

HPMC-based ocular insert

Cyclosporin A (CsA) is the most effective in the manufacturing process for the physicochemical analysis and it is loaded with HPMC inserts. Mechanical features such as thickness and wettability have been shown to reduce eye irritation. The CsA concentration in the polymer matrix was uniform throughout. According to the *in vitro* release studies, the drug continued to leak for up to 20 h. Xanthan gum improves folding endurance and extends the time the medicine is in contact with the ocular layer in addition to increasing the time of CsA production. The cytotoxicity investigation did not show any evidence of harm to the bovine corneal cells, in contrast to the control group.⁷¹ The research's conclusions show that when CsA was added to the anti-inflammatory study in Jurkat T cells activity by reducing interleukin-2 (IL-2) and interferon gamma (IFN- γ) production (Fig. 3, Table 3,4).

Conclusions

Some of the problems with the present formulations result in a very little fraction of active moiety in the posterior section of the ocular region. Due to a shorter residence time, reduced penetration and an absence of optimal viscosity behavior, topical ophthalmic medicine has a lower

Table 3. Commercially available products containing viscosity-enhancing agents for ophthalmic use

Brand name	Viscosity-enhancing agent	Role	References
Rugby	poly(vinyl alcohol)	relieves dry and irritated eyes	[9]
Lacrymed	carbomer	relieves dry eye and soreness	[13]
Biogran	sodium alginate	astringent in ophthalmic leverage	[27]
Optimox	xanthan gum	bacterial conjunctivitis	[33]
Lubifresh	sodium carboxymethylcellulose	relief from burning	[60]
COSS-HPMC	HPMC	prevents conjunctival and corneal damage	[68]

HPMC – hydroxypropylmethylcellulose.

Table 4. Patents for viscosity enhancers in their clinical studies

Patent No.	Polymers	Clinical studies	References
US 2018/0243294 A1	carbomer	treat ocular surface disease	[60]
US,8,541,426 B2	HPMC	treat corneal surface	[62]
WO 2018/034569 A1	hyaluronic acid	dry eye syndrome	[72]
WO 02/100376 A1	chitosan	ocular allergic condition	[73]
US 2011/008221 A1	sodium alginate	sustained release in the eye	[74]
US 2008/0039423 A1	xanthan gum	superior corneal epithelial disorder treating effect	[75]
US 2011/0082128 A1	gellan gum	prevention of cataracts	[76]
US 2004/0009893 A1	guar gum	LASIK surgery	[77]
US 10,813,923 B1	xyloglucan	retinal bioavailability	[78]
EP 2 446 878 B1	sodium carboxymethylcellulose	preventing ocular pain	[79]

HPMC – hydroxypropylmethylcellulose; LASIK – laser-assisted in situ keratomileusis.

ocular bioavailability. The viscosity agents employed in ophthalmic formulations can be crucial in extending the active moiety's precorneal residence time on the epithelial corneal surface. It is challenging for manufacturers to use selected viscosity components at an appropriate concentration in an ophthalmic formulation. Furthermore, the viscosity-improving components are crucial in lowering surface tension (between the formulation and the corneal surface), which improves corneal surface contact time and ocular bioavailability of the relevant formulations.




It has been established that the use of viscosity enhancers is successful in treating the symptoms of dry eye caused by a lack of aqueous tears. Viscous topical ophthalmic solutions provide significant efficacy and prolonged residence time while delaying rapid drainage from the ocular surface. The concentration of the eye solution should be adjusted to minimize viscosity in order to prevent blurry vision. A medication delivery method intended to prolong the duration of drug interaction at the ocular site is known as a viscosity enhancer. Additionally, the viscosity enhancer has been demonstrated to improve corneal absorption by altering the integrity of corneal epithelium. Further developments in ocular medication delivery systems are expected in future in order to improve and preserve eye health, enhance patient compliance, and accomplish superior results in the management of ocular disorders.

Expert opinion

Over the last 2 decades, there have been major advancements in the study of ocular drug delivery, turning away from the use of traditional solutions, suspensions and ointments and towards viscosity-improving in situ gel systems, various inserts, colloidal systems, etc. Even though significantly higher bioavailability and controlled release systems have been achieved with the use of various novel formulation approaches for ophthalmic drug delivery, research is mainly limited to in vitro and in vivo studies, with very few reports on phase I clinical trials. The commercialization of newer dosage formulations is severely constrained by this issue. The physical stability problems linked to vesicular systems, another barrier to the commercialization of innovative dosage forms, need to be resolved through extensive research.

Due to the ability of the medications to penetrate deeper tissues, the use of topical chemotherapy for the treatment of ocular melanoma (uveal, corneal and conjunctival melanoma) is restricted. Owing to the CS capacity to disrupt the deeper corneal layers, as opposed to synthetic penetration enhancers such as ethylenediaminetetraacetic acid (EDTA), azone compounds, sodium deoxycholate, polycarboxylates, etc., it can increase the bioavailability of chemotherapeutic medications. Melanoma cells can be targeted with chemotherapeutic drug-loaded nanoparticles identified with specific moieties, and sustained release can be achieved.

ORCID iDs

Pravin Kondiba Pawar  <https://orcid.org/0000-0001-9541-1977>
 Raju Dubaji Rathod  <https://orcid.org/0000-0002-5216-3923>
 Satyajeet Ramesh Jagadale  <https://orcid.org/0009-0007-1885-0117>

References

- Wadhwa S, Paliwal R, Paliwal S, Vyas S. Nanocarriers in ocular drug delivery: An update review. *Curr Pharm Des.* 2009;15(23):2724–2750. doi:10.2174/138161209788923886
- Urtti A, Salminen L. Minimizing systemic absorption of topically administered ophthalmic drugs. *Surv Ophthalmol.* 1993;37(6):435–456. doi:10.1016/0039-6257(93)90141-5
- Järvinen K, Järvinen T, Urtti A. Ocular absorption following topical delivery. *Adv Drug Deliv Rev.* 1995;16(1):3–19. doi:10.1016/0169-409X(95)00010-5
- Azari AA, Barney NP. Conjunctivitis: A systematic review of diagnosis and treatment. *JAMA.* 2013;310(16):1721–1729. doi:10.1001/jama.2013.280318
- Weinreb RN, Aung T, Medeiros FA. The pathophysiology and treatment of glaucoma: A review. *JAMA.* 2014;311(18):1901–1911. doi:10.1001/jama.2014.3192
- Sharma N, Bagga B, Singhal D, et al. Fungal keratitis: A review of clinical presentations, treatment strategies and outcomes. *Ocul Surf.* 2022;24:22–30. doi:10.1016/j.jtos.2021.12.001
- Rouen PA, White ML. Dry eye disease: Prevalence, assessment, and management. *Home Healthc Now.* 2018;36(2):74–83. doi:10.1097/NHH.0000000000000652
- Harthan J, Fromstein S, Moretton C, Opitz D. Diagnosis and treatment of anterior uveitis: Optometric management. *Clin Optom (Auckl).* 2016;8:23–35. doi:10.2147/OPTO.S72079
- Rathore K, Nema R. An insight into ophthalmic drug delivery system. *IJPSR.* 2009;1(1):1–5. doi:10.25004/IJPSR.2009.010101
- Alonso MJ, Sánchez A. The potential of chitosan in ocular drug delivery. *J Pharm Pharmacol.* 2010;55(11):1451–1463. doi:10.1211/0022357022476
- Nasr El-Din WA, Nooreldin N, Essawy AS. The potential therapeutic efficacy of intravenous versus subconjunctival mesenchymal stem cells on experimentally ultraviolet-induced corneal injury in adult male albino rats. *Folia Morphol.* 2022;81(4):900–916. doi:10.5603/FM.a2021.0085
- Singla A, Chawla M. Chitosan: Some pharmaceutical and biological aspects: An update. *J Pharm Pharmacol.* 2001;53(8):1047–1067. doi:10.1211/0022357011776441
- Bowman K, Leong KW. Chitosan nanoparticles for oral drug and gene delivery. *Int J Nanomedicine.* 2006;1(2):117–128. doi:10.2147/nano.2006.1.2.117
- Song S, Zhou W, Wang Y, Jian J. Self-aggregated nanoparticles based on amphiphilic poly(lactic acid)-grafted-chitosan copolymer for ocular delivery of amphotericin B. *Int J Nanomed.* 2013;8:3715–3728. doi:10.2147/IJN.S51186
- Nagpal K, Singh SK, Mishra DN. Chitosan nanoparticles: A promising system in novel drug delivery. *Chem Pharm Bull (Tokyo).* 2010;58(11):1423–1430. doi:10.1248/cpb.58.1423
- de Campos AM, Sánchez A, Alonso MJ. Chitosan nanoparticles: A new vehicle for the improvement of the delivery of drugs to the ocular surface. Application to cyclosporin A. *Int J Pharm.* 2001;224(1–2):159–168. doi:10.1016/S0378-5173(01)00760-8
- de Campos AM, Diebold Y, Carvalho ELS, Sánchez A, José Alonso M. Chitosan nanoparticles as new ocular drug delivery systems: In vitro stability, in vivo fate, and cellular toxicity. *Pharm Res.* 2004;21(5):803–810. doi:10.1023/B:PHAM.0000026432.75781.cb
- Vasir JK, Tambwekar K, Garg S. Bioadhesive microspheres as a controlled drug delivery system. *Int J Pharm.* 2003;255(1–2):13–32. doi:10.1016/S0378-5173(03)00087-5
- Genta I, Conti B, Perugini P, Pavanetto F, Spadaro A, Puglisi G. Bioadhesive microspheres for ophthalmic administration of acyclovir. *J Pharm Pharmacol.* 1997;49(8):737–742. doi:10.1111/j.2042-7158.1997.tb06103.x
- Gratieri T, Gelfuso GM, De Freitas O, Rocha EM, Lopez RFV. Enhancing and sustaining the topical ocular delivery of fluconazole using chitosan solution and poloxamer/chitosan in situ forming gel. *Eur J Pharm Biopharm.* 2011;79(2):320–327. doi:10.1016/j.ejpb.2011.05.006
- Gupta H, Jain S, Mathur R, Mishra P, Mishra AK, Velpandian T. Sustained ocular drug delivery from a temperature and pH triggered novel in situ gel system. *Drug Deliv.* 2007;14(8):507–515. doi:10.1080/10717540701606426
- Gurny R, Ibrahim H, Buri P. The development and use of in situ formed gels, triggered by pH. In: Edman P, ed. *Biopharmaceutics of Ocular Drug Delivery.* Boca Raton, USA: CRC Press; 2019. doi:10.1201/9780429284755
- Li N, Zhuang C, Wang M, Sun X, Nie S, Pan W. Liposome coated with low molecular weight chitosan and its potential use in ocular drug delivery. *Int J Pharm.* 2009;379(1):131–138. doi:10.1016/j.ijpharm.2009.06.020
- Zhang J, Wang S. Topical use of coenzyme Q10-loaded liposomes coated with trimethyl chitosan: Tolerance, precorneal retention and anti-cataract effect. *Int J Pharm.* 2009;372(1–2):66–75. doi:10.1016/j.ijpharm.2009.01.001
- Di Colo G, Zambito Y, Burgalassi S, Nardini I, Saettone M. Effect of chitosan and of N-carboxymethylchitosan on intraocular penetration of topically applied ofloxacin. *Int J Pharm.* 2004;273(1–2):37–44. doi:10.1016/j.ijpharm.2003.12.018
- Thanou M, Verhoef JC, Marbach P, Junginger HE. Intestinal absorption of octreotide: N-trimethyl chitosan chloride (TMC) ameliorates the permeability and absorption properties of the somatostatin analogue in vitro and in vivo. *J Pharm Sci.* 2000;89(7):951–957. doi:10.1002/1520-6017(200007)89:7<951::AID-JPS13>3.0.CO;2-1
- Liu Y, Liu J, Zhang X, Zhang R, Huang Y, Wu C. In-situ gelling gelrite/alginate formulations as vehicles for ophthalmic drug delivery. *AAPS PharmSciTech.* 2010;11(2):610–620. doi:10.1208/s12249-010-9413-0
- Taghe S, Mirzaeei S. Preparation and characterization of novel, mucoadhesive ofloxacin nanoparticles for ocular drug delivery. *Braz J Pharm Sci.* 2019;55:e17105. doi:10.1590/s2175-97902019000117105
- Shinde UA, Shete JN, Nair HA, Singh KH. Design and characterization of chitosan-alginate microspheres for ocular delivery of azelastine. *Pharm Dev Technol.* 2014;19(7):813–823. doi:10.3109/10837450.2013.836217
- Cohen S, Lobel E, Trevogoda A, Peled Y. A novel in situ-forming ophthalmic drug delivery system from alginates undergoing gelation in the eye. *J Control Release.* 1997;44(2–3):201–208. doi:10.1016/S0168-3659(96)01523-4
- Noreen S, Ghumman SA, Batool F, et al. Terminalia arjuna gum/alginate in situ gel system with prolonged retention time for ophthalmic drug delivery. *Int J Biol Macromol.* 2020;152:1056–1067. doi:10.1016/j.ijbiomac.2019.10.193
- Ceulemans J, Vinckier I, Ludwig A. The use of xanthan gum in an ophthalmic liquid dosage form: Rheological characterization of the interaction with mucin. *J Pharm Sci.* 2002;91(4):1117–1127. doi:10.1002/jps.10106
- Talukdar MM, Michael A, Rombaut P, Kinget R. Comparative study on xanthan gum and hydroxypropylmethyl cellulose as matrices for controlled-release drug delivery I. Compaction and in vitro drug release behaviour. *Int J Pharm.* 1996;129(1–2):233–241. doi:10.1016/0378-5173(95)04355-1
- Zirnsak MA, Boger DV, Tirtaatmadja V. Steady shear and dynamic rheological properties of xanthan gum solutions in viscous solvents. *J Rheol.* 1999;43(3):627–650. doi:10.1122/1.551007
- Zatz JL, Knapp S. Viscosity of xanthan gum solutions at low shear rates. *J Pharm Sci.* 1984;73(4):468–471. doi:10.1002/jps.2600730410
- Morris ER, Foster TJ. Role of conformation in synergistic interactions of xanthan. *Carbohydr Polym.* 1994;23(2):133–135. doi:10.1016/0144-8617(94)90038-8
- Rupenthal ID, Green CR, Alany RG. Comparison of ion-activated in situ gelling systems for ocular drug delivery. Part 1: Physicochemical characterisation and in vitro release. *Int J Pharm.* 2011;411(1–2):69–77. doi:10.1016/j.ijpharm.2011.03.042
- Singh M, Bharadwaj S, Lee KE, Kang SG. Therapeutic nanoemulsions in ophthalmic drug administration: Concept in formulations and characterization techniques for ocular drug delivery. *J Control Release.* 2020;328:895–916. doi:10.1016/j.jconrel.2020.10.025
- Jansson PE, Lindberg B, Sandford PA. Structural studies of gellan gum, an extracellular polysaccharide elaborated by *Pseudomonas elodea*. *Carbohydr Res.* 1983;124(1):135–139. doi:10.1016/0008-6215(83)88361-X
- Kuo MS, Mort AJ, Dell A. Identification and location of l-glycerate, an unusual acyl substituent in gellan gum. *Carbohydr Res.* 1986;156:173–187. doi:10.1016/S0008-6215(00)90109-5

41. Kanari B, Banik RR, Upadhyay SN. Effect of environmental factors and carbohydrate on gellan gum production. *Appl Biochem Biotechnol*. 2002;102–103(1–6):129–140. doi:10.1385/ABAB:102-103:1-6:129
42. Chandrasekaran R, Puigjaner LC, Joyce KL, Arnott S. Cation interactions in gellan: An X-ray study of the potassium salt. *Carbohydr Res*. 1988;181:23–40. doi:10.1016/0008-6215(88)84020-5
43. Balasubramaniam J, Kant S, Pandit JK. In vitro and in vivo evaluation of the Gelrite gellan gum-based ocular delivery system for indomethacin. *Acta Pharm*. 2003;53(4):251–261. PMID:14769232.
44. Gupta H, Velpandian T, Jain S. Ion- and pH-activated novel in-situ gel system for sustained ocular drug delivery. *J Drug Target*. 2010; 18(7):499–505. doi:10.3109/10611860903508788
45. Balasubramaniam J, Pandit JK. Ion-activated in situ gelling systems for sustained ophthalmic delivery of ciprofloxacin hydrochloride. *Drug Deliv*. 2003;10(3):185–191. doi:10.1080/713840402
46. Ramaiah S, Kumar TMP, Ravi V. Studies on biopolymers for ophthalmic drug delivery. *J Macromol Sci A*. 2007;44(2):229–234. doi:10.1080/10601320601031416
47. Verma D, Sharma SK. Recent advances in guar gum based drug delivery systems and their administrative routes. *Int J Biol Macromol*. 2021;181:653–671. doi:10.1016/j.ijbiomac.2021.03.087
48. Dodi G, Pala A, Barbu E, et al. Carboxymethyl guar gum nanoparticles for drug delivery applications: Preparation and preliminary in-vitro investigations. *Mater Sci Eng C Mater Biol Appl*. 2016;63:628–636. doi:10.1016/j.msec.2016.03.032
49. Soumya RS, Ghosh S, Abraham ET. Preparation and characterization of guar gum nanoparticles. *Int J Biol Macromol*. 2010;46(2):267–269. doi:10.1016/j.ijbiomac.2009.11.003
50. Abdelkader H, G. Alany R. Controlled and continuous release ocular drug delivery systems: Pros and cons. *Curr Drug Deliv*. 2012;9(4): 421–430. doi:10.2174/156720112801323125
51. Kumar S, Issarani R, Nagori B, Ahuja M. Design and evaluation of guar gum-based ofloxacin sustained release ocular insert. *Asian J Pharm*. 2014;6(3):198–203. <http://www.asiapharmaceutics.info/index.php/ajp/article/view/55>. Accessed April 15, 2023.
52. Shirakawa M, Yamatoya K, Nishinari K. Tailoring of xyloglucan properties using an enzyme. *Food Hydrocoll*. 1998;12(1):25–28. doi:10.1016/S0268-005X(98)00052-6
53. Freitas R, Martin S, Santos G, et al. Physico-chemical properties of seed xyloglucans from different sources. *Carbohydr Polym*. 2005;60(4): 507–514. doi:10.1016/j.carbpol.2005.03.003
54. Burgalassi S, Raimondi L, Pirisino R, Banchelli G, Boldrini E, Saettone MF. Effect of xyloglucan (tamarind seed polysaccharide) on conjunctival cell adhesion to laminin and on corneal epithelium wound healing. *Eur J Ophthalmol*. 2000;10(1):71–76. doi:10.1177/112067210001000112
55. Ghelardi E, Tavanti A, Celandroni F, et al. Effect of a novel mucoadhesive polysaccharide obtained from tamarind seeds on the intraocular penetration of gentamicin and ofloxacin in rabbits. *J Antimicrob Chemother*. 2000;46(5):831–834. doi:10.1093/jac/46.5.831
56. Rao P, Ghosh T, Krishna S. Extraction and purification of tamarind seed polysaccharide. *J Sci Ind Research*. 1946;4:705.
57. Goyal P, Kumar V, Sharma P. Carboxymethylation of tamarind kernel powder. *Carbohydr Polym*. 2007;69(2):251–255. doi:10.1016/j.carbpol.2006.10.001
58. Ghelardi E, Tavanti A, Davini P, et al. A mucoadhesive polymer extracted from tamarind seed improves the intraocular penetration and efficacy of rifloxacin in topical treatment of experimental bacterial keratitis. *Antimicrob Agents Chemother*. 2004;48(9):3396–3401. doi:10.1128/AAC.48.9.3396-3401.2004
59. Mahajan HS, Deshmukh SR. Development and evaluation of gel-forming ocular films based on xyloglucan. *Carbohydr Polym*. 2015; 122:243–247. doi:10.1016/j.carbpol.2015.01.018
60. Vijaya C, Goud K. Ion-activated in situ gelling ophthalmic delivery systems of azithromycin. *Indian J Pharm Sci*. 2011;73(6):615–620. doi:10.4103/0250-474X.100234
61. Guillaumie F, Furrer P, Felt-Baeyens O, et al. Comparative studies of various hyaluronic acids produced by microbial fermentation for potential topical ophthalmic applications. *J Biomed Mater Res A*. 2010; 92(4):1421–1430. doi:10.1002/jbm.a.32481
62. Aragona P, Papa V, Micali A, Santoccono M, Milazzo G. Long term treatment with sodium hyaluronate-containing artificial tears reduces ocular surface damage in patients with dry eye. *Br J Ophthalmol*. 2002;86(2):181–184. doi:10.1136/bjo.86.2.181
63. Condon PI, McEwen CG, Wright M, Mackintosh G, Prescott RJ, McDonald C. Double blind, randomised, placebo controlled, cross-over, multicentre study to determine the efficacy of a 0.1% (w/v) sodium hyaluronate solution (Fermavisc) in the treatment of dry eye syndrome. *Br J Ophthalmol*. 1999;83(10):1121–1124. doi:10.1136/bjo.83.10.1121
64. Lin J, Wu H, Wang Y, Lin J, Chen Q, Zhu X. Preparation and ocular pharmacokinetics of hyaluronan acid-modified mucoadhesive liposomes. *Drug Deliv*. 2016;23(4):1144–1151. doi:10.3109/10717544.2014.991952
65. Zeng W, Li Q, Wan T, et al. Hyaluronic acid-coated niosomes facilitate tacrolimus ocular delivery: Mucoadhesion, precorneal retention, aqueous humor pharmacokinetics, and transcorneal permeability. *Colloids Surf B Biointerfaces*. 2016;141:28–35. doi:10.1016/j.colsurfb.2016.01.014
66. Bao S, Yu A, Shi H, et al. Glycol chitosan/oxidized hyaluronic acid hydrogel film for topical ocular delivery of dexamethasone and levofloxacin. *Int J Biol Macromol*. 2021;167:659–666. doi:10.1016/j.ijbiomac.2020.11.214
67. Toda I, Shinozaki N, Tsubota K. Hydroxypropyl methylcellulose for the treatment of severe dry eye associated with Sjögren's syndrome. *Cornea*. 1996;15(2):120–128. doi:10.1097/00003226-199603000-00003
68. Donschik PC, Nelson JD, Abelson M, McCulley JP, Beasley C, Laibovitz RA. Effectiveness of BION tears, Cellufresh, Aquasite, and Refresh Plus for moderate to severe dry eye. In: Sullivan DA, Dartt DA, Meneray MA, eds. *Lacrimal Gland, Tear Film, and Dry Eye Syndromes 2*. Vol. 438. *Advances in Experimental Medicine and Biology*. Boston, USA: Springer US; 1998:753–760. doi:10.1007/978-1-4615-5359-5_106
69. Tundisi LL, Mostaçõ GB, Carricondo PC, Petri DFS. Hydroxypropyl methylcellulose: Physicochemical properties and ocular drug delivery formulations. *Eur J Pharm Sci*. 2021;159:105736. doi:10.1016/j.ejps.2021.105736
70. El-Sousi S, Nâcher A, Mura C, et al. Hydroxypropylmethylcellulose films for the ophthalmic delivery of diclofenac sodium. *J Pharm Pharmacol*. 2013;65(2):193–200. doi:10.1111/j.2042-7158.2012.01587.x
71. Al-Saedi ZHF, Alzhrani RM, Boddu SHS. Formulation and in vitro evaluation of cyclosporine-A inserts prepared using hydroxypropyl methylcellulose for treating dry eye disease. *J Ocul Pharmacol Ther*. 2016;32(7):451–462. doi:10.1089/jop.2016.0013
72. Donnerfeld ED, Holland EJ, Durrie DS, Raizman MB. Double-masked study of the effects of nepafenac 0.1% and ketorolac 0.4% on corneal epithelial wound healing and pain after photorefractive keratectomy. *Adv Ther*. 2007;24(4):852–862. doi:10.1007/BF02849978
73. Chen X, Li X, Zhou Y, et al. Chitosan-based thermosensitive hydrogel as a promising ocular drug delivery system: Preparation, characterization, and in vivo evaluation. *J Biomater Appl*. 2012;27(4):391–402. doi:10.1177/0885328211406563
74. Ashri LY, Abou El Ela AESF, Ibrahim MA, Alshora DH, Naguib MJ. Optimization and evaluation of chitosan buccal films containing tenoxicam for treating chronic periodontitis: In vitro and in vivo studies. *J Drug Deliv Sci Technol*. 2020;57:101720. doi:10.1016/j.jddst.2020.101720
75. Koji D, Hiroshi A. Ophthalmic composition containing xanthan gum and amino acid. US patent US7939511B2. May 10, 2011. <https://patents.google.com/patent/US7939511B2/en>.
76. Moji C, Vieki L, Uday K. In-situ gel ophthalmic drug delivery system of estradiol or other estrogen for prevention of cataracts. US patent US20110082128A1. March 25, 2014. <https://patents.google.com/patent/US20110082128A1/en>.
77. Kraja AT, Liu C, Fetterman JL, et al. Associations of mitochondrial and nuclear mitochondrial variants and genes with seven metabolic traits. *Am J Hum Genet*. 2019;104(1):112–138. doi:10.1016/j.ajhg.2018.12.001
78. Wolkoff P, Skov P, Franck C, Petersen LN. Eye irritation and environmental factors in the office environment-hypotheses, causes and a physiological model. *Scand J Work Environ Health*. 2003;29(6):411–430. doi:10.5271/sjweh.748
79. West SD, Turnbull C. Eye disorders associated with obstructive sleep apnoea. *Curr Opin Pulm Med*. 2016;22(6):595–601. doi:10.1097/MCP.0000000000000322.